Multi-Axis Laser-Assisted Milling of Difficult-to-Machine Alloys

Ali Ibrahim

Department of Mechanical Engineering

McGill University

Montreal, Quebec, Canada

August 2021

A thesis submitted to McGill University in partial fulfillment of the requirements of the degree of Doctor of Philosophy

Abstract

The ever increasing demand for developing advanced difficult-to-cut materials for aerospace, automotive and medical applications is hindered by the materials' poor machinability, when conventional material removal processes are used. Machining of these materials is characterized by high cutting forces, low material removal rates, excessive tool wear, poor surface quality due to micro cracking and flaking, the use of expensive cutting tools, and the use of large amount of coolants. Therefore, to exploit the full potential application of this class of materials, the development of innovative hybrid machining processes is necessary.

In this thesis, a novel external laser delivery system was developed for laser-assisted milling (LAML) of parts of 3D complex features that require 3- to 5-axis machining centers. Through the use of independent linear and rotary actuators, this system can readily be retrofitted to existing CNC machining centers of different configurations. Additionally, this system can deliver the laser beam in any direction ahead of the cutting tool, and precisely control the size of the heating spot, and its leading distance from the cutting tool.

A control system to automate and synchronize the movements of the developed multi-axis laser delivery system with CNC machining center was developed. The system design is based on industry standard real-time communication protocols and has the ability to be integrated into CNC machining centers with closed architecture controllers that restrict the access to vital programming and configuration information.

A fundamental understanding of the effect of laser parameters on surface roughness, residual stresses, micro-structure transformations, and machining forces was gained through numerical modeling and experimental investigation of surface heat treatment and laser-assisted milling (LAML) of AISI H13 tool steel.

Extensive experimental testing of the LAML system was conducted on AISI H13 tool steel. Compared to conventional milling processes, LAML significantly reduced the cutting forces by up to 40%, improved surface roughness by up to 23%, and allowed for higher material removal rates by up to 30%.

Three-dimensional finite-element-based models were developed, and validated experimentally, to simulate laser surface heating (LSH), laser surface heat treatment (LSHT) and LAML processes. These

models considered the effects of the surface inclination and the asymmetric Gaussian intensity distribution of the incident laser beam, which reflect the real applications of the LAML process. The models included an integrated microstructure evolution module and considered the thermal and mechanical processes interactions with phase transformations. The predicted surface temperatures, cutting forces, and hardened zones depths were found to be in good agreement with experimental results, confirming the reliability of this predictive capability for process development, design, and optimization.

Résumé

La demande sans cesse croissante de développement de matériaux avancés difficiles à couper pour les applications aérospatiales, automobiles et médicales est entravée par la faible usinabilité des matériaux, lorsque des procédés d'enlèvement de matière conventionnels sont utilisés. L'usinage de ces matériaux se caractérise par des forces de coupe élevées, de faibles taux d'enlèvement de matière, une usure excessive des outils, une mauvaise qualité de surface due aux microfissures et à l'écaillage, l'utilisation d'outils de coupe coûteux et l'utilisation d'une grande quantité de liquide de refroidissement. Par conséquent, pour exploiter tout le potentiel d'application de cette classe de matériaux, le développement de procédés d'usinage hybrides innovants est nécessaire.

Dans cette thèse, un nouveau système de livraison laser externe a été développé pour le fraisage assisté par laser (LAML) de pièces de caractéristiques complexes 3D qui nécessitent des centres d'usinage 3 à 5 axes. Grâce à l'utilisation d'actionneurs linéaires et rotatifs indépendants, ce système peut facilement être installé sur des centres d'usinage CNC existants de différentes configurations. De plus, ce système peut délivrer le faisceau laser dans n'importe quelle direction devant l'outil de coupe et contrôler avec précision la taille du point de préchauffage et sa distance par rapport à l'outil de coupe.

Un système de contrôle a été développé pour automatiser et synchroniser les mouvements du système de livraison laser multiaxes développé avec ceux du centre d'usinage CNC. La conception du système est basée sur des protocoles de communication en temps réel conformes aux normes industrielles et peut être intégrée dans des centres d'usinage CNC avec de contrôleurs à architecture fermée qui limitent l'accès aux informations vitales de programmation et de configuration.

Une compréhension fondamentale de l'effet des paramètres du laser sur la rugosité de surface, les contraintes résiduelles, les transformations de la microstructure et les forces d'usinage a été acquise par la modélisation numérique et l'étude expérimentale du traitement thermique de surface et du fraisage assisté par laser (LAML) de l'acier à outils AISI H13.

Des tests expérimentaux approfondis du système LAML ont été réalisés sur de l'acier à outils AISI H13. Comparé aux procédés de fraisage conventionnels, LAML a considérablement réduit les forces de coupe jusqu'à 40 %, a amélioré la rugosité de surface jusqu'à 23 % et a permis des taux d'enlèvement de matière plus élevés jusqu'à 30 %.

Des modèles tridimensionnels basés sur les éléments finis ont été développés et validés expérimentalement pour simuler le chauffage de surface au laser (LSH), le traitement thermique de surface au laser (LSHT) et les processus LAML. Ces modèles prennent en compte les effets de l'inclinaison de la surface et de la distribution d'intensité gaussienne asymétrique du faisceau laser incident, qui reflètent les applications réelles du procédé LAML. Les modèles comprenaient un module intégré d'évolution de la microstructure et prenaient en compte les interactions des processus thermiques et mécaniques avec les transformations de phase. Les températures de surface, les forces de coupe et les profondeurs des zones durcies prédites se sont avérées en bon accord avec les résultats expérimentaux, confirmant la fiabilité de cette capacité prédictive pour le développement, la conception et l'optimisation de processus.

Acknowledgements

First and foremost, I would like to express my sincere gratitude and appreciation to Professor Helmi Attia, Professor Vincent Thomson, and Professor Yaoyao Zhao for supervising my research work. I am especially grateful to Professor Attia and Professor Thomson for accepting me as a Ph.D. student at McGill University. I would like to thank them for their continuous support, guidance, and insightful feedback throughout the past four years. I am also very grateful to Professor Attia for providing me with the great opportunity to conduct my entire Ph.D. research work at the Aerospace Manufacturing Technologies Centre (AMTC) at the National Research Council Canada (NRC), where I gained access to state-of-the-art research facilities in aerospace manufacturing engineering. I am also very grateful to Dr. Bin Shi, from AMTC, for his co-supervision of the work carried out at the NRC, continuous support, fruitful discussions, and invaluable feedback on my research work. I would like also to thank all the research officers and technical officers of AMTC for being very supportive and helpful.

I would like to acknowledge the financial support from the McGill Engineering Doctoral Award (MEDA) and the Natural Sciences and Engineering Research Council of Canada (NSERC). I would like also to acknowledge the permissions provided by Elsevier and Springer Nature to include figures from cited references in this thesis.

Finally, I would like to express my most sincere gratitude to my family for their unconditional love, support, patience, and understanding throughout my Ph.D. journey.

Claims of Originality

The research carried out in this work is highly significant in addressing important gaps related to multi-axis laser-assisted milling of difficult-to-machine materials, which are of critical importance to many industrial applications. The following are the main original contributions of this work:

1. The development of a novel external laser delivery system that allows laser-assisted milling (LAML) of difficult-to-cut materials and parts of 3D complex features that require 3- to 5-axis machining centres. This system is composed of independent electric actuators, with the following advantages: (1) easily retrofittable to existing CNC machining centers, (2) easily customizable to suit standard tool holders, cutting tools and machine tool configurations, (3) can deliver the laser beam in all directions ahead of the cutting tool, while simultaneously controlling (3.a) the leading distance between the laser heating spot and the cutting tool, and (3.b) the size of the heating spot by controlling the position of the laser beam focal plane relative to the workpiece surface, and (4) capable of performing hybrid processes that combine multi-axis laser-assisted milling with laser surface heat treatment, using the same laser source and setup.

2. The development of a control system to automate and synchronize the movements of the multi-axis laser delivery system with CNC machining centers, with the following advantages: (1) it is based on industry standard real-time communication protocols, which allow the same control system to control a wide range of actuators of different sizes and from different manufacturers, and (2) it has the ability to be integrated to any CNC machining center, even those with closed architecture controllers with restricted access to vital programming and configuration information.

3. Fundamental understanding of the effect of laser surface heat treatment and laser-assisted milling on surface roughness, residual stresses, micro-structure transformations, and machining forces using numerical modeling and experimental investigation of LAML of AISI H13 tool steel.

4. The development of generalized 3D finite-element-based numerical models for the simulation of laser surface heating (LSH), laser surface heat treatment (LSHT), and laser-assisted milling (LAML) operations, considering the effects of the surface inclination and the asymmetric Gaussian intensity distribution of the incident laser beam, which reflect the real application in LAML processes. These models provide a reliable and feasible predictive capability for process development, design and optimization.

Table of Contents

List of Figures

List of Tables

Nomenclature

Symbols

A	Local area of the heat exchange window
A_{T_1} to A_{T_7}, A_{C_1}, A_{C_2}, and A_s	Coefficients determined from the steel material Time-Temperature-Transformation (TTT) diagrams
C	Carbon content
C_p	Specific heat
d	Leading distance between the laser heating spot and the cutting tool
d_{et}	Distance between the endmill start position and thermocouple position
D_{HAZ}	Total heat affected zone depth
D_{cone}	Imaginary base diameter of the laser cone
D_{cyl}	Diameter of cylinder
D_{fc}	Distance between laser focal point and the imaginary bottom diameter of the laser cone
D_{fw}	Defocusing distance
D_m	Depth of formed martensite
f	Federate / scanning speed
F_X	Cutting force measured in X direction
F_Y	Cutting force measured in Y direction
F_Z	Cutting force measured in Z direction
F_r	Resultant cutting force
h_A	Position of point A along the major axis

h_B	Position of point B
$h_{B.max}$	Length between the major axis and the outer boundary of the laser heating area
h_c	Heat transfer coefficient at the tool-chip interface
$h_{conv.}$	Heat transfer coefficient for convection
h_{eqv}	Equivalent convective coefficient of heat transfer
k_s	Local material shear flow stress
K	Thermal conductivity
$L_{m.axis}$	Major axis length of laser heating spot
n	Rotational speed
P	Laser power
P_d	Laser power density
$Plane_n$	Horizontal plane intersecting with moving point A
$\dot{Q}$	Radiative heat transferred per unit time
$\dot{Q}_V$	Power generation per unit volume
r	Radius
R	Laser beam radius at $Plane_n$
R_a	Surface roughness
t_{et}	Time taken by the endmill to move from the start position to the thermocouple position
T	Instantaneous temperature
T_0	Room temperature
T_{Ae}	Ending temperature of the transformation to austenite
T_{As}	Starting temperature of the transformation to austenite

$T_{induction}$	Surface preheating temperature by the induction heater
T_{laser}	Surface preheating temperature by the laser beam
T_{melt}	Material melting temperature
T_s	Temperature of the workpiece surface
T_w	Temperature of the window
U	Laser scanning speed
v	Velocity
V_z	Velocity in feed direction
w_1 to w_4	Material constants identified from the material TTT diagrams
x_p	Moving point A coordinate on X-axis
y_p	Moving point A coordinate on Y-axis
ε	Emissivity
$\bar{\varepsilon}$	Effective plastic strain
η	Absorptivity
θ	Workpiece inclination angle
$\theta_{L_{eff}}$	Laser beam effective inclination angle
$\theta_{L_{sur}}$	Laser inclination relative to the workpiece 3D surface
θ_L	Laser beam inclination angle relative to the workpiece surface
θ_d	Laser beam angle of divergence
θ_m	Torque motor angular position / position of the heating spot around the cutting tool, relative to the x-axis
μ	Friction coefficient
ξ_A	Volume fraction of austenite

ξ_m	Volume fraction of martensite
ρ	Density
σ	Stefan–Boltzmann constant for radiation
$\bar{\sigma}$	Flow stress
σ_m	Mean stress
σ_n	Normal stress acting along the tool rake face
τ_f	Frictional shear stress
Δa	Linear displacement of laser head actuator along its stroke
Δx	Distance between the cutting tool center and the laser heating spot center in X direction
Δy	Distance between the cutting tool center and the laser heating spot center in Y direction
Δz	Displacement of the laser beam focal point in the Z-axis direction

Acronyms and Abbreviations

AISI	American Iron and Steel Institute
ASTM	American Society for Testing and Materials
AMTC	Aerospace Manufacturing Technologies Centre
B&F	Back-and-forth
CAD	Computer-Aided Design
CAM	Computer-Aided Manufacturing
CCT	Continuous Cooling Transformation diagram
cDAQ	Compact Data Acquisition device

CIRP	Collège International pour la Recherche en Productique (International Academy for Production Engineering)
CNC	Computer Numerical Control
Conv.	Conventional
DAQ	Data Acquisition
DEFORM	Design Environment for FORMing
DIO	Digital Input/Output
DLAM	Direct Laser Assisted Machining
DOC	Depth of Cut
Ethernet/IP	Ethernet Industrial Protocol
Exp.	Experimental result
FE	Finite Element
FEM	Finite-Element-based numerical Modeling
Freq.	Frequency
G-code	Geometric code
HAZ	Heat Affected Zone
HSK	German acronym for 'Hohl Schaft Kegel', which means 'hollow taper shank'
I/O	Input/Output
JC	Johnson-Cook
LAB	Laser-Assisted Burnishing
LabVIEW	Laboratory Virtual Instrument Engineering Workbench
LAM	Laser-assisted machining
LAML	Laser-assisted milling
LAT	Laser-Assisted Turning

LSH	Laser Surface Heating
LSHT	Laser Surface Heat Treatment
MATLAB	MATrix LABoratory
M-code	Machine functions code
MMC	Metal Matrix Composites
MRR	Material Removal Rate
NRC	National Research Council Canada
PAM	Plasma-Assisted Machining
PLC	Programmable Logic Controller
SFTC	Scientific Forming Technologies Corporation
Sim.	Simulation result
TAM	Thermally-Assisted Machining
Ti-MMC	Titanium Metal Matrix Composite
TTT	Time-Temperature-Transformation diagram

Chapter 1: Introduction

1.1 Research Motivation and Terminal Objectives

The ever-growing demand for innovations in many industries over the past years has resulted in a continuously increasing need for advanced materials with superior mechanical, thermal, and chemical properties, such as titanium alloys, nickel-based alloys, cobalt-based alloys, metal matrix composites (MMC), structural ceramics, and high strength steels. Such advanced materials have a wide range of application potential in various industries, including the manufacturing of highly-stressed components for die and forming tool manufacturing, aircraft engine components, gas turbine components, and medical implants [1-4].

For example, there are three noticeable growing requirements in the engineering of aircraft engines and gas turbines [5]: 1) increasing fuel efficiency, 2) reduction of pollutants emission, and 3) conservation of resources. These three requirements can be directly achieved by improving the thermal efficiency of the turbine. The turbine becomes more efficient at higher inflow temperatures and higher compression ratios. Therefore, utilizing temperature resistant and high strength materials like Ni- and Ti- based alloys (e.g., Inconel718) enables higher energy efficiency. These alloys therefore allow the manufacturing of new enhanced aero engine materials and gas turbines, which are subjected to high alternating stresses and temperatures.

Another example is the utilization of advanced ceramics, such as Si_3N_4, in the die manufacturing industry. It was reported that using Si_3N_4 form inserts for the deep drawing of stainless steel sheet metal leads to a significant increase in the tool service life of up to 100 times [5] [6], since Si_3N_4 ceramics have exceptional wear resistance when subjected to high abrasive stress which occurs frequently in metal forming processes such as deep drawing.

AISI H13 tool steel, which is the material extensively used in this research work, is another example of an advanced material that is characterized by high hardenability, high strength, high toughness, high thermal fatigue resistance, and high resistance to thermal softening [7-9]. Therefore, this type of steel has been widely used in the manufacturing of many different types of hot working dies, such as die-casting dies, extrusion dies, and forging dies [10]. AISI D2 is another example of a tool steel with moderate toughness combined with excellent wear resistance. This type of steel has been widely used in the manufacturing of many different types of cold working tools for punching, bending, deep-drawing, and dies for molding abrasive materials [11].

The main factor that hinders the broad use of the above-mentioned advanced materials is their poor machinability using conventional material removal technologies, which significantly increases their production cost. Machining of these advanced materials is characterized by:

- High cutting forces.
- Extensive use of cooling lubricants.
- Excessive wear of cutting tools.
- Poor surface quality due to micro-cracking and flaking.
- Inefficient machining due to low material removal rates.

Therefore, to exploit the full potential application of this class of materials, development of innovative and economic machining processes is necessary.

Several novel emerging processes and technologies are being developed to improve the machinability of difficult-to-cut materials. This includes external-energy-assisted machining, cryogenic cooling, and vibration-assisted machining. In recent years, research efforts are being directed towards hybrid processes that combine thermally-assisted machining, to soften the workpiece by heating, with cryogenic tool cooling [12, 13]. By making the workpiece softer and the tool cooler, one can achieve lower cutting forces and higher cutting speeds.

Thermally-assisted machining (TAM) is a process that uses an external heat source to preheat the workpiece material just prior its engagement with the cutting tool. As a result of heating, the yield strength, hardness, and strain hardening rate of the workpiece material is reduced and the deformation behaviour of the difficult-to-machine materials, especially ceramics, changes from brittle to ductile. This allows this class of materials to be machined more easily and with lower machine power consumption, which leads to an increase in material removal rate, productivity, and process sustainability. It is necessary for the external heat source to be localized, to have high energy density, and to be controllable since inappropriate application of the heat source may excessively heat the cutting tool, which shortens its life, or introduce undesirable tensile residual stresses and microstructural degradation of the workpiece material after machining. In recent years, the main research efforts in this area have been focused on laser-assisted machining (LAM) at both the macro and micro scale, mostly because of the ease of controllability of laser and its relatively high energy density.

Most of the research work previously performed in the area of LAM was limited to simple machining operations, such as turning, while very limited effort was made in multi-axis laser-assisted milling (LAML) processes. This is because the integration of laser heating with multi-axis milling is a complicated task, since the process involves complex movements in multiple independent axes, a continuously changing feed direction to produce parts with complex three-dimensional geometric features. However, the increasing demand for machining such components that are made of advanced materials necessitates the development of multi-axis laser-assisted milling systems. In the next chapter, a detailed discussion and a critical literature review are presented for TAM, with special consideration of LAM.

The terminal objectives of this research work are: 1) development of a multi-axis laser-assisted milling system that is capable of machining workpieces with complex three-dimensional geometries, 2) testing the developed multi-axis LAML system for machining of AISI H13 tool steel (52 HRC as-received in room temperature), 3) investigating the effect of LAML parameters on the preheating temperatures, cutting forces, micro-structure evolution, heat affected zone size, and surface integrity (surface roughness and induced-residual stresses) of H13 tool steel, and comparing the results to conventional dry and wet milling, and 4) developing three-dimensional finite-element-based numerical models to be used as predictive tools for LAML process design and optimization.

Each of the terminal objectives is discussed in more detail in chapter 2, section 2.5, following the identification of the gaps in the current state-of-the-art of LAML that need to be filled (section 2.4). In order to achieve these research objectives, a research methodology is discussed in detail in section 2.6 that combines experimental and finite-element-based numerical modeling techniques.

This research work is part of a joint research project between McGill University and the Aerospace Manufacturing Technologies Centre (AMTC), the National Research Council Canada (NRC).

1.2 Thesis Outline

The outline of the thesis is presented below with a brief description of the content of each chapter:

- **Chapter 1:**

  The motivation behind the research work is discussed, and its terminal objectives are presented.

- **Chapter 2:**

  This chapter presents a critical literature review of previous research work performed in laser-assisted machining and, more generally, thermally-assisted machining. Analysis of the gaps in previous research work is presented, followed by a detailed discussion of the specific research objectives and methodology to be adopted to achieve these objectives.

- **Chapter 3:**

  This chapter presents the work carried out to develop, design, and integrate a multi-axis laser-assisted milling system. This system utilizes a set of actuators to deliver the laser beam anywhere around the cutting tool. Two electric linear actuators are controlled to maintain a certain size of the heating spot in front of the tool by actively adjusting the laser focal point position relative to the workpiece and the leading distance relative to the cutting tool. Another rotational electric direct drive torque motor is used to change the position of the heating spot around the cutting tool, allowing the tool to cut in different directions.

- **Chapter 4:**

  This chapter presents the work done to experimentally test the multi-axis LAML system developed in Chapter 3 for different workpiece geometries using different cutting conditions and laser heating parameters. In addition, the LAML system performance is compared to conventional milling.

- **Chapter 5:**

  This chapter presents experimental and finite-element-based numerical investigations for the microstructure transformations that occur during LAML and laser surface heat treatment (LSHT) of AISI H13 tool steel, where a laser beam is applied on the workpiece to rapidly heat its surface, which results in the formation of a hardened outer surface layer without changing desirable bulk material properties, such as ductility and toughness. The LSHT experiments were conducted with different laser power levels and different heating times. A three-dimensional finite-element-based model was developed for the LSHT process, which included an integrated microstructure evolution model to consider the thermal and mechanical processes interactions with phase transformations. The FE model was validated using the experimental results.

- **Chapter 6:**

  This chapter presents the work performed to develop finite-element-based numerical models for laser surface heating and laser-assisted milling of flat and 3D surfaces. In addition, the development of a Matlab code is presented in-detail to generate three-dimensional laser power density curves for laser beams inclined at any angle. The effects of workpiece surface curvature, laser inclination angle, and laser oscillation are investigated using several FE models.

- **Chapter 7:**

  This chapter summarizes the main findings of the research work and presents recommendations for future work based on the research findings.

Chapter 2: Critical Literature Review

This chapter presents a critical literature review of previous research work performed in the field of thermally-assisted machining (TAM), and more specifically laser-assisted machining (LAM), aimed at improving the machinability of advanced and difficult-to-cut materials.

Section 2.1 of this chapter discusses the general effect of TAM processes on the machinability of difficult-to-machine materials, with their advantages and limitations. In addition, it presents the different heat sources utilized for TAM. A more detailed discussion of the techniques developed for laser-assisted machining (LAM), specifically laser-assisted turning (LAT) and laser-assisted milling (LAML), is then presented in section 2.2 and section 2.3, respectively, with special focus on the work carried out for LAM modeling. Section 2.4 focuses on the analysis of the gaps in previous research work performed on LAML. Finally, section 2.5 presents the objectives and methodology of the research conducted in this thesis to address the mentioned research gaps.

2.1 Thermally-Assisted Machining (TAM)

2.1.1 Effect of TAM on Machinability

Thermally-assisted machining involves the use of an external heat energy to soften the material before its removal by cutting. Increasing the temperature of the workpiece decreases its hardness and strength, which leads to several improvements in its machinability, but it may lead to some undesirable consequences. Figure 2.1 shows the significant reduction of strength of several difficult-to-cut materials as a result of heating [14]. The improvements in material machinability include reduced cutting forces, increased material removal rates, improved surface finish, and enhanced cutting tool life [15-24]. These improvements together can lead to significant reduction in machining costs, reaching nearly 30 to 40% for TAM of titanium alloys, for example [13]. However, care must be taken not to heat the cutting tool itself, as this reduces its useful life [25]. In addition to this possible drawback, the heating effect usually introduces undesirable tensile residual stresses on the workpiece surface and deeper into the material subsurface [26-37], which could worsen the workpiece fatigue life. Furthermore, excessively heating the workpiece leads to transformations in the microstructure of machined components [20, 38], which could be undesirable for some applications, as in the formation of the brittle white layer. The opposite effects of the thermally-assisted machining process highlights the need for fundamental understanding of various mechanisms and interactions involved in such a process, in order to optimize its performance and reduce its negative effects.

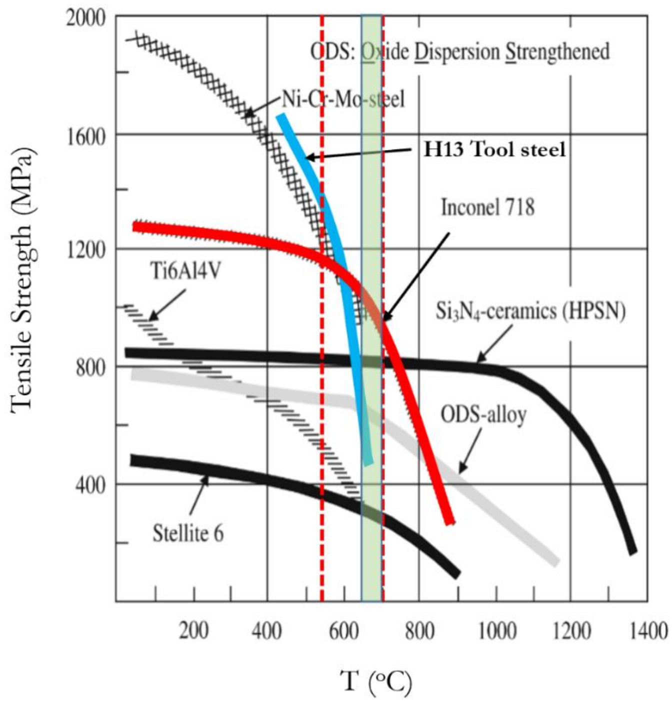

Figure 2.1. Effect of heating on the strength of several difficult-to-cut materials. The figure is adapted from [2, 14].

Considering TAM of Inconel 718 as an example, the primary strengthening mechanism of this material is age hardening due to the existence of fine uniform metastable 'γ' precipitates dispersed throughout the matrix. By heating this material to temperatures between 540 and 700 ºC (shown in Figure 2.1 as red dotted lines), the deformation becomes homogenously distributed, consisting of uniformly tangled dislocations. Further heating to temperatures above 700 ºC causes the precipitations to reach their stability limit, leading to a significant drop in the material yield strength [39]. These transitions can be seen in Figure 2.1. The investigation carried out by Attia et al. [40] showed that the optimum TAM conditions, using laser as the external heat source, for turning Inconel 718 was achieved for surface temperatures between 650 to 700 ºC (shaded area in Figure 2.1). It was also shown that if the power density of the localized laser heating exceeded a certain level (of about 1 W/mm^2), it may cause plasma gas generation and surface damage.

In terms the surface integrity of Inconel 718, the investigation carried out by Xu et al. [26] for laser-assisted milling of Inconel 718 revealed that a complex residual stress distribution was induced in the Inconel 718 workpieces due to primarily the addition of external heating, as shown in Figure 2.2. High tensile residual stresses were formed on the workpiece surface due to the thermal loading resulting from both external heating and the heat generated by cutting. Due to the mechanical loading of the cutting operation, compressive residual stresses were found beneath the surface up to a depth of roughly 100 µm. Then, at a depth of around 300 µm, tensile residual stresses of up to 1100 MPa reappeared, owing to the mechanical loading of the cutting process failing to fully counteract the substantial tensile residual stresses induced by the combined heat generated by external heating and cutting at deeper depths of the workpiece material. These significant tensile residual stresses increased the workpiece vulnerability to fatigue loading, which led to lowering its fatigue life [26].

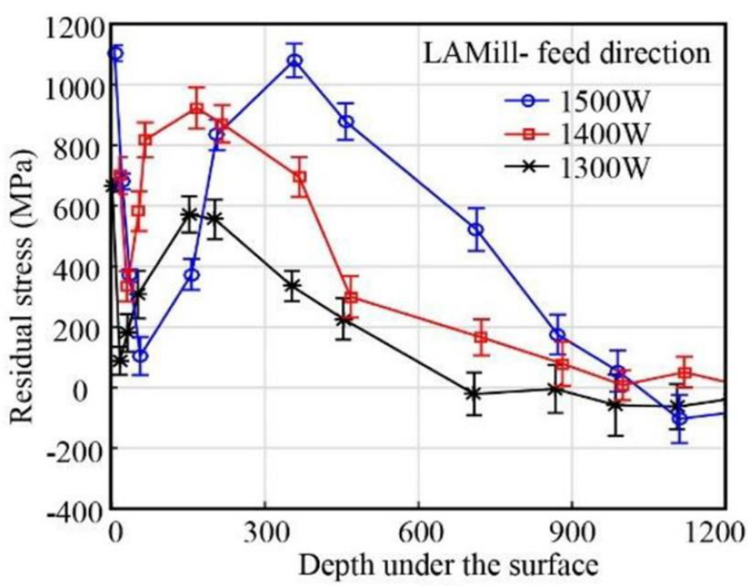

Figure 2.2. Complex residual stress distributions induced by TAM in Inconel 718 at different power levels [26].

In addition to the undesirable tensile residual stresses, TAM of different materials resulted in microstructure changes occurring in the heat affected zones with depths proportional to the power and time used for heating [20, 41-46]. The desirability of these microstructure changes depends on the application. For some applications, such as laser surface heat treatment (LSHT), the microstructure changes are done intentionally to locally harden the top surface of the workpiece without changing the desirable bulk properties of the workpiece material [38]. However, for other applications, microstructure transformation could be undesirable such as the formation of the white layer, which has negative effect on the surface integrity and the fatigue life of components subjected to dynamic loading [26, 47-51].

To avoid the possible drawbacks of TAM in altering surface integrity and microstructure, and to reap the maximum benefits of increased material removal rates and decreased cutting forces, TAM could be used mainly for *roughing* machining operations, followed by finishing machining operation(s) without external heating. This finishing operation could be utilized to remove the undesirable tensile residual stresses and/or the undesirable microstructure changes, while mechanically inducing compressive stresses. Alternatively, other subsequent processes such as shot peening could be used to induce compressive residual stresses on the workpiece top surface [52-55], when the deeper tensile residual stresses are not critical to the application. For steels, conventional shot peening could achieve compressive residual stresses to depths between 0.4 to 0.9 mm [56-58].

TAM has also been used for a wide range of other difficult-to-machine materials. For example, as reported in [59], although ceramic particles in Titanium Metal Matrix Composites (Ti-MMCs) improve its wear resistance properties, they also cause high abrasive tool wear. Application of TAM, using localized laser heating, for Ti-MMCs machining showed significant increase in tool life by up to 180%. The unexpected phenomenon of increased tool life at higher cutting speeds was consistently observed in all machining conditions and was related to fewer broken TiC particles that are embedded into the soft chip, and consequently less abrasion wear.

It is interesting to note that TAM has also a great potential to improve the machinability of high ductility materials that are difficult-to-machine due to the strong adhesion of the chip to the cutting edge, which leads to poor surface finish. This can be attributed to the softening of inclusions or the phase transformations in the chip during thermally enhanced machining, causing a reduction in local ductility of the workpiece [2]. Germain et al. [60] experimentally investigated the TAM of the ductile low alloyed steel '42CrMo4' and reported a significant improvement of up to 56% in workpiece surface finish compared to conventional machining of the same material.

For TAM of high strength tool steels, Kaselouris et al. [61, 62] investigated the TAM of AISI H13 tool steel using localized laser heating, and reported a reduction in cutting forces by up to 15%, compared to conventional machining. Dumitrescu et al. [11, 63] investigated the TAM of AISI D2 tool steel using a high-power diode laser and reported a 100% increase in cutting tool life, prevention of saw-tooth chip formation and machining chatter, and reduction of cutting forces by up to 50 %.

2.1.2 TAM Heat Sources

Several heating sources have been reported in the literature for TAM such as gas flame torches, induction coils, plasma, laser beams, and electron beams [16]. These sources are discussed in this section, except for electron beam heating, as it is considered unpractical, as it requires vacuum to work, and is very costly [1].

2.1.2.1 Gas Flame Heating

In machining processes assisted by gas flame heating, a torch is used to generate a flame to heat the workpiece above its recrystallization temperature [64, 65]. As mentioned earlier, this decreases the workpiece resistance to cutting, and consequently improves its machinability. A system proposed by Özler et al. [65] is shown in Figure 2.3, where a gas flame heating torch was retrofitted on the carriage of a conventional lathe to provide external heating to the cutting zone. In the used torch, a mixture of oxygen and liquid petroleum gas is burned to heat an austenitic manganese steel workpiece. A workpiece temperature control system was integrated to control the heating process. It was shown that when this technique was used to machine austenitic manganese steels at temperatures higher than 600°C, the tool life was improved by up to 150% and the productivity was enhanced, by increasing the feedrate by up to 700% and the cutting speeds by up to 240%. However, this method suffers from a number of drawbacks; (1) it is limited to a unidirectional motion, i.e., a single degree of freedom, (2) the extreme difficulty of concentrating the heat affected zone on the work piece, and (3) the difficulty of precisely controlling the workpiece temperature. For this material, the selection of 400°C as the maximum heating temperature, prevents unwanted structural changes.

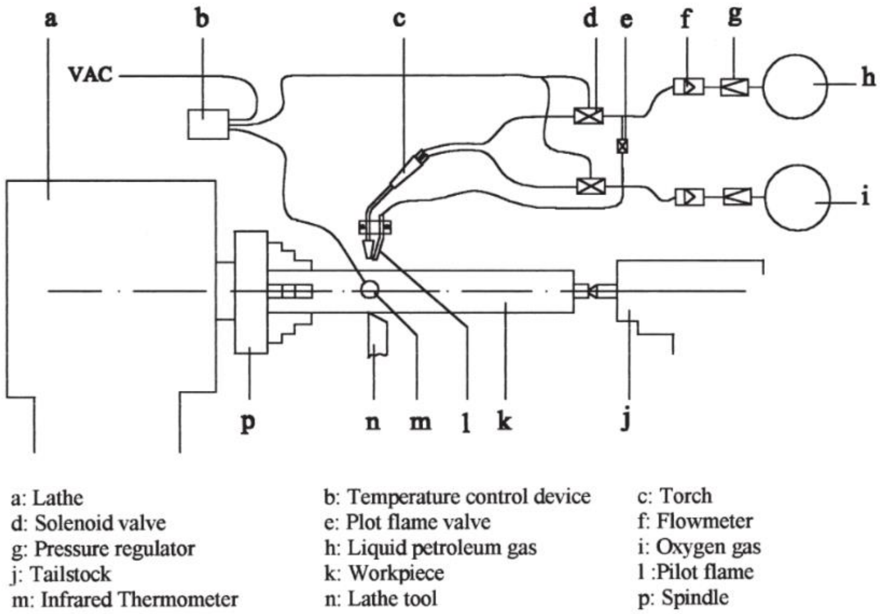

Figure 2.3. Schematic representation of the experimental setup used for machining assisted by gas flame heating [65].

2.1.2.2 Induction Heating

In machining processes assisted by induction heating, the workpiece is preheated prior to cutting by electromagnetic induction. Figure 2.4 shows the experimental setup developed by Lajis et al. [66]. In this setup, a 25 kVA induction coil is positioned in close proximity of the workpiece (AISI D2 hardened tool steel) and in front of the milling cutter (TiAlN coated carbide cutting tool). At cutting speed of 40 m min^{-1}, the preheating temperature was in the range of 250 to 450°C. The workpiece temperature was monitored by an infrared pyrometer and was varied by controlling the current supplied to the induction coil. In this work, the authors reported an improvement of workpiece surface finish by up to 50%, and a significant increase in tool life by up to 240%. Nonetheless, this technique still suffers from the same drawbacks of gas flame heating; unidirectional movement of the heat source, the difficulty of concentrating the heat affected zone on the work piece, and the difficulty of controlling the workpiece temperature.

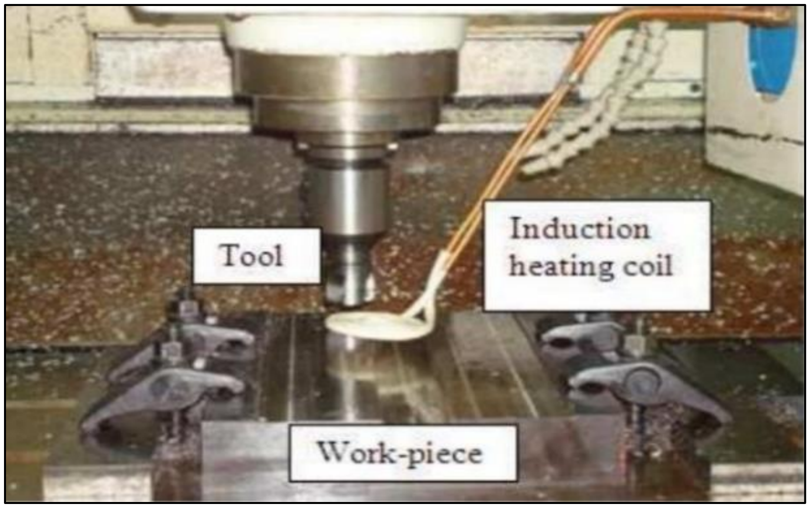

Figure 2.4. Experimental setup used by Lajis et al. for machining assisted by induction heating [66].

2.1.2.3 Plasma Heating

In plasma-assisted machining technique (PAM), a plasma arc is used to preheat the workpiece before cutting [17, 39, 67]. Figure 2.5 shows a typical plasma arc generator [39]. The PAM system used by De Lacalle et al. [17] is shown in Figure 2.6, where a plasma arc generator is attached to the spindle of a conventional milling machine, and the nozzle is fixed in position in front of the cutting tool (sintered tungsten carbide coated with TiAlN) in the direction of feed. This PAM system lacked a mechanism to change the position of the nozzle around the tool axis, which limited this system to unidirectional PAM. The workpiece surface temperature was monitored using an infrared camera. The authors used three workpiece materials: Inconel 718 (Ni-based alloy), Haynes 25 (Co-based alloy), and Ti6Al4V (Ti-based alloy). Although the temperature of the ionized gas (Argon) is well over 15,000 K, the speed at which the plasma jet impact the material surface (~ 400 m/s) produces work surface temperature in the range of 400 to 1,000°C. With Inconel 718 and Haynes 25, the PAM technique improved tool life by up to 100%, decreased cutting forces by up to 45% and did not affect material structural integrity. However, with Ti6Al4V, the PAM technique resulted in the degradation of the microstructure of the alloy, even with low plasma intensity and high feedrates. Additionally, since the plasma arc has a relatively large heating spot size (at least 4 mm in diameter), the removal of the whole heat affected material is not guaranteed by cutting. In addition, this makes the plasma arc not suitable for use with smaller cutting tools and intricate workpiece features. In this case, a laser beam is more suitable as a heating source, as it enables further reduction of the heating spot size [42].

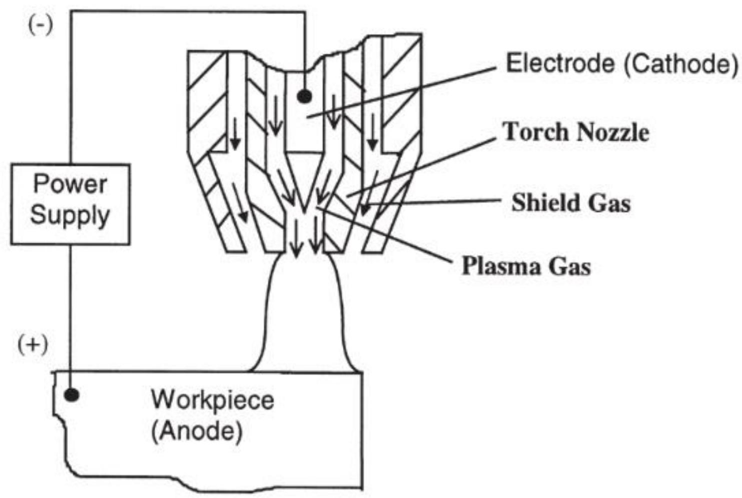

Figure 2.5. Details of a typical plasma arc generator used in PAM [39].

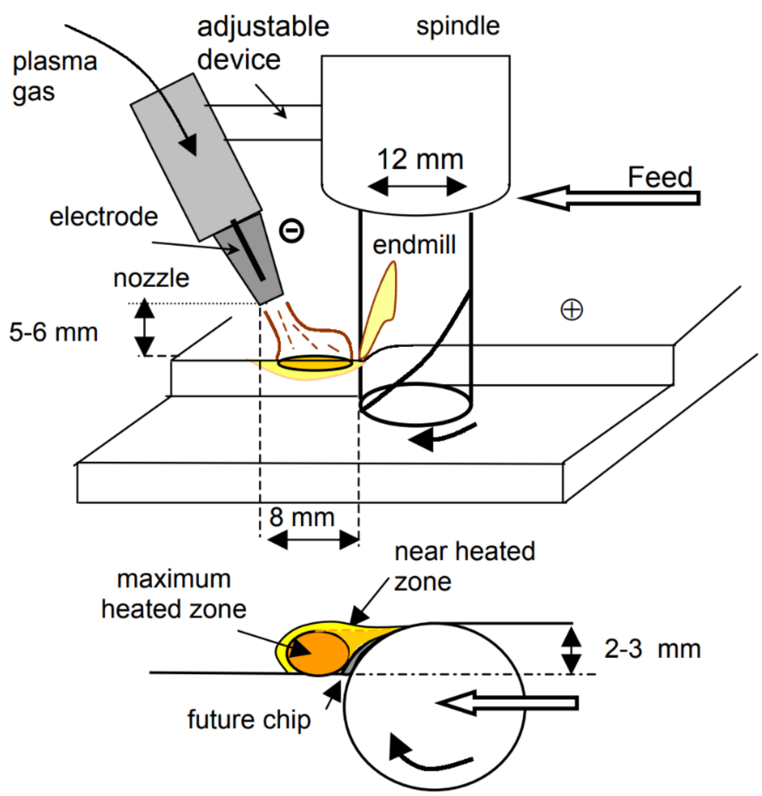

Figure 2.6. Main components of the PAM system [17].

2.1.2.4 Laser Beam Heating

In laser-assisted machining (LAM), a laser beam is used to precisely preheat a small spot on the workpiece before its removal by the cutting tool, as shown in the schematic in Figure 2.7. The diameter of the heating spot could be precisely controlled by controlling the focal point position relative to the workpiece. For macro LAM the size of the heating spot could be as small as 0.8 mm in diameter, which is the typical diameter of the focal point of high-power diode laser beams [68]. The depth and width of the heat affected zone are dependent on the following parameters [42]: (1) feedrate, (2) laser power, (3) laser beam angle, (4) diameter of heating spot, and (5) material properties, such as thermal conductivity and specific heat.

LAM has been successfully applied to a wide range of difficult-to-cut materials [69], and has been successfully commercialized for simple turning operations in Germany [70] and the United States [71]. LAM has been extensively studied in literature for machining titanium alloys [13, 72-76], nickel-based alloys [30, 40, 77-80], ceramics [31, 81-92], tool steels [11, 61, 62, 93], other ferrous alloys [34, 94-98], and composites [59, 99-103]. For example, while PAM failed to improve the machinability of Ti6Al4V [17], Dandekar et al. [13] reported a significant machinability improvement for the same material using LAM. The authors reported negligible effect of laser on Ti6Al4V microstructure and micro-hardness, increase of tool life by 170%, and 30% reduction of the machining cost. Furthermore, Bejjani et al. [59] have performed laser-assisted machining of Titanium metal matrix composites (TiMMC) and have reported a significant increase in cutting tool life by up to 180%.

For laser-assisted machining of nickel-based superalloys, Shi et el. [77] have investigated LAM of Inconel 718 and reported a significant reduction of cutting forces by up to 46%. Furthermore, Attia et al. [40] investigated the high-speed machinability of the same alloy under laser-assisted machining and dry conditions, and reported a 25% improvement in surface roughness compared to conventional dry machining. They contributed this improvement to the ease of material removal, which prevented surface tearing and smearing, in addition to the reduced the feed marks sharpness on the machined surface. The same authors also reported a 40% increase in tool life and a significant increase in the material removal rate by approximately 800%, compared to conventional machining.

Compared to other TAM techniques, the main advantages of LAM are: (1) the heat affected zone size could be precisely controlled by optimizing few parameters, (2) smaller heating spots could be achieved compared to the other TAM techniques, (3) laser has a relatively high energy density which can achieve much higher preheating temperatures, compared to the other heat sources, and (4) degradation of the microstructure of the workpiece could be avoided by optimizing laser heating parameters.

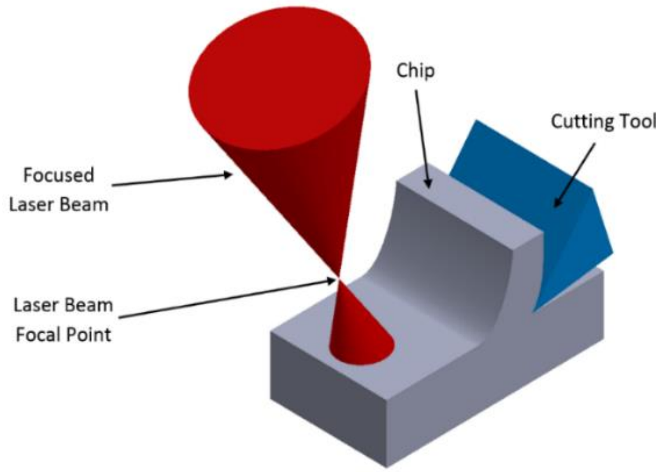

Figure 2.7. Schematic of laser assisted machining (LAM) principle.

2.2 Laser-Assisted Machining Processes

Over the past years, laser assisted turning (LAT) has been extensively studied in the open literature as the dominant application of LAM due to its simplicity; being only a 1- or 2-axis process [3, 11, 13, 34, 40, 72, 75, 79-81, 86-88, 95, 101, 104-112]. On the other hand, there are very few studies on laser-assisted milling (LAML) with 5-axis capability, because of the milling process complexity. Therefore, the laser heating spot position in LAML must keep changing to accommodate the continuously changing feed direction and the complex three-dimensional geometric features of the workpiece.

The demand for components with a wide range of geometric shapes has moved the application of LAM from the dominant turning operation toward milling [5, 21, 25, 32, 76, 91, 113-125], micro-milling [97, 126-132], planning [109], and grinding [133, 134].

The next two sections present the most common techniques used for turning, since it is the most common LAM process, and milling, since it is the focus of this research work.

2.2.1 Turning

Due to the simplicity of the turning process, integrating laser to a lathe is relatively easy. The most important parameters to control in laser-assisted turning (LAT) are [2]: (1) the leading distance between the laser heating spot and the cutting tool, (2) the laser power, (3) the laser beam angle, (4) the feedrate, and (5) the size of heating spot, which is controlled by varying the defocusing distance, which is the distance between the laser focal point and the workpiece surface, since the laser beam has a conical shape.

In the LAT work reported in the literature, the laser beam heating had different configurations as shown in Figure 2.8. The laser heating spot could be applied on the unmachined workpiece surface, as shown in Figure 2.8(a) [77, 135]. Another configuration has the laser beam directed to the chamfer surface instead, as shown in Figure 2.7(b). This second configuration was reported to achieve higher reduction in cutting forces and less heating of the cutting tool [75]. Shin et al. [136, 137] used two laser sources (a 1.5 kW CO2 laser and a 500 W Nd:Yag laser) strategically placed around the workpiece to heat it simultaneously, as shown in Figure 2.7(c), achieving the optimum temperature distribution for LAM across the material depth of cut.

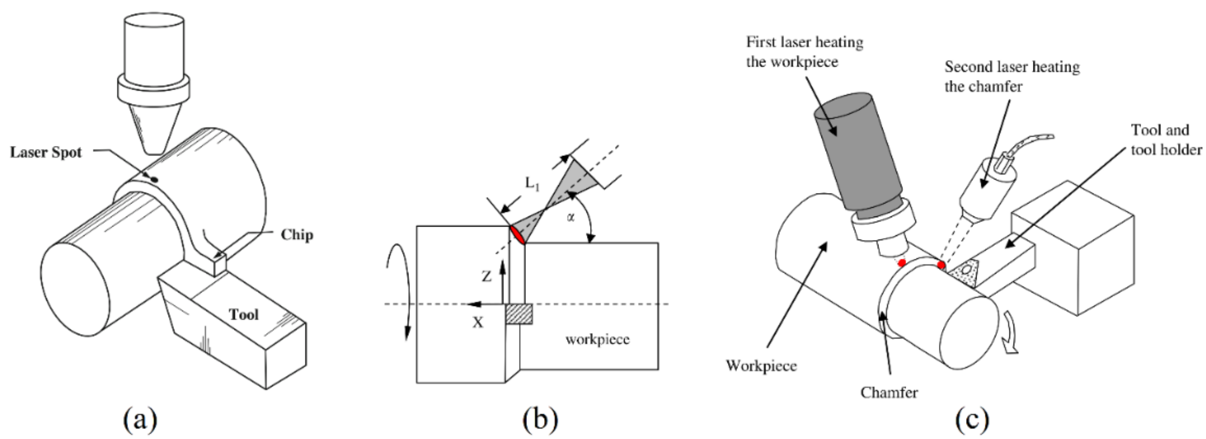

Figure 2.8. Possible LAT configurations. a) Laser beam heating is applied on workpiece surface [135]. b) Laser beam heating is applied on the chamfer surface [75]. c) Two laser beams are used; one applied to workpiece surface, and the other applied to the chamfer surface [75], [136].

In addition to applying the laser beam on the workpiece via an external laser head, such as the configurations previously shown in Figure 2.8, another LAT technique was developed to apply the laser beam through a transparent sapphire cutting tool to directly heat the interface between the tool and the workpiece [138-141]. This technique is known as direct laser-assisted machining (DLAM). Figure 2.9 shows a comparison between the concepts of conventional LAM and DLAM. When compared to conventional LAM, DLAM is advantageous in minimizing the laser-tool distance and minimizing heat loss. However, DLAM major disadvantage is that it could only work with transparent cutting tools.

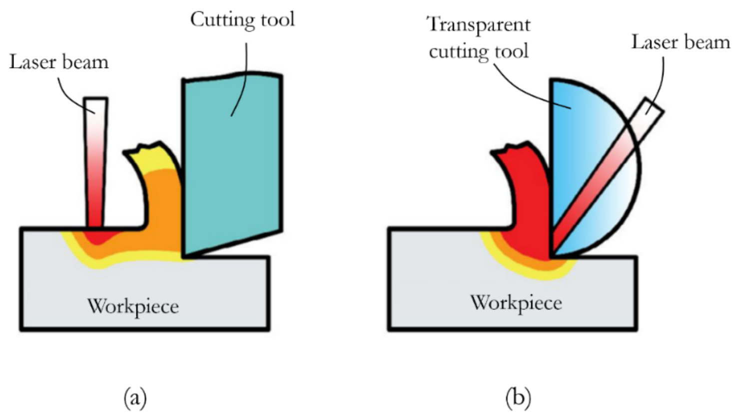

Figure 2.9. Comparison between the concepts of conventional laser-assisted machining (a) and direct laser-assisted machining (b). The figure is adapted from [141].

2.2.2 Milling

As mentioned earlier, there are several difficulties encountered in implementing LAM to milling processes: (1) the laser beam must always be ahead of the cutting tool in the direction of feed, which requires the development of a mechanism (with additional control axis or axes) to be able to precisely control the laser beam position, depending on the direction of cutting feed, and (2) the control of the heat affected zone size and temperature requires other mechanisms to actively control the position of the laser beam focal point and the beam's angle of inclination, relative to the workpiece surface. State-of-the-art laser-assisted milling (LAML) techniques are classified below according to the technique of laser beam delivery to the workpiece.

2.2.2.1 Coaxial Laser Beam Delivery

In this LAML technique, the laser beam is delivered to the workpiece through the center of the machine spindle [5, 116, 142]. The system proposed by Brecher et al. is shown in Figure 2.10. In this system, the laser beam is delivered through a hollow HSK[1] interface through the center of a *customized* spindle system. The optics necessary for laser beam guidance are integrated inside this customized spindle and tool holder.

The main advantage of this technique is its compactness. However, it suffers from several drawbacks: (1) it is impossible to integrate this system into existing CNC machines, without modifying the whole spindle, which makes this system harder, if not impossible, to be adopted by established industries, (2) this system cannot work with small cutting tool diameters in end milling. It could only work with large cutting diameters in face milling processes, and (3) the specially designed tool holder can only accommodate a limited number of cutting inserts (one or two inserts).

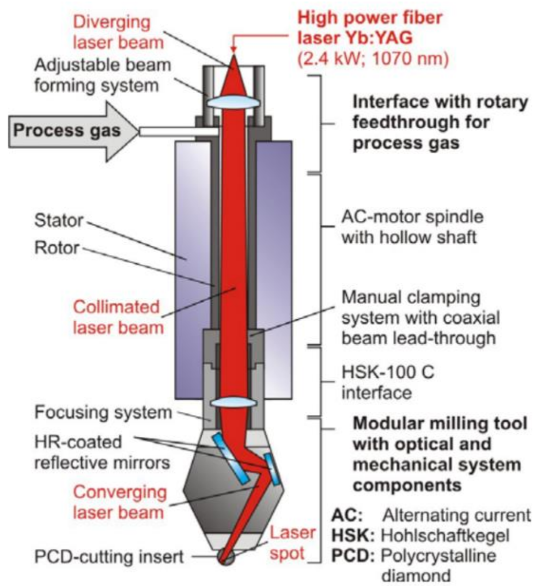

Figure 2.10. Coaxial laser beam delivery through the center of a modified machine spindle [5].

2.2.2.2 External Laser Beam Delivery

In this LAML technique, the laser beam is delivered to the workpiece via an external laser beam focusing head [113-115, 118, 119, 121]. The laser head position is controlled by one or more actuators. Examples from literature are shown in Figure 2.11. Figure 2.11(a) shows a LAML system developed by Bermingham et al. [118, 121], where the laser head is integrated into a conventional milling machine. Although the laser head in this system is controlled by three actuators, the laser beam could be

---

[1] HSK is the is the German abbreviation for 'Hohl Schaft Kegel', which means 'hollow taper shank'.

delivered only from one side, ahead of the cutting tool, which severely limits the cutting tool path for multi-axis milling, even when using a rotating CNC table. This system was also retrofitted with a rotating adaptor for the laser head, as shown in Figure 2.11(b).

For applications in which the size of the laser heating spot is very small compared to the size of the workpiece, the heat transfer process approaches that of a finite moving heat source on a semi-infinite body. Examination of the solution of this problem [143] shows that the surface temperature decreases rapidly by the time the tool reaches the heated zone. To overcome this problem, the system presented in Figure 2.11(b) enables the laser beam to oscillate in a zigzag motion along the longitudinal direction (perpendicular to the feed direction) ahead of the cutting tool and delays the cooling of the targeted preheating area. As pointed out by Hwang et al. [144], the preheating path of zigzag can be designed for overlapping the heat sources, and the amplitude of the oscillation is chosen, depending on the depth of cut and the cutting tool diameter. It is nevertheless worth noting that this modified system still lacked automated control over the laser beam inclination angle and its focal point height relative to the workpiece surface, which in turn controls the size of the laser heating spot.

Shang et al. [145] developed another system that utilizes an oscillating laser beam to preheat a wider area ahead of larger diameter cutting tools, as shown in Figure 2.11(c). This system utilized a 2D laser galvanometric device to oscillate the laser beam, as opposed to oscillating the laser head itself in the system developed by Bermingham et al. [118, 121]. This allows the laser beam to move with higher velocities and oscillation frequencies. However, 2D laser galvanometric devices are 2 to 3 times heavier and larger in size than conventional laser heads with the same power ratings [146], which limits the application of 2D laser galvanometers in multi-axis LAML.

Wiedenmann et al. [115, 119] developed the LAML system shown in Figure 2.11 (d). They attached the laser head to a torque motor integrated onto the machine spindle. This allows laser beam delivery anywhere around the cutting tool. However, similar to the modified system of Bermingham et al. [118, 121], it had no automated control over the position of the laser beam focal point relative to the workpiece surface and its inclination angle, which are necessary to control the heat affected zone size and surface preheating temperature.

An more flexible system was developed by Kim et al. [114] and shown in Figure 2.11(e). This system uses four actuators to control the orientation of a laser head attached onto the spindle. These additional four axes allow complex cutting tool paths. However, since this system relies on the CNC machine table rotation to achieve full coverage around the cutting tool, it cannot be integrated to 3- or 4-axis milling machines – it is only limited to 5-axis machines.

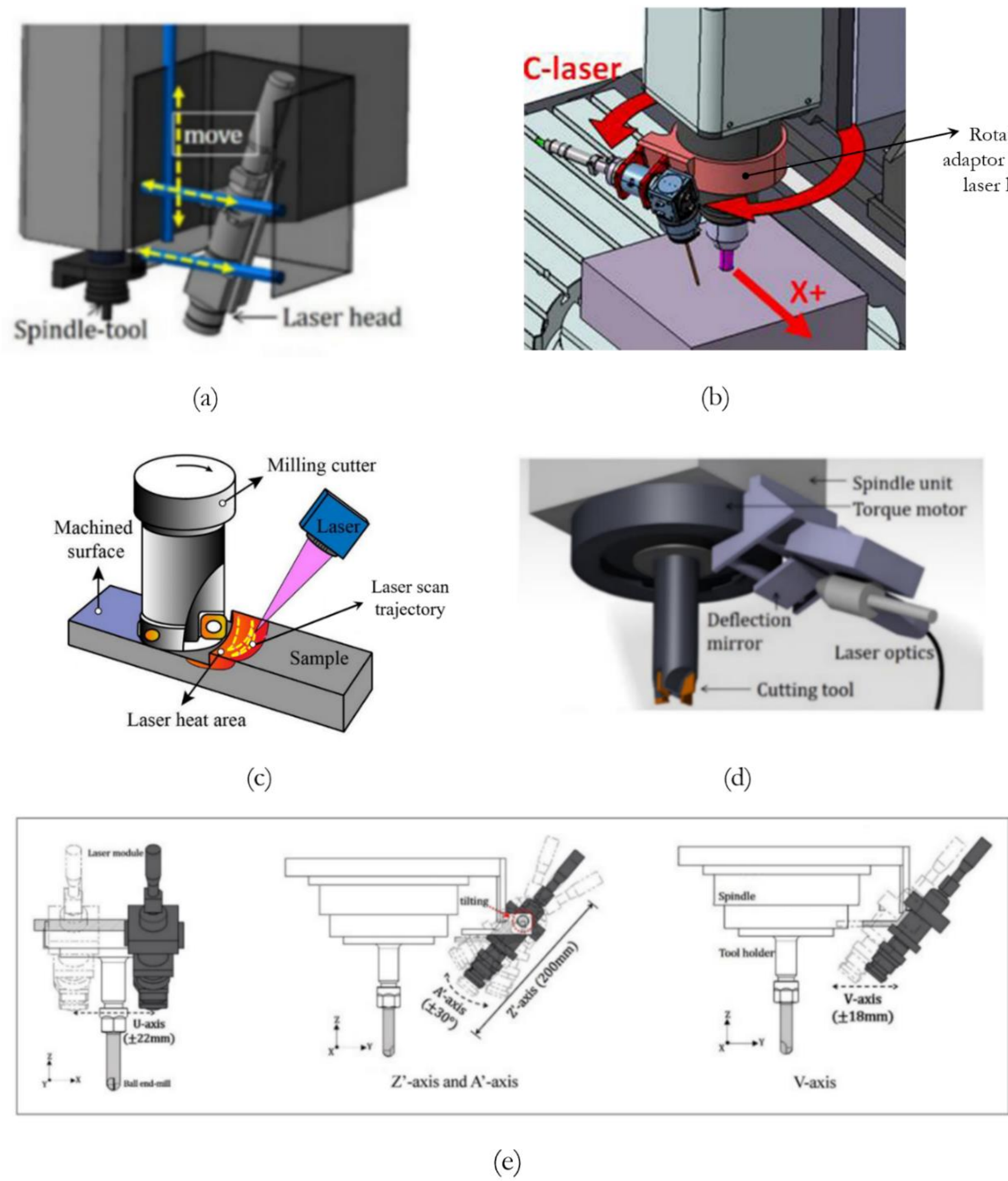

Figure 2.11. Examples of external laser beam delivery techniques (a,b) [118, 121], (c) [26, 145], (d) [115, 119], (e) [114].

The capability of oscillating the laser beam ahead of the cutting tool becomes of critical importance for multi-axis LAML when the size ratio between the cutting tool and the laser beam increases. Since the laser power density of heating spots are not uniform, except at their focal point, increasing the laser heating spot size to accommodate large cutting tools would not be practical since this would lead to nonhomogeneous heating of the workpiece with areas partially over or under heated. In this case, oscillating the laser heating spot itself, as opposed to increasing its size, would allow the homogeneous heating of a wider workpiece area using a relatively small heating spot [145].

An alternative to the oscillation of the laser beam, a back-and-forth (B&F) preheating method was proposed by Kang et al. [147]. When used to LAM of silicon nitride, it reduced the require laser power, extended the tool life, and reduced the surface roughness, and cutting forces. To further optimize the LAML process, the authors applied the B&F preheating a number of times 'n' before the tool reached the heated area. The selection of the optimum number 'n' allows obtaining the desired preheating temperature and satisfy the productivity, cost and desired surface integrity requirements [144]. Later, Kim et al. [148] used the B&F preheating method for LAML of Inconel 718 and showed that the surface roughness Ra decreased by 57%, compared to conventional milling. An interesting aspect of this investigation is the effect of the workpiece inclination angle θ. By increasing θ from 0 to 10^o and 20^o, the authors demonstrated the reduction of the cutting force components, the surface roughness, and the tool wear damage.

Hwang et al. [144] investigated the two preheating patterns of zigzag oscillation and back-and-forth motion and compared them with the conventional one-way motion of the laser beam in front of the tool when LAML of silicon nitride. They found that: (1) for the same laser power, the back-and-forth preheating shows a higher maximum preheating temperature than that of the zigzag method, producing a larger and stable heat distribution on the machining area, (2) the distance between the laser spot and the tool is a very important factor in this machining process. As the distance was increased, the machining showed unfavorable results because the heat was rapidly dissipated by convection and conduction. In contrast, as the distance was decreased, the machining also showed unfavorable results because of burning of the tool. The proper distance between the center of the laser spot and the end of the tool was about 5 to 6 mm.

Ha et al. [24] proposed another solution of the problem of rapid cooling of the laser pre-heated spot by using multiple heat sources. Both a laser beam and an induction heater were used in tandem and moved together ahead of the cutting tool. This allowed increasing the machining speed by maintaining the preheating temperature. In this study, two strategies were tested: strategy-1, where $T_{laser} > T_{induction}$, and strategy-2, where $T_{laser} < T_{induction}$, where T_{laser} and $T_{induction}$ are the surface preheating temperature by the laser beam and the induction heater, respectively. It was reported that at low feedrate (of 100 mm/min), the cutting forces and surface roughness were similar for both strategies. However, at higher feedrate (of 300 mm/min), strategy-1 produced lower cutting forces and surface roughness, since induction preheating effect is drastically decreased as the feed rate is increased.

2.3 Modeling of LAM

Accurate modeling of machining processes proved to be extremely useful, as it reduces the dependency on experimental trial and error approach, provides the ability to investigate some physical phenomena occurring during machining that are impossible to be measured experimentally, provides a powerful tool to gain fundamental understanding of the effects of the dominant parameters in machining processes, and provides a powerful predictive capability for processes design and optimization.

Many modelling techniques for conventional and laser-assisted machining processes have been developed over the years, including: empirical modeling, analytical modeling, mechanistic modeling, and finite-element-based numerical modeling (FEM) [27, 149]. Compared to other modeling techniques, FEM has constituted the majority of metal cutting modeling and simulation research since it allows a more faithful description of the physical process, and more comprehensive understanding of the underlying mechanisms and various parameters effects in conventional and advanced machining processes [27, 149, 150]. In addition, FEM allows the coupling of mechanical, metallurgical, and thermal aspects of complex machining processes, such as laser-assisted machining, into the same simulation.

The primary disadvantage, however, for FEM is that it is usually computationally expensive, which increases the time needed to run the full process simulation, especially for three-dimensional process modeling, where the simulation could take days to complete, depending on the complexity of the model and computer hardware configuration [151].

To achieve an accurate FEM of laser-assisted machining, it is necessary to determine, as inputs to the numerical model, the cutting tool material properties, the workpiece material properties, the flow stress of the workpiece material under high strain, strain rate, and temperature, the characteristics of the tool/material interface including heat transfer and friction, and an accurate method of modeling laser heating and microstructure transformations [27, 38, 149, 152].

2.3.1 Material Constitutive Models

Several material constitutive models were developed to describe material flow stress behavior. The most commonly used models in open literature are: Johnson-Cook [153, 154], Zerilli-Armstrong [155-157], Oxley [158, 159], Power law [160-162], Vinh [163] and Strain History (Maekawa et al.) [164]. Table 2.1, adapted from [149, 160, 165], summarizes the mathematical formulations of these models, where $\bar{\sigma}$ is the flow stress, $\bar{\varepsilon}$ is the effective plastic strain, T is the instantaneous temperature, T_{melt} is the material melting temperature, and T_0 is the room temperature.

Table 2.1. Most common constitutive models used in literature, adapted from [149, 160, 165].

Model	Mathematical formula	Model Coefficients
Johnson-Cook [153, 154]	$\bar{\sigma} = [A + B\bar{\varepsilon}^n]\left[1 + C\ln\left[\frac{\dot{\bar{\varepsilon}}}{\dot{\bar{\varepsilon}}_0}\right]\right]\left[1 - \left(\frac{T - T_0}{T_{melt} - T_0}\right)^m\right]$	A, B, C, m, n
Power law [160-162]	$\bar{\sigma} = \sigma_0\bar{\varepsilon}^n\left(\frac{\dot{\bar{\varepsilon}}}{\dot{\bar{\varepsilon}}_0}\right)^m\left(\frac{T}{T_0}\right)^{-v}$	σ_0, m, n, v
Vinh [163]	$\bar{\sigma} = \sigma_0\bar{\varepsilon}^n\left(\frac{\dot{\bar{\varepsilon}}}{\dot{\bar{\varepsilon}}_0}\right)^m exp\left(\frac{G}{T}\right)$	σ_0, m, n, G
Zerilli-Armstrong [155-157]	For b.c.c.* metal $\bar{\sigma} = C_0 + C_1\, exp\left(-C_3T + C_4T\ln\left[\frac{\dot{\bar{\varepsilon}}}{\dot{\bar{\varepsilon}}_0}\right]\right) + C_5\bar{\varepsilon}^n$	C_0 to C_5
	For f.c.c.* metal $\bar{\sigma} = C_0 + C_2\bar{\varepsilon}^{0.5}\exp\left[T\left(-C_3 + C_4\, ln\left[\frac{\dot{\bar{\varepsilon}}}{\dot{\bar{\varepsilon}}_0}\right]\right)\right]$	
Oxley [158, 159]	$\bar{\sigma} = \sigma_0(T, \dot{\bar{\varepsilon}})\ x\ \bar{\varepsilon}^{n\,(T,\dot{\bar{\varepsilon}})}$	$\sigma_0(T, \dot{\bar{\varepsilon}})$, $n\ (T, \dot{\bar{\varepsilon}})$
Strain History (Maekawa et al.) [164]	$\bar{\sigma} = \sigma_0(T, \dot{\bar{\varepsilon}})\left(\int_{strain\ i\ path} e^{\left(\frac{k}{n}\right)T}\ \dot{\bar{\varepsilon}}^{\frac{-m}{n}}\ d\bar{\varepsilon}\right)^n$	$\sigma_0(T, \dot{\bar{\varepsilon}}), k, m, n$

* b.c.c is body centred cubic and f.c.c. is face centred cubic.

For finite-element-based modeling of machining processes, the most commonly used constitutive model is the Johnson-Cook (JC) model, due to its numerical robustness [165]. It is also widely adopted by commercial FEM software packages used for machining simulation, such as Deform 2D and 3D [152] and Abaqus [166]. This model assumes that each of the separate terms for the effective strain, effective strain rate, and temperature independently affect the material flow stress.

The JC model, along with its modified versions, have been utilized extensively in the open literature to accurately model the behaviour of many materials in machining processes [167-172], including AISI H13 tool steel [172-175], which is utilized extensively in the research work of this thesis. The work done by Ng and Aspinwall [173] to simulate the machining of H13 tool steel confirmed the validity of the JC model for this material by reporting good agreement of the simulation with experimental results. This has been confirmed as well through the work done by Sartkulvanich et al. [172] and Shatla et al. [174, 175] for H13 tool steel.

2.3.2 Modeling Tool-Chip Interaction

In addition to the material constitutive model, modeling of the tool-chip interaction is important to the finite-element-based modeling of machining processes [176]. For modeling the heat transfer at the tool-chip interface, it was reported in literature that setting the heat transfer coefficient at the tool-chip interface, h_c, to large values, such as 10^3 to 10^6 kW/m^2 °C, accelerates the realization of steady-state conditions during the FE simulations of machining operations and produces predictions in good agreement with experimental results [27, 177, 178]. Attia et al. [176, 179] have developed a model to account for the thermal constriction resistance and the effect of the tool's multi-layer coating on the heat transfer across the tool-chip interface.

The friction between the tool and material is commonly modeled in literature using one of the following models [152]: (1) shear friction model [180], (2) Coulomb friction model [181], and (3) a hybrid friction model, such as Zorev's sticking-sliding friction model [182], which is stated mathematically as:

$$\tau_f = \mu \, \sigma_n \text{ in the sliding region, where } \mu \, \sigma_n < k_s, \qquad \text{(Equation 2.1)}$$

and

$$\tau_f = k_s \text{ in the sticking region, where } \mu\, \sigma_n \geq k_s, \qquad \text{(Equation 2.2)}$$

where τ_f is the frictional shear stress, μ is the friction coefficient, σ_n is the normal stress acting along the tool rake face, and k_s is the local material shear flow stress.

It was reported in literature that the predictions of the hybrid friction models are more accurate than the basic constant shear and Coulomb friction models [27, 149]. A comprehensive review of modelling the tool-chip interaction was recently given in a Keynote CIRP paper by Melkote et al. [183].

2.3.3 Modeling Microstructure Transformations in LAM

Since laser heating in LAM can change the near-surface layer microstructure at elevated temperatures, a microstructure transformation model needs to be integrated into the model of LAM to get more accurate simulation results, since microstructure transformations induce latent heat and transformation residual stresses. One of the advantages of finite-element-based modeling, over the other previously mentioned types of modeling, is its ability to easily integrate such additional models. Since the research work in this thesis is focused on LAML of tool steel, a more detailed discussion of finite-element-based modeling of steel microstructure transformations is presented below.

Figure 2.12 shows an example of the two-way interrelationships between different modules of the finite element-based software package Deform [152] that allow the software to integrate the modeling of microstructure transformations of different materials, with different compositions, with the modeling of machining processes. The example shown here is for carbon steel alloys.

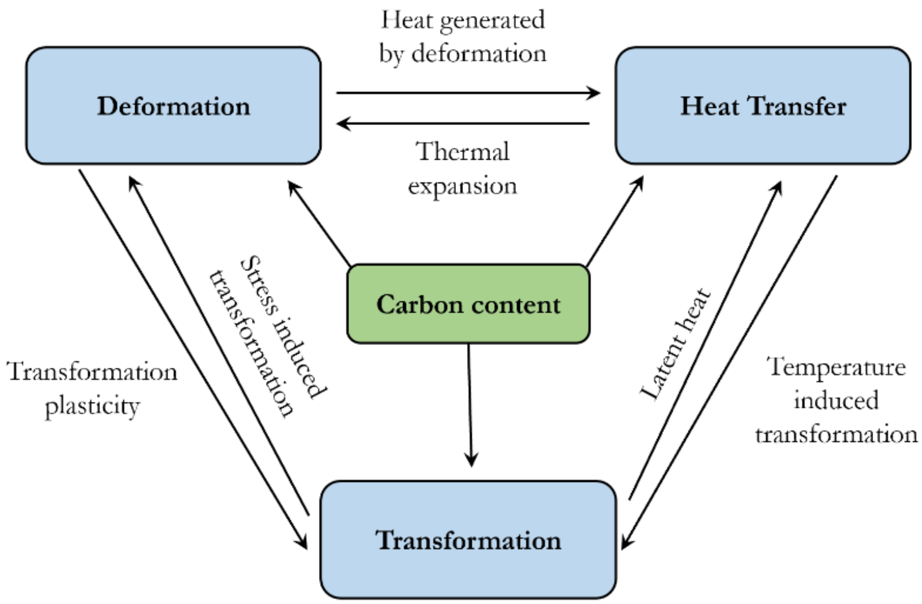

Figure 2.12. Coupling between deformation, microstructure transformation, material composition (carbon content in the case of steel alloys), and temperature [150],[152].

Microstructure transformation in carbon steels is a complex process, as it is coupled with carbon content, temperature, and material deformation, as illustrated in Figure 2.12. In modeling the steel microstructure transformations, the volume fraction of each possible phase of steel in every mesh element of the modeled workpiece could be defined. Therefore, each mesh element could contain different volume fractions of austenite, martensite, pearlite, ferrite, or bainite. Each of these phases has its own set of material properties which define the thermal properties of that phase, as well as its elastic and plastic behavior. The transformation from one phase to another is defined in terms of a kinetics model, volume change and latent heat. A kinetics model is a function which defines the manner and conditions at which one phase transforms to another phase. For carbon steels, there are generally two types of phase kinetics models: 1) diffusion-type transformations, and 2) diffusion-less type transformations. Examples for diffusion-type transformations are the austenite-to-ferrite and austenite-to-pearlite transformations, and vice versa. However, the transformation of austenite to martensite is diffusion-less [38, 152, 166].

For LAM of steels, and during the heating cycle, the volume fraction of the austenite phase is dependent on temperature, mean stress, and carbon content. This dependence can be represented by the Avrami's diffusion kinetics model as follows [152, 184, 185]:

$$\xi_A = 1 - \exp[\, -f_t(T)\, f_s(\sigma_m)\, f_c(C) t^n], \qquad \text{(Equation 2.3)}$$

$$\text{where } f_t(T) = A_{T_1} \left(\frac{T - A_{T_2}}{A_{T_3}}\right)^{A_{T_4}} \left(\frac{A_{T_5} - T}{A_{T_6}}\right)^{A_{T_7}}, \qquad \text{(Equation 2.4)}$$

$$f_s(\sigma_m) = \exp(A_s \sigma_m), \qquad \text{(Equation 2.5)}$$

$$\text{and } f_c(C) = \exp\,(A_{C_1}(C - A_{C_2})). \qquad \text{(Equation 2.6)}$$

where ξ_A is the volume fraction of austenite, T is the instantaneous absolute temperature, C is the carbon content, σ_m is the mean stress, A_{T_1} to A_{T_7}, n, A_{C_1}, A_{C_2}, and A_s are coefficients determined from the steel material Time-Temperature-Transformation (TTT) diagrams [152].

During the cooling cycle in LAM, the cooling rate specifics the type of the final microstructure formed. In laser assisted machining of steels, the cooling rates are usually very high, typically in the range of 600 to 1500 °C/s [38, 68]. This rapid cooling results in the formation of martensite only. To model the transformation from austenite to martensite, the diffusion-less Magee's model could be used:

$$\xi_m = 1 - \exp[w_1\, T + w_2(C - C_0) + w_3\sigma_m + w_3\bar{\sigma} + w_4], \qquad \text{(Equation 2.7)}$$

where ξ_m is the volume fraction of martensite, T is the instantaneous absolute temperature, and w_1 to w_4 are material constants identified from the TTT diagrams [152].

Shi and Attia [38] have used simplified versions of the above Avrami and Magee equations to model the microstructure transformation in laser surface heat treatment of AISI 1536 carbon steel, and reported a good agreement of the predicted depths of martensite with experimental results, with a maximum error of 15%. A probable cause of this error is the neglection of the effect of carbon content and the mean stress in the simplified equations used. Another probable cause is the simplification of the distribution of the laser power density as uniform, as discussed in the next section. This simplification affects the resulting temperature field, which consequently affects the calculations of the volume fractions of transformation phases, as discussed previously.

2.3.4 Modeling of Laser Heating in LAM

For laser-assisted machining, accurate modeling of the laser heating is important to attain accurate predications of temperatures, which have critical effects on deformation and microstructure transformations, as discussed in the previous section.

Heat is generated by the random motion of matter particles, but since the laser beam itself is not made of matter but of 'photons', or 'light particles' which have no mass, unlike other TAM sources, a laser beam can have no temperature. Through its interaction with solid surfaces, the photons energy is partially absorbed by the atomic or molecular structure of the material. The primary product of absorbed laser light is, strictly speaking, not heat but particle excess energy - excitation energy of bound electrons, kinetic energy of free electrons, perhaps excess phonons [186]. The degradation of the ordered and localized primary excitation energy into uniform heat involves three steps: (1) spatial and temporal randomization of the motion of excited particles, (2) energy equipartition that tends to involve a large number of elementary collisions and intermediate states, and finally (3) heat flow.

On a macroscopic scale, the laser energy that is converted to heat tends to be highly localized, as a result of the thermal spreading resistance phenomenon [187]. The finite-element-based modeling of the temperature distribution generated in a workpiece due to laser heating is based on a 3-D transient time-dependent heat conduction analysis of a moving heat source applied to the workpiece surface, which can be described in a x–y–z coordinate system as follows [188]:

$$\rho C_p \left(\frac{\partial T}{\partial t} + U\frac{\partial T}{\partial y}\right) = \frac{\partial}{\partial x}\left(k\frac{\partial T}{\partial x}\right) + \frac{\partial}{\partial y}\left[k\frac{\partial T}{\partial y}\right] + \frac{\partial}{\partial z}\left[k\frac{\partial T}{\partial z}\right] + \dot{Q}_V, \qquad \text{(Equation 2.8)}$$

where $\rho, C_p, K, \dot{Q}_V$, and U are the density, specific heat, thermal conductivity, power generation per unit volume, and the laser scanning speed, respectively.

The initial condition at time t = 0 is given as:

$$T(x, y, z, 0) = T_0. \qquad \text{(Equation 2.9)}$$

The natural boundary condition considers the imposed heat flux, radiation and convection at the laser irradiated surface and can be defined as:

$$-k\frac{\partial T}{\partial z} = q(x, y) - h_{conv}\,(T - T_0) - \sigma\varepsilon(T^4 - T_0^4), \qquad \text{(Equation 2.10)}$$

where the heat flux q is normal to the laser irradiated surface, T_0 is the ambient temperature, h_{conv} is heat transfer coefficient for convection, σ is the Stefan–Boltzmann constant for radiation (5.67×10^{-8} W/ m^2 K^4), and ε is the emissivity.

The inclusion of the temperature-dependent thermophysical properties and a radiation term in Equation 2.10 makes the analysis highly nonlinear [189]. To avoid this, simpler FE-based modeling approaches are used, including modeling the effect of laser heating using a moving heat exchange window that defines heat transfer in its local area through an equivalent convection mode of heat transfer [38, 77, 120, 151]. The heat transferred per unit time ($\dot{Q}$) in such heat exchange window can be expressed by:

$$\dot{Q} = h_{eqv}\, A\, (T_w - T_s), \qquad \text{(Equation 2.11)}$$

where h_{eqv} is the equivalent convective coefficient of heat transfer, A is the local area of the heat exchange window, T_w is the temperature of the window, and T_s is the temperature of the workpiece surface. If a fictitious temperature T_w is selected to be much higher than T_s, then changes in T_s would be negligible and $\dot{Q}$ would remain approximately constant.

In most of the research work that used the simplified approach of Equation 2.11, the equivalent convective coefficient of heat transfer 'h_{eqv}' of the heat exchange window was assumed to be constant, resulting in a uniform distribution of the heat transferred per unit area inside the window. This assumption does not reflect the actual complex laser power density distribution, which is usually *Gaussian* for perpendicular laser beams [68, 190, 191], and *asymmetric* for inclined laser beams. The limitations of the mechanical design of most CNC machines used for multi-axis LAML of workpieces of complex shapes necessitate the inclination of laser beam focusing heads at an angle, which affects the shape and power density distribution of the laser heating spot, as well as the surface emissivity and absorptivity [192]. This inclination is also necessary to avoid undesirable laser reflections to protect the operator, the machine components, and the laser head lens from damage.

Although analytical models were developed to model moving Gaussian-distributed laser sources [145], these models are only valid for limited specific cases in LAM and can not be used in modeling a generalized multi-axis LAML process, since, for example, these models cannot consider the dependence of the workpiece material properties on temperatures. However, this could be easily considered in FE based modeling.

The Gaussian-distributed laser power density P_d at a distance r from the axis of the laser beam could be expressed as follows [191]:

$$P_d = \eta \frac{2\,P}{\pi\,R^2} \exp\left(\frac{-2\,r^2}{R^2}\right) \qquad \text{(Equation 2.12)}$$

where η is the absorptivity, which is defined as the ratio between energy absorbed by the solid surface and the laser beam incident energy, P is the laser power, and R is the beam radius.

Therefore, there is a need for developing a generalized FE model for multi-axis LAML that considers the effects of the laser beam inclination, complex distribution of laser power, and 3D complex workpiece geometry.

2.4 Gap Analysis of Research Work in LAML

Based on this literature review, there are critical gaps related to LAML research that need to be filled. These gaps are identified as follows:

1. Most developed LAM techniques are limited to turning process, due to its simplicity of being only a 1- or 2-axis process and cannot be further extended to work with multi-axis milling. Very limited number of LAM techniques were developed for milling and work only with simple one directional cutting tool paths. LAML for more complex tool paths was attempted, but still needs further development to attain full multi-axis LAML.

2. Most current LAML techniques for milling applications are difficult or almost impossible to be directly retrofitted to existing milling machines to be adopted by industry. The LAML systems that are retrofittable, are still limited to 1D or 2D LAML and cannot handle multi-axis LAML of complex geometries. For such a system to be economically competitive and attractive to industry, a new retrofittable multi-axis actuating mechanism needs to be developed to work with all standard tool holders, spindles, and cutting tools.

3. There is a need to develop generalized three-dimensional finite-element-based models that predict the thermal performance, machining forces, surface integrity, and the microstructure evolution during multi-axis LAML processes to ensure its satisfactory performance in precision milling operations. These models need to consider the complex laser power density distribution used in LAML, which is usually Gaussian. The models need to also consider the different geometries of laser heating spots created by the inclination of laser beam to the machined surface. Furthermore, the models need to be easily extended to multi-axis laser-assisted milling by considering the effect of complex three-dimensional workpieces surfaces. This will allow more accurate predictions for the size of heat affected zones and microstructure transformations, which in turn have a counter effect on temperature analysis and deformation calculations in machining modeling, making modeling more accurate.

2.5 Research Objectives

Based on the above state-of-the-art literature review and the gap analysis, the specific objectives of this research work are defined as follows:

1. Development of a laser delivery system for multi-axis LAML which satisfies the following requirements: (a) easily retrofittable to existing CNC machines, (b) can work with all standard tool holders, cutting tools and spindles, (c) can deliver the laser beam in every direction around the cutting tool, which guarantees the laser spot is always placed in front of the tool (in the feed direction), (d) has the ability to accommodate larger cutting tools by oscillating the laser beam or by performing a "back-and-forth" movement ahead of the tool, (e) has control over the position of the laser beam focal point relative to the workpiece surface to control the size of the heating spot, (f) has control over the distance between the laser heating spot and the cutting tool, and (g) capable of performing laser surface heat treatment, using the same setup and laser source with different laser heating parameters.

2. Development of a central control system that: (a) integrates high-power diode laser source with the multi-axis LAML system, (b) automate and synchronize all aspects of the integrated system, (c) is able to be integrated with older closed-architecture CNC milling machines (CNC machines

with restricted access to vital programming and configuration information), and (d) should be based on industry standard real-time communication protocols, in order to be adaptable to a wide range of actuators of different manufacturers.

3. Experimental investigation of the parameters that maximize the material removal rate (MRR) for roughing operations in LAML of AISI H13 tool steel, which is the difficult-to-machine material under investigation in this research work. These parameters are the laser power, the heating spot size, the heating time/scanning speed/feedrate, and the depth of cut.

4. Experimental and numerical investigation of the effect of the mentioned LAML parameters (point 3, above) on preheating surface temperatures, cutting forces, micro-structure evolution, heat affected zone depth, and surface integrity (surface roughness and induced-residual stresses) of the workpiece material, and comparing the results to conventional dry and wet milling.

5. Development of a generalized three-dimensional FE-based numerical model for simulation of the full laser-assisted milling process, that is applicable to multi-axis LAML of complex geometries. The FE model should consider the complex shape and distribution of laser power density inside the laser heating spot, the laser beam inclination angle, and the curvature of complex shapes. The model will be used as a predictive tool for LAML process design and optimization.

2.6 Research Methodology

A flowchart for the proposed research methodology to achieve the above objectives is illustrated in Figure 2.13. It combines experimental and theoretical investigations. As shown in the figure, three tracks of work are followed in parallel (**A**, **B**, and **C**). Tracks **A** and **B** are experimental work (highlighted in blue), while Track **C** is theoretical work (highlighted in purple). Outputs are highlighted in green, and the dashed black arrows show the flow of information/results. In the next sections, each of the three tracks and their interrelationships are explained.

2.6.1 Track A: LSH, LSHT, and LAML Investigations

In track **A**, experimental investigations for laser surface heating (LSH), laser surface heat treatment (LSHT), and laser-assisted milling (LAML) of H13 tool steel are carried out.

In task **A.1**, conventional dry and wet milling tests of H13 tool steel are performed to determine the machining parameters that maximize the material removal rate (MRR). The same machining parameters are used in task **A.3**, which is the testing of the multi-axis LAML system in order to compare the benefits/drawbacks of LAML to conventional milling. In task **A.2**, unidirectional LSH and LSHT are performed in order to investigate the effect of laser parameters on preheating temperatures, residual stresses, and microstructure. In addition, measurement of the laser power density is carried out, since it is important for calibration of the FE models developed in track **C**. Task **A.3** involves testing the performance of the multi-axis laser deliver system, developed in Track **B**. This will be followed by performing 1-axis LAML (task **A.4)**, and 3-axis and 5-axis LAML (task **A.5)**. In task **A.4**, 1-axis LAML is performed in order to investigate the effect of LAML parameters, compared to conventional milling, on cutting forces, surface roughness, and residual stresses. In task **A.5**, using the same setup as task **A.3**, 3-axis and 5-axis LAML tests are performed, and the results are compared with conventional milling as well (cutting forces and surface roughness).

2.6.2 Track B: Multi-axis Laser Delivery System Development and Integration

The goal of track **B** is to develop and integrate a multi-axis laser delivery system with the CNC machining center in order to enable the experimental investigations of track **A** and the validation of the FE numerical models of track **C**.

In task **B.1**, the design, and integration of the different components of the laser delivery system are performed. The main components of this system include: the laser source, the optical laser fiber to transmit the laser from the source to the CNC machining center, the laser focusing head, the actuators attached to the laser focusing head to perform 5-axis LAML, the cooling system, and the operator's safety system. In task **B.2** to **B.4**, the control system of the laser delivery system is integrated with the control system of the CNC machining center, in order to enable the simple unidirectional and the multi-directionality of the laser delivery system tests in track **A**. In the last step, the synchronization of all systems is tested in order to achieve the required performance.

2.6.3 Track C: Theoretical Work

In track **C**, theoretical models are developed to: (a) assist the experimental investigations (Track **A**), (b) assist the development of the multi-axis LAML system (Track **B**), and (c) have the capability for performing process development, design, and optimization.

In task **C.1**, a kinematic model is developed for the multi-axis LAML system. This model is used to assist in the selection of the strokes and sizes of the actuators used in the system and to find their optimum orientations to accommodate the mechanical design of the spindle of the CNC machining center, to determine the minimum bending radius of the laser optical fiber, and to account for the workspace limitations of the machining chamber of the horizontal CNC machining center. In task **C.2**, an offline tool path translator is developed to translate the cutting tool path of simple 3D geometries for LAML to laser heating spot path, which is necessary to perform the multi-axis LAML tests. In task **C.3**, finite-element-based numerical models are developed for LSH, LSHT, and LAML, taking into consideration the complex distribution of the inclined laser heat spot using in the experimental testing. The numerical models are validated using the experimental results of LAML of H13 tool steel (performed in **A.2** to **A.5**) and are used to investigate the effect of different process parameters on preheating surface temperatures, microstructure transformations, and machining forces.

2.6.4 Interrelationships between tracks A, B, and C

As seen from the discussion above, there are many tasks that need to be carried out sequentially. One important task to start with is task **C.1** since the kinematic model is important for the development of the multi-axis laser delivery system (task **B.1**) and for the integration of the laser head actuators with the CNC machining center (task **B.3**). Task **C.2** is important for the development of the central workstation since the offline tool path translator is required to validate the synchronization of the laser head actuators with the movements of the spindle of the CNC machining center. Tasks **B.1** to **B.4** will be done sequentially, as illustrated by the dashed arrows, since each task is a prerequisite to its following task. Tasks **B.1** and **B.2** are important to be carried out following task **C.1** in order to enable task **A.2**. Tasks **B.3** and **B.4**, as well as the synchronization testing, are needed for tasks **A.4** and **A.5**. Task **C.3** does not have a prerequisite, but the output of this task (the developed models) needs to be validated by the experimental results of the completed track **A**.

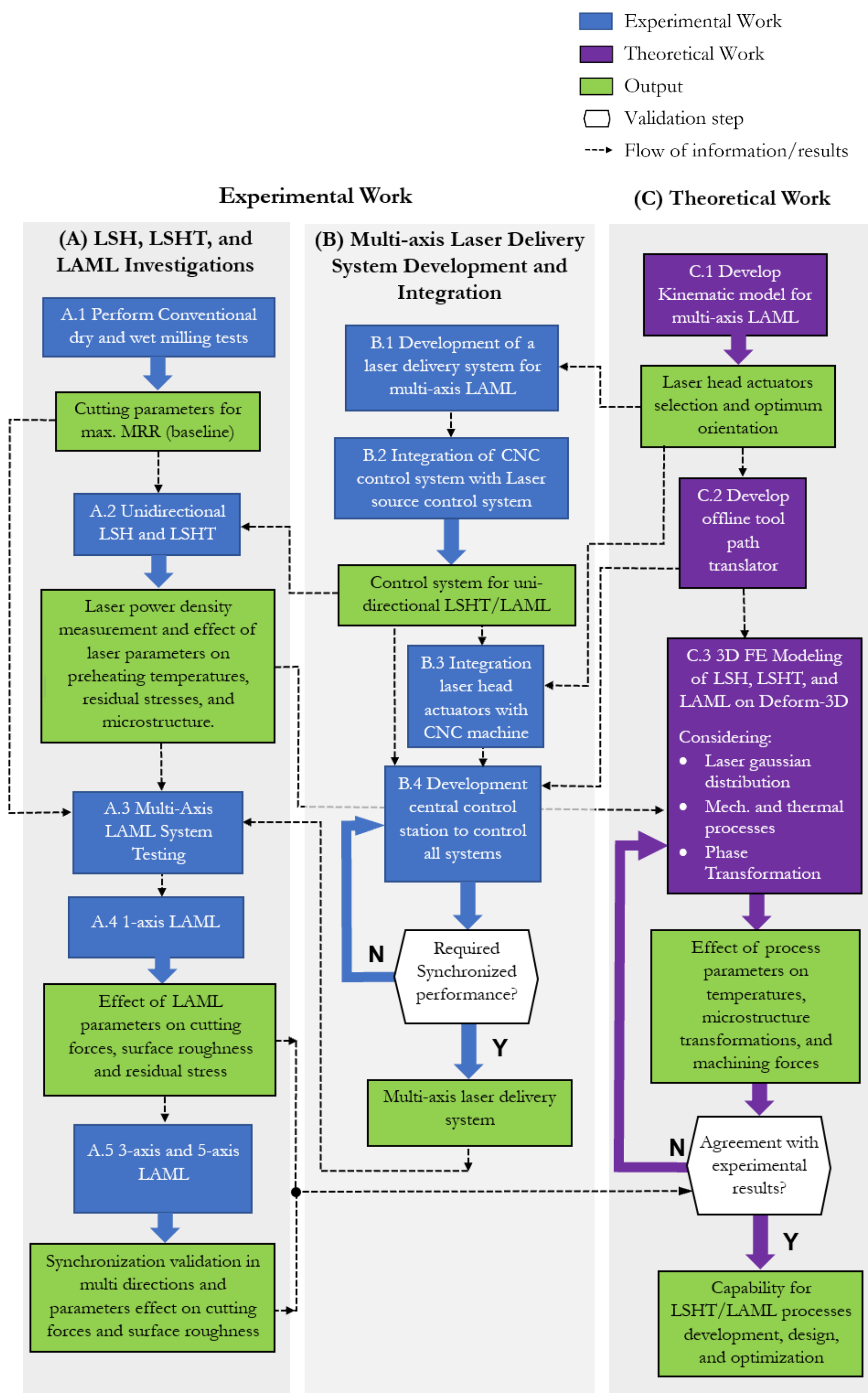

Figure 2.13. Proposed Research Methodology.

Chapter 3: Development of a Multi-Axis Laser-Assisted Milling System

3.1 Introduction

This chapter presents the work done to develop, design, and integrate a multi-axis laser-assisted milling system. In this system the laser beam is delivered to the workpiece via an external laser beam focusing head to precisely preheat a small volume on the workpiece to soften it before its removal by the cutting tool. The size of the heated spot can be controlled to be as small as 0.8 mm in diameter (the size of the laser focal point). This system utilizes a set of electric actuators to deliver the laser beam anywhere around the cutting tool. One electric linear actuator is actively controlled to maintain a certain size of the heating spot in front of the tool by actively adjusting the laser focal point position relative to the workpiece surface (defocusing distance). Another electric actuator controls the leading distance between the laser heating spot and the cutting tool. A third rotational electric direct drive torque motor is used to change the position of the heating spot around the cutting tool, allowing the tool to cut in different directions. This system incorporates several independent controllers which are linked together by means of one central workstation, as discussed in detail in section 3.4. This multi-axis system is capable of performing laser-assisted milling of 3D features with higher material removal rates (MRR) than conventional 5-axis milling, as discussed later in detail in Chapter 4.

Figure 3.1 shows a schematic for the concept of the multi-axis laser-assisted milling system. A laser beam is applied at a certain leading distance (d) ahead of the cutting tool with a certain power, scanning speed, and inclination angle (θ_L) relative to the XY plane, where Z is the axis of the cutting tool. The scanning speed is equal to the feedrate (f) of the cutting tool. The laser focal point position relative to the workpiece surface is actively controlled to accommodate the workpiece geometry in order to maintain a constant defocusing distance (D_{fw}) between the workpiece surface and the laser focal point. The position of the heating spot around the cutting tool, θ_m (measured relative to the X-axis), is actively controlled to allow the cutting tool to cut in any direction. The laser locally heats the workpiece surface to decrease its hardness and strength before cutting, as shown previously in Figure 2.1, hence improving its machinability.

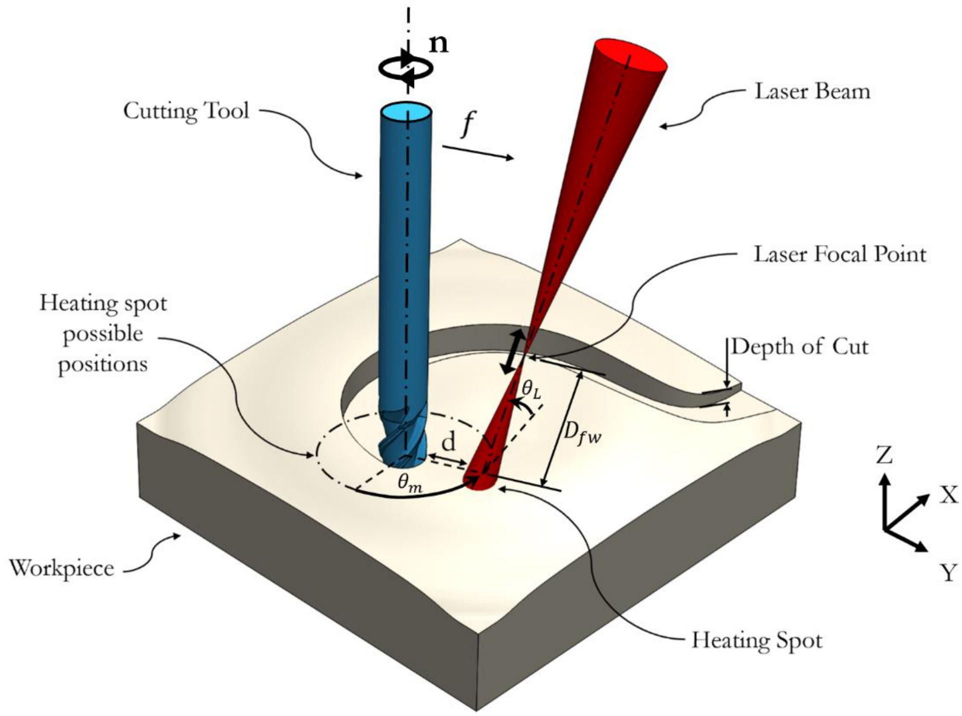

Figure 3.1. Schematic of multi-axis laser-assisted milling of a 3D curved surface.

3.2 Concept of the Developed Multi-axis LAML System

Figure 3.2 shows the kinematics of the developed multi-axis laser-assisted milling (LAML) system. This system has three axes activated by two electric linear actuators (1 and 4) and a direct drive torque motor (5), which rotates the whole setup concentrically around the axis of the CNC machining center spindle, allowing the delivery of the laser beam in all cutting feed directions, while having control over the defocusing distance and the leading distance between the heating spot and the cutting tool. In addition, the rotational actuator (5) can oscillate ahead of the cutting tool in order to cover a wider area of heating to accommodate larger tools [118, 145]. Furthermore, the horizontal actuator (4) can actively increase and decrease the leading distance in a “back-and-forth movement” to achieve higher preheating temperatures for a wider area ahead of the cutting tool [144]. This system is capable of being integrated into 3-, 4- and 5-axis machining centres, as it does not need the table rotation or the workpiece inclination. If it is integrated into a 5-axis machining center, then the LAML process would have up to 8+2 axes. The +2 axes are the capability of performing oscillation, and the back-and-forth movement.

A kinematic model was created to enable the selection of the sizes and strokes of the electric actuators and to find their optimum orientations to accommodate the size of the spindle housing, the size of the workspace of the machining chamber of the used horizontal CNC machining centre, and the minimum bending radius of the laser optical fiber.

This kinematic model was used to assist in programing an offline tool path translator to convert the cutting tool path into laser heating spot path. As illustrated in view A in Figure 3.2, the linear displacement Δa of the laser head actuator ((1) in Figure 3.2) along its stroke was related to the displacement of the laser beam focal point in the Z-axis direction Δz as follows:

$$\Delta a = \frac{\Delta z}{cos\,(90-\theta_L)}\,, \qquad \text{(Equation 3.1)}$$

where θ_L is the laser beam inclination angle relative to the XY plane. For LAML of 3D surfaces, Δz is the difference between the Z coordinate of the endmill tip and the Z coordinate of the laser heating spot.

As illustrated in Figure 3.3, the rotational actuator angle θ_m is calculated, knowing the coordinates of the cutting tool path, as follows:

$$\theta_m = tan^{-1}\left(\frac{\Delta y}{\Delta x}\right), \qquad \text{(Equation 3.2)}$$

where Δx and Δy are the distances between the cutting tool center and the laser heating spot center in X and Y directions, respectively.

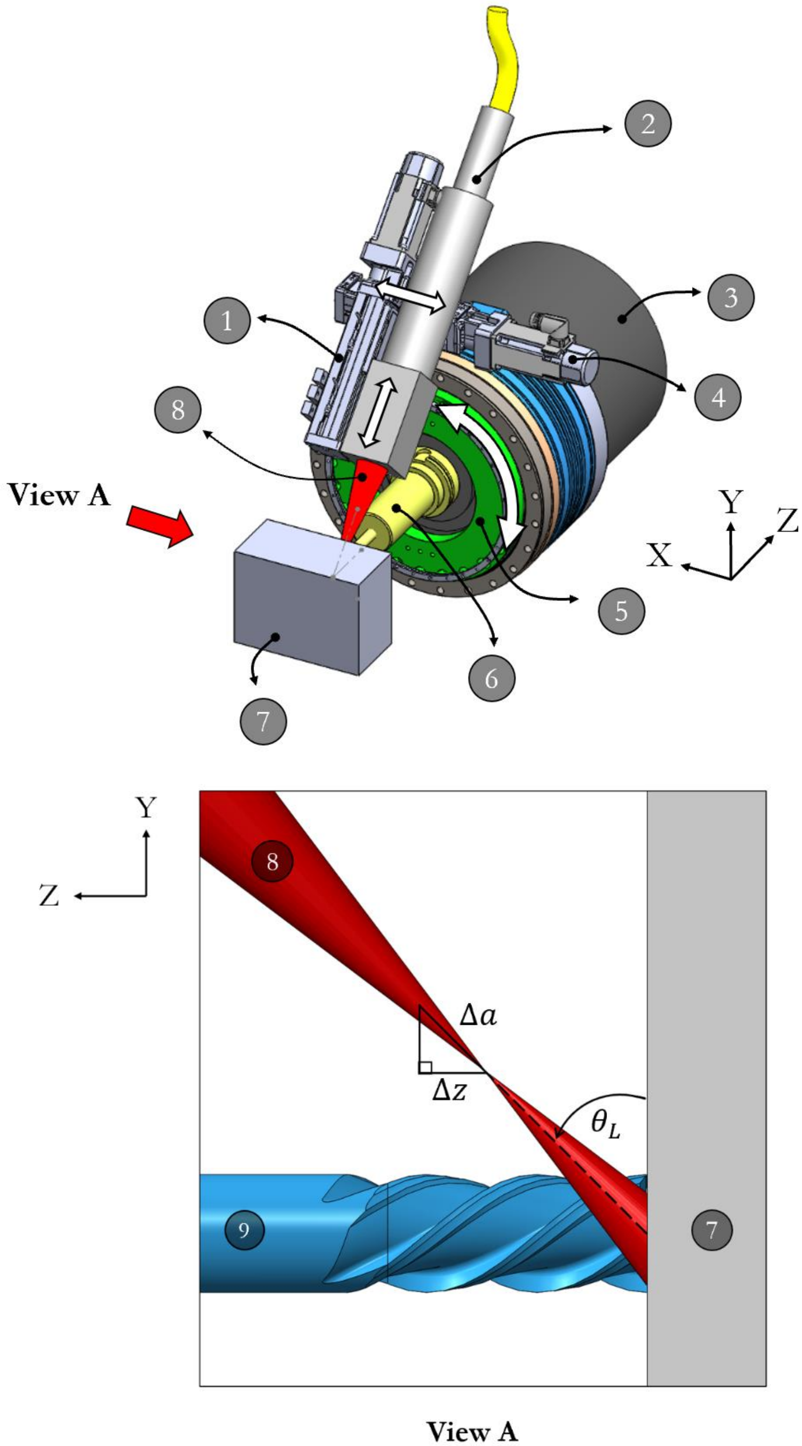

Figure 3.2. Kinematic model created for the multi-axis laser-assisted milling system. (1) Linear actuator for defocusing distance control. (2) Laser focusing head. (3) Spindle of the horizontal CNC machining center. (4) Linear actuator for leading distance control. (5) Direct drive torque motor. (6) Tool holder. (7) Workpiece. (8) Laser beam. (9) Cutting tool (endmill).

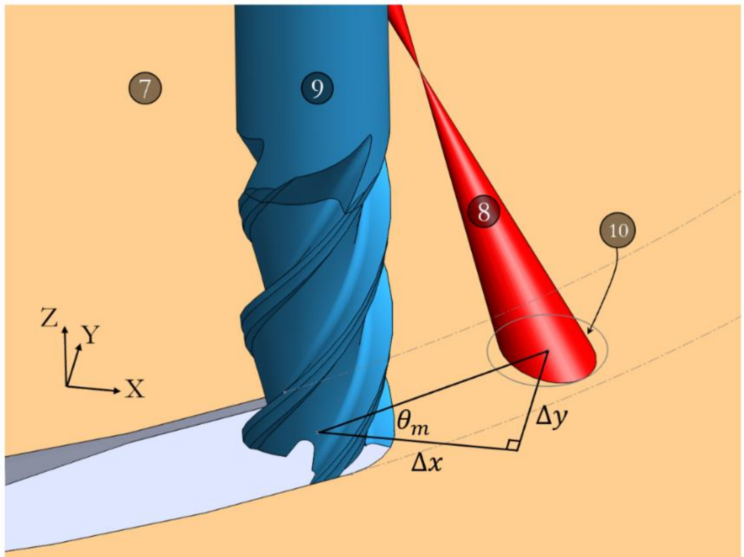

Figure 3.3. Calculation of the rotational actuator angle θ_m from the X and Y coordinates of the endmill path. (7) Workpiece. (8) Laser beam. (9) Cutting tool (endmill). (10) Heating spot.

3.2 Design of the Multi-axis LAML System

The strokes of the two electric linear actuators (B3S, Tolomatic, Minnesota, USA) were selected to be 50 mm for the horizontal actuator ((4) in Figure 3.2), and 100 mm for the laser head actuator ((1) in Figure 3.2). These actuator uses an enclosed recirculating ball bearing system which can accommodate loads up to about 400 N with a maximum backlash of 0.05 mm.

An exploded view of the direct drive torque motor (SIMOTICS T Torque motor, 1FW6150, Siemens, Munich, Germany), shown as an assembly (5) in Figure 3.2, is presented in Figure 3.4. The motor operates on a 400 V direct current. This torque motor is a self-cooled, permanently-excited, three-phase synchronous motor with a large-aperture rotor of 265 mm. Only the stator and rotor (parts 6 and 7 in Figure 3.4) were supplied by the manufacturer (Siemens, Munich, Germany). The rest of the components were either custom designed and manufactured as part of this research work (parts 2, 4, 5, 8 in Figure 3.4) or selected and supplied by other manufacturers (parts 1 and 3 in Figure 3.4).

This direct drive torque motor was selected for this application because it is supplied in different aperture sizes, which can accommodate different spindle sizes for different CNC machining centers, which makes the system easily retrofittable to different machining centers. In addition, the motor operates without any mechanical transmission elements, such as gears or couplings, which significantly reduces the weight and the required mounting space, compared to conventional motors with the same torque and precision. Furthermore, not having transmission elements eliminates undesirable elasticity in the drive train, as well as backlash when there is a change in the direction of motion, such as the oscillation movements of the laser heating spot required to cover a wider area ahead of larger tools.

The kinematic model was used to calculate the mass moment of inertia for all rotating masses around the motor's axis and to estimate the required maximum torque for the motor for this application. The estimated maximum torque (T_{max}) needed from the torque motor was calculated at the case when the load is stationary at a horizontal position, and torque motor starts rotation against the weight with acceleration 360 degrees/sec^2. In that case:

$$T_{max} = (\mathrm{M} \times \mathrm{g} \times d_{tm}) + [\ a_t \times I_{M.tot}] \qquad \text{(Equation 3.3)}$$

where M is the mass of the load, g is the acceleration due to gravity, d_{tm} is the distance between the torque motor axis and the center of mass of the load, a_t is the torque motor angular acceleration, and $I_{M.tot}$ is the total mass moment of inertia around the torque motor's axis. The required maximum torque was estimated to be approximately 100 N.m. The selected motor has a rated torque range up to 298 N.m (when air cooled) and up to 1,050 N.m (when water cooled), so no external cooling was required for this application [193].

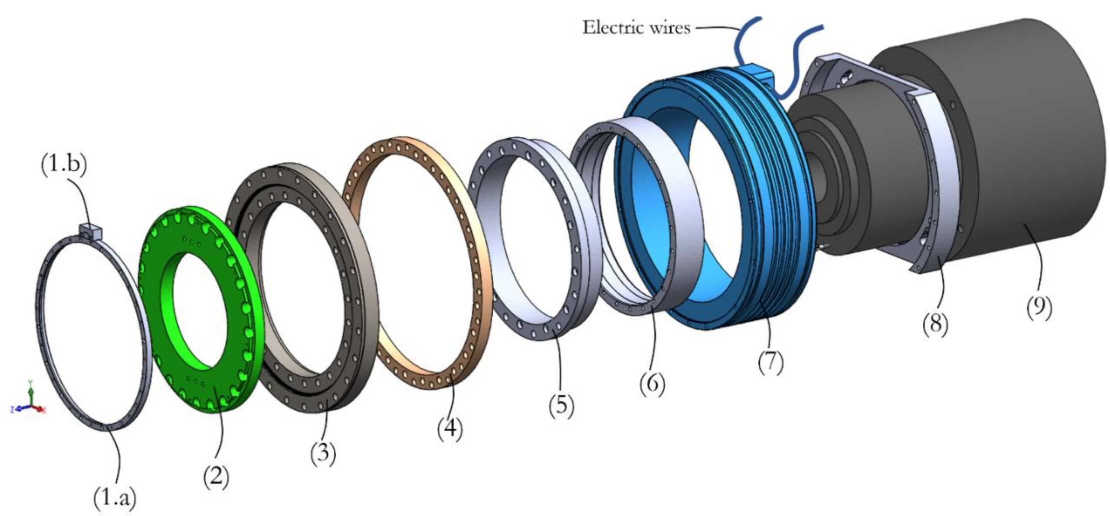

Figure 3.4. Exploded view of the direct drive torque motor used in the multi-axis laser-assisted milling system. (1.a) Optical encoder ring. (1.b) Reading head for the optical encoder ring. (2) Optical encoder flange. (3) Slewing bearing. (4) Flange for the outer race of the slewing bearing. (5) Flange for the inner race of the slewing bearing. (6) Rotor of the torque motor. (7) Stator of the torque motor. (8) Flange for the stator of the torque motor. (9) Spindle of the CNC machining center.

A slewing bearing, shown as item (3) in Figure 3.4, (VU140, Schaeffler Technologies AG & Co. KG, Bavaria, Germany) enables the relative motion between the motor's rotor and stator. Slewing bearings can reliably support axial, radial, and tilting moment loads, which eliminates the need for setups involving a combination of axial and radial bearings [194]. Two steel flanges ((4) and (5) in Figure 3.4) were designed and manufactured in accordance with the kinematic model. Flange (4) attaches the outer race of the slewing bearing (3) to the stator of the torque motor (7), while flange (5) attaches the inner race of the slewing bearing (3) to the rotor of the torque motor (6). One Steel flange (8) was designed and manufactured to fix the stator of the torque motor (7) to the spindle of the CNC machining center (9).

A two-part optical non-contact absolute encoder (1.a) and (1.b) (RESOLUTE™ angular, Renishaw, Wotton-under-Edge, United Kingdom) was used to accurately measure the angular position of the torque motor. The encoder consisted of a stainless steel ring (1.a) with an absolute scale code marked directly on its periphery, and a reading head (1.b) to read the marked code on the stainless steel ring.

An aluminium flange (2) was designed and manufactured to fix the optical encoder's ring (1.a) to the inner race of the slewing bearing (3) which rotates with the rotor of the torque motor (6). The encoder's reading head (1.b) was fixed to the outer race of the slewing bearing (3) which is fixed to the torque motor's stator (7). The optical encoder was capable of reading the position of the rotor of the torque motor within ± 0.95 arc seconds accuracy, with a maximum reading speed of 6,300 rpm. The scale of the encoders' ring (1.a) has 536,870,912 distinct positions (29-bit resolution). The encoder's reading head (1.b) functions as a very high-speed miniature digital camera, taking photos of the ring's scale to determine its absolute position. The encoder's head (1.b) is capable of detecting the encoder's ring (1.a) angular position in greasy and/or particle contaminated environments, which made the encoder suitable for use in this application [195].

3.3 Implementation of the Multi-axis LAML System in the Machining Center

Figure 3.5 shows the implementation of the multi-axis LAML system inside a horizontal 5-axis machining center (A88E, Makino, Tokyo, Japan). The laser was generated for this system using a 3000 W diode laser source (TruDiode 3006, Trumpf, Ditzingen, Germany). The diode laser was delivered to the machining center using an 80-meter optical laser fiber (Trumpf, Ditzingen, Germany) and a laser focusing head (1) (CSC BEO D70, Trumpf, Ditzingen, Germany). As presented in section 3.2, the latter was mounted on two electric ball screw linear actuators, which were attached to the spindle of the CNC machine through the rotor of a direct drive torque motor (4). Although the maximum rotation for this setup, with this particular laser head, is 180 degrees, smaller laser heads that are commercially available allow one full 360-degree rotation. The inclination angle of the laser focusing head was set manually using a small manual adjustable stage (6) (A40 Series, Velmex, New York State, USA).

A 2D cable carrier (5) (triflex® series, Igus, Cologne, Germany) was used to protect the laser optical fiber from over bending. The minimum bending radius of the laser fiber and the cable carrier was 100 mm. A chiller (HRS series, SMC, Tokyo, Japan) was used to cool the laser focusing head and the laser optical fiber ending using a closed-loop running water circuit. A monochromatic ethernet camera (10) (Mako G-030B, Thuringia, Germany) was used to record the process inside the CNC machine.

The cutting tool (endmill) was held by a standard HSK-A100 tool holder (3) with a 200 mm extension (Toprun, D'andrea, Lainate, Italy). An air nozzle, capable of providing 860 kPa of air pressure, was used to blow chips away from the laser head to protect its lens. The laser beam was aligned relative to the cutting tool with the help of the pilot light. A water flow sensor (PF2D520, SMC, Tokyo, Japan), was added to the cooling water circuit to communicate the water flow rate value to a controller to ensure the safe operation of the laser system.

The workpiece (7) was held in place in a vice (8) that was mounted on a 3-component dynamometer (9) (Type 9255C, Kistler, Winterthur, Switzerland) to measure the cutting forces in three directions.

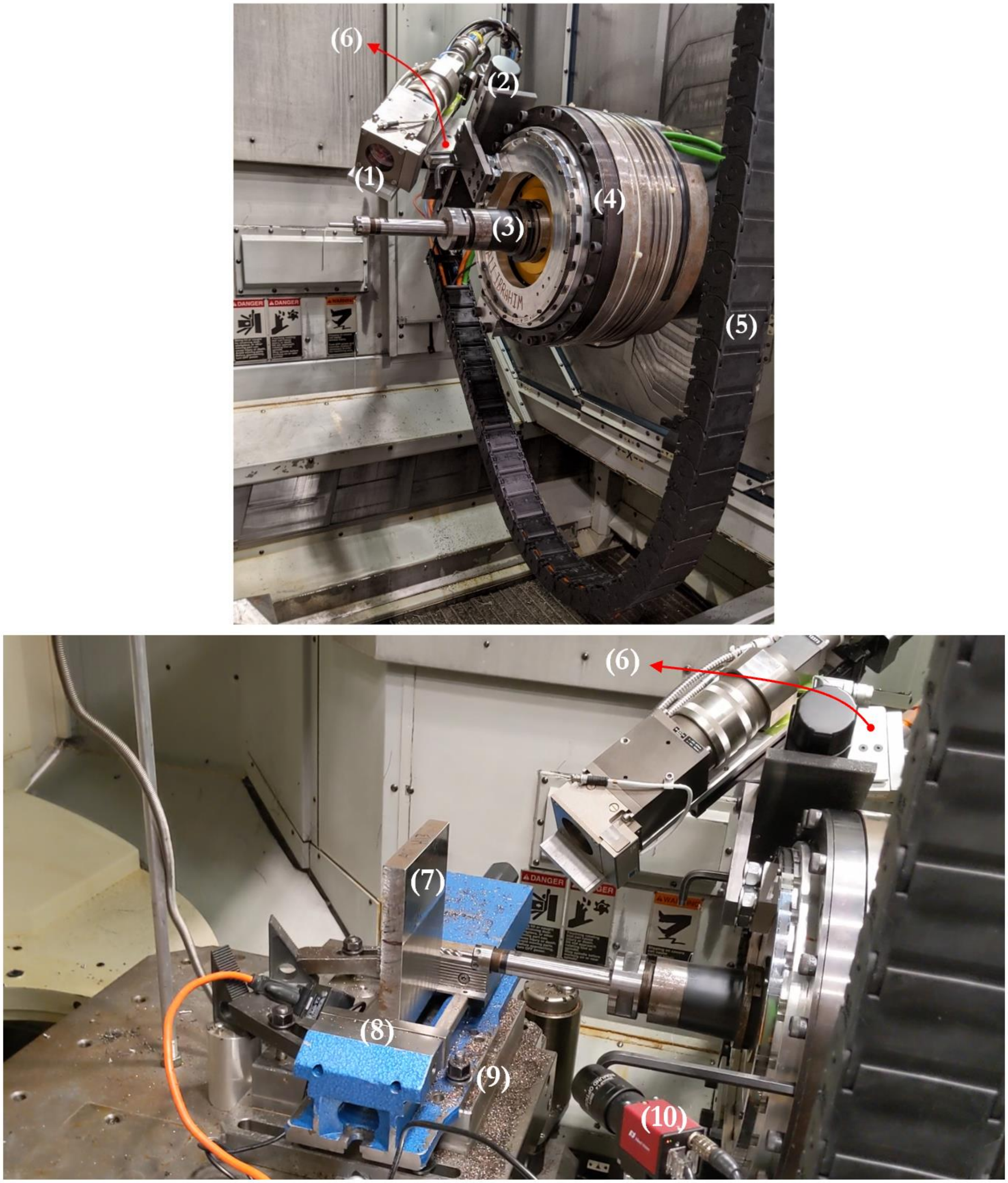

Figure 3.5. Implementation of the multi-axis laser-assisted milling system inside a horizontal machining center. (1) Laser focusing head. (2) Linear electric actuator. (3) HSK tool holder mounted on the spindle. (4) Direct drive torque motor. (5) 2D cable tray. (6) Manual rotary stage. (7) Workpiece. (8) Vise. (9) 3-component dynamometer. (10) Camera.

3.4 Control and Synchronization of the of the Multi-axis LAML System

A control system was developed to control and synchronize all the different components of the multi-axis LAML system, as shown in Figure 3.6. This control system has three main blocks: a central workstation **(A)**, the CNC machining center **(B)**, and the diode laser source **(C)**. In this system, independent control/communication modules are labeled **(D.x)**, where 1<**x**<7. The central workstation **(A)** (Z420, Hewlett-Packard, California, United States) was used to control the entire LAML system. A virtual instrument (VI) **(A1**) was created and programmed on the workstation using LabVIEW software (National Instruments, Texas, United States) to start and stop the operation of both the CNC machining center **(B)**, and the diode laser source **(C)**, through ports A2 to A6. The **(A1)** controller was also used to automate and synchronize the laser head actuators movements with the CNC machining center spindle. For the operator's safety, emergency and fault signals of the workstation **(A)**, the machining center **(B)**, and the laser source **(C)** were hardwired to the laser source safety circuit in order to shut down the laser source immediately in case of faults and emergencies.

The user inputs for the three main blocks and their interactions with each other are discussed in detail in the coming subsections.

3.4.1 Laser Source Control

A programmable logic controller (PLC) **(C.2)** (Micrologix 1400, Allen-Bradley, Rockwell Automation Inc. Wisconsin, USA) was added to the laser source controller **(C.1)** to allow communication with the central workstation **(A)** via EtherNet/IP industrial network protocol (port **A.3**). The initial user inputs for the laser source controller **(C.1)** are the laser power level and its time function, which could be specified to be constant, pulsating in a square/trapezoidal manner, or any other custom function.

3.4.2 CNC Machining Center Control

A multifunction input/output (I/O) device (**A.2**) (PCIe-6321, National Instruments, Texas, United States) was added to the workstation **(A)** to acquire and send data in *real-time* to the digital I/O module (**B.2**) of the CNC machining center. The initial user inputs needed for the main controller of the CNC machining center **(B.1)** were a G-code and a M-code. The G-code controlled the movements (position, feedrate, spindle speed, etc.) of the CNC machining center, while the M-code was used for: (1) receiving and sending digital signals to and from the I/O device of the central workstation **(A.2)** via the DIO module **(B.2)**. These signals control the start and end of LAML process execution, and

(2) sending digital signals to the central workstation **(A)** to request the diode laser source **(C)** to turn on or off.

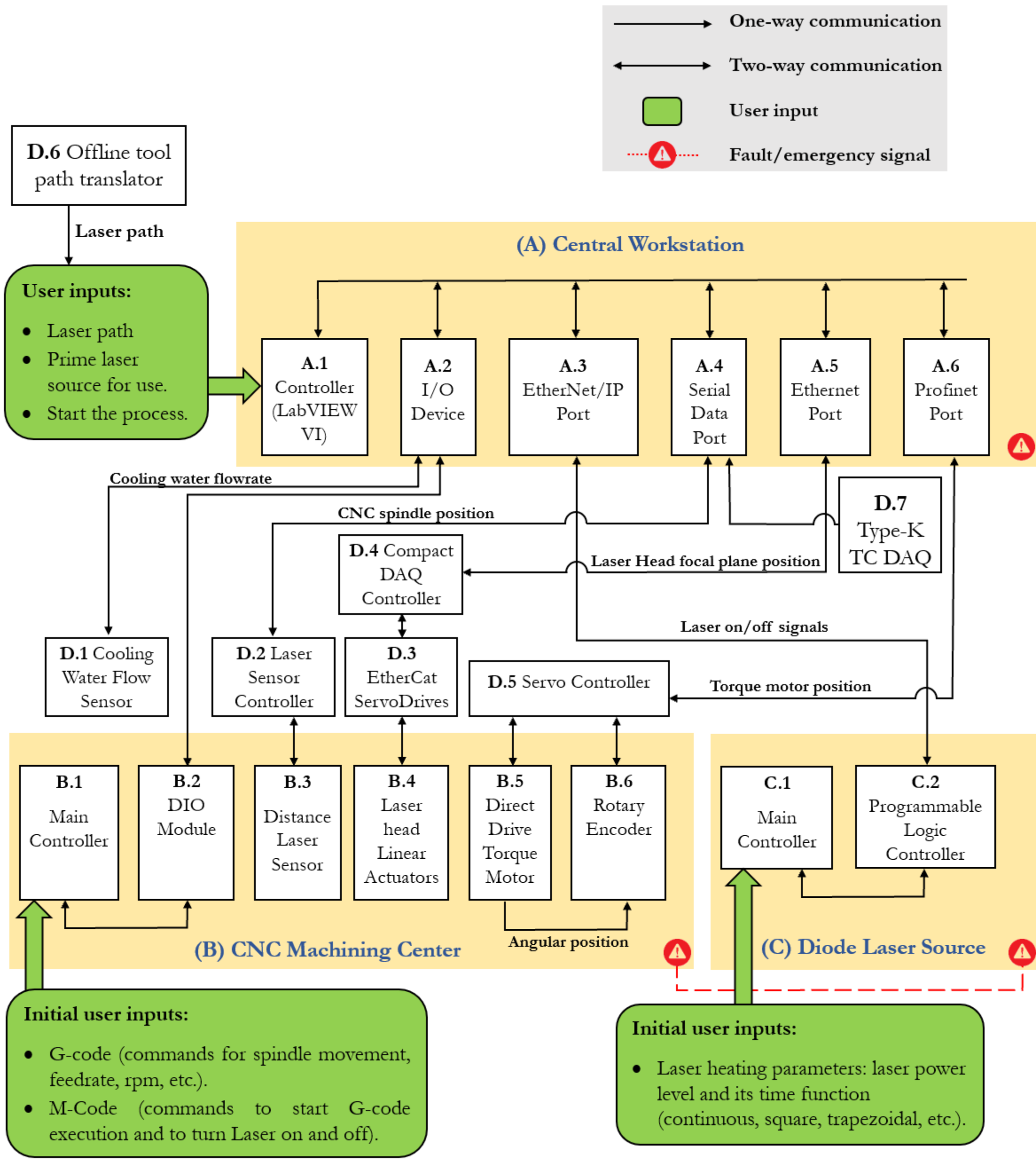

Figure 3.6. Flow chart for the control system of the multi-axis laser-assisted milling system.

3.4.3 Laser Focusing Head Positioning Control

Two servo drives **(D.3)** were connected to the two linear actuators **(B.4)** that control both the laser defocusing and leading distances. A compact DAQ controller **(D.4)** (cDAQ-9137, National Instruments, Texas, USA) was also used to allow communication between the servo drives **(D.3)** and the central workstation **(A)** in real-time via EtherCAT network protocol. An offline tool path translator **(D.6)** was programmed in MATLAB (MathWorks, Massachusetts, USA) to translate the cutting tool path of a 3D geometry to laser beam path.

A flowchart explaining the concept of the offline tool path translator is shown in Figure 3.7. As shown in the figure, the first step is to construct and export the CAD model of the workpiece geometry to a CAM software, such as Fusion360. Then, the cutting tool path is determined and subsequently exported to an appropriate post-processor (FANUC in this case) to convert the designed tool path to cartesian X, Y, Z coordinates. These coordinates are then converted on Matlab to laser heating spot path by using Equations 3.1 and 3.2.

The laser heating spot path, obtained from the offline tool path translator, is then fed by the central workstation controller **(A.1)**, via the Ethernet port **(A.5)**, to the electric actuators through the compact DAQ controller **(D.4)** and the servo drives **(D.3)**.

The LabVIEW virtual instrument on the central workstation (**A.1**) controlled the torque motor angular position via an independent control unit (**D.5**) (CU320-2, Siemens, Munich, Germany) controlling a single-axis servo drive (SINAMICS S120, Siemens, Munich, Germany). The protocol of communication was real-time Profinet (Profibus Nutzerorganisation e.V, Karlsruhe, Germany) through port **A.6**. To achieve closed loop control over the torque motor, the optical encoder reading head (**B.6**) communicated with the torque motor servo controller (**D.5**) via an open encoder interface (Drive-CLiQ, Siemens, Munich, Germany).

Similar to the linear actuators, the offline tool path translator was used to translate the cutting tool path and feed it to the controller of the central station (**A.1** in Figure 3.6) in real-time to control the angular position of the laser beam using the torque motor.

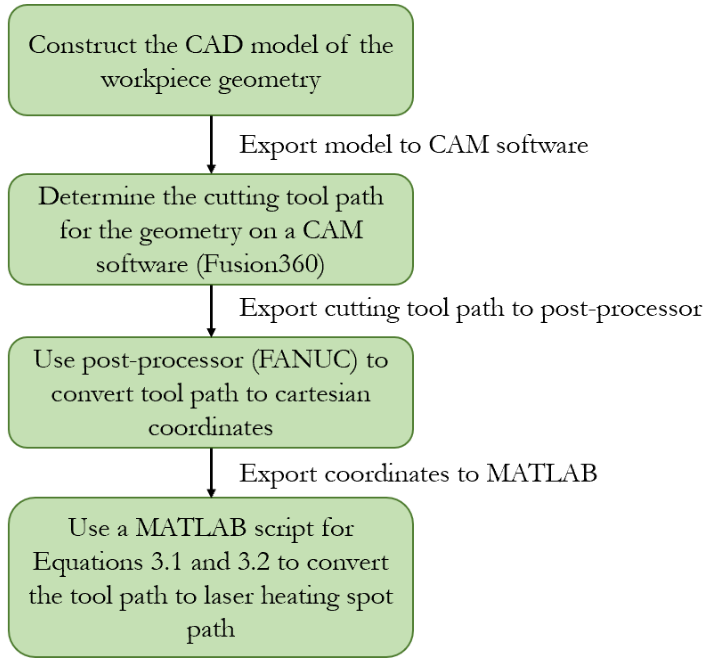

Figure 3.7. Flowchart for converting the workpiece geometry to laser heating spot path.

The torque motor was air cooled and was used at its lower rated torque range, which proved enough for the application requirements. However, to ensure that the temperature of the torque motor did not exceed its maximum operating temperature of 130°C, an embedded temperature sensor communicated the motor's temperature to the motor control unit via a terminal module (SINAMICS TM120, Siemens, Munich, Germany). If the motor temperature exceeds the maximum operating temperature, the motor control unit (**D.5**) sends a warning signal to the controller of the central station (**A.1**) to request stopping the torque motor operation.

The synchronization between the movements of the CNC machining center, the torque motor, and the linear actuators was achieved by utilizing a 2D laser profiler (LJ-V series, Keyence, Osaka, Japan) to monitor the spindle position in real-time. Figure 3.8 shows the location of the 2D laser profiler sensor in the CNC machine used for this multi-directional system. A controller (**D.2**) for the 2D laser profiler was used to communicate its measurements serially to the virtual instruments of the central workstation through a serial data port (**A.4**). As discussed later in more detail in section 4.6.1, the synchronization between the electric actuators and the CNC machining center was validated, and the maximum errors in positioning the laser heating spot were found to be 200 μm and 100 μm for the linear actuators and the torque motor, respectively, which are acceptable compared to the size of the typical heating spots used (2 to 5 mm).

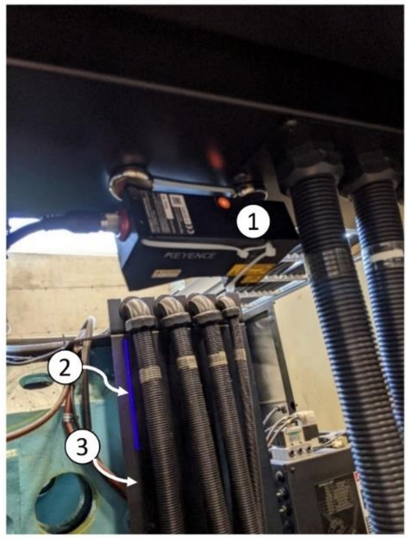

(a)

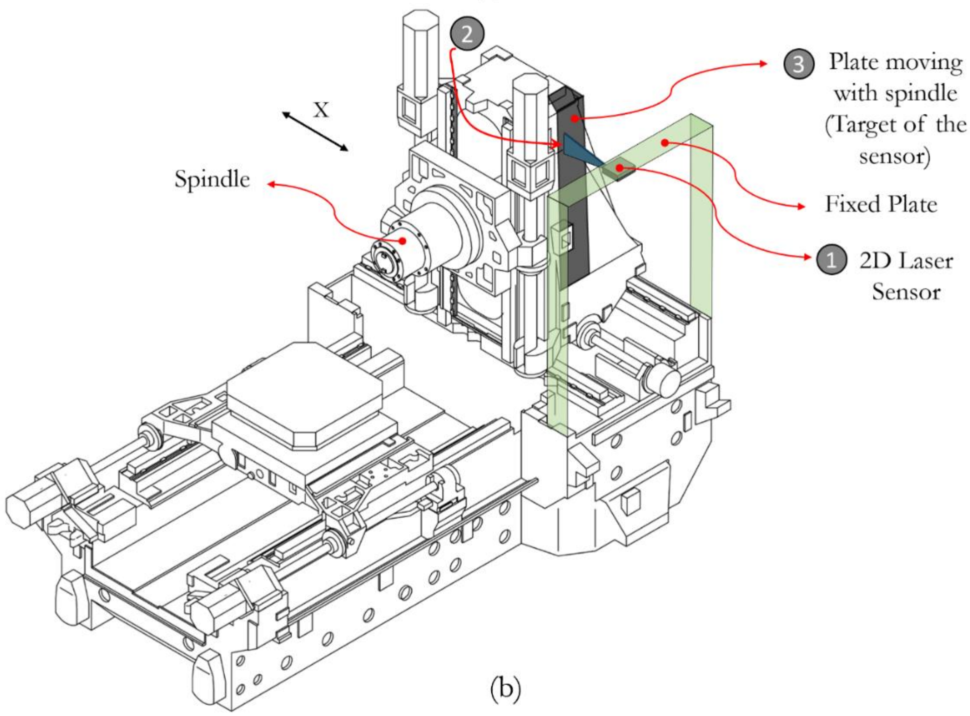

(b)

Figure 3.8. Location of the 2D laser profiler sensor (1) used to monitor the position of the CNC machine spindle in real-time. (2) is the laser beam projection (blue line) on plate (3). (Figure (b) is adapted from [196]).

To ensure that the laser focusing head and the laser optical fiber are cooled properly, a water flow rate sensor **(D.1)** was added to the water cooling circuit to communicate the water flow rate value to the central workstation **(A)** with an analogue signal via its multifunction I/O device **(A.2)**. The central workstation main controller **(A.1)** was programmed to stop the laser source immediately if the cooling water flow rate was less than a pre-set value (1.5 L/min).

All temperature measurements were done using Type-K thermocouples connected to USB data acquisition interface module **(D.7)** (D8000 series, Omega, Connecticut, USA) controlled by the central workstation **(A)** via port **(A.4)**.

In the next Chapter, the multi-axis LAML system is tested for different workpiece geometries using different cutting conditions and laser heating parameters, and its performance is compared to conventional milling.

3.5 Summary

This chapter presented the work done to develop, design, and integrate a multi-axis laser-assisted milling system. In this system, the laser beam is delivered to the workpiece through an external laser focusing head to locally preheat a small volume on the workpiece to soften it before its removal by the cutting tool. The size of the laser heating spot can be controlled to be as small as 0.8 mm in diameter, which is the size of the focal point of the laser beam used.

This system utilizes a set of electric actuators to deliver the laser beam anywhere around the cutting tool. One linear actuator is actively controlled to maintain a certain size of the heating spot in front of the tool by actively adjusting the laser focal point position relative to the workpiece surface. Another linear actuator controls the leading distance between the laser heating spot and the cutting tool. A third rotational direct drive torque motor is used to change the position of the heating spot around the cutting tool, allowing the tool to cut in different directions. This system was integrated in a horizontal 5-axis machining center, and a control system was developed and integrated in order to control and communicate with the several independent controllers of the LAML system via one central workstation. The synchronization between the control system and the CNC machining center was validated, and the maximum error in positioning the laser heating spot was found to be 200 μm which is negligible compared to the size of a typical laser heating spot.

Chapter 4: Experimental Investigation of the Performance of the Multi-axis LAML

4.1 Introduction

In this chapter, experimental testing of the multi-axis LAML system developed in Chapter 3 is presented here for different workpiece geometries using different cutting conditions and laser heating parameters. The performance of the LAML system was validated and compared to conventional milling.

Section 4.2 presents the measuring instruments used in the experimental investigation of the multi-axis LAML system. Section 4.3 investigates the cutting parameters, which maximize the material removal rate (MRR) of AISI H13 tool steel (as-received with 52 HRC) in conventional milling, in order to provide a baseline for comparison with LAML tests. Section 4.4 investigates the effect of laser surface heating (LSH) parameters on surface temperature and induced residual stresses when preheating of H13 tool steel. In section 4.5, the multi-axis LAML system is tested for different workpiece geometries using the same cutting conditions as the conventional milling in section 4.3, and the same laser heating parameters as the LSH tests in section 4.4. Section 4.6 presents and discussed the results of the multi-axis LAML tests in comparison to conventional milling.

4.2 Measuring Instruments

This section presents the measuring instruments used for all the experimental testing carried out in this research work.

4.2.1 Residual Stress Measurement

Residual stresses were measured using an automatic system utilizing the hole-drilling strain-gauge method (MTS3000 RESTAN, Sint Technology, Florence, Italy). The hole-drilling strain-gauge method followed the ASTM E837 standard [197]) for measuring residual stress, in which a tungsten carbide inverted cone milling cutter is used in conjunction with a high speed compressed air turbine (up to 400,000 rpm at 4 bars of pressure) to drill a hole (typically 1.8 to 2 mm) incrementally (typical increment is 0.02 to 0.05 mm) at the centre of a strain gauge to relieve the material's residual stress, as shown in Figure 4.1. The strain gauge measures the resulting material deformation in three directions, and the residual stress profile is calculated automatically using a software, in accordance with the ASTM E837 standard [197]. High-speed drilling has the advantage of not changing the state of the material's stresses. This enables the drilling of relief holes without introducing new stresses.

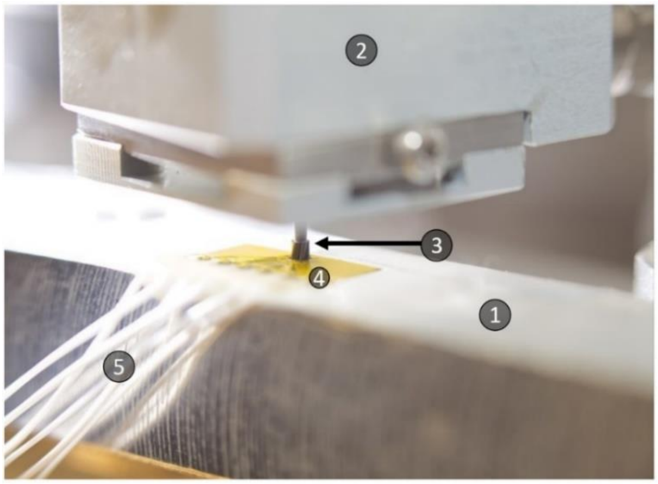

Figure 4.1. Residual stress measurement. (1) Workpiece. (2) Automatic residual stress hole-drilling measurement system. (3) Tungsten carbide inverted cone milling cutter. (4) Strain gauge. (5) Strain gauge wires.

4.2.2 Surface Roughness Measurement

All surface roughness measurements were done using a portable measuring device (Surtronic 25, Taylor Hobson, Leicester, United Kingdom). Each surface roughness measurement length was 4 mm. Four different measurements were taken along each surface. To evaluate the surface roughness, the arithmetical mean roughness value *Ra* was chosen as a representative parameter.

4.2.3 Cutting Forces Measurement

All cutting forces were measured using a 3-component dynamometer (Type 9255C, Kistler, Winterthur, Switzerland) to acquire cutting forces in three directions.

4.2.4 Temperature Measurement

All temperature measurements were done using Type-K thermocouples (Omega, Connecticut, USA) connected to USB data acquisition interface module (D8000 series, Omega, Connecticut, USA), which is controlled by the central workstation of the LAML system.

4.3 Conventional Milling of AISI H13 Tool Steel

This section presents the work done to investigate the cutting parameters which maximize the material removal rate (MRR) for conventional milling of AISI H13 tool steel (as-received with 52 HRC), with and without the use of coolant, using conventional cutting tools. The results of this work are to provide a baseline for comparison with the laser-assisted milling process.

4.3.1 Methodology

The experimental setup is shown in Figure 4.2. The tests were carried out on a vertical 5-axis CNC machining center, (DMU 100 P duoBLOCK, 77 kW and 30,000 rpm maximum power and speed, DMG MORI, Bielefeld, Germany). The test conditions are shown in Table 4.1. Conventional carbide uncoated 4-flute 6.35 mm flat endmills (110-0250-401, De Boer Tool, Ontario, Canada) were used to mill straight slots in H13 tool steel, with a constant depth of cut and speed of 0.5mm and 4000 rpm, respectively. The cutting tool feedrate was varied between 600 and 1200 mm/min, and milling was performed with and without flood coolant.

For these tests, cutting forces, surface roughness, and residual stresses were measured using the instruments discussed in section 4.2.

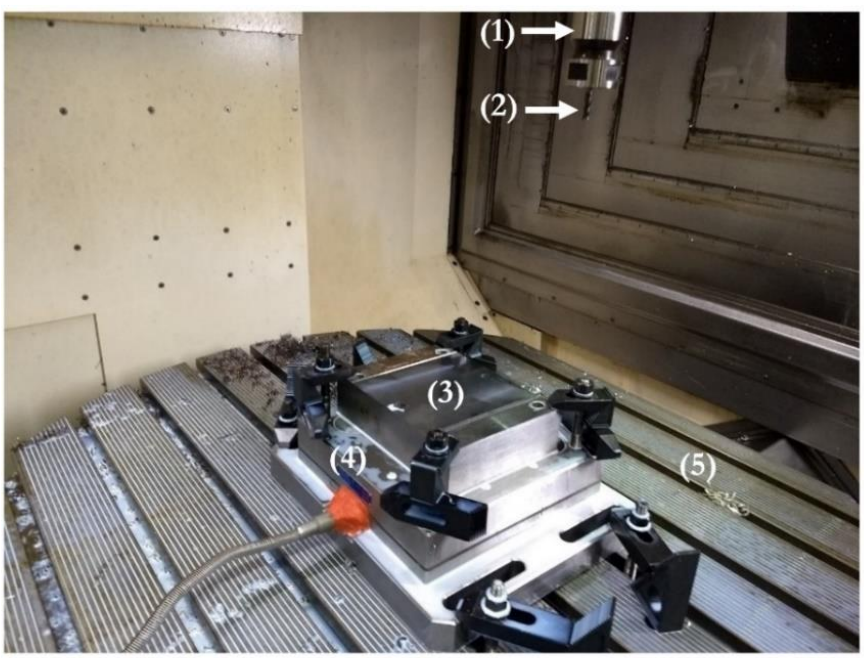

Figure 4.2. Experimental setup used. (1) Cutting tool holder, (2) 6.35 mm endmill, (3) H13 tool steel workpiece, (4) 3-axis dynamometer, (5) Rotary table of the CNC machining center.

Table 4.1. Test conditions used for conventional milling of H13 with and without flood coolant.

Tool Diameter [mm]	Depth of Cut [mm]	Speed [RPM]	Feedrate [mm/min]
6.35	0.5	4000	600
			800
			1000
			1200

4.3.2 Results and Discussion

To establish a baseline for comparison with the LAML process, the effects of conventional cutting parameters on cutting forces and surface integrity (surface roughness and residual stresses) were investigated.

4.3.2.1 Cutting Forces

Figure 4.3 shows an example for cutting force measurement for half a second in the feed direction when the feedrate was 600 mm/min without the use of coolant. As shown in the figure, the cutting force has a mean value of approximately 61 N and varies between approximately 39 to 83 N. Figure 4.4 compares the mean cutting force in three directions, measured during conventional dry milling and milling with flood coolant, at feedrates of 600, 800 and 1000 mm/min. The variation of cutting forces around their mean values are represented as dashed vertical bars. As shown in the figures, as the feedrate increases, the mean of cutting forces increases. In addition, the use of coolant reduced the mean of cutting forces by approximately 11%, 17%, and 18% for the 600, 800, and 1000 mm/min feedrates, respectively. However, this decrease in the cutting force was not enough to allow for milling at a feedrate of 1200 mm/min, which led to the breakage of the endmill.

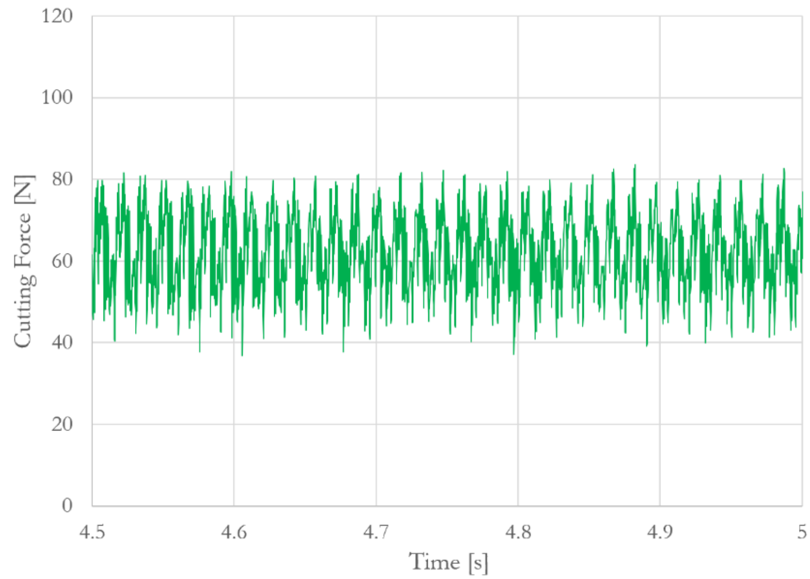

Figure 4.3. Example of cutting force measurement in feed direction. Tool diameter was 6.35 mm, cutting feedrate was 600 mm/min, axial depth of cut was 0.5 mm, and spindle speed was 4000 rpm

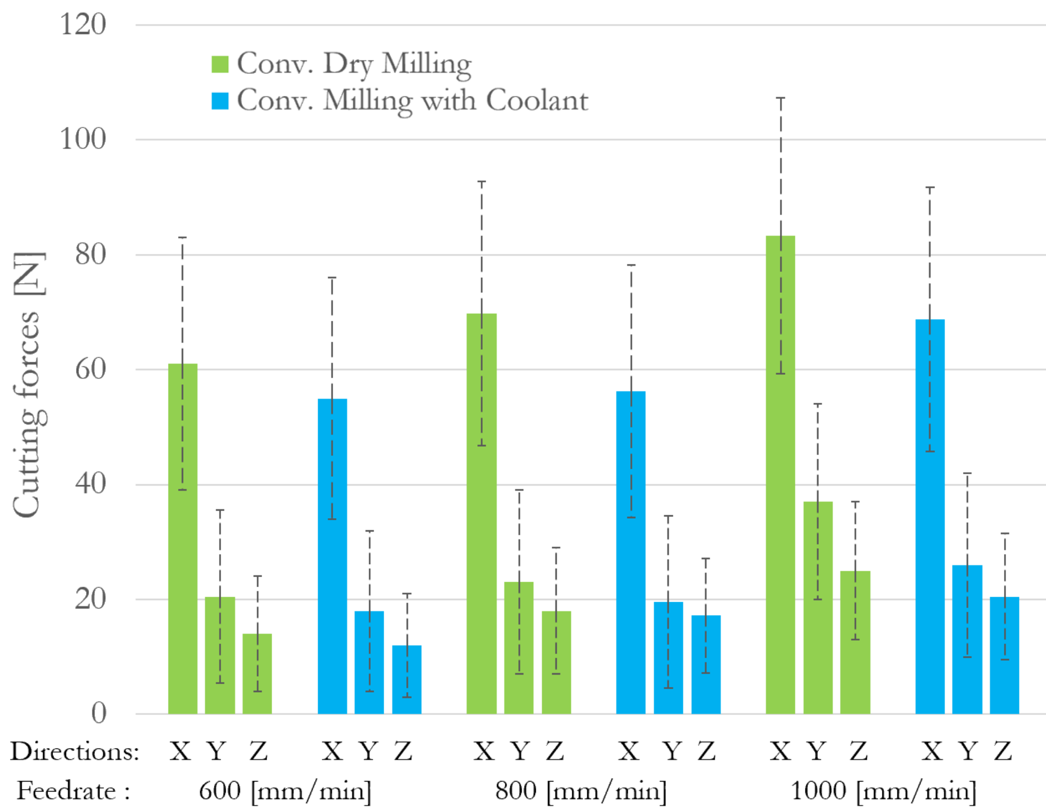

Figure 4.4. Mean of cutting forces measurements in three directions. Dashed vertical bars represent the variation of cutting forces around the mean.

4.3.2.2 Surface Integrity

4.3.2.2.1 Surface roughness

Figure 4.5 compares the mean of the measured surface roughness Ra obtained with and without coolant at the highest feedrates possible for conventional milling (600, 800, and 1000 mm/min). The vertical bars represent the highest and lowest measured values. As shown in the figure, with the aid of flood coolant, the surface roughness was reduced by about 12%, 11% and 9% at feedrates of 600, 800, and 1000 mm/min, respectively.

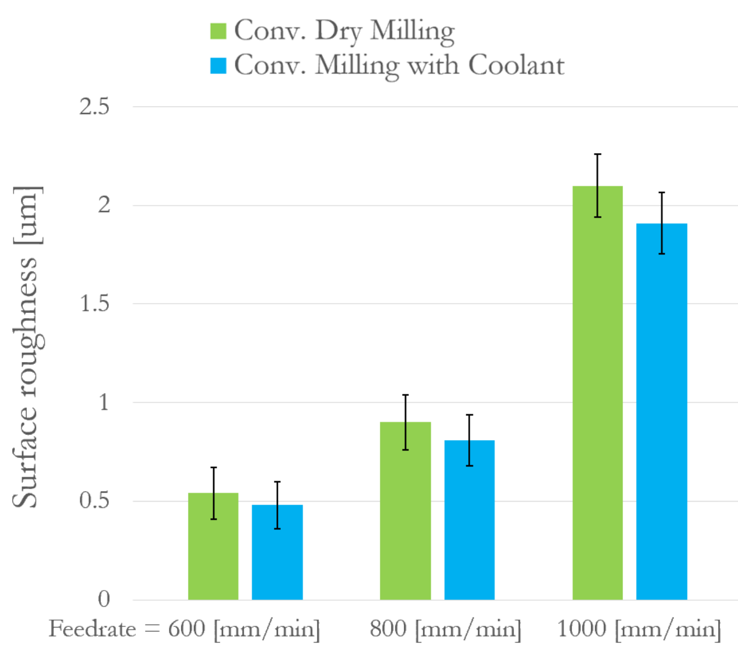

Figure 4.5. Mean of measured surface roughness Ra. The vertical bars represent the highest and lowest measured values.

4.3.2.2.2 Residual stresses

Residual stresses were measured, using the method discussed previously in section 4.2, for one feedrate (800 mm/min) of conventional dry milling in order to be compared later to the residual stresses induced by laser surface heating and laser-assisted milling at the same feedrate and the same laser scanning speed of 800 mm/min. A plot for the measured residual stresses in the feed direction is shown in Figure 4.6. For a feedrate of 800 mm/min, spindle speed of 4000 rpm, and axial depth of cut of 0.5 mm, the figure shows that the residual stress curve was "hook"-shaped, which is in agreement with previously reported data in the open literature [26, 198-200].

Undesirable tensile residual stresses were formed near the top surface due to the heating effect generated by cutting. However, this stress fell rapidly to become compressive due to the mechanical effect of cutting forces. Then, the stress went back to a steady state level, at a depth of approximately 0.25 mm, which corresponds to the initial state of the bulk material.

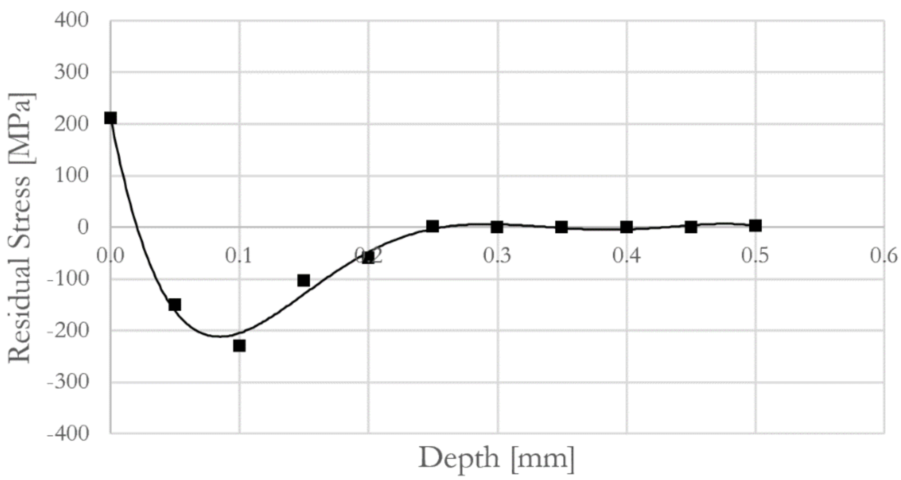

Figure 4.6. Measured residual stresses in the feed direction for conventional dry milling. Feedrate was 800 mm/min, spindle speed was 4000 rpm, and axial depth of cut 0.5 mm.

4.4 Laser Surface Heating of AISI H13 Tool Steel

This section presents the work done to investigate the effect of laser surface heating (LSH) parameters on the preheating surface temperatures, and the induced residual stresses developed in H13 tool steel. The effect of laser heating parameters on microstructure transformations will be investigated experimentally and numerically in Chapter 5. In the LSH process, shown schematically in Figure 4.7, a laser beam is applied with a certain power P, inclination angle θ_L, and scanning speed f to create a moving heating spot on the workpiece surface. When the laser beam is not perpendicular to the surface, the heating spot becomes elliptical in shape with a major axis and a minor axis, as illustrated in Figure 4.7. In this work, two parameters were varied; the scanning speed and laser power, while the inclination angle and heating spot size were kept constant. Type-K thermocouples were used to measure the surface temperature 1 mm away from the edge of the laser heating spot, as shown in Figure 4.7.

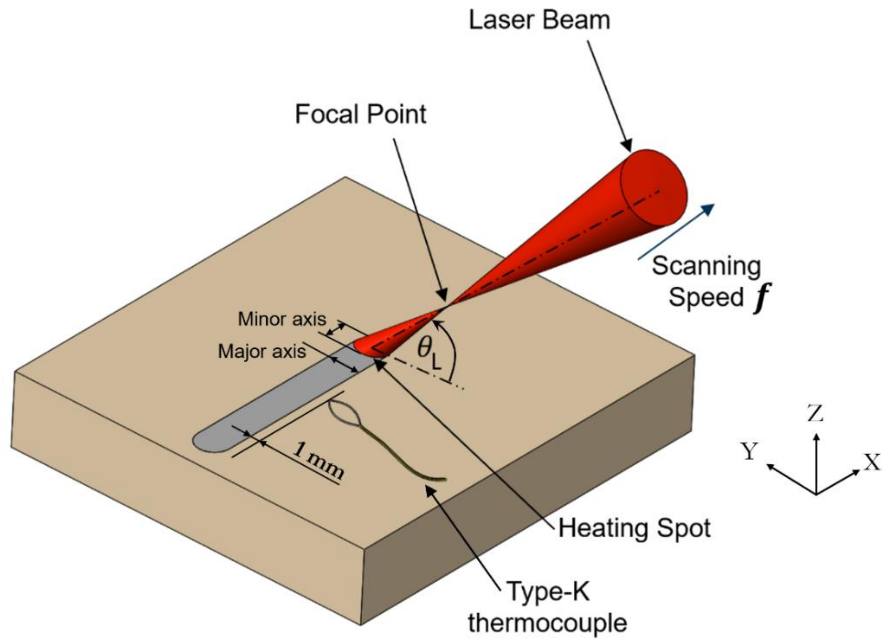

Figure 4.7. Schematic presentation of the laser surface heating (LSH) process (not to scale).

4.4.1 Methodology

4.4.1.1 Laser Power Calibration

Before performing the laser surface heating tests on H13 tool steel, the output laser power had to be calibrated at the delivery point using a laser power measuring sensor (PowerMonitor 48, Primes gmbh, Pfungstadt, Germany), shown in Figure 4.8. The figure shows that the sensor has an entrance mirror, which reflects the beam 90 degrees to a cylindrical absorber cooled with a closed-loop water circuit. The maximum power measurable by this sensor is 8,000 W, with a reproducibility and accuracy of ± 1% and ± 2%, respectively. The full experimental setup used in this work is shown in Figure 4.9. The calibration was performed inside the same horizontal 5-axis CNC machining center mentioned in section 3.3, with the same laser focusing head and 3,000 W diode laser source. As shown in Figure 4.9, the laser head was mounted on a set of linear and angular manual actuators (4) (UniSlide, Velmex, New York State, USA) attached on the spindle of the CNC machining center (1), to accurately align the laser beam with the power measuring sensor.

The internal optics of the laser source were aligned until the output measured power of the delivered beam was within ± 1% of the specified power level. The output measured laser power is shown in Figure 4.10.

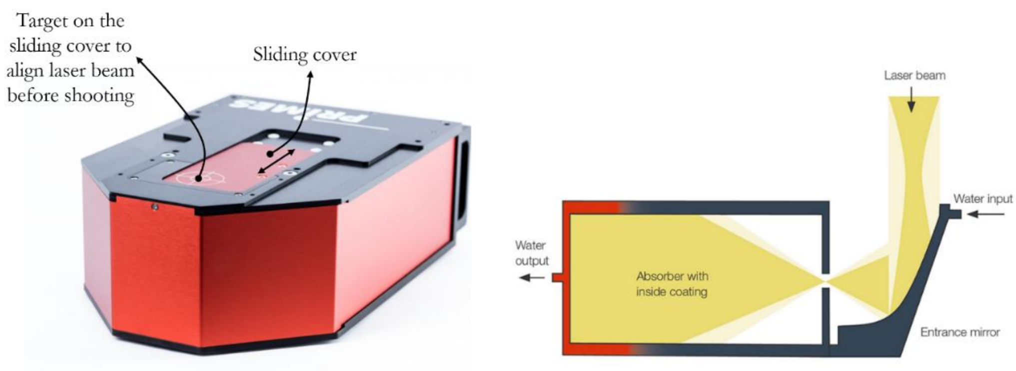

Figure 4.8. Schematics for the sensor used to calibrate the power delivered by the diode laser [201].

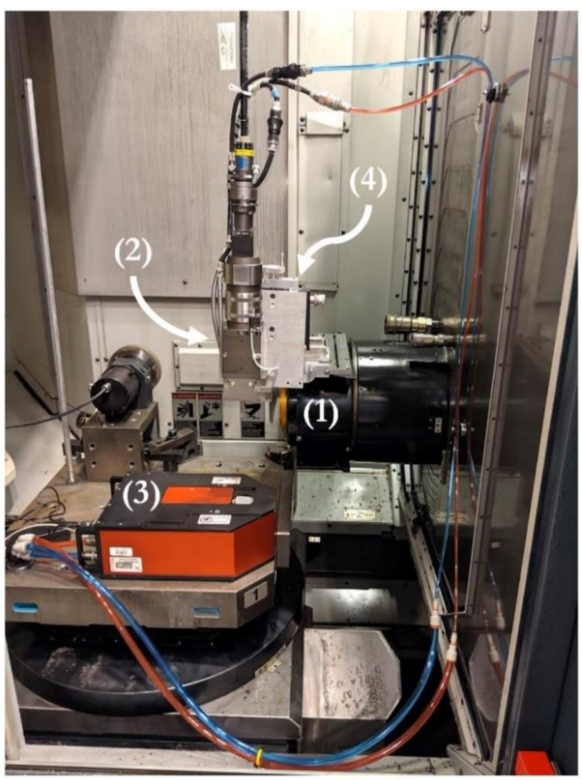

Figure 4.9. Experimental setup used to calibrate the power delivered by the diode laser. (1) Spindle of the CNC machining center, (2) Laser focusing head, (3) Sensor used in calibration of diode laser power, and (4) Actuators used for alignment.

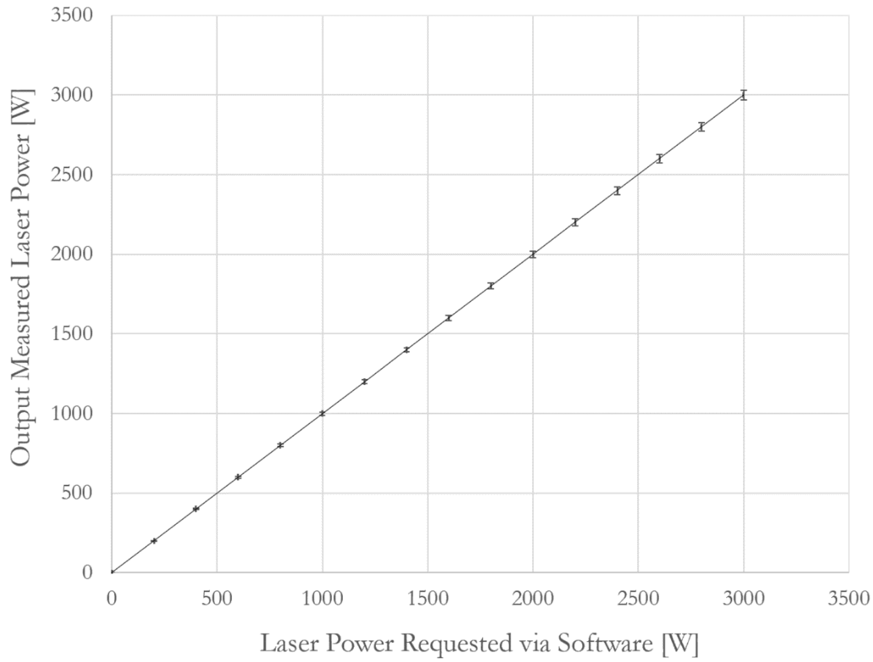

Figure 4.10. Output measured laser power at delivery point. The vertical bars represent the variation in measured laser power (maximum variation is ± 1%).

4.4.1.2 Measurement of Laser Beam Power Density

The laser beam power density was measured at 20 different horizontal planes above and below the plane of the laser beam focal point to verify the position of the focal point, to measure its size, and to determine the density of laser beam power. The device used for this purpose is shown in Figure 4.11 (FM48, Primes gmbh, Pfungstadt, Germany). This device can be adjusted in the y-axis to accurately align the measuring tip with the laser beam. It can also move in the z-axis to move the measuring tip vertically in order to measure the laser power density at different horizontal planes.

The laser head used in this work had a focal length of 200 mm, which generated a laser spot diameter of about 0.8mm at the focal plane. As shown in Figure 4.12, the laser power density distribution at the focal plane is nearly uniform, with a variation of ±1%. However, the distribution becomes Gaussian as the distance between the heating plane and the focal plane increases in both directions.

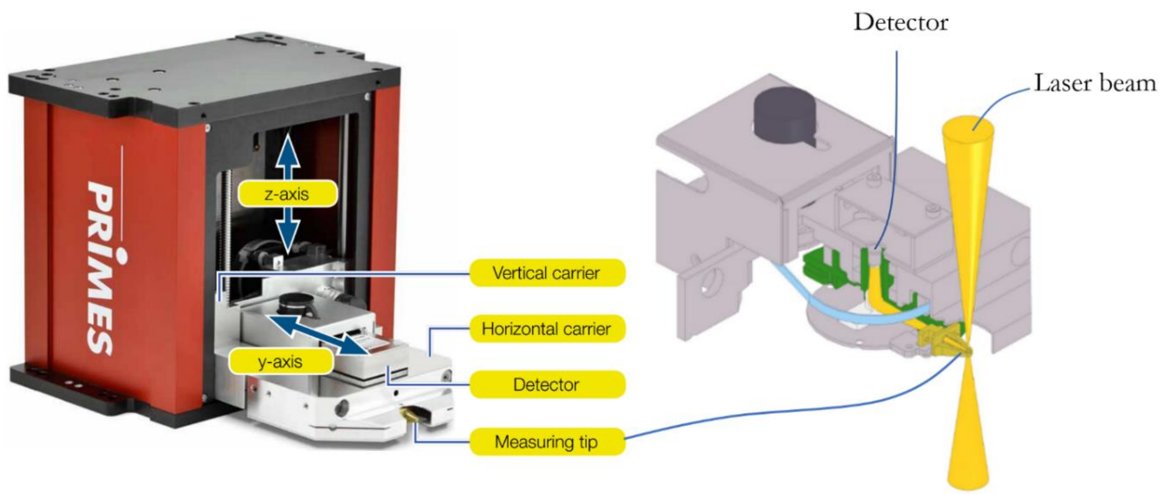

Figure 4.11. Device used for diode laser power density measurement [202].

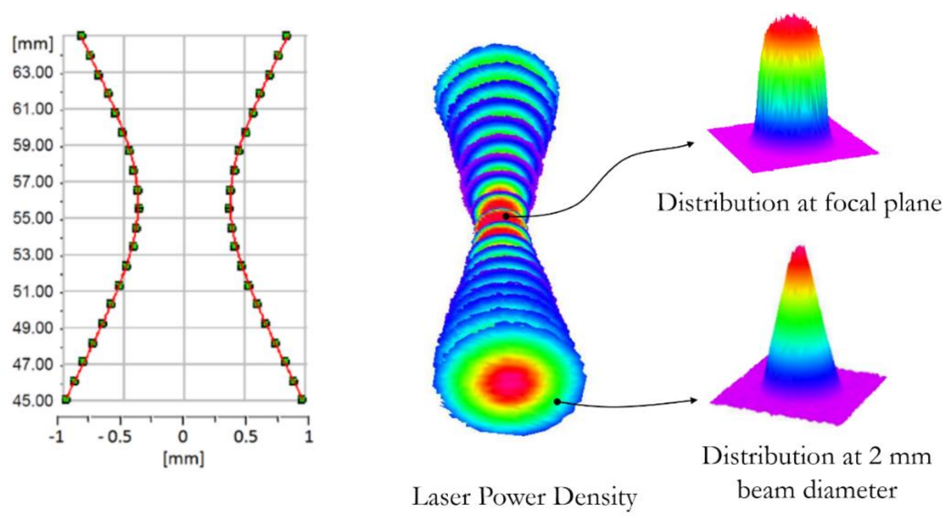

Figure 4.12. Diode laser beam profile and power density.

4.4.1.3 Laser Surface Heating (LSH) of H13 Tool Steel

The experimental setup used for laser surface heating of H13 tool steel is the same setup shown previously in Figure 3.5, but without the cutting tool and its holder. The workpiece used (76.2 x 203.2 x 304.8 mm) is shown in Figure 4.13. An array of 16 type K thermocouples were spot welded to the workpiece to measure its surface temperature, as shown in the figure. Figure 4.14 shows the workpiece setup on the table of the CNC machining center. The laser beam was initially aligned on the workpiece surface with the help of a pilot light generated from the diode laser source (shown in Figure 4.15 as a red ring).

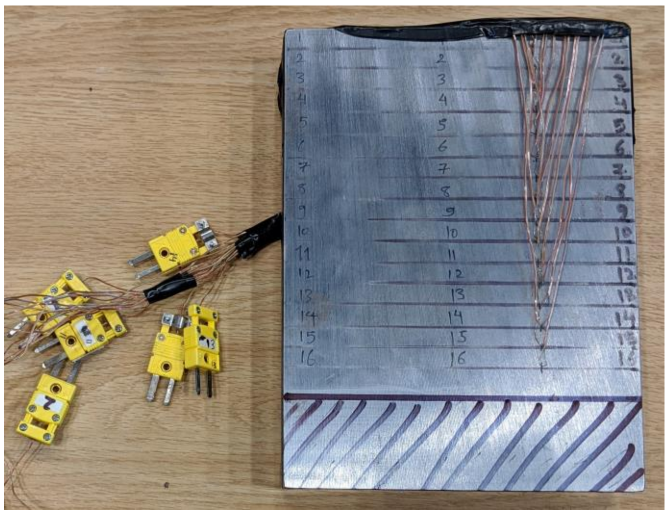

Figure 4.13. Type-K thermocouples welded on the H13 tool steel workpiece.

Figure 4.14. Setup on the CNC table side. (1) Workpiece, (2) Camera, (3) CNC machine table.

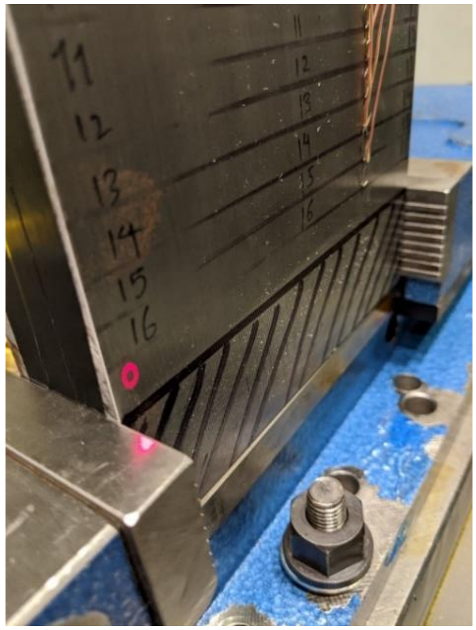

Figure 4.15. Laser pilot light (red ring) used for aligning the laser focusing head with the workpiece.

The test conditions used for laser surface heating of H13 tool steel are shown in Table 4.2. Laser scanning speeds were the same as the cutting feedrates which maximized the material removal rate (MRR) for conventional milling of H13 tool steel (section 4.3). The laser power was varied from 500 W to 1,100 W. The laser heating spot size was fixed at 5 mm (major axis length shown in Figure 4.7), and the laser beam inclination angle was fixed at 45 degrees. Sixteen type-K thermocouples were spot welded 1 mm away from each laser heating path.

Table 4.2. Test conditions used for laser surface heating of H13 tool steel.

Path no.	Laser Power [W]	Scanning Speed [mm/min]
1	500	600
2		800
3		1000
4		1200
5	700	600
6		800
7		1000
8		1200
9	900	600

10		800
11		1000
12		1200
13	1100	600
14		800
15		1000
16		1200

4.4.2 Results and Discussion

4.4.2.1 Maximum Surface Temperatures

The maximum temperatures measured at 1 mm away from the edge of the laser heating spot by the type-K thermocouples are shown in Figure 4.16. As expected, as the laser power increases, the surface temperature increases. It can also be seen that as the scanning speed decreases, the temperature increases since a lower scanning speed provides the laser beam with more time to heat the surface. The maximum temperature of the surface inside the heating spot is estimated using a numerical model developed in Chapter 6.

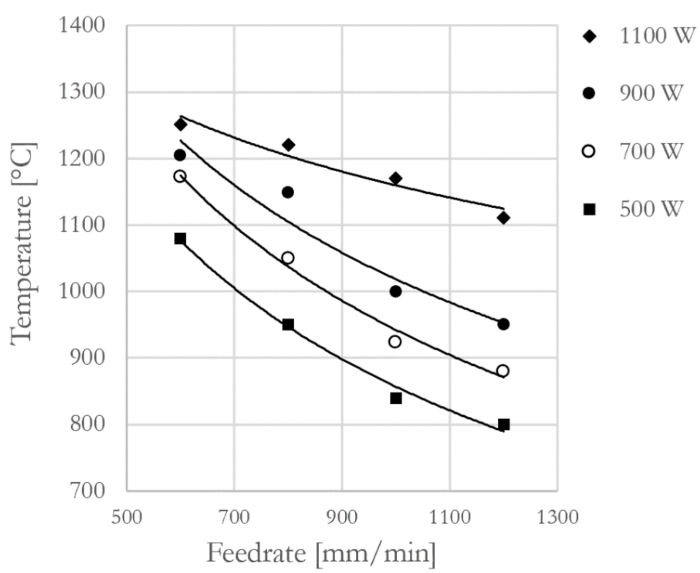

Figure 4.16. Effect of laser power and scanning speed on the maximum surface temperature measured at the thermocouples positioned at 1 mm away from the edge of the laser heating spot.

4.4.2.2 Residual Stresses

Residual stresses were measured at a scanning speed of 800 mm/min, which is the same cutting feedrate for conventional dry milling at which the residual stresses were measured previously in section 4.3.2.2.2. As shown in Figure 4.17, the measured residual stresses were all in a tensile state from the top surface to a depth of 0.6 to 0.8 mm, around which the residual stress became more stable, approaching that of the initial state of the bulk material. As expected, as the laser power increased, tensile stresses closer to the surface increased, since thermal loads are known to produce tensile residual stresses [27].

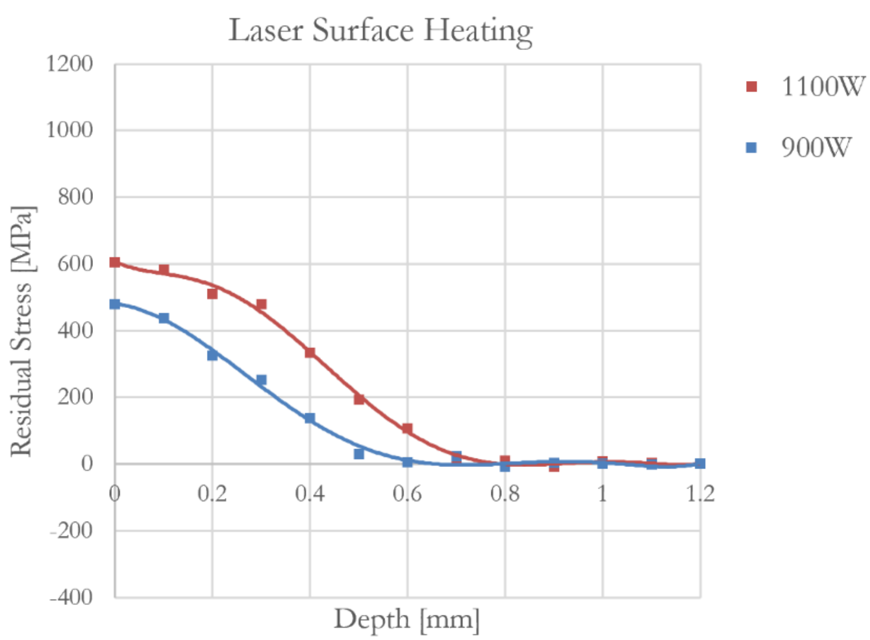

Figure 4.17. Measured residual stresses at 800 mm/min for laser surface heating of H13 tool steel at two laser power levels.

4.5 Multi-Axis Laser-Assisted Milling (LAML) of H13 Tool Steel

This section presents the work done to test the multi-axis LAML system developed in Chapter 3 (section 3.3), and to investigate the effect of different laser heating parameters and cutting conditions on cutting forces, surface roughness, and residual stresses. These tests allowed us to compare the benefits of LAML to conventional milling. All the LAML tests presented in the coming sections are using the same experimental setup shown in Figure 3.5 without using any kind of coolants, i.e., under dry condition.

The cutting forces, surface roughness, and residual stresses were measured using the measuring instruments discussed previously in section 4.2.

4.5.1 Convention of Identifying the Degrees of Freedom of LAML Operations

The convention used in this research work to identify the degrees of freedom of LAML operations is presented in Table 4.3. The word **"axis"** is used to denote any independent movement performed by either the cutting tool **or** the laser beam. The word **"directional"** is used only for the case of 3-axis LAML tests to denote the direction of the feedrate in the cartesian XY plane. If the feedrate direction does not change in the XY plane, i.e., the torque motor is not used, then the 3-axis LAML is considered **"unidirectional"**. Otherwise, it is considered **"multi-directional"**, implying that the torque motor is used.

Table 4.3. Labeling convention for LAML tests.

Label for LAML test	Cutting tool independent movements	Laser beam independent movements	Total number of independent movements
1-axis	Moves along one axis	▪ No independent movement	**1**
3-axis unidirectional	Moves along two axes	▪ Moves linearly to control defocusing distance (D_{fw})	**3 (2+1)**
3-axis multi-directional	Moves along two axes	▪ Moves its angular position around the cutting tool (θ_m)	**3 (2+1)**
5-axis	Moves along three axes	▪ Moves linearly to control defocusing distance (D_{fw}) ▪ Moves its angular position around the tool (θ_m)	**5 (3+2)**
7-axis	Moves along five axes	▪ Moves linearly to control defocusing distance (D_{fw}) ▪ Moves its angular position around the tool (θ_m)	**7 (5+2)**

4.5.2 One-Axis Laser-Assisted Milling

A schematic for the 1-axis LAML process is shown in Figure 4.18. In this process the laser beam heating spot has the same Z and Y position as the cutting tool and is shifted in X direction by a fixed distance. Both the laser beam and the cutting tool are moving in X direction with the same constant speed. The G-code for this process was created using Fusion360 and M-code commands were added to the G-code program to wait for a signal from the central workstation to begin execution, switch laser on (Figure 4.18 (a)), and switch laser off before the end of the slot (Figure 4.18 (b)).

The test conditions for the 1-axis LAML tests are shown in Table 4.4. The cutting feedrates were chosen to be the same as the laser scanning speeds, and identical to the cutting feedrates which maximized the material removal rate (MRR) in conventional milling of H13 tool steel (section 4.2). The depth of cut, and the cutting speed for the 6.35 mm endmill were fixed at 0.5 mm and 4,000 rpm, respectively. The leading distance between the laser heating plane and the cutting tool was fixed to 5 mm. The laser power was varied from 500 W to 1,100 W. The laser beam inclination angle was fixed to 45 degrees, and the major axis of the laser heating spot size was fixed to 5 mm.

The material surface temperature at the edge of the endmill during 1-axis LAML was estimated from the temperatures measurements performed during LSH by thermocouples (section 4.4.2.1). Figure 4.19 illustrates the method used for these estimations for a general case. Considering Figure 4.19(a), the distance between the endmill start position and thermocouple position (d_{et}) is known for all cases of 1-axis LAML, since the start position and the thermocouple position were fixed for all cases. The time taken by the endmill to move from the start position to the thermocouple position (t_{et}), Figure 4.19 (b), is calculated as follows:

$$t_{et} = \frac{d_{et}}{f} \qquad \text{(Equation 4.1)}$$

Since the endmill movement and the thermocouples temperatures logging started at the same time by the central workstation, the calculated values of t_{et} are used to estimate the surface temperature at the moment the endmill edge reaches the thermocouple position.

The effects of laser power and cutting parameters on cutting forces, surface roughness, and residual stresses were investigated and compared to conventional milling. The results are presented in section 4.6.

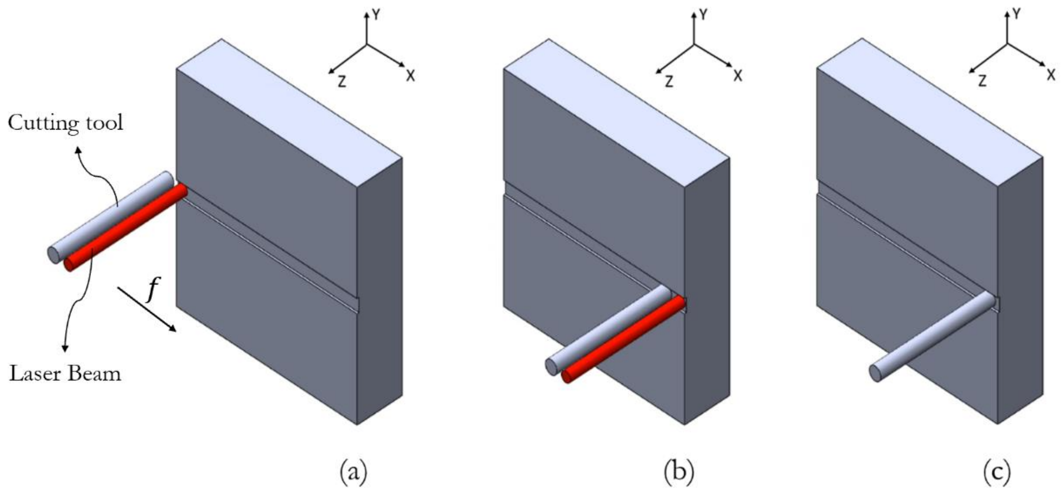

Figure 4.18. Sequence of operation schematic for the 1-axis laser-assisted milling process. a) Laser is turned on and tool starts moving in X direction, b) Laser is turned off, and c) Tool continues movement to finish milling the slot. The schematic is not drawn to-scale.

Table 4.4. Test conditions used for the 1-axis LAML tests.

Path no.	Laser Power[W]	Tool Diameter [mm]	Spindle speed [rpm]	Depth of Cut [mm]	Feedrate [mm/min]
1	500	6.35	4,000	0.5	600
2					800
3					1,000
4					1,200
5					1,300
6	700				600
7					800
8					1,000
9					1,200
10					1,300
11	900				600
12					800
13					1,000
14					1,200
15					1,300
16	1,100				600
17					800
18					1,000
19					1,200
20					1,300

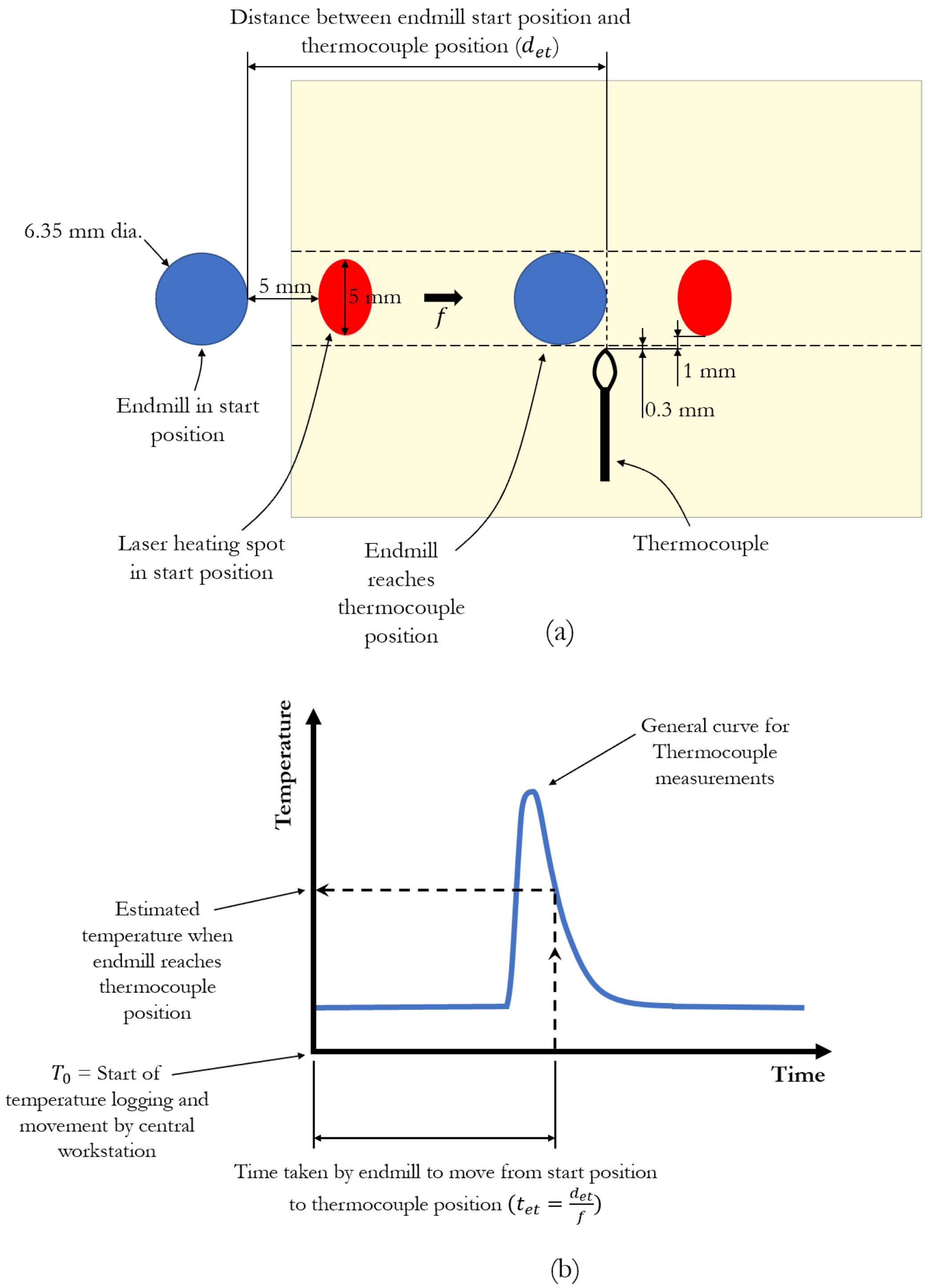

Figure 4.19. Method of estimating the material surface temperature at the endmill edge during 1-axis LAML.

4.5.3 Three-Axis Unidirectional Laser-Assisted Milling

A schematic for the 3-axis unidirectional LAML of a 3D surface is shown in Figure 4.20. As shown in Figure 4.20(a), the laser is turned on and tool starts moving. In Figure 4.20(b), the laser is turned off, and in (c) the tool continues movement to finish milling. Figure 4.21 shows the geometrical details of the 3D surface.

Three independent simultaneous movements (3 axes) are needed for this LAML process. The cutting tool must move in 2 axes simultaneously (X and Z). This movement is controlled by G-code. On the other hand, the laser beam must move along the Z-axis independently from the cutting tool to keep the defocusing distance constant along the geometry of the workpiece. This movement is controlled by a linear actuator. The displacement required by the linear actuator was calculated by the Matlab based offline translator using Equation 3.1 based on the changing Z-axis coordinates of the laser beam path. Both the laser beam and the cutting tool are moving in X direction with the same constant speed. However, the laser heating spot is shifted in X direction away from the cutting tool by a fixed distance.

The workpiece used in these LAML tests is shown in Figure 4.22. The 3D profile of the workpiece was initially machined conventionally from a rectangular flat H13 tool steel block. Then, during the 3-axis unidirectional LAML process, multiple parallel cutting paths were performed to remove a constant depth of material along the 3D profile. The G-code for the LAML process was created using the CAM software Fusion360 and a post-processor for the CNC machining center controller (FANUC). The M-code commands were then embedded into the G-code. Similar to the 1-axis LAML tests, M-code commands were used to achieve the sequence of operation shown in Figure 4.20.

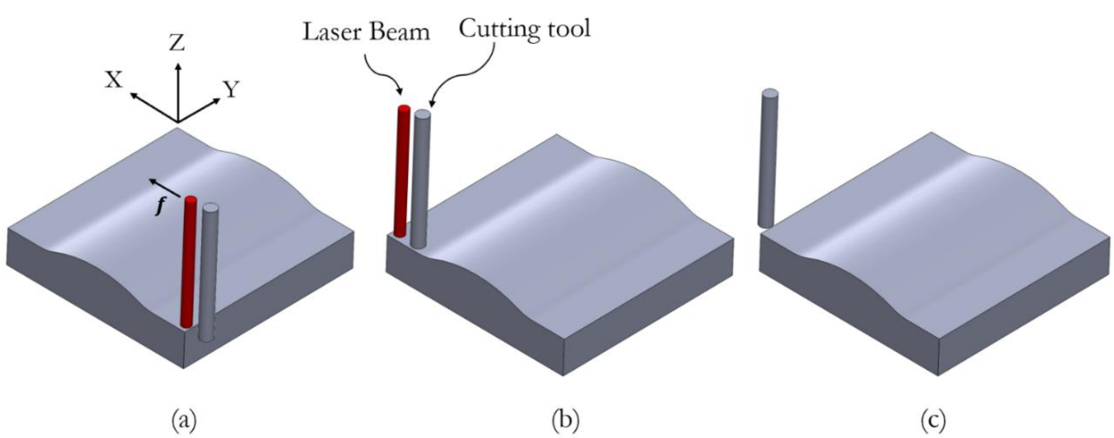

Figure 4.20. Schematic for the sequence of operation for the 3-axis unidirectional laser-assisted milling process.

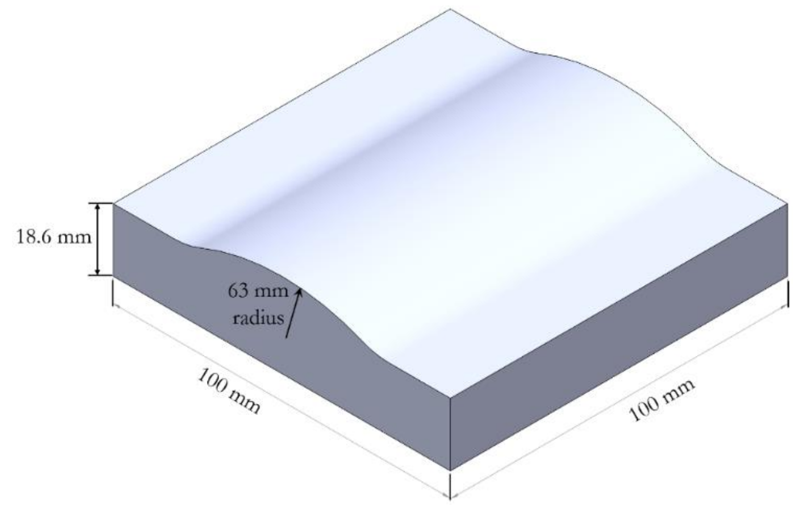

Figure 4.21. Geometry of the 3D surface for 3-axis unidirectional LAML.

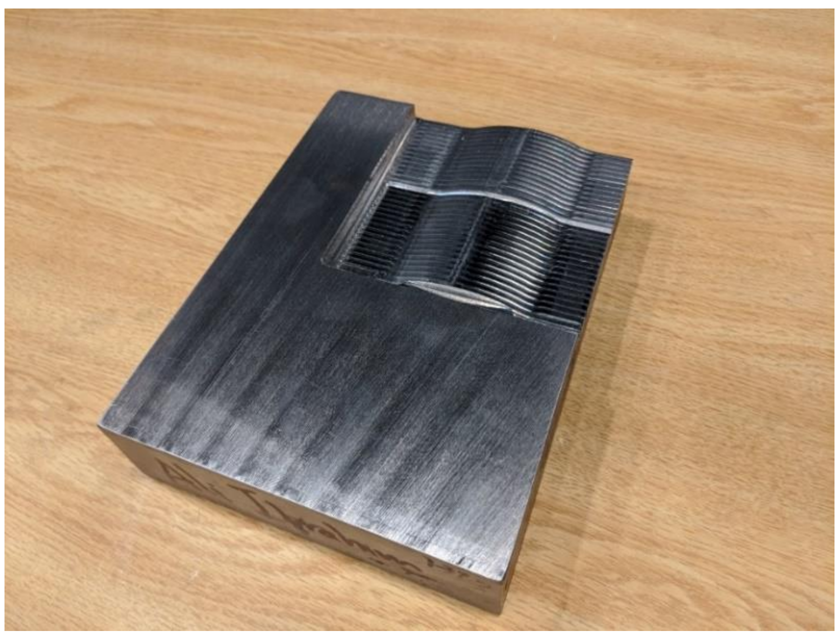

Figure 4.22. Workpiece used for 3-axis unidirectional LAML.

The test conditions for the 3-axis unidirectional LAML tests are shown in Table 4.5. Twenty-four cutting paths were milled at 800 mm/min feedrate, and ten were milled at 1000 mm/min. Laser power for both feedrates was either zero (conventional dry milling) or 1,100W. The depth of cut and cutting speed were fixed at 0.5 mm, and 4,000 rpm, respectively. The distance between the laser heating spot and the cutting tool was fixed at 5 mm. The laser beam inclination angle was fixed at 45 degrees, and the laser heating spot major axis was fixed at 5 mm. Cutting forces and surface roughness were measured for comparison. The results are presented in section 4.6.

Table 4.5. Test parameters used for 3-axis unidirectional LAML.

Number of Paths	Tool diameter [mm]	Feedrate [mm/min]	Laser Power[W]	Spindle speed [rpm]	Depth of Cut [mm]
12	6.35	800	1,100	4,000	0.5
12	6.35	800	0	4,000	0.5
5	6.35	1000	1,100	4,000	0.5
5	6.35	1000	0	4,000	0.5

4.5.4 Three-Axis Multi-Directional Laser-Assisted Milling

A schematic for the 3-axis multi-directional LAML process is shown in Figure 4.23. This 3-axis LAML process is demonstrated by milling a curved slot (70 mm in radius) with a constant axial depth of cut. As shown in Figure 4.23(a), laser is turned on, the cutting tool starts moving in X and Y directions, and torque motor starts changing the laser beam position to be ahead of the tool. In Figure 4.23(b), the laser is turned off when the heating spot reaches the end of the curved slot. In Figure 4.23(c), the cutting tool continues movement to finish milling the curved slot.

Three independent simultaneous movements are needed during LAML of such slot: a) the cutting tool must move in two axes, X and Y, simultaneously and b) the laser heating spot must move simultaneously around the tool axis while it is changing its feed direction, in order to heat the spot that would be removed by the cutting tool in the direction of the tool feed.

The Matlab-based tool path translator was used to translate the cutting tool path to laser heating spot path by calculating the required torque motor angle θ_m using Equation 3.2. During the LAML tests, the calculated values for the torque motor angle were fed in real-time by the central workstation controller to the direct drive torque motor through its servo drive. Since the torque motor was mounted on the spindle of the CNC machining center, both the laser heating spot and the cutting tool were moving with the same constant linear feedrate but shifted away from each other by a fixed distance.

The conditions of the 3-Axis multi-directional LAML tests are shown in Table 4.6. Ten cutting paths were milled at 800 mm/min feedrate, and ten cutting paths were milled at 1,000 mm/min. Laser power for both feedrates was either zero (for conventional dry milling) or 1100 W (for dry LAML). The cutting tool diameter was 6.35 mm, the axial depth of cut was constant at 0.5 mm, and spindle rotational speed was constant at 4,000 rpm. The distance between the laser heating spot and the cutting tool was fixed to 5 mm. laser beam inclination angle was fixed to 45 degrees, and the laser heating spot major axis was fixed to 5 mm. The AISI H13 tool steel workpiece used was 75 x 200 x 300 mm.

Cutting forces were measured using the dynamometer. The resultant cutting force F_r in the feed direction was calculated as:

$$F_r = \sqrt{{F_X}^2 + {F_Y}^2}, \qquad \text{(Equation 4.2)}$$

where F_X and F_Y are the cutting forces measured in X and Y directions respectively.

The effects of laser power and cutting parameters on cutting forces and surface roughness were investigated and compared to conventional milling. The results are presented in section 4.6.

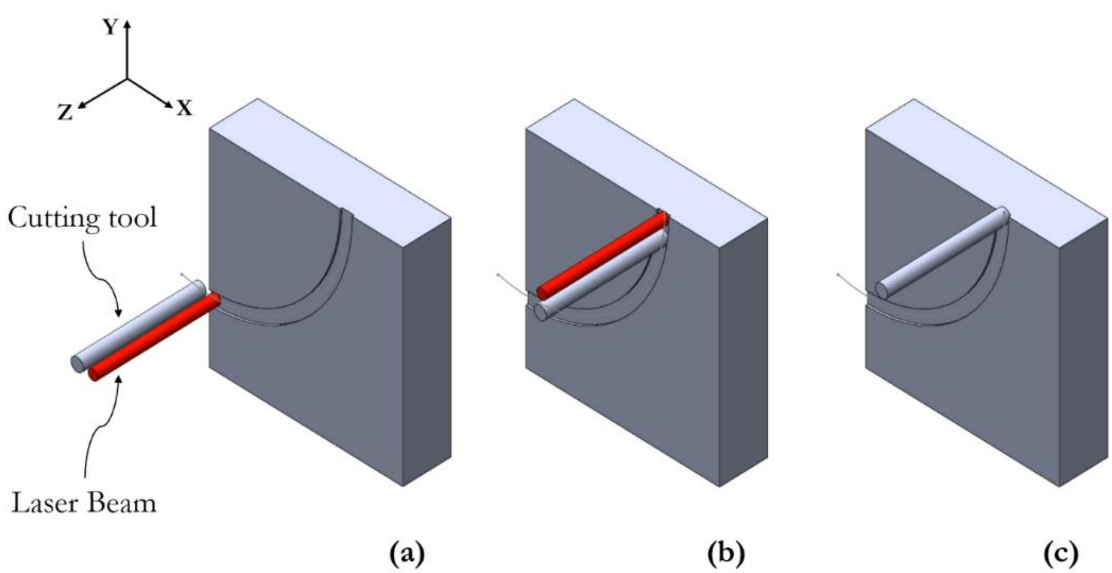

Figure 4.23. Sequence of operation schematic for the 3-xis multi-directional laser-assisted milling tests.

Table 4.6. Conditions for the 3-Axis multi-directional LAML tests.

<table>
<tr><th>Number of Paths</th><th>Tool diameter [mm]</th><th>Feedrate [mm/min]</th><th>Laser Power[W]</th><th>Spindle speed [rpm]</th><th>Depth of Cut [mm]</th></tr>
<tr><td>5</td><td rowspan="4">6.35</td><td rowspan="2">800</td><td>1,100</td><td rowspan="4">4,000</td><td rowspan="4">0.5</td></tr>
<tr><td>5</td><td>0</td></tr>
<tr><td>5</td><td rowspan="2">1,000</td><td>1,100</td></tr>
<tr><td>5</td><td>0</td></tr>
</table>

4.5.5 Five-Axis Laser-Assisted Milling

Figure 4.24 shows a schematic for the 5-Axis LAML of a curved slot that has a 3D surface, whose geometrical details are shown in Figure 4.25(a). In step (a), the laser is turned on. In step (b), the tool starts moving in X, Y and Z directions. Step (C) is the position where laser is turned off. Finally, in (d) the tool continues movement to finish milling the 3D slot.

For LAML of such 3D slot, five independent simultaneous movements are needed: a) the cutting tool has to move in X, Y, and Z axes simultaneously, (b) the laser heating spot angular position around the cutting tool axis must be actively controlled to accommodate the change in feed direction, and (c) the laser beam defocusing distance must be actively controlled to accommodate the changing 3D surface of the slot as the laser beam is moving along its path.

It should be noted that if the 3D slot (colored blue in Figure 4.25(a)) was on a curved workpiece surface, as is the case in Figure 4.25(b), then in order to mill this workpiece, the table of the CNC machine would need to rotate in two axes, as shown in Figure 4.25(b). In this case the LAML process would be 7-axis (5 machine movements + 2 laser movements). However, the programming needed for the movements of the laser head actuators for this curved workpiece would be the same as the case shown in Figure 4.25(a). Therefore, the same LAML system is capable of performing the 7-axis LAML of case (b).

The conditions for this 5-axis LAML test are the same as those given in Table 4.6. The 3D tool path in the X,Y, and Z directions was designed such that the depth of the material removed along the 3D surface of the slot was constant at 0.5 mm. Both the laser heating spot and the cutting tool were also moving with the same constant linear federate of 800 or 1,000 mm/min. The workpiece used was 76 x 203 x 304 mm AISI H13 tool steel. The resultant cutting forces and surface roughness at 1,100 W power were measured and compared with conventional dry milling without laser assistance.

In the case of this LAML process, the resultant cutting force F_r was calculated as:

$$F_r = \sqrt{{F_X}^2 + {F_Y}^2 + {F_Z}^2}, \quad \text{(Equation 4.3)}$$

where F_Z is the cutting force measured in the Z direction.

The effects of laser power and cutting parameters on cutting forces and surface roughness were investigated and compared to conventional milling. The results are presented in section 4.6.

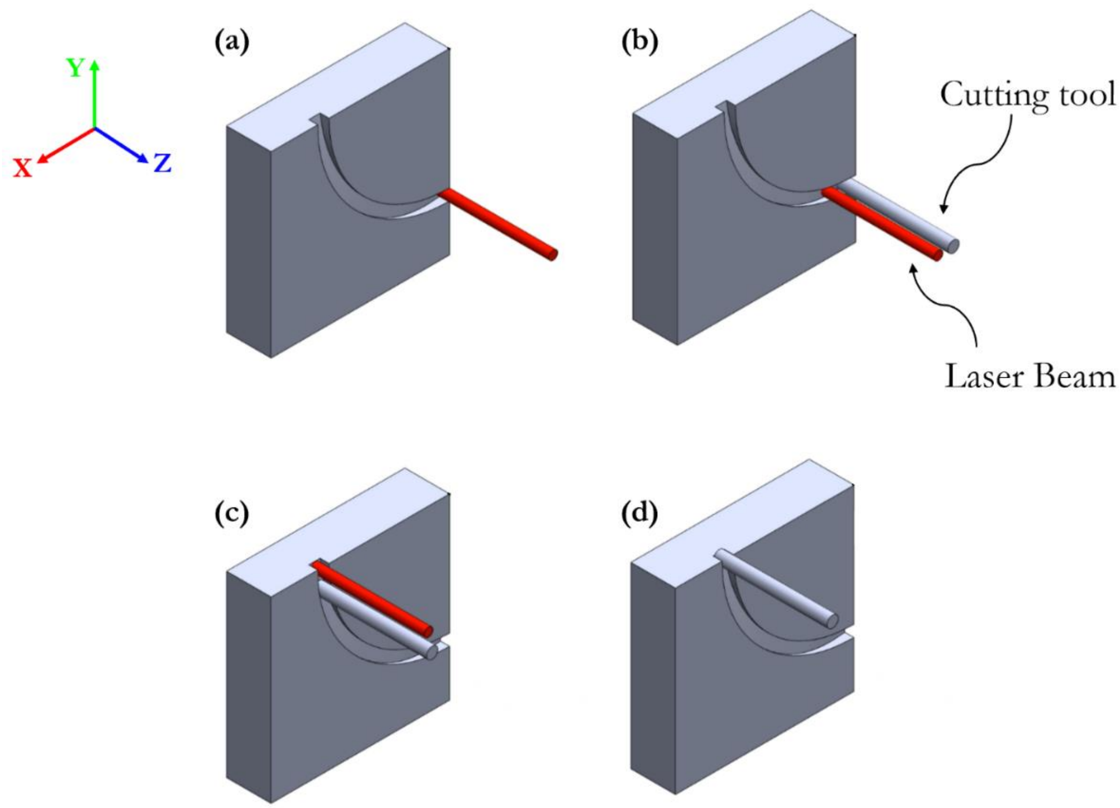

Figure 4.24. Schematic for the sequence of operation of the 5-axis laser-assisted milling tests of a curved 3D slot.

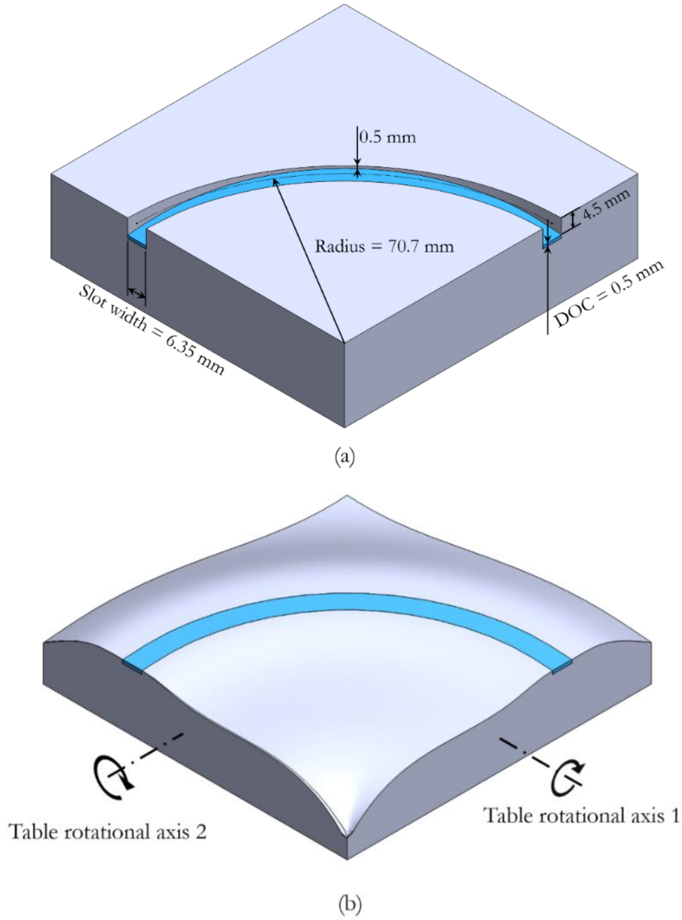

Figure 4.25. Geometry of the curved 3D slot milled during multi-axis LAML. (a) 5-axis LAML case tested experimentally. (b) 7-axis LAML case of the same slot of case (a) but on a curved workpiece.

4.6 Results and Discussion for Multi-Axis LAML of H13 Tool Steel

4.6.1 Validation of Synchronization

To validate the synchronous communications protocol required in the 3-axis unidirectional LAML case, the positions measured by the encoder of the linear actuator and by the 2D laser profiler were used to create the plot given in Figure 4.26. In the figure, the actual path of the center of the laser heating spot is plotted against the ideal surface geometry. It can be that seen the actual linear stage movements lagged slightly behind the ideal path. The maximum position error caused by this lag was approximately 150 μm in the Z direction. Adding the maximum backlash in the ball screw linear actuator, 50 μm, then, the maximum error is 200 μm. This error caused only a maximum of 80 μm error in the size of the laser heating spot, as calculated in the to-scale plot shown in Figure 4.27. The 80 μm error is negligible in this case; and therefore, the synchronisation was considered accurate enough for this application.

To validate the synchronization for the 3-axis multi-directional case of LAML, the acquired angular position measurements of the rotary encoder used by the direct drive torque motor were converted to cartesian X, Y coordinates and compared to the movement of the spindle measured by the 2D laser profiler. From this comparison, the maximum error in the torque motor's positioning was approximately 100 μm, as shown in Figure 4.28. Since the torque motor design does not induce backlash error, the positioning error is only ~3% and 4% of the 3.18 mm tool radius and the 2.5 mm heating spot radius, respectively, which is negligible in this case.

For the 5-axis LAML case, a similar methodology was used to find the maximum error in synchronization. The maximum position errors were 180 μm, in the Z direction, and 100 μm in the XY plane, which are, again, negligible.

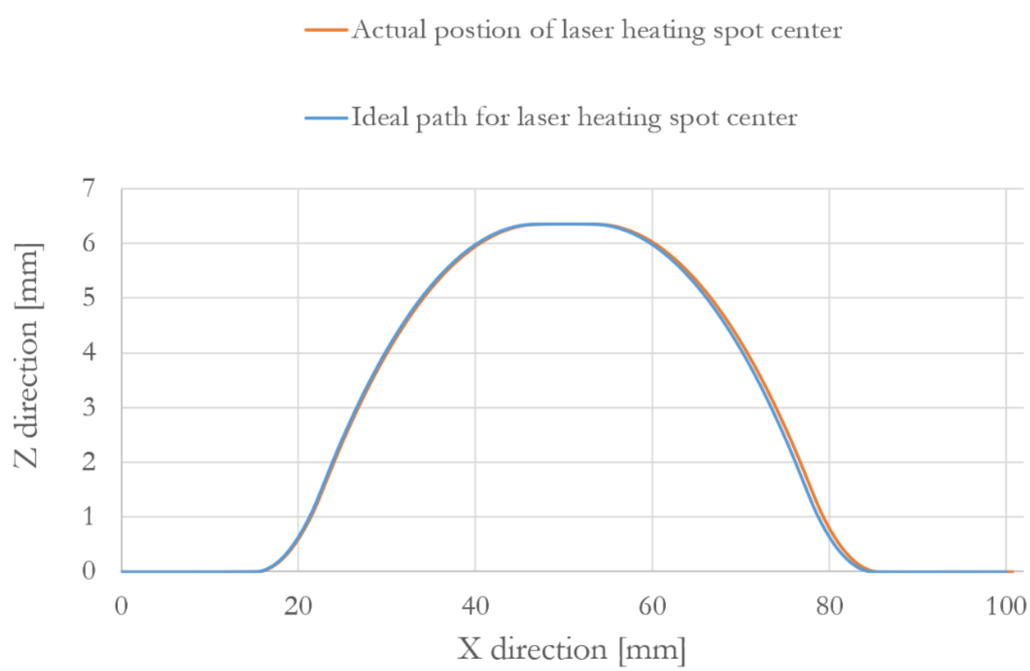

Figure 4.26. Comparison between the actual and ideal laser paths for 3-axis unidirectional laser-assisted milling tests.

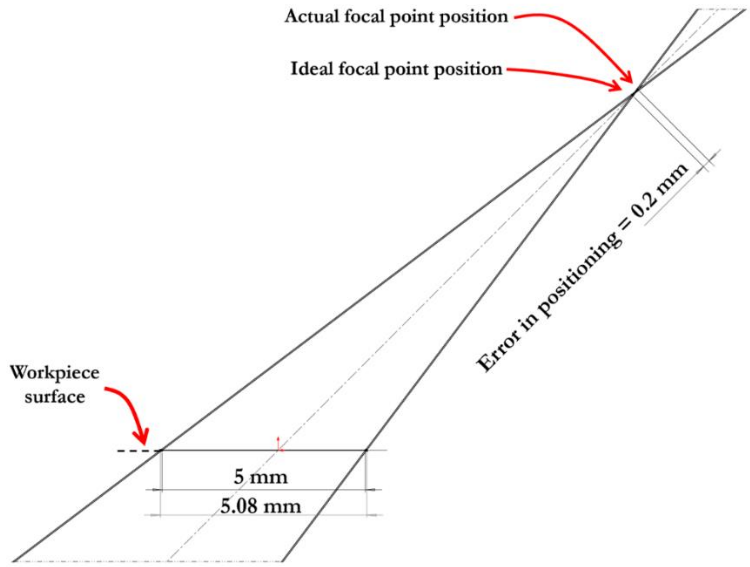

Figure 4.27. The effect of a positioning error of 0.2 mm on laser heating spot size. The laser beam is inclined by 45 degrees as was the case in the actual experimental testing. The sketch is drawn to scale with the exact laser beam dimensions.

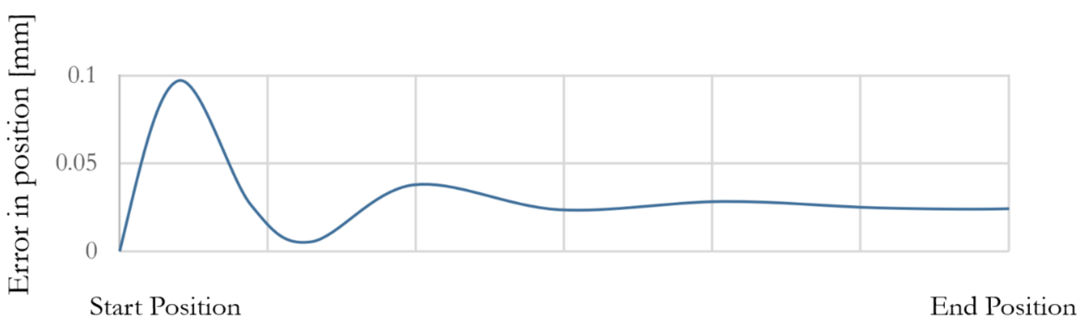

Figure 4.28. Error in positioning the torque motor along the heating spot path.

4.6.2 Surface Temperature

The material surface temperature at the edge of the endmill during 1-axis LAML was estimated and presented in Figure 4.29. These temperatures were estimated using the method illustrated previously in Figure 4.19. As shown in Figure 4.29, the estimated temperature at the thermocouple position (0.3 mm away from the endmill edge) is ranging between approximately 450º C to 710ºC, depending on feedrate and laser power. For a certain feedrate, as the laser power increases, the surface temperature increases. For a given laser power level, the surface temperature increases by decreasing the feedrate, as slower feedrates provide the laser with more time to heat the surface. At 710^o C, the strength of H13 tool steel is significantly reduced by approximately 57% [9]. This significant reduction in material strength leads to significant reduction in cutting forces as discussed in the next section.

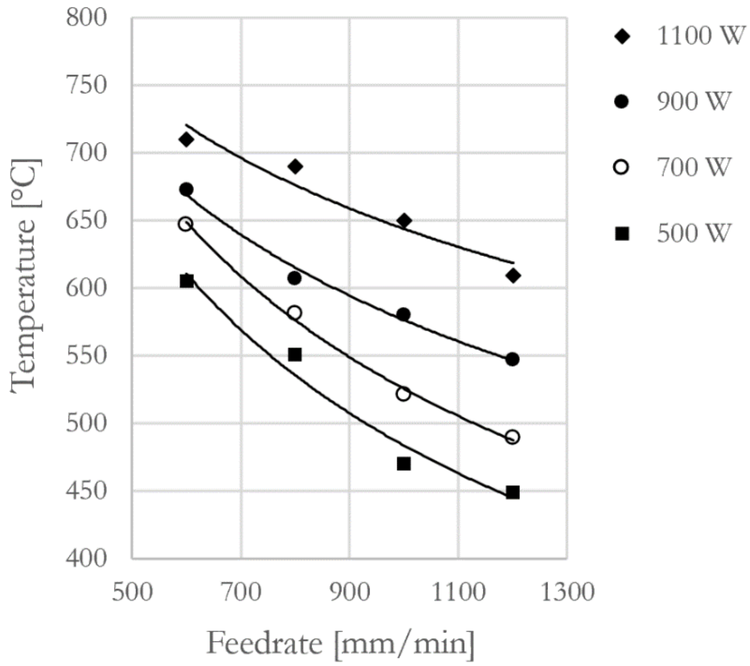

Figure 4.29. Estimated material surface temperatures for 1-axis LAML at the moment the endmill edge reaches the thermocouple position. The thermocouple position is shown in Figure 4.19(a).

4.6.3 Cutting forces

For the 1-axis LAML case, Figure 4.30 compares the cutting force in the feed direction measured during 1-axis laser-assisted milling to the cutting forces measured in conventional milling, with and without flood coolant. As shown in the figure, as the laser power increased, the cutting forces decreased. The cutting forces were reduced by up to 40% with the assistance of the 1,100 W power laser compared to dry milling, and up to 31% compared to milling with coolant. In addition, the implementation of the laser assisted machining showed a consistent reduction in the fluctuation of cutting forces in all cases. These fluctuations are shown in the figure as vertical dotted bars. This suggests an improvement in the process stability as the preheating temperature is increased. This significant reduction in machining forces is due to the decrease in the steel strength at high temperatures, as shown previously in Figure 2.1.

As shown in Figure 4.31, the significant reduction in cutting force allowed the increase of the maximum permissible feedrate for 1-axis LAML up to 1,300 mm/min, which was not possible for conventional milling even with the use of coolant. This results in a 30% increase in the material removal rate (MRR), compared to conventional milling with or without a coolant.

Similar reduction in cutting forces and fluctuations occurred in the rest of the LAML cases investigated using the same power level of 1100W. For the 3-axis unidirectional LAML case (Figure 4.32), the mean value of the absolute of the cutting forces in the X, Y, and Z directions along the cutting path was significantly reduced by up to approximately 39%. For the 3-axis multi-directional LAML case (Figure 4.33), the mean of the resultant cutting force was significantly reduced by up to 35%. For the 5-axis LAML case (Figure 4.34), the mean of the resultant cutting forces was reduced by up to 38%.

As reported in literature, the reduction of cutting forces for laser-assisted milling results in the increase in material removal rate, which consequently results in direct cost savings compared to conventional milling. Wiedenmann et al. [119, 203, 204] performed a comparative cost analysis for LAML and conventional milling of turbine blades using a simplified turbine blade geometry. They estimated that a 33% increase in MRR could result in a cost saving of up to 10.5%. Furthermore, Hedberg and Shin [117] estimated a cost saving of up to 33% for producing parts using LAML, compared to conventional milling, when considering costs for cutting tools, tool change, laser source, and operation.

Another notable advantage of laser-assisted milling is the elimination of coolant usage during cutting. Because of the hidden expenses of these fluids, calculating the true economic benefit of eliminating coolants is challenging. These include for example the environmental impact of non-recyclable components in the coolant and employee health benefits [117].

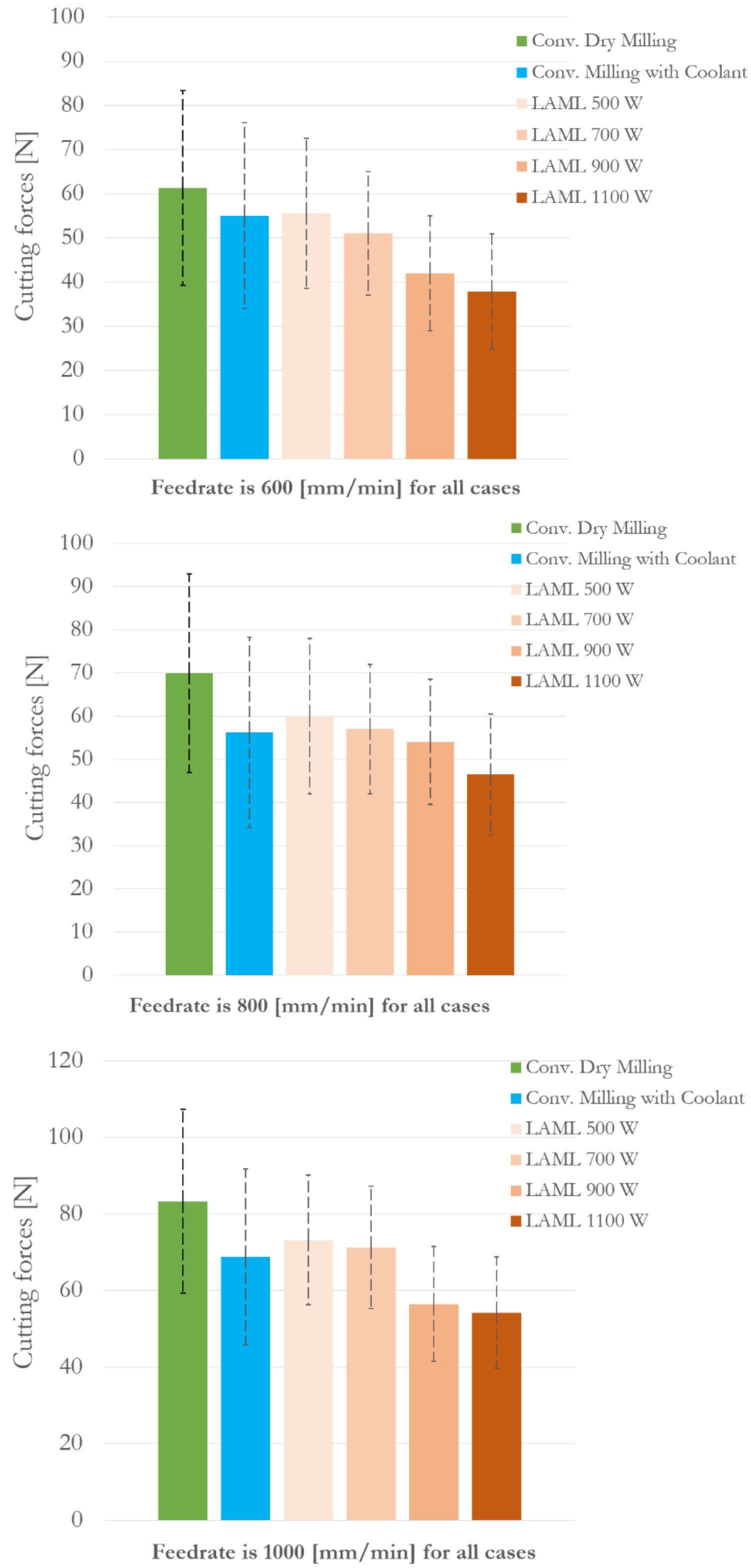

Figure 4.30. Effect of feedrate and laser power on the mean value of the measured cutting force in the feed direction for 1-axis LAML and conventional milling with and without coolant. Vertical bars represent the variation in forces.

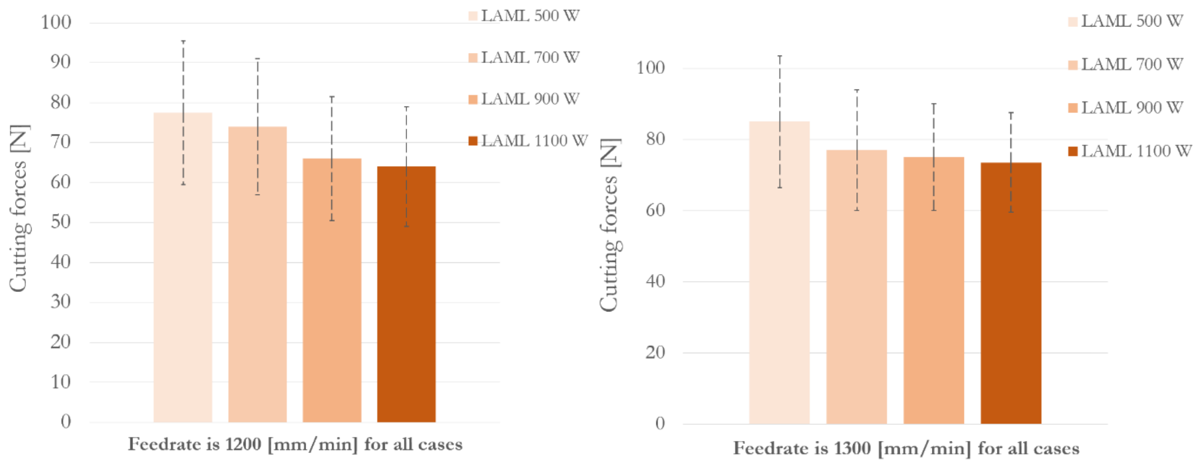

Figure 4.31. Mean value of the measured cutting force in the feed direction for 1-axis LAML with feedrates that were impossible for conventional milling. Vertical bars represent the variation in forces.

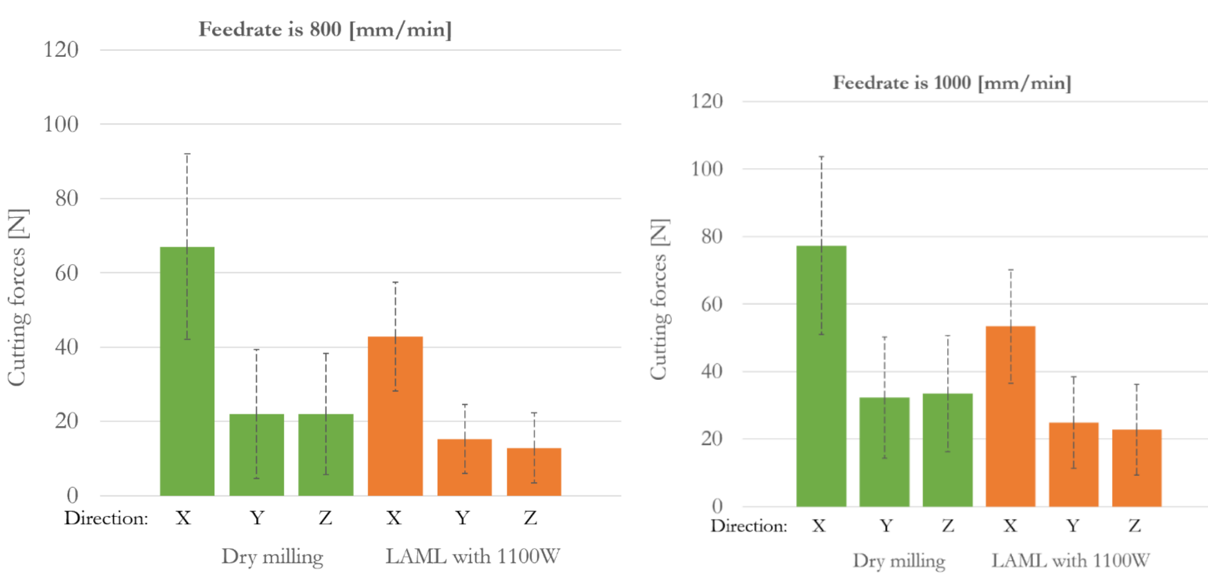

Figure 4.32. Mean of measured cutting forces during 3-axis unidirectional LAML in the three directions X, Y, and Z. Vertical bars represent the variation in forces.

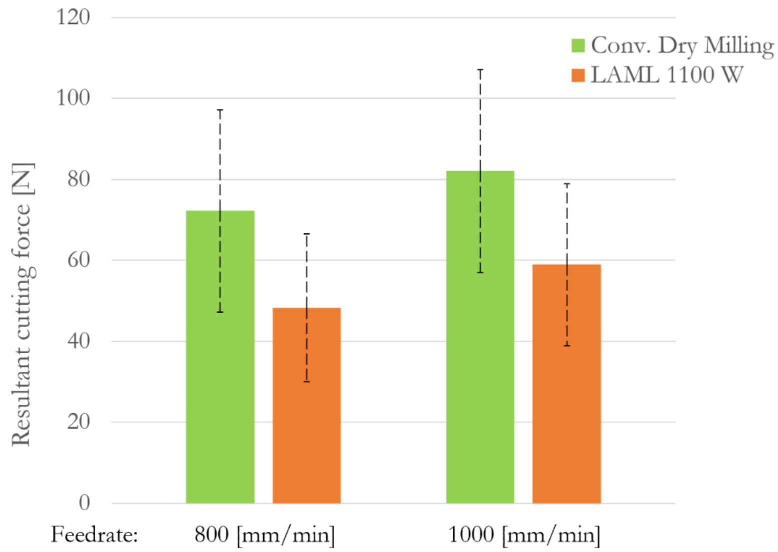

Figure 4.33. Mean of the resultant cutting force F_r measured during 3-axis multi-directional LAML at a feedrates of 800 and 1000 mm/min. Vertical bars represent the variation in forces.

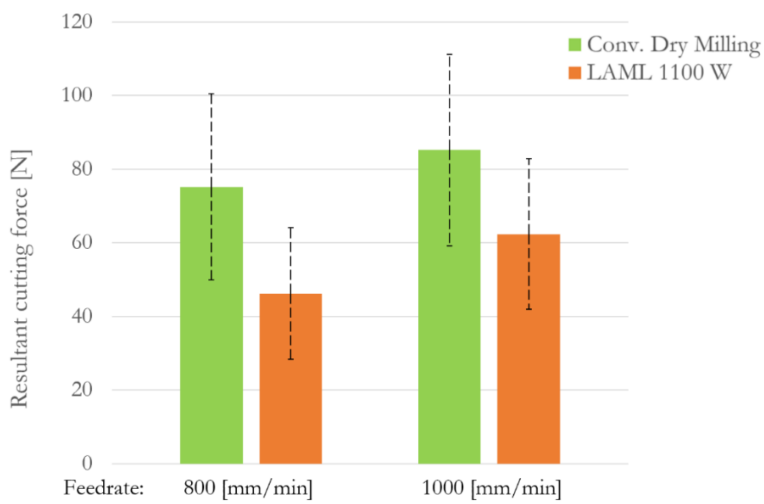

Figure 4.34. Mean of the resultant of the cutting forces in X, Y and Z directions measured during 5-axis LAML at 800 and 1000 mm/min. Vertical bars represent the variation in forces.

4.6.4 Surface Roughness

For the 1-axis LAML case, Figure 4.35 compares the workpiece average surface roughness (Ra) obtained with and without the use of laser heating at the two highest feedrates possible for conventional milling; 800 and 1000 mm/min. The vertical bars represent the highest and lowest measured values. As shown in the figure, surface roughness was improved by up to 20% when machining with laser assistance at 1,100W. Comparing the two plots of Figure 4.35, it is obvious that decreasing the feedrate from 1000 to 800 mm/min significantly decreases the surface roughness by 56% for LAML at the same power level of 1,100W.

Similar improvement in surface roughness occurred in the rest of the LAML cases investigated using the same power level of 1,100W. For the 3-axis unidirectional LAML case (Figure 4.36), the surface roughness was improved by 23% and 19% at 800 and 1,000 mm/min, respectively. For the 3-axis multi-directional LAML case (Figure 4.37), the surface roughness was improved by 17% and 19% at 800 and 1,000 mm/min, respectively. Finally, for the 5-axis LAML case (Figure 4.38), the surface roughness was reduced by 11% and 16% at 800 and 1,000 mm/min, respectively.

The surface finish improvement in LAML are primarily due to the thermal softening that the material, which facilitates material removal, and thus, reduces surface tearing. In addition, laser heating reduces the sharpness of the feed marks on the machined surfaces [137, 205].

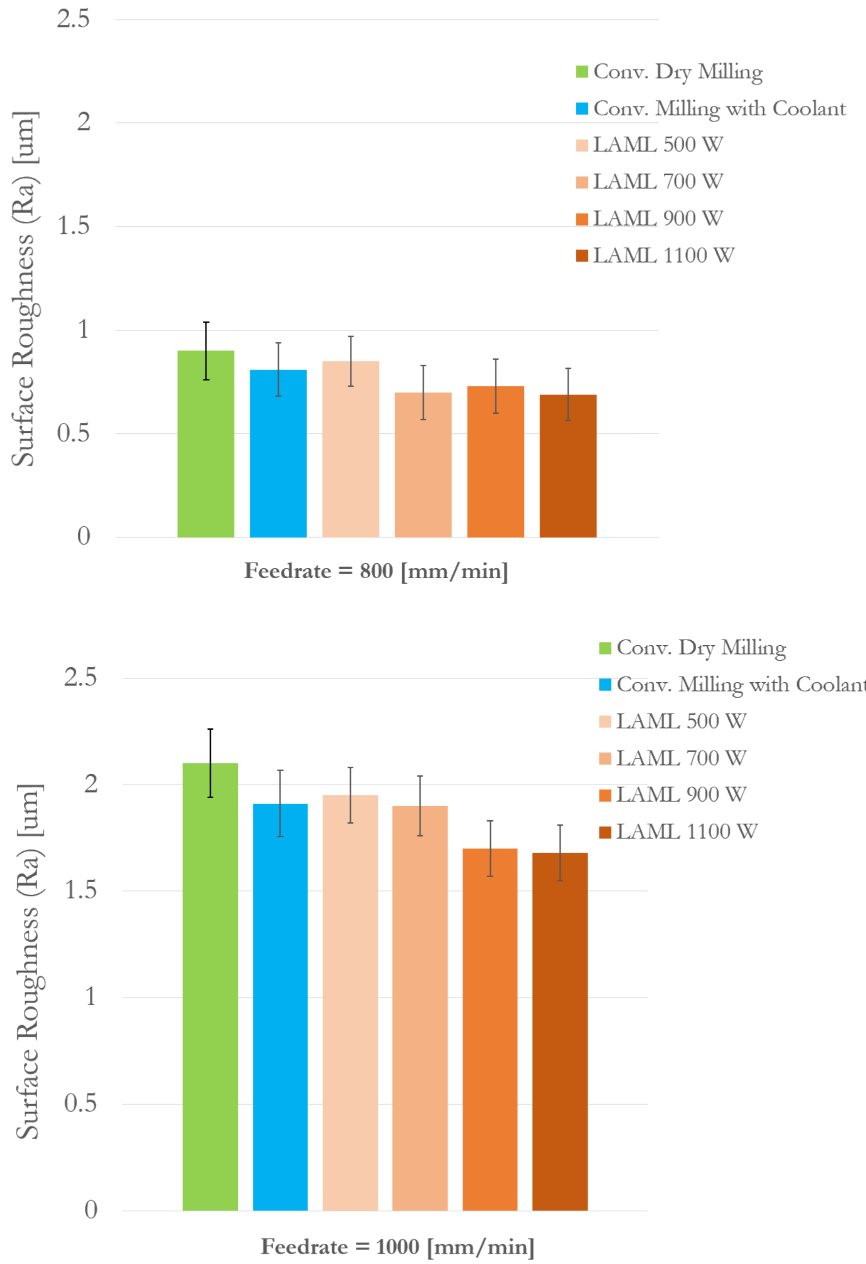

Figure 4.35. Surface roughness Ra measurements for 1-axis LAML and conventional milling.

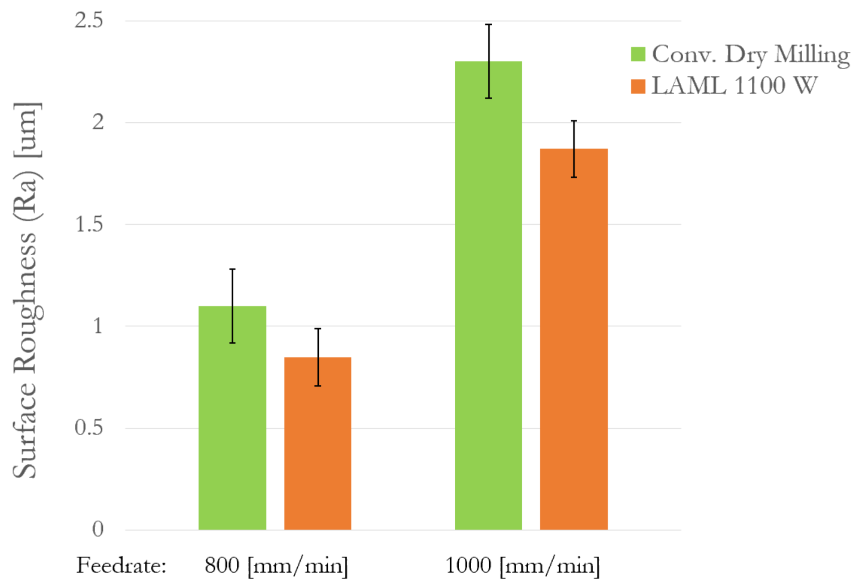

Figure 4.36. Surface roughness Ra measurements obtained with and without laser for 3-axis unidirectional LAML and conventional milling.

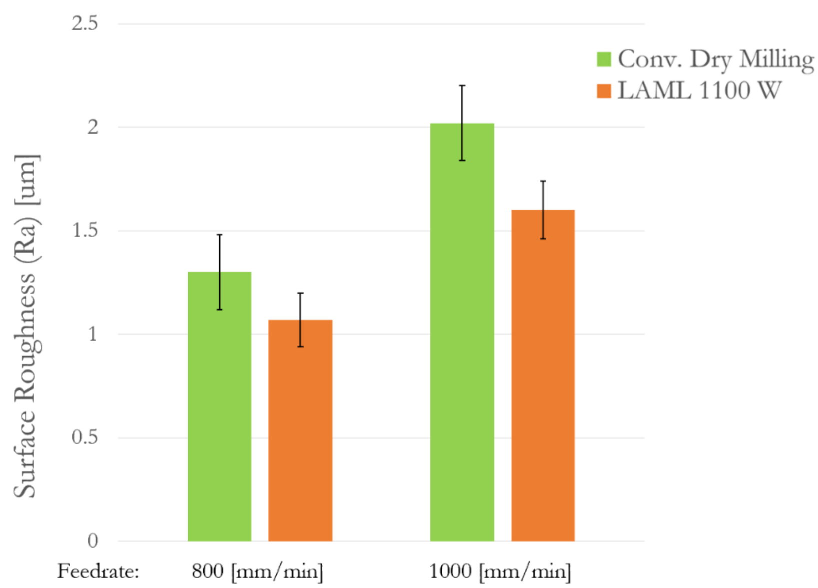

Figure 4.37. Measured surface roughness Ra for 3-axis multi-directional LAML and conventional milling.

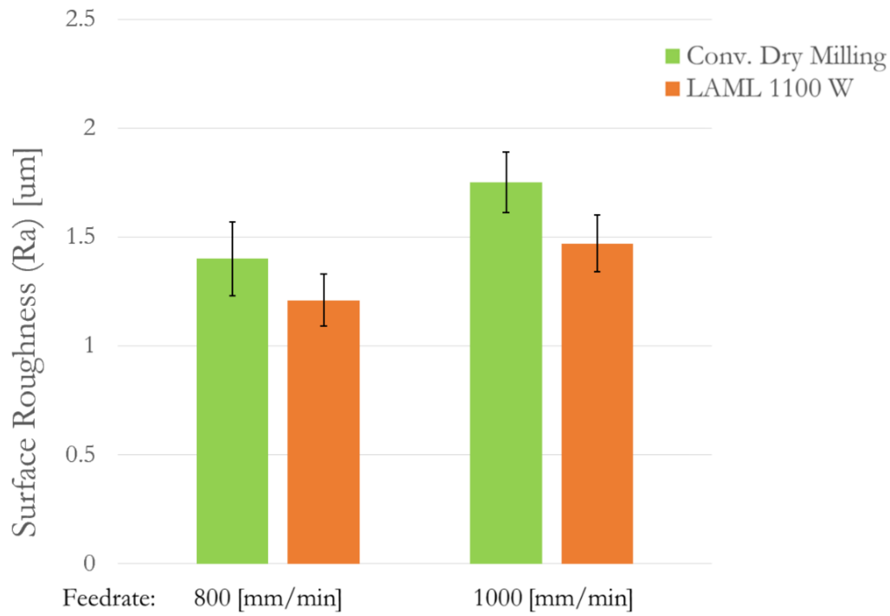

Figure 4.38. Measured surface roughness Ra for 5-axis LAML and conventional milling.

4.6.5 Residual Stress

In order to investigate the effect of laser-assisted milling on surface integrity, residual stresses were measured for the two 1-axis LAML cases, in which the laser power was 900 W and 1,100 W, the feedrate was 800 mm/min, the spindle speed was 4,000 rpm, and the axial depth of cut was 0.5 mm. The measured residual stress is shown in Figure 4.39. Figure 4.40 compares these measurements to the previous residual stress measurements for conventional dry milling at the same feedrate (section 4.3) and for laser surface heating at the same power levels (section 4.4). In these figures, the tensile stresses are presented as positive. As discussed previously in section 4.4.2.2, for laser surface heating, residual stresses were all in a tensile state from the top surface to a depth of 0.6 to 0.8 mm, around which the residual stress became closer to the state of bulk material. For conventional dry milling (section 4.3.2.2.2), tensile residual stresses were formed near the top surface due to the heating effect generated by cutting, then fell rapidly to become compressive due to the mechanical effect of cutting, and then went back to steady state at around 0.25 mm. The combination of conventional dry milling with laser surface heating in laser-assisted milling, LAML, resulted in a complex residual stress profile, as shown in Figure 4.39. High tensile residual stresses, reaching 800 to 880 MPa, were induced at the top surface due to laser heating, then it decreased rapidly to -250 to -330 MPa to be compressive due to the mechanical loading. However, unexpectedly, the stress increased again as tensile up to 440 MPa for the 900 W case and 912 MPa for the 1,100 W case. Then, it decreased again to zero as it got closer to the state of bulk material. Similar complex residual stress profile was reported by Xu et al. [26] for laser-assisted milling of Inconel 718, as shown previously in Figure 2.2.

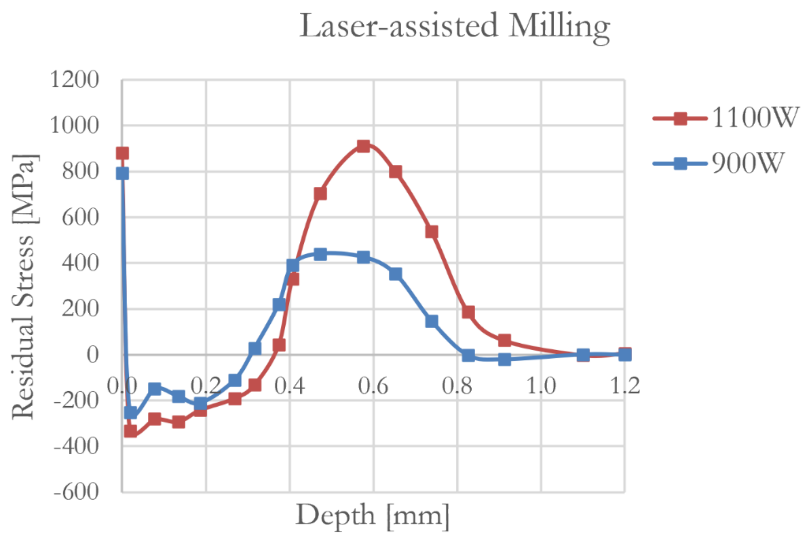

Figure 4.39. Residual stress measurements for 1-axis LAML at two laser power levels. Feedrate was 800 mm/min, spindle speed was 4000 rpm, and axial depth of cut was 0.5 mm.

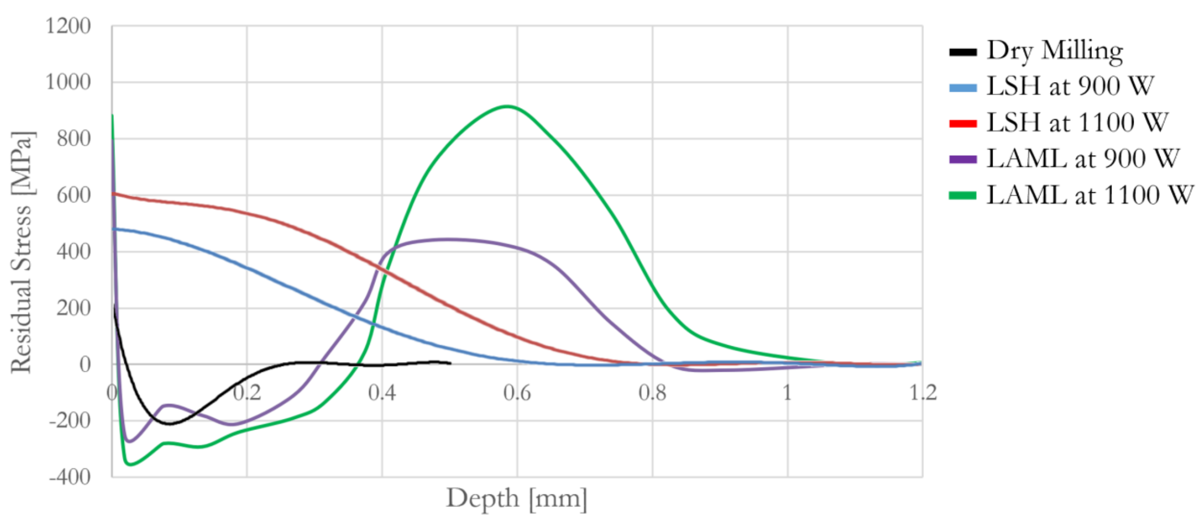

Figure 4.40. Comparison between measured residual stress curves for conventional dry milling, LSH, and 1-axis LAML for different laser power levels. Feedrates and laser scanning speeds for all cases were 800 mm/min. Spindle speed was 4000 rpm and axial depth of cut was 0.5 mm for conventional milling and LAML.

Comparing the residual stress measurements for LAML and conventional dry milling, shown in Figure 4.40, it is obvious that the tensile residual stress generated by LAML at the workpiece surface is much higher (up to 75% higher) than that generated by conventional dry milling. This is because in LAML, there is the added effect of laser heating that increases the tensile residual stress, as shown in the residual stress profile for LSH (Figure 4.40). In addition, the mechanical compressive effect of cutting alone exists to only about 0.25 mm beneath the surface. However, the thermal effect of laser heating penetrates to 0.6 to 0.8 mm. Hence, when combining laser heating with dry milling, the generated mechanical loading could not fully counteract the combined high thermal stress that had a deeper impact, thus generating the complex residual stress distribution shown in Figure 4.39.

4.6.5.1 Induction of Compressive Residual Stresses through Post-Processing

Surface tensile residual stresses are not desirable for many applications, especially under dynamic fatigue loadings, since they increase the effective net stress range and mean stress. This state of stress speeds up the initiation of fatigue cracks and increases the rate of fatigue crack propagation, leading to reduction of the component fatigue life [206-208]. For laser-surface heating processes (without cutting), tensile residual stresses could be avoided by controlling the laser heating parameters. For example, heating titanium alloys up to temperatures below 500 ºC induces compressive residual stresses, while heating above 500 ºC induces tensile residual stresses [27]. When high laser heating temperatures are needed to soften the material before cutting or to induce microstructure transformations for laser surface heat treatment, a post process such as shot peeing, burnishing, or hybrid laser surface burnishing [209, 210] could be used to intentionally induce compressive stresses to improve the fatigue resistance and damage tolerance of components [56].

Shot peening is a cold working process which involves bombarding the component surface with a stream of small spherical hard media. As a result, elastic and plastic deformations are induced in the component's near surface layer. This induces compressive residual stress field in the near surface layer because the plastically stretched surface layer wants to expand and the neighbouring elastically reacting material around and below the impact restrains that expansion [56, 211-216]. The depth of the compressive layer beneath the component's surface is influenced by variations in the shot peening parameters and the component material. As mentioned earlier in Chapter 2, section 2.1.1, conventional shot peening could achieve compressive residual stresses to depths between 0.4 to 0.9 mm for steels [56-58]. Furthermore, Harada and Mori [217] demonstrated experimentally that shot peening of heated steel can result in increased hardness and larger residual stresses in the workpiece surface layer compared to conventional cold shot peening.

Burnishing is a finishing operation in which a hard ball or roller is pressed on a workpiece surface layer to cause plastic deformation resulting in compressive residual stresses on the workpiece surface, increased hardness, and improved surface finish. Many studies have demonstrated that burnishing can increase workpiece quality in a variety of ways, including improving corrosion and wear resistance, and enhancing fatigue life [218-222]. Research efforts have been made to apply this process in machining operations. For example, Segawa et al. [223] integrated burnishing into milling to induce compressive residual stress on the milled surface by developing a unique endmill with a round pin projecting from the cutter. However, most conventional burnishing techniques are limited to comparatively soft materials, such as annealed steels [221, 224], aluminium alloys [225], and brass [220, 226], because burnishing hard materials requires high burnishing forces, which can result in rapid tool wear, substantial workpiece deflection, or workpiece failure. To overcome this problem, recent research efforts were directed to a hybrid burnishing process involving laser heating [209, 210].

In laser-assisted burnishing process (LAB), the workpiece surface is locally softened by a laser beam right before being processed by a conventional burnishing tool. This material softening leads to lowering the required burnishing forces and more plastic deformation which consequently leads to higher surface hardness, improved surface finish, and similar compressive residual stress compared to conventional burnishing. Tian and Shin [210] experimentally investigated laser-assisted burnishing using a setup retrofitted to a CNC lathe. They reported large compressive residual stresses of up to 600 MPa at the workpiece surface, 30 to 40% improvement in surface finish, and 40% reduction in tool wear.

Shi [209] numerically investigated laser-assisted burnishing of steel using the two-dimensional finite-element model shown in Figure 4.41. The model created using DEFORM-2D software, consisted of a moving roller, with a radius r equals to 5mm, that was pressing on a steel workpiece surface layer to cause plastic deformation. Ahead of the roller is a moving heat exchange window that applies a constant heat flux to the workpiece surface to simulate the effect of laser heating. A more detailed discussion of this method of modeling laser heating was previously presented in section 2.3.3. Both of the laser moving heat source and the roller were moving with the same speed v= 3 mm/s, with a 3 mm distance apart. The workpiece was modeled as a 2D rectangle (8 x 80 mm) and had approximately 7400 mesh elements ranging in size from 0.18 to 1 mm. The roller was modeled as a 2D rigid cylinder. The laser heating power was selected to heat the workpiece surface up to approximately 1,200 °C.

This FE model was adapted in this study to predict the induced residual stress in H13 tool steel material. The material properties were provided by Deform-2D database. The predicted induced residual stress profile across a 4 mm depth is shown in Figure 4.42. Following the standard convention, the compressive stresses are plotted as negative and the tensile stresses are plotted as positive. As shown in Figure 4.42, laser-assisted burnishing induced compressive stresses up to approximately 680 MPa to a depth of approximately 1.3 mm. Then the residual stress raised to approximately 39 MPa, possibly due to a thermal effect of heating that was not fully counteracted by the mechanical loading of burnishing. At a depth of approx. 1.85 mm, the residual stress decreased again to be compressive and then became close to zero which is the state of the bulk material.

From the discussion above, it is clear that laser-assisted burnishing is a promising finishing process that could be used after laser-assisted milling operations to improve the workpiece surface finish and to induce compressive residual stresses, using the same laser and setup but with different heating parameters. While shot peening could be used as well, it requires physically moving the workpiece to a different setup which wastes more time compared to LAB.

Laser shot peening (LSP) is also a good candidate for integration into a LAML process to improve the part's fatigue life, and its abrasion and corrosion resistance through the induced refined grains and excessive deformation twins and persistent slid bands [227]. Compared with other competing processes such as shot peening and liquid peening processes, LSP can provide surface treatment of selected areas [112].

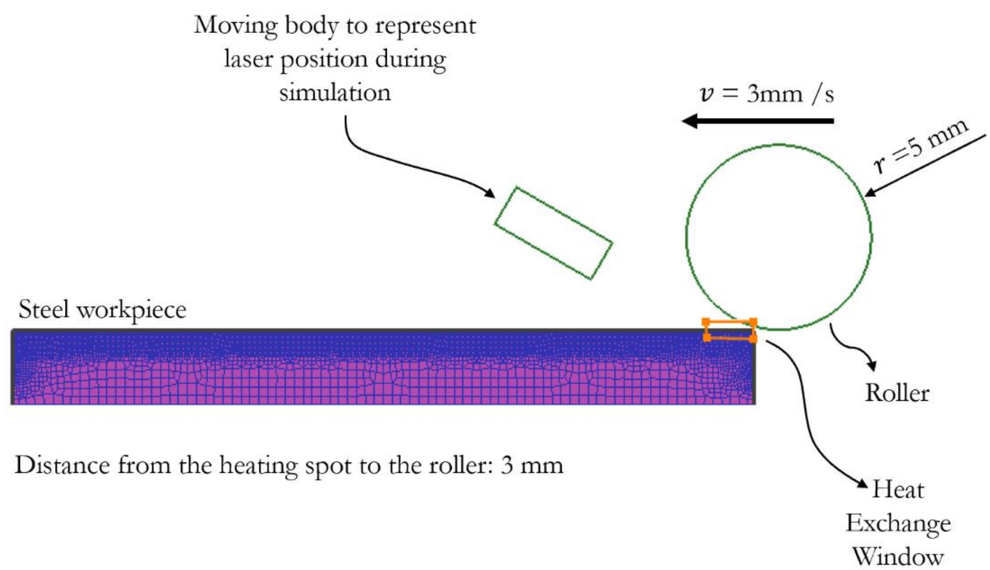

Figure 4.41. Two-dimensional finite-element model developed by Shi [209] using the software Deform-2D to investigate the residual stresses induced by laser-assisted burnishing of steel. The figure is adapted from [209].

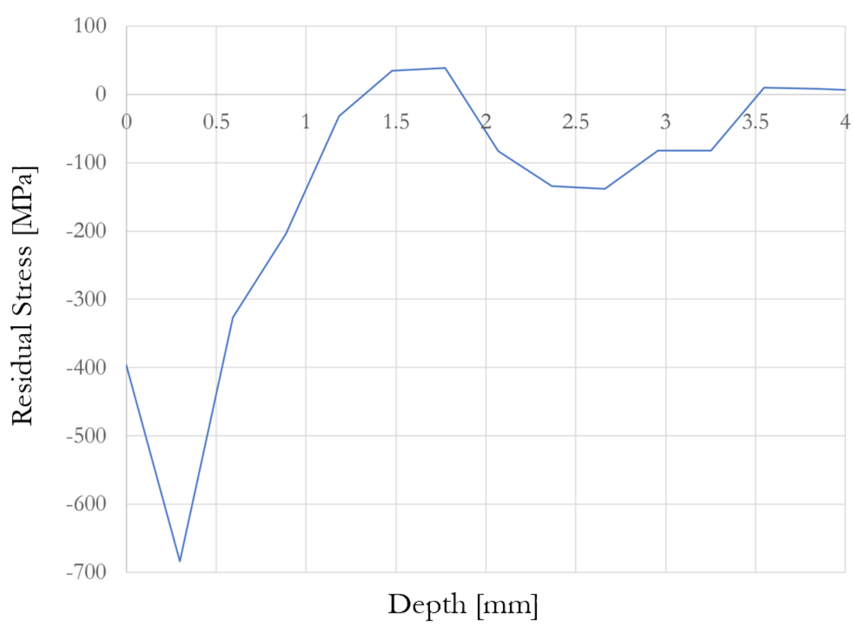

Figure 4.42. FEM prediction of the residual stress profile across a 4 mm depth of an H13 tool steel workpiece induced by laser-assisted burnishing. Compressive stress is plotted as negative and tensile stress is plotted as positive. The FE model used is adapted from [209].

4.7 Summary

In this chapter, experimental testing of the multi-axis LAML system developed in Chapter 3 was presented for different workpiece geometries using different cutting conditions and laser heating parameters. The LAML system performance was also compared to conventional milling.

The synchronization for the multi-axis laser-assisted milling system was validated by acquiring the encoders' measurements used by the torque motor and the linear actuator and comparing these measurements to the movement of the spindle measured by external laser sensors. The maximum error in synchronization was found to be approximately 200 μm, which is acceptable, considering the typical sizes of the laser heating spot.

Compared to conventional milling, the implementation of laser preheating reduced the cutting forces by up to 40% and improved the stability of the milling process by consistently reducing the fluctuation of cutting forces in all directions. In addition, the significant reduction in the cutting forces allowed the increase of the maximum permissible feedrate, which is translated to a 30% increase in material removal rate, in the cast of H13 tool steel. The improvement in the process dynamics and stability was shown to be consistent in all LAM tests of different configurations.

With regard to workpiece surface integrity, the implementation of LAML reduced the surface roughness by up to 23%. However, laser-assisted milling resulted in a complex residual stress profile of three zones: tensile, compressive, and then tensile stresses at a deeper depth. This occurred because the mechanical loading of the milling process could not fully counteract the tensile residual stresses induced by the combined heating effect of laser and machining in the deep areas of workpiece.

To compensate for the undesirable tensile residual stresses induced into the workpiece by the LAML process, it is suggested that LAML could be used only for roughing machining, then a subsequent finishing operation, without laser, can be performed to intentionally induce compressive stresses. Alternatively, a post-process such as shot peening, burnishing, laser-assisted burnishing, or laser shot peening could be used for that purpose as well.

Chapter 5: Microstructure Transformations in Laser Surface Heat Treatment of AISI H13 tool steel

5.1 Introduction

This chapter presents experimental and numerical investigations for the microstructure transformations during laser surface heat treatment (LSHT) of AISI H13 tool steel. The numerical model developed in this chapter is adopted in the next chapter for predicting microstructure transformations during laser surface heating and laser-assisted milling processes.

The process of LSHT is typically used to obtain hardened wear-resistant surface layers with a depth of 0.5 mm to 1.5 mm. In the LSHT process, a laser beam is applied on the workpiece to rapidly heat its surface. The heat is quickly dissipated through the bulk material, which acts as an efficient heat sink. This rapid heating and cooling processes result in quenching phase transformations. As a result, a hardened outer surface layer is formed without changing desirable bulk material properties, such as ductility and toughness. LSHT has the advantage of minimal workpiece distortion, high reliability, and repeatability with well controlled size of the hardened layers. Shi et al. demonstrated the advantages of integrating the laser-assisted machining (LAM) and laser surface heat treatment (LSHT) in a single operation using the same laser source with different laser heating parameters. This integration is well suited for the production of crankshafts, gears, bearing rings, etc., which require surface heat treatment after machining [38].

In this chapter, experimental investigation of LSHT is presented in section 5.2 followed by a numerical investigation in section 5.3. The LSHT experiments of H13 tool steel were conducted with different heating parameters using a high-power diode laser. Laser power was varied from 800 W to 1,200 W, and the laser heating time was varied from 100 ms to 800 ms (laser flashing). For the LSHT numerical modeling, a three-dimensional finite-element-based model was developed, which coupled the thermal and mechanical process interactions with phase transformations. This model is a building stone towards complete prediction of residual stresses in LSHT and LAM.

Predicted temperatures, microstructure transformations, and heat affected zones depths were compared with experimental measurements to validate the developed finite element model. The comparisons indicated a good agreement with experimental results, which allows the model to provide a reliable and feasible predictive capability for LSHT process design and optimization.

5.2 Experimental Work

5.2.1 Methodology

5.2.1.1 Experimental Setup

The experimental setup of laser surface heat treatment is shown in Figure 5.1. The workpiece used was a rectangular (100x150x200 mm) H13 tool steel block. The laser focusing head was aligned in position, perpendicular to the workpiece surface. The laser used for heat treatment was a diode laser generated using a 3kW diode laser source. A heat exchanger (OTI-20WL, OptiTemp, Michigan, USA) was used to cool the laser focusing head and the laser optical fiber using a closed-loop running water circuit.

5.2.1.2 Test Conditions

The test conditions are shown in Table 5.1. An array of 12 type-K thermo-couples were spot welded on the workpiece surface to measure the temperature histories of the 12 surface heat treatment tests. Each thermocouple was welded 1 mm away from the center of the laser heating spot, as shown in the schematic in Figure 5.2. The temperatures were measured in real time using a USB data acquisition interface module (D8000 series, Omega, Connecticut, USA). The laser power was varied between 800 and 1,200 W, the laser heating spot was fixed to 2 mm in diameter in all cases, and the heating time was varied between 100 and 800 ms.

5.2.1.3 Microstructure Analysis

To perform microstructure analysis of the heat affected zone, the H13 tool steel block was first cut into smaller pieces. Then, a precision cutting machine (Discotom 60, Struers, Ohio, United States) was used to cut the H13 parts at the center of each heated spot to obtain the specimens. The H13 specimens were then mounted into resin, and then, ground and polished using an automatic polishing machine (Tegramin 30, Struers, Ohio, United States). Finally, the H13 specimens were chemically etched in Nital 3% solution, which is a mixture of nitric acid and methanol, to reveal the different microstructure phases. A microscope (GX71, Olympus Corporation, Tokyo, Japan) was used to examine the different microstructure phases and measure the heat affected zone depth for each specimen.

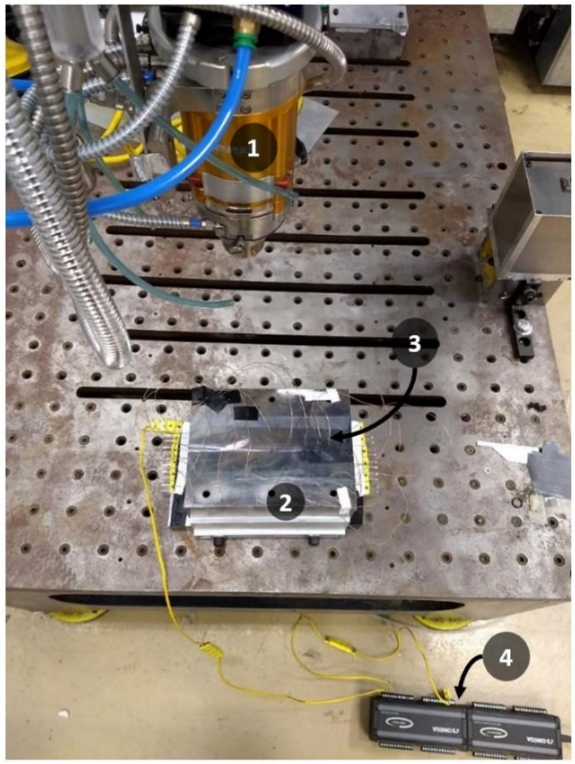

Figure 5.1. Experimental setup of the laser surface heat treatment of AISI H13 tool steel. (1) Laser focusing head. (2) H13 tool steel workpiece. (3) Type-K thermocouple wire. (4) Data acquisition device.

Table 5.1. Test conditions for laser surface heat treatment of H13 tool steel.

Case No.	Laser Power [W]	Heating Time [ms]
1	800	100
2		200
3		400
4		800
5	1000	100
6		200
7		400
8		800
9	1200	100
10		200
11		400
12		800

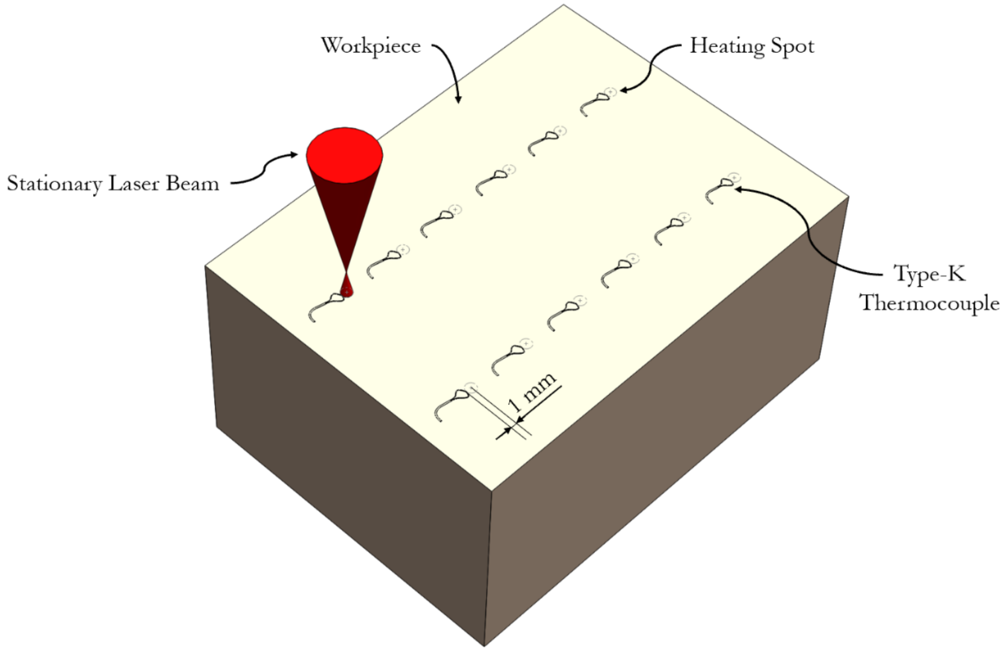

Figure 5.2. Schematic for the experimental setup used for laser surface heat treatment of H13 tool steel. The schematic is not drawn to scale.

5.2.2 Results and Discussion

5.2.2.1 Surface Temperatures

Figure 5.3 shows an example of typical heating and cooling cycles occurring in the laser surface heat treatment of H13 tool steel. This plot is obtained from the thermocouple measurements for case 2, with laser power of 800 W and heating time of 200 ms. The plot shows the rapid cooling rate of steel (approximately 600 ^{o}C/s from 800 ^{o}C to 200 ^{o}C) happening after the laser heating cycle, which has an effect on the microstructure transformations as discussed in the following sections.

The maximum measured temperatures, for each case, are shown in Figure 5.4. As expected, by increasing the laser power or increasing the heating time, the surface temperature increases. It should be noted that the maximum temperature of the steel surface at the center of the heating spot is estimated to be approximately 240 ^{o}C more than the temperatures measured by the thermocouples which were located 1 mm away from the center. This is estimated using the numerical model presented in the section 5.3.

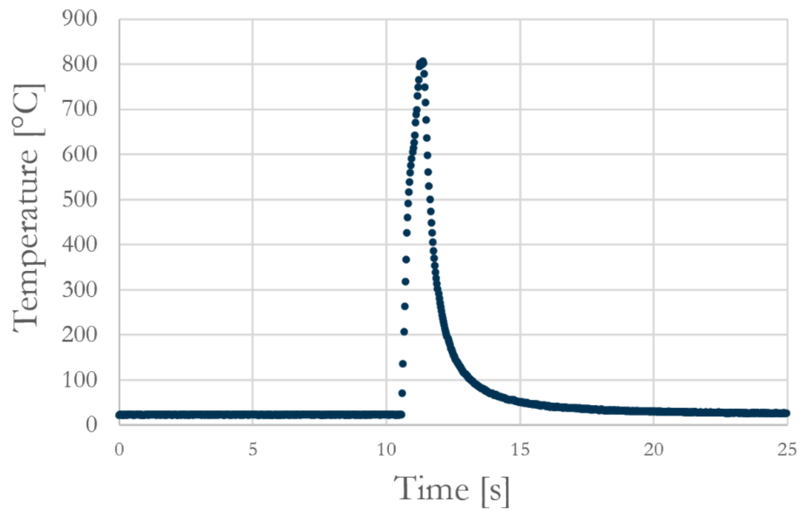

Figure 5.3. Thermocouple measurements showing the high cooling rate of steel after laser surface heating. Laser power used was 800 W and heating time was 200 ms (case 2). Cooling rate is approximately 600 °C/s from 800 °C to 200 °C.

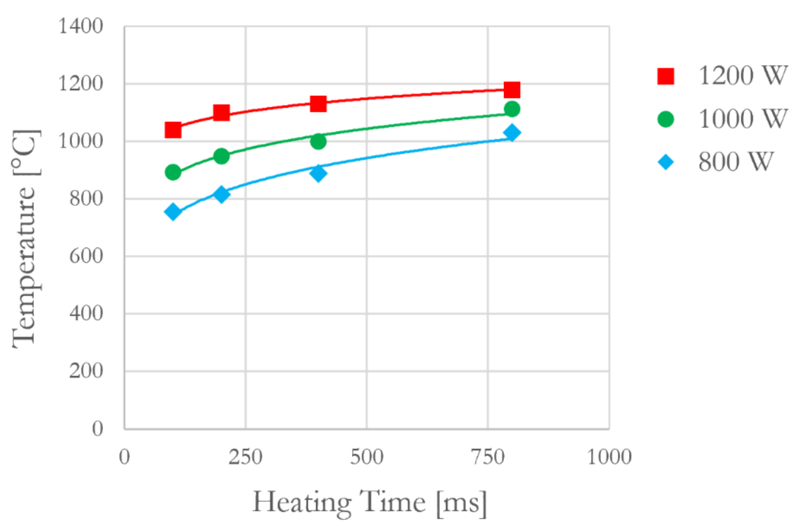

Figure 5.4. Effect of laser power and heating time on the maximum surface temperature measured by the type-K thermocouples 1 mm away from the center of the laser heating spot.

5.2.2.2 Microstructure Transformations

Figure 5.5 shows an example (Case 3 listed in Table 1) of the microstructure transformation after the laser surface heat treatment of steel. Under the conditions, a total heat affected zone depth (D_{HAZ}) of approximately 1.2 mm was obtained. As illustrated in Figure 5.5, the top portion of the steel surface layer, zone (1) with a depth of D_m, is the zone where only needle-shaped martensite was formed due to the high cooling rate. Zone (2) is the transition zone where some martensite remains, but mixed with ferrite. In zone (3), which is the bulk material, there is a mix of ferrite and pearlite. Figure 5.6 shows the D_{HAZ} obtained for the rest of the cases. As expected, by increasing laser power or increasing heating time, the depth of the heat affected zone increases.

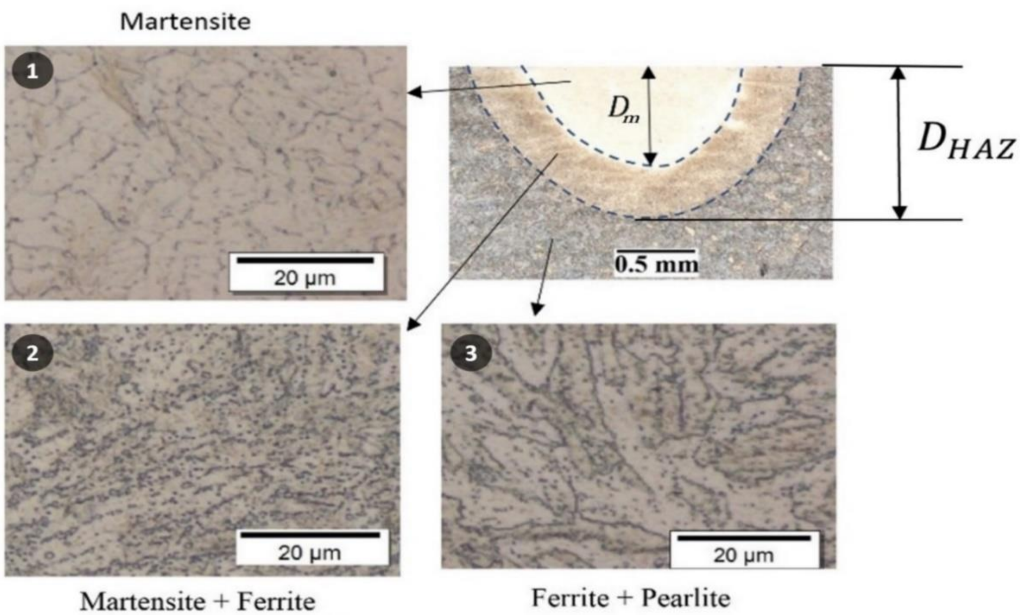

Figure 5.5. Microstructure transformation resulting from the laser surface heat treatment of steel, showing case 3 corresponding to a laser power of 800 W and a heating time of 400 ms.

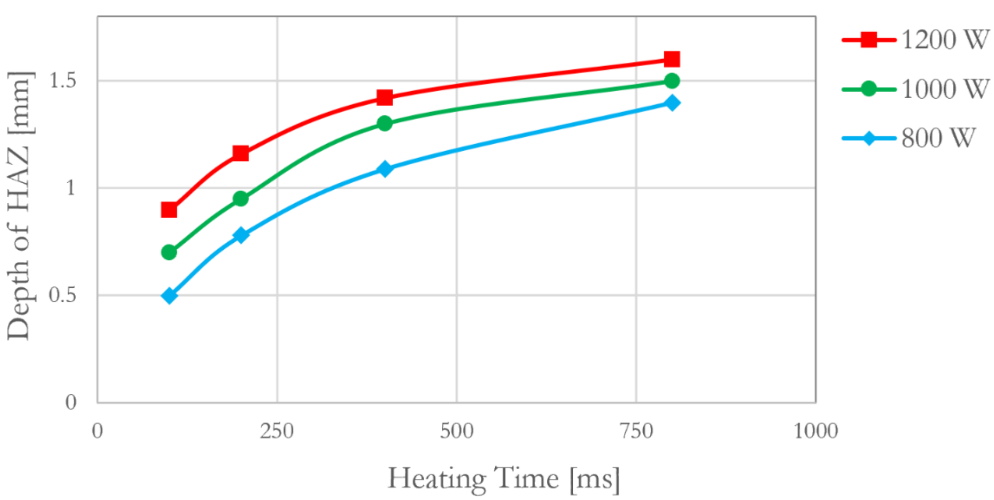

Figure 5.6. Depth of the heat affected zone for different laser powers and heating times.

5.3 Numerical Modeling

5.3.1 Modeling Methodology

A three-dimensional, finite element (FE)-based model was developed to simulate the laser surface heating process and microstructure transformations of H13 tool steel using Deform-3D (V.11, SFTC Scientific Forming Technologies Corporation, Ohio, United States) [152]. As shown in Figure 5.7, the model consists of a workpiece (10x30x80 mm) with approximately 100,000 mesh tetrahedral elements (with element size ranging from 0.1mm to 3.5mm). A mesh grading strategy was applied to maintain a dense mesh with a size of 0.1 mm in the vicinity of the laser heating zone to capture high temperature gradient. A large element size of 3.5 mm was applied outside of the heating zone to accelerate simulation time. Since the meshed model is also to be used for laser heating simulation in Chapter 6, the region with the dense mesh was extended to the whole length of the workpiece, as shown in Figure 5.7. Ten concentric stationary heat exchange windows were utilized to simulate the Gaussian distribution of the laser power density used in the experimental work. Outside of the heat exchange windows, the heat transfer coefficient was set to a constant value of 20 W/m^2 K to simulate free air convection.

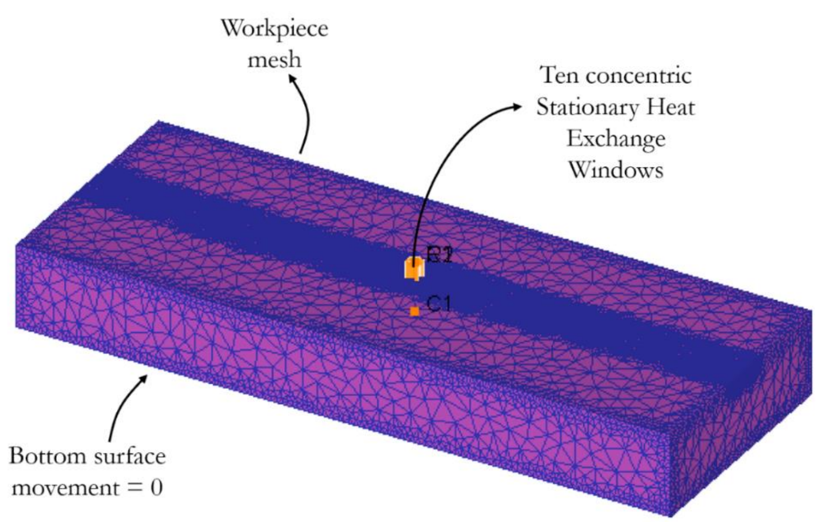

Figure 5.7. Three-dimensional model developed for laser surface heat treatment of H13 tool steel.

The laser power density (power per unit area) for the focused beam used in the experimental work was measured at a 2 mm beam diameter, which has a certain distance from the focal plane as shown in Figure 5.8, and the distribution was found to be Gaussian., as shown in Figure 5.8. This was measured by a laser sensing device (FM48, Primes gmbh, Pfungstadt, Germany) as previously discussed in Chapter 4 in section 4.4.1.2.

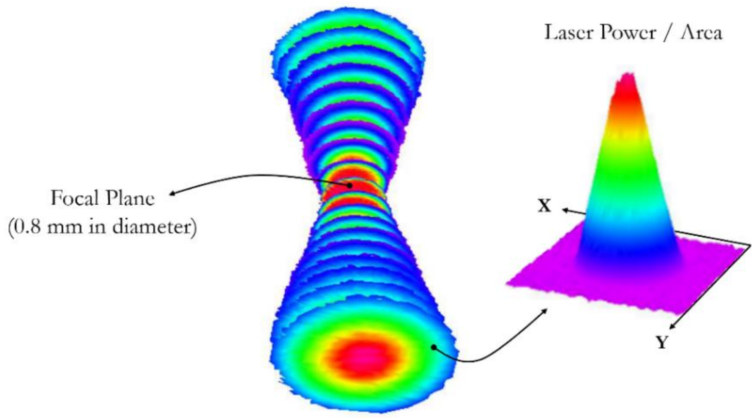

Figure 5.8. Distribution of actual measured laser power density at a 2 mm beam diameter. The smallest cross section at the focal plane is 0.8mm.

Since Deform-3D cannot directly simulate Gaussian distributed heat flux, ten concentric heat exchange windows were used in the FE model to approximate the Gaussian distribution of the laser power density. Each heat exchange window was in the shape of a ring except for the most inner window, which was a circle as shown in Figure 5.9. The outer diameter of the outer most ring was equal to the laser beam diameter of 2 mm. Each heat exchange window defined heat transfer in its local area through Equation 2.11, as discussed previously in section 2.3.4. Each of the ten heat exchange windows had a uniform h_{eqv}, which is the equivalent convective coefficient of heat transfer. The actual laser power P can be related to Equation 2.11 by:

$$P = \frac{\sum_{n=1}^{10} \dot{Q}_n}{\eta} = \frac{\sum_{n=1}^{10} h_{eqv.n} A_n \ (T_w - T_{sn})}{\eta}, \quad \text{(Equation 5.1)}$$

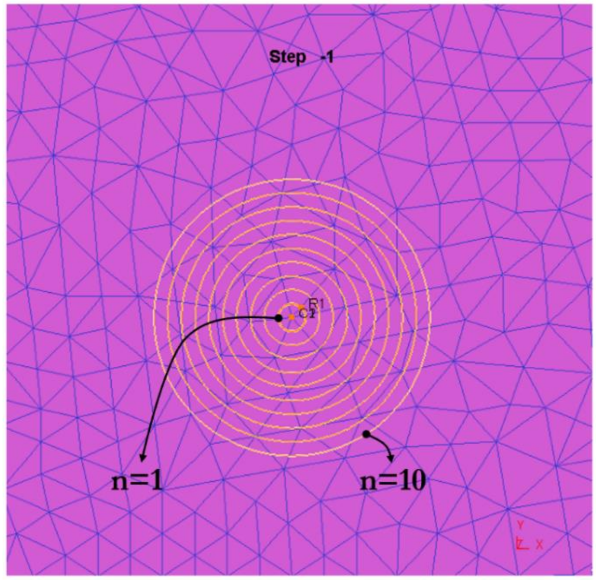

Figure 5.9. Ten heat exchange windows used in the model to simulate the Gaussian distribution of the laser power density.

where n is the number of the heat exchange window, and η is the absorptivity, since the workpiece material only absorbs a fraction of the energy applied by laser. For steel absorbing energy from a perpendicular high-power diode laser, η was considered to be 0.86 [191].

In the model, all ten heat exchange windows were assigned the same constant pseudo high temperature (130,000 ºC), but were assigned different h_{eqv} values based on the location of each heat exchange window to match the measured power density. As shown in Figure 5.10, ten values of laser power density were considered from the measured curve, and Equations 2.11 and 5.1 were solved to determine the approximate value of h_{eqv} for each window.

The general material properties of the workpiece (H13 tool steel) were provided by the Deform-3D database. The key properties of H13 tool steel used in Deform-3D are listed in Table 5.2. In addition, the inter-material properties and the kinetic models for the possible different phases of steel (austenite, martensite, pearlite, ferrite, and bainite) were specified for the integrated microstructure evolution model, as discussed in the following section.

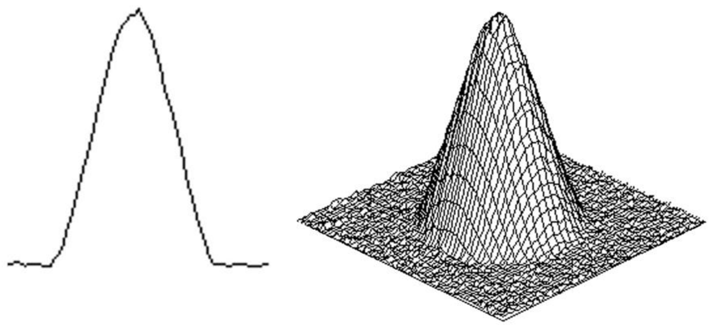

a) Actual measured gaussian laser power density.

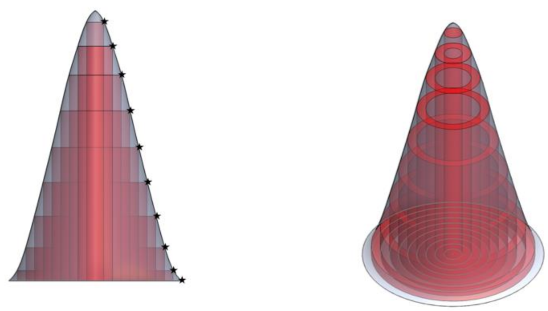

b) Ten values of laser power density were considered to approximate the actual case.

Figure 5.10. Schematic for the approximation of the Gaussian distribution of the laser power density.

Table 5.2. Key H13 tool steel material properties used in Deform-3D [152].

Thermal conductivity [W/m K]	Specific Heat [J/kg K]	Density [kg/m^3]	Absorptivity
24.5	460	7780	0.86

5.3.2 Microstructure Evolution Model

A microstructure evolution model was integrated into the three-dimensional finite element model described in the previous section, by which the phase volume fractions were calculated at each time step, based on the temperature level. Modeling microstructure transformations in carbon steels was discussed in detail in section 2.3.3. In the model, microstructure transformations were modeled by calculating the volume fraction of each possible phase of steel (austenite, martensite, pearlite, ferrite, or bainite) in every mesh element of the workpiece, using the kinetics models for diffusion-type and diffusion-less-type transformations discussed in Chapter 2.

In the model, the following simplified version of Equation 2.3 was used during the heating cycle to calculate the volume fraction of austenite at each step [152, 185].

$$\xi_A = 1 - \exp\left\{-4\left(\frac{T - T_{As}}{T_{Ae} - T_{As}}\right)^2\right\}, \qquad \text{(Equation 5.2)}$$

where ξ_A is the volume fraction of austenite, T is the instantaneous temperature, T_{As} is the starting temperature of the transformation to austenite, and T_{Ae} is the ending temperature of the transformation to austenite. The values of these two temperatures are dependent on the rate of cooling. As the cooling rate increases, the transformation temperatures increase. For this model, T_{As} and T_{Ae} were simplified to be constants: T_{As}= 800 ºC and T_{Ae}= 850 ºC [228].

For the cooling cycle, the cooling rate specifics the type of the final microstructure formed. As shown in the continuous cooling transformation (CCT) diagram of H13 tool steel in Figure 5.11, when the cooling rate is around 100 ºC/s or higher, the only microstructure formed is martensite. This was validated experimentally, as shown in zone (1) of the heat affected zone in Figure 5.5, where the cooling rate measured on the surface was approximately 600 ºC/s from 800 ºC to 200 ºC, as shown in Figure 5.3.

To model the transformation from austenite to martensite, a simplified version of Magee's diffusion-less kinetics model (Equation 2.7) was used [152, 229]:

$$\xi_m = 1 - \exp[w_1 T + w_2], \qquad \text{(Equation 5.3)}$$

where ξ_m is the volume fraction of martensite, T is the instantaneous temperature, and w_1 and w_2 are material constants identified from the martensite start temperature and the 90% martensite formed temperature of 351.9 and 236 ºC respectively, identified from the calculated CCT diagram for AISI H13 in Figure 5.11 [152, 230]. This simplified equation neglects the dependency of the volume fraction of martensite on stress and carbon content.

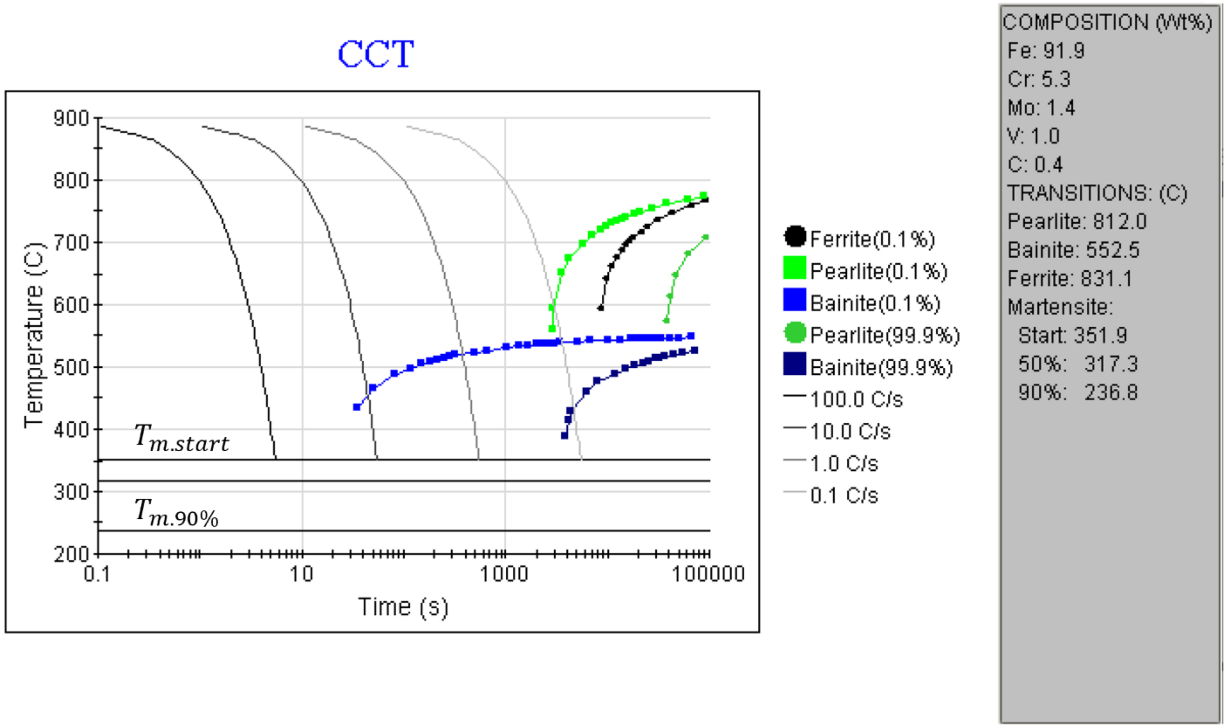

Figure 5.11. CCT diagram for AISI H13 tool steel calculated by the software JMatPro based on a standard H13 chemical composition [230].

5.3.3 Model Results

Since the three-dimensional numerical model was computationally very demanding, only six cases out of the twelve experimental cases (previously shown in Table 5.1) were simulated, which proved to be enough to validate the model. Table 5.3 shows the cases considered in the simulations.

Table 5.3. The six cases considered in the numerical model.

Case No.	Laser Power [W]	Heating Time [ms]
2	800	200
3		400
6	1000	200
7		400
10	1200	200
11		400

5.3.3.1 Workpiece Surface Temperatures

Figure 5.12 shows the temperature distribution on the workpiece surface predicted by the numerical model at the end of the heating cycle at 800 W laser power and 200 ms heating time. The model predicted that the maximum temperature at the center of the heating spot, which was not possible to be measured using a thermocouple as it would melt, was approximately 240°C greater than the temperatures measured at the thermocouple position 1 mm away from the heating spot's center. Figure 5.13 shows a comparison of the heating and cooling cycles, for the same case, for predicted and measured temperatures verses time. Furthermore, Figure 5.14 shows the comparison for the rest of the cases in Table 5.3 for the maximum predicted and measured temperatures at the thermocouples positions. The temperature comparisons show an excellent agreement with the experimental results with a maximum error of ± 7 %.

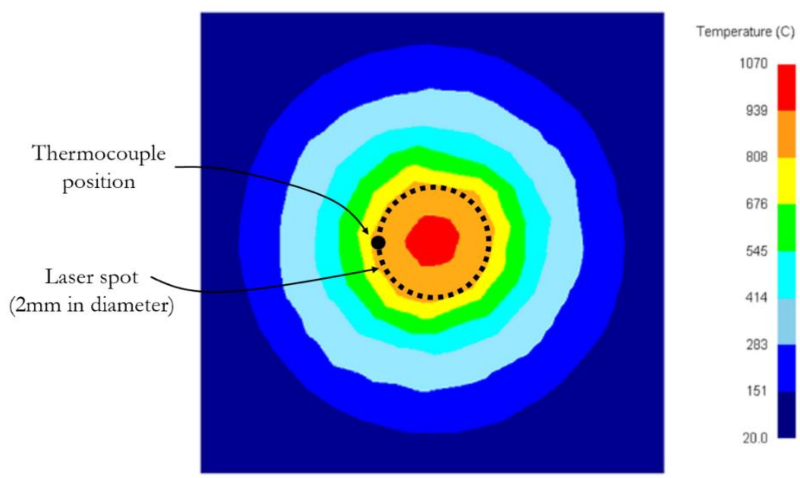

Figure 5.12. Predicted temperature distribution on the workpiece surface at the end of the heating cycle for 800 W laser power and 200 ms heating time.

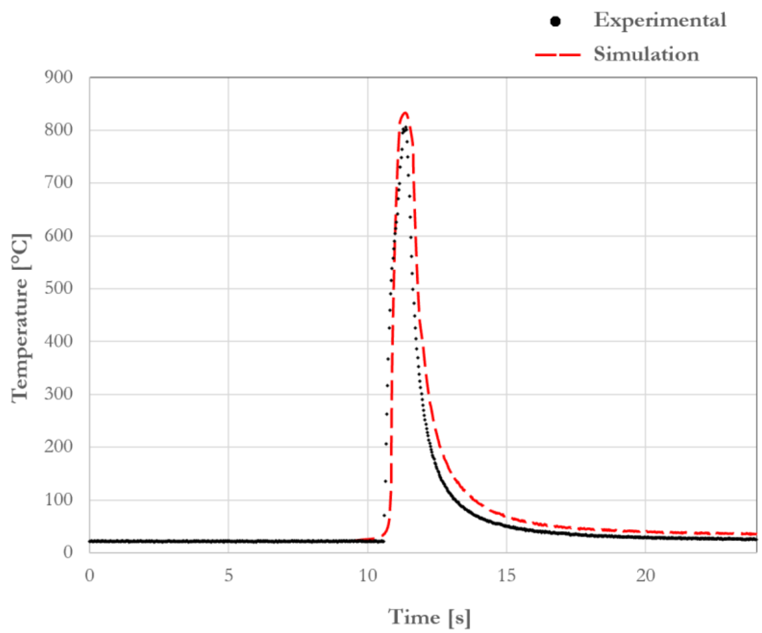

Figure 5.13. Thermocouple temperature measurement verses numerical model prediction for 800 W laser power and 200 ms heating time.

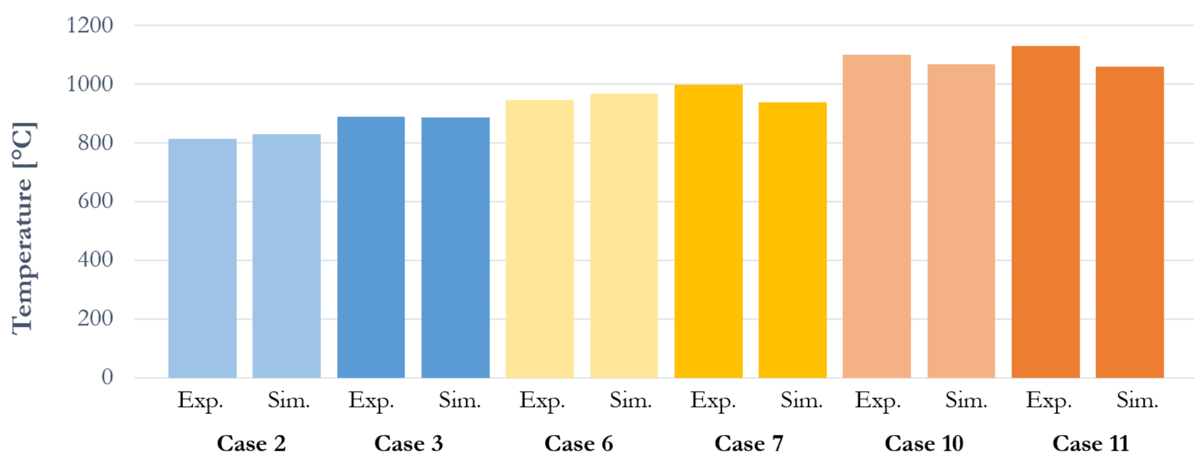

Figure 5.14. Comparison between the maximum surface temperatures predicted and measured at thermocouples positions.

5.3.3.2 Heat Affected Zone Depth

Figure 5.15 shows the excellent agreement between the model predictions of the volume fraction of martensite formed after cooling and the corresponding microstructure obtained for the experiments (case 3, 800 W laser power and 400 ms heating time). As shown in the figure, the heat affected zone consisted of mainly three zones; zone (1), the nearest to the surface, where mostly only martensite is formed, zone (2) where the martensite volume fraction kept decreasing as the depth increased, and zone (3) where there was no martensite formed. Furthermore, Figure 5.16 shows the depths of the heat affected zones obtained numerically and experimentally for all the cases mentioned in Table 5.3. The comparison shows an excellent agreement with the experimental results, which validates the microstructure evolution model. The predictions were approximately $\pm$ 10 % of the depths obtained experimentally. This acceptable prediction error could be attributed to the simplifications made to the kinetics models used in the microstructure evolution model, and also to the approximations made to modeling the Gaussian distribution of laser power.

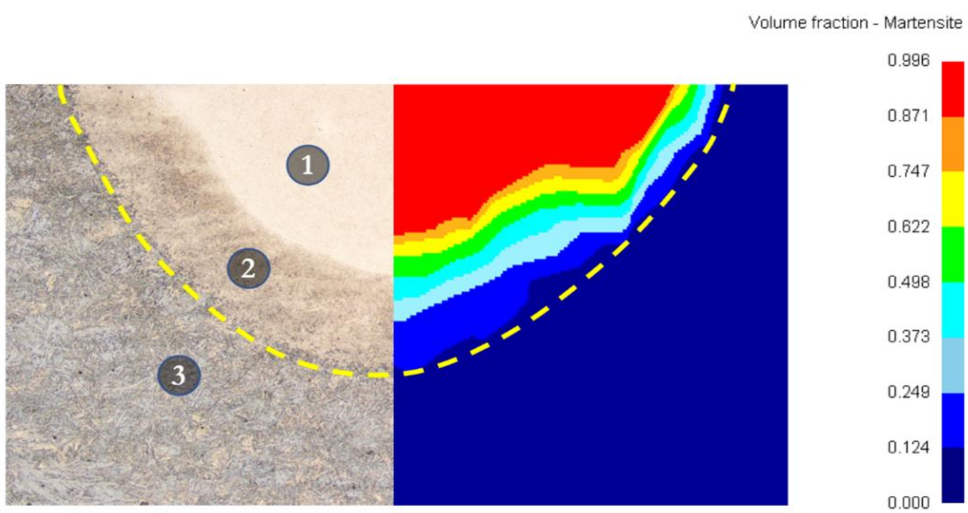

Figure 5.15. Comparison between microstructures obtained experimentally and numerically for 800 W laser power and 400 ms heating time. Zone (1) has the highest martensite volume fraction, which keeps decreasing through transition zone (2) until it becomes zero at zone 3.

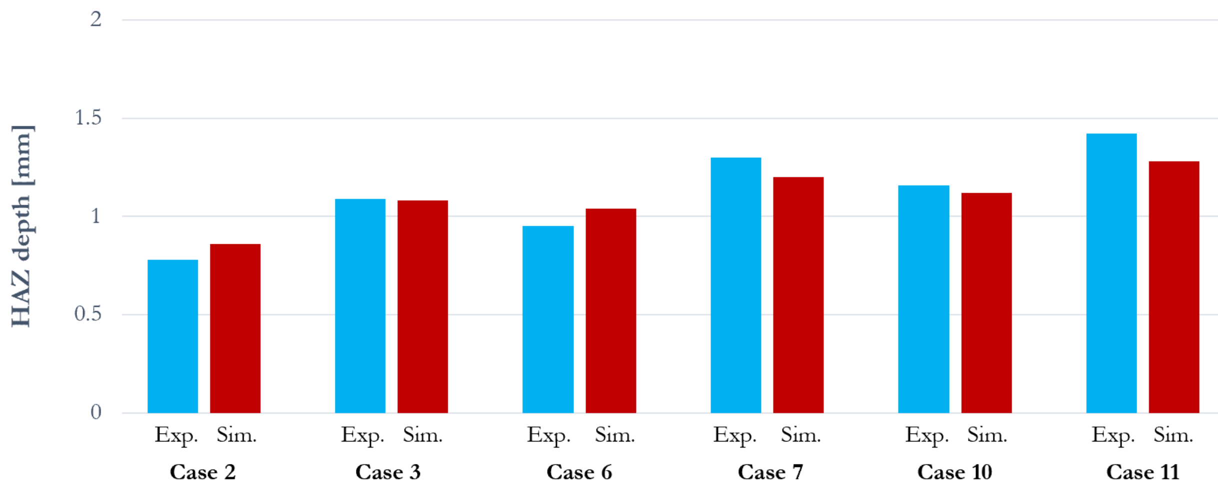

Figure 5.16. Depths of the heat affected zones for the six cases considered in the model (Table 5.3) compared to the experimental results.

5.4 Summary

This chapter presented experimental and numerical investigations of the microstructure transformations for the laser surface heat treatment of AISI H13 tool steel.

The LSHT experiments of H13 tool steel were conducted with different heating parameters using a high-power diode laser. The laser power was varied from 800 W to 1200 W, the laser heating time was varied from 100 ms to 800 ms, and a heating spot with a constant diameter of 2 mm was used in all the cases. For the LSHT numerical modeling, a three-dimensional finite-element-based model was developed, which coupled the microstructure evolution, thermal and mechanical processes. The Gaussian laser power density was approximated in the model with ten heat exchange windows. The predicted temperatures, microstructure transformations, and heat affected zones depths were compared with the experimental measurements to validate the developed finite element model. The comparisons indicated a good agreement with the experimental results with maximum errors of ± 7 % in temperatures predictions and ± 10 % in HAZ depths predictions, which allows the model to provide a reliable and feasible predictive capability for LSHT process design and optimization. To further improve the accuracy of the predictions, it is suggested to conduct a sensitivity study on the effect of the number of heat exchange windows used for Gaussian distributed power density on the temperature distribution and HAZ depth.

The experimentally validated microstructure evolution model developed in this chapter is to be used in Chapter 6 to predict the heat affected zones depth in laser surface heating and laser-assisted milling processes.

Chapter 6: Numerical Modeling of Multi-Axis LAML and LSHT: Special Issues and Considerations

6.1 Introduction

This chapter presents the work done to develop FE based numerical models for laser surface heating (LSH) and laser-assisted milling (LAML) of flat and 3D surfaces. Section 6.2 discusses the effect for the inclination of laser beams on the shape and the laser power density distribution of the heating spot. Section 6.3 presents the formulation of the laser power density distribution inside the heating spot of a laser beam inclined at any angle on a flat workpiece surface. The output of this section is adopted in the FE modeling presented in Section 6.5. Section 6.4 numerically investigates the effect of the workpiece surface curvature on the surface temperature during laser heating. Finally, section 6.5 presents the development and results of FE numerical models for LSH and LAML of flat and 3D surface, considering the asymmetric Gaussian power intensity distribution of inclined laser beams and the simulation of oscillating laser beams. The FE models are used to predict surface preheating temperatures, depths of the heat affected zones, and cutting forces.

6.2 Heating Spot Geometry of Inclined Laser Beams

As discussed in Chapter 5, when the laser beam is perpendicular to the workpiece surface, the shape of the resulting heat spot is circular, with a Gaussian distribution of laser power density, which is symmetrical around the laser beam axis. However, as discussed previously in Chapters 3 and 4, the laser beams used for laser surface heating (LSH) and laser-assisted milling (LAML) were always inclined at an angle 'θ_L' relative to the workpiece surface. This inclination angle was necessary to accommodate the design of the laser focusing head assembly, to not exceed the laser fiber minimum bending radius, and to avoid laser beam reflections that could damage the laser head optics. In addition, for LAML, the inclination angle was necessary to properly align the laser heating spot in front of and close to the cutting tool. As illustrated in the schematic shown in Figure 6.1, the resulting shape of the heating spot for an inclined laser beam is not circular, but elliptical with minor and major axes. Moreover, the laser beam inclination results in shifting the laser beam axis away from the center of the elliptical heating spot, which consequently leads to an asymmetric distribution of the laser beam power density inside the laser heating spot. The amount of this shifting is dependent on the inclination angle θ_L.

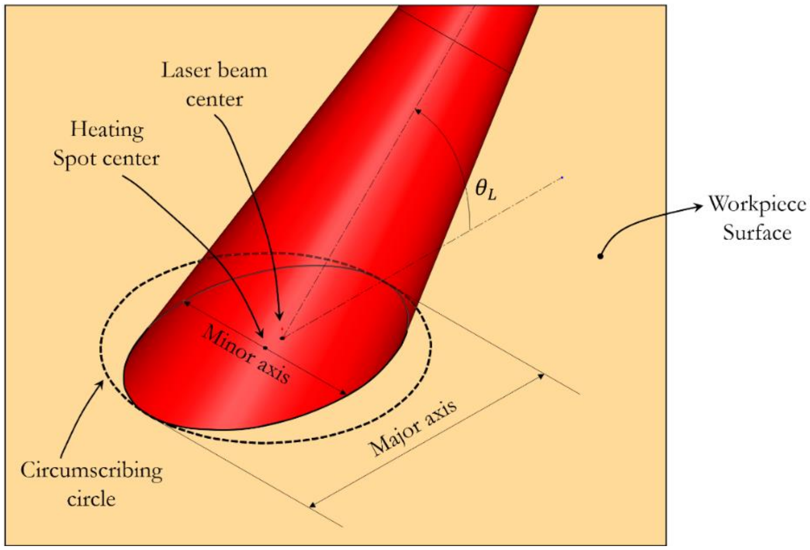

Figure 6.1. Geometry of the laser heating spot created by a laser beam inclined with an angle θ_L.

For all the LSH and LAML experimental work previously discussed in Chapter 4, the inclination angle was selected to be the same, 45 degrees, in order to get the same surface preheating temperatures. For the 45^o inclination angle, the resulting elliptical heating spot had a 5 mm major axis and a 3.54 mm minor axis (aspect ratio = 1.42), and the shift between the laser beam centre and the heating spot center was 0.35 mm.

As discussed previously in Chapters 4, the distribution of the laser power density for perpendicular laser beams was measured at twenty different horizontal planes and was found to be Gaussian and symmetrical around the laser beam axis. These measurements were done with an automatic device (shown previously in Figure 4.11) that moves a sensor vertically to measure laser power density in the region illustrated in Figure 6.2. However, for inclined laser beams, the laser power density distribution of the resulting heating spot is not Gaussian, as illustrated in Figure 6.2. Therefore, in order to create accurate FE numerical models for LSH and LAML, it is necessary to calculate the distribution of the laser power density for the asymmetric, elliptic heating spot of the inclined laser beam shown in Figure 6.2 and adopt this power density distribution in modeling.

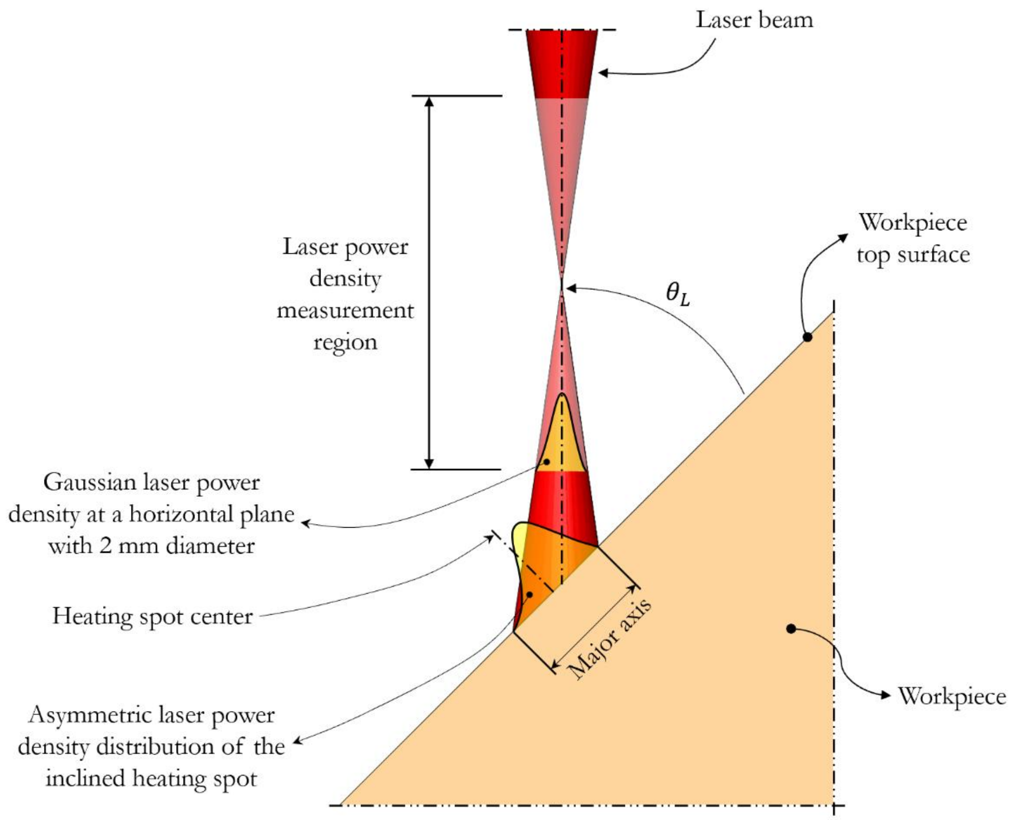

Figure 6.2. Schematic for laser heating using an inclined laser beam. The beam inclination results in an asymmetric distribution for the laser power density inside the heating spot.

6.3 Laser Power Density Distribution of Inclined Laser Beams

This section presents the formulation of the laser power density distribution inside the heating spot of a laser beam inclined at an angle 'θ_L' on a flat workpiece surface. The effect of the workpiece surface curvature is discussed later in section 6.4. Furthermore, this section presents the development of a Matlab script to automate the laser power density calculations for different user inputs. The input variables needed to generate a power density curve are: (1) the laser inclination angle, (2) the distance between the laser focal point and the workpiece surface, which is denoted as the defocusing distance, (3) the laser beam angle of divergence, (4) the laser power, and (5) the absorptivity η,

Figure 6.3 shows a general case of an inclined laser beam heating a flat workpiece, with an inclination angle θ_L, where D_{fw} is the defocusing distance, and θ_d is the laser beam angle of divergence.

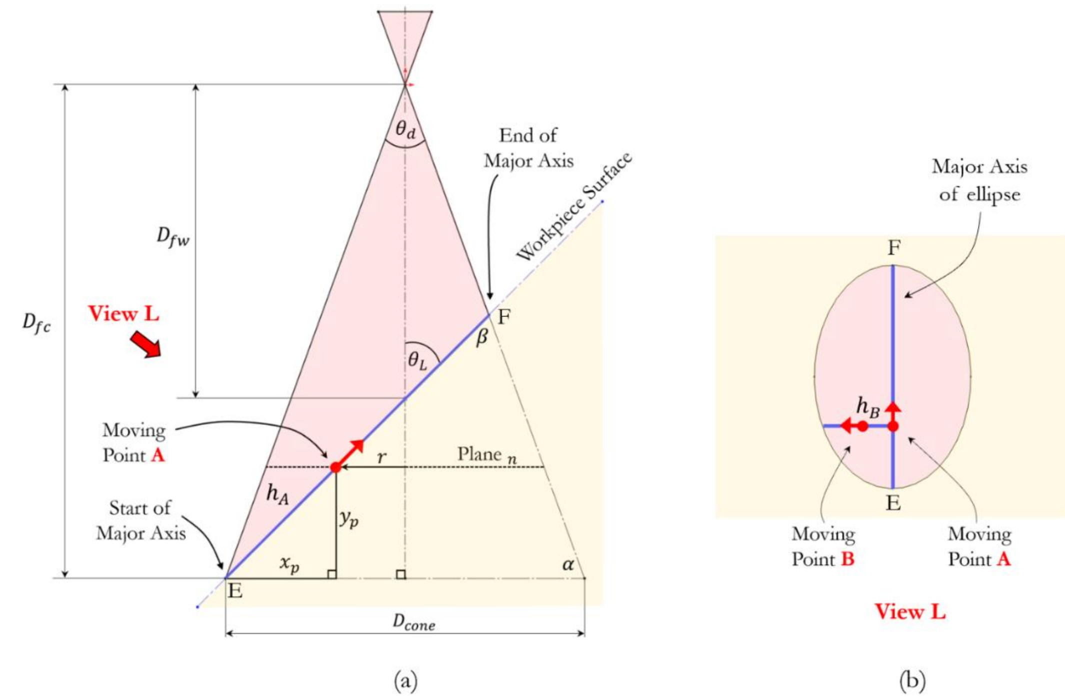

Figure 6.3. General case of an inclined laser beam heating a flat workpiece surface.

In order to calculate the laser power density for the workpiece surface area subjected to laser heating (red area in Figure 6.3(b)), two moving points, A and B, are utilized (shown as red points in the figure) to scan the whole laser heating area, shown as a red area. Point A moves from the start of the major axis of the ellipse to its end with a certain adjustable increment. At each position of point A, point B travels perpendicularly starting from the major axis to the outer boundary of the area with a certain adjustable increment. Point B only moves in one direction (left direction in Figure 6.3(b)) since the power density distribution is symmetric around the major axis of the ellipse. For each position of point B, the laser power density is calculated at that point based on the Gaussian distribution of the laser power density on the corresponding horizontal plane ($Plane_n$ in Figure 6.3(a)).

The major axis length $L_{m.axis}$ is calculated using the law of sines as follows:

$$L_{m.axis} = D_{cone} \times \frac{\sin(\alpha)}{\sin(\beta)}, \qquad (Equation\ 6.1)$$

which is expressed as a function of the user inputs θ_d and θ_L as follows:

$$L_{m.axis} = D_{cone} \times \frac{\sin\left(90^o - \frac{\theta_d}{2}\right)}{\sin\left(\theta_L + \frac{\theta_d}{2}\right)} . \qquad (Equation\ 6.2)$$

where D_{cone} is the imaginary base diameter of the laser cone, and is calculated as follows:

$$D_{cone} = 2\tan\left(\frac{\theta_d}{2}\right) \times D_{fc} , \qquad (Equation\ 6.3)$$

where D_{fc} is related to the input D_{fw} as follows:

$$D_{fc} = \frac{D_{fw}}{1 - \tan(90^o - \theta_L)\tan\left(\frac{\theta_d}{2}\right)} . \qquad (Equation\ 6.4)$$

The above equations 6.1 to 6.4 are used to calculate the major axis length as a function of the user inputs θ_d, θ_L, and D_{fw}. The position of point A along the major axis is denoted as h_A, which takes values starting from zero up to the value of the calculated major axis length in increments of a certain adjustable small value.

The moving point A has coordinates x_p and y_p that are calculated as follows:

$$x_p = h_A \times \cos(90^o - \theta_L), \qquad (Equation\ 6.5)$$

and

$$y_p = h_A \times \sin(90^o - \theta_L). \qquad (Equation\ 6.6)$$

The position of point B is denoted as h_B, which takes values starting from zero (starting at the major axis and going left in Figure 6.3(b)) up to the value $h_{B.max}$ of the length between the major axis and the outer boundary of the area. This length $h_{B.max}$ changes as point A moves along the major axis. It is calculated using the general equation of an ellipse as follows:

$$h_{B.max} = \sqrt{(\sin(\theta_L) \times \frac{L_{m.axis}}{2})^2 \times (1 - \frac{\left(h_A - \frac{L_{m.axis}}{2}\right)^2}{\left(\frac{L_{m.axis}}{2}\right)^2})} \qquad (Equation\ 6.7)$$

where $L_{m.axis}$ is the length of the major axis of a laser heating spot. For each position of point B, the laser power density has to be calculated. The value of laser power density P_d absorbed by the workpiece surface at the 3D position of point B (x_p , y_p, h_B) at a distance r from the axis of a laser beam with Gaussian-distributed power density can be calculated based on Equation 2.12 as follows:

$$P_d = \eta \frac{2 \, P L_{ma.90}}{\pi \, R^2 L_{m.axis}} \exp\left(\frac{-2 \, r^2}{R^2}\right) \qquad (Equation\ 6.8)$$

where η is the absorptivity, P is the laser power, R is the beam radius at plane$_n$, and $L_{ma.90}$ is the length of the major axis of the heating spot of a perpendicular laser beam. The ratio $L_{ma.90}/L_{m.axis}$ was used in this equation to ensure that the total power inside the heating spot is unchanged regardless of the inclination angle of the laser beam. The value of R changes as point A moves from E to F, and is calculated as follows:

$$R = \tan\left(\frac{\theta_d}{2}\right) \times (D_{fc} - y_p). \qquad (Equation\ 6.9)$$

The radius r changes with the movement of both points A and B. It is calculated as follows:

$$r = \sqrt{\left(\frac{D_{cone}}{2} - x_p\right)^2 + (h_B)^2}\ , \qquad (Equation\ 6.10)$$

Equations 6.1 to 6.10 were then written in one Matlab script, and two nested iterative for-loops were used to move points A and B to determine the power density curves for given θ_d, θ_L, D_{fw}, P, and η. The first for-loop moves point A by a certain increment, and the second for-loop, which is nested within the first loop, moves point B from the major axis to the outer boundary of the ellipse with a certain increment. Figure 6.4 shows an example of a 3D plot created using the developed Matlab script. This example was created with the following inputs: θ_L=45°, θ_d=16°, D_{fw}= 12.33 mm, P = 1000 W, and η=1. Figure 6.4(a) shows the discrete positions of point B, using an increment value of 0.1 mm, at which the laser power density was calculated. Figure 6.4(b) shows the same case but with a smaller increment of 0.0001 mm.

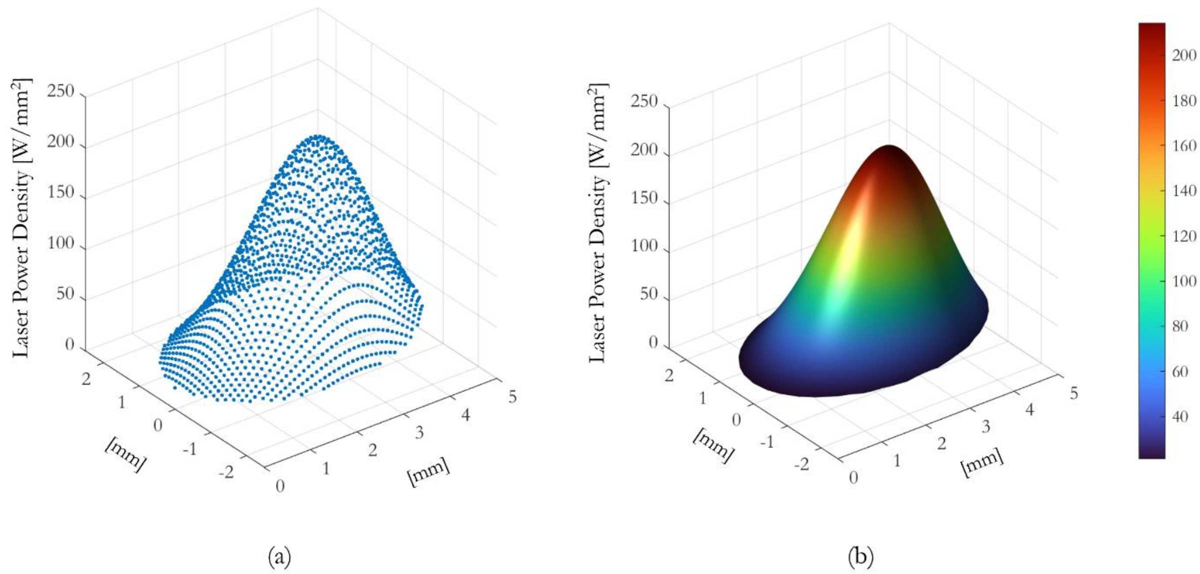

Figure 6.4. Calculated laser power density applied on a flat workpiece surface with θ_L=45°, θ_d=16°, D_{fw}= 12.33 mm, P = 1000 W, and η=1. (a) Plot showing the discrete points, which are 0.1 mm apart, at which laser power density was calculated. (b) The result for the same case, but with a smaller increment of 0.0001 mm.

In order to investigate the effect of the laser beam inclination angle on the laser power density distribution, Figure 6.5 compares the laser power density curves along the major axis of the heating spot at any value for D_{fw}, for different inclinations angles ranging from 30 to 90 degrees. In these plots, the distance along the major axis is normalized with respect to the length of the major axis of the heating spot of a perpendicular laser beam, $L_{ma.90}$. The rest of the inputs were held at constant values: P = 1000 W and θ_d=16°. Moreover, for these plots, the absorptivity is assumed to be 1 for all inclination angles. However, it should be noted that in the actual laser heating applications, the absorptivity decreases as the laser beam inclination angle is increased or decreased away from 90° [192, 231-233]. Furthermore, it should be noted that the actual diode laser beam used in the experimental work of Chapters 4, and 5 had the same value for the divergence angle θ_d (16 degrees).

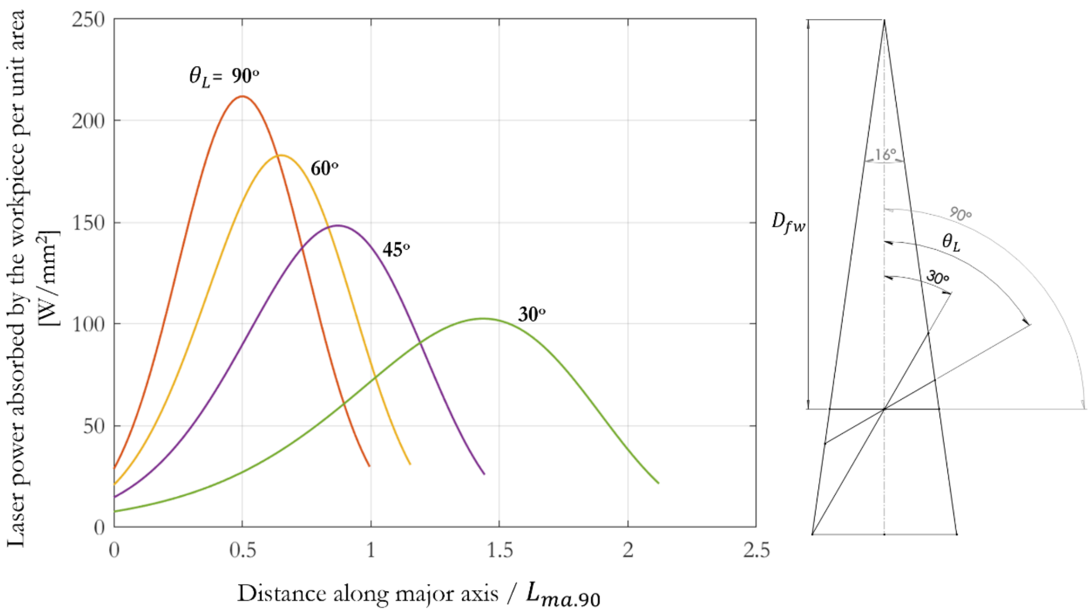

Figure 6.5. The effect of changing the inclination angle on the absorbed laser power density along the major axis of the elliptical laser heating zone at any value for D_{fw}. The distance along the major axis is normalized with respect to the length of the major axis of the heating spot of a perpendicular laser beam $L_{ma.90}$. θ_d=16°, P = 1000 W, and η=1.

As shown in Figure 6.5, the only symmetric power density curve is the curve generated at θ_L= 90°, which corresponds to the case when the laser beam is perpendicular to the workpiece surface and has a circular heating spot with a symmetric Gaussian distribution of power density. The asymmetry in the power density curves becomes larger by tilting the beam away from 90°. It is also clear that as the beam tilts more away from 90°, the heating spot size increases (i.e., the length of the ellipse major axis increases), and the peak of the power density decreases since the laser power is applied over a wider area.

Figure 6.6 shows the effect of the laser beam inclination angle on the ratio between the length of the major axis of the inclined laser heating spot to the length of the major axis of the perpendicular laser heating spot at any value for D_{fw}, while the laser beam divergence angle is constant at 16°. As shown in the figure, tilting the laser beam significantly increases the length of the major axis (more than double the length at 30°) compared to the major axis of the perpendicular beam.

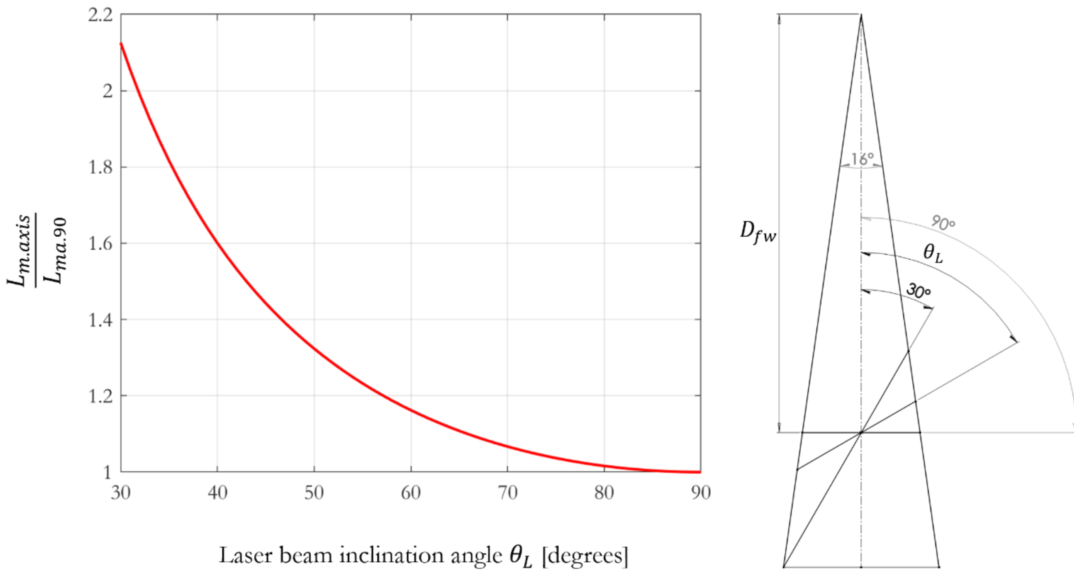

Figure 6.6. The effect of laser beam inclination angle on the ratio between the length of the major axis of the inclined laser heating spot to the major axis of the perpendicular laser heating spot at any value for D_{fw}. The laser beam divergence angle is constant at 16°.

The results discussed in this section were adopted by the FE models developed in this research work for LSH and LAML as discussed in-detail in section 6.5. In the next section, the effect of the workpiece surface curvature on the surface temperature during laser heating is numerically investigated and discussed.

6.4 Effect of Surface Curvature on the Surface Temperature during Laser Heating

In this section, the effect of the workpiece surface curvature on the surface temperature during laser heating is numerically investigated. When complex 3D geometries are heated by laser, the workpiece surface experiences varying degrees of local laser power absorption, even if the laser beam orientation is kept unchanged [233]. Consider the two cases shown in the schematic of Figure 6.7. In Case 1, the laser beam is heating a flat surface area, and in Case 2, the laser beam is heating a curved surface area. In Case 2, the laser beam has the same orientation as in Case 1. For Case 1, all segments of the heated surface area on the workpiece have the same angle relative to the laser beam axis (θ_L). However, for Case 2, the relative inclination angle between the laser beam axis and various segments of the heated area θ_i will vary. The smaller this angle becomes; the less laser power is absorbed by the surface (i.e., the local absorptivity η decreases [232]).

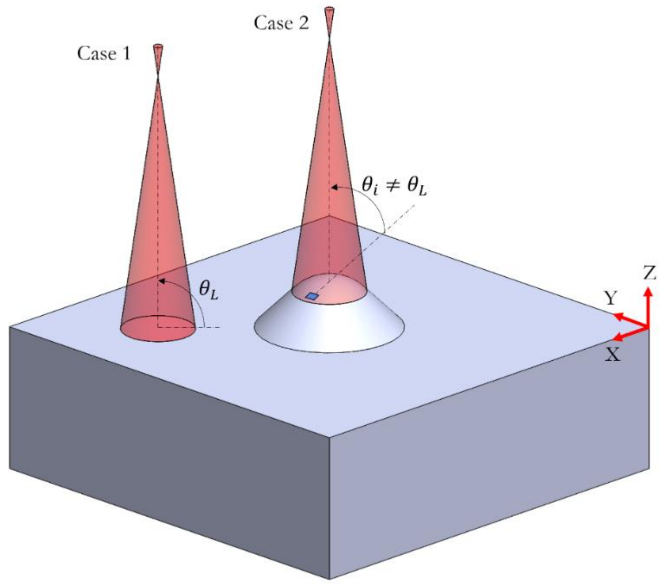

Figure 6.7. Schematic for laser heating of a complex 3D surface

Since the absorptivity depends on many factors, other than the laser beam inclination angle, such as the workpiece material properties, the surface roughness, and the laser wavelength, it is very difficult to find in the open literature the absorptivity values for the exact conditions of the laser – workpiece combination. In this research work, the values 0.86 and 0.55 for the absorptivity of H13 tool steel at 90° and 45° laser inclination angles, respectively, were utilized in the FE models developed in sections 5.3.1 and 6.5.2, respectively, and both of those absorptivity values were found to produce results in good agreement with the experimental results. From the review of literature, it was found that for the inclination angle range of 45° to 90°, the relationship between η and θ_L for steels could be approximated to be linear [232]. Therefore, based on the two validated absorptivity values, a linear variation for the absorptivity with the laser beam inclination angle was assumed.

Four different workpiece geometries, shown in Figure 6.8, were considered for the numerical investigation of laser heating using a 5 mm diameter laser beam, when the surface is flat and θ_L =90°

(Case (a)). Cases (b), (c), and (d) are workpieces with 3D spherical surfaces with radii 12.8 mm, 6.5 mm, and 3.5 mm, respectively. At the steepest point inside the heated area on these curved surfaces, the minimum local laser inclination angle θ_i are 75º, 60º, and 45º, respectively.

From surveying the die and mould manufacturing industry, it was concluded that the diameter of the bull nose and ball nose end mills used for rough machining of typical flat and curved ribs and die cast inserts made of H13 tool steel is in the range of 2-6 mm. Surface features commonly have relatively large radius of curvature > 5 mm. Consequently, for laser beam spot size ~ 5 mm, the minimum local laser inclination angle at the steepest point on curved surfaces is expected to be greater than 45 º. For cases, in which the surface radius of curvature is < 5 mm, a smaller end mill size has to be used, and consequently the laser heating spot has to be smaller than 5 mm as well, which would make the minimum local inclination angle increase over 45º.

Four FE numerical models were created using the software Deform-3D to model laser heating of the four cases using a stationary laser beam (1,000 W) and 400 ms heating time. The FE model for Case (d) is shown in Figure 6.9 as an example that illustrates the modeling methodology used.

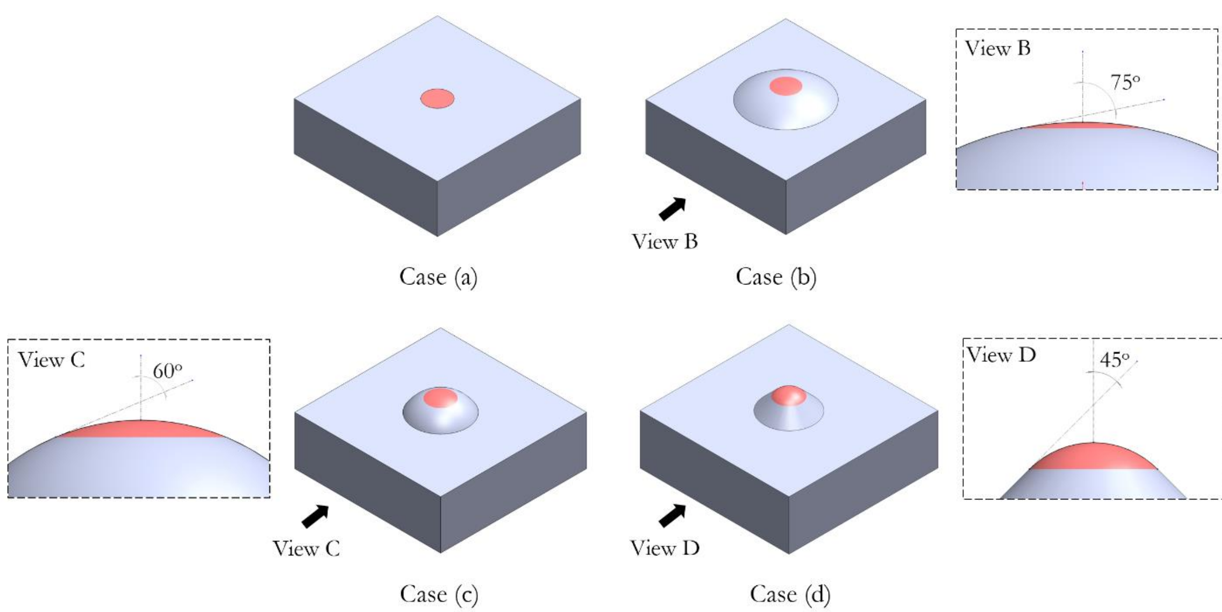

Figure 6.8. The four workpieces considered in the FE numerical investigation. The red areas are the heated area. Case (a) Flat surface. Case (b) Spherical surface with 12.8 mm radius. Case (c) Spherical surface with 6.5 mm radius. Case (d) Spherical surface with 3.5 mm radius.

The FE model consisted of a workpiece (12.5x30x30 mm) with approximately 75,000 tetrahedral elements, with element sizes ranging from 0.1 mm, inside the heating area, to 1.7 mm, outside the heating area. The workpiece material was assigned the general properties of H13 tool steel (Table 5.2). Ten concentric stationary heat exchange windows were used to simulate the Gaussian distribution of the laser power density with different values for the local absorptivity. Each heat exchange window was in the shape of a hollow cylinder except for the most inner window, which was a solid cylinder. The outermost diameter of the heat exchange windows was equal to 5 mm. For each heat exchange window, a local equivalent convective heat transfer coefficient h_{eqv} was defined, based on Equation 2.11 (section 2.3.4). The laser power density was calculated for each heat exchange window using Equation 6.8, for a laser power P= 1,000 W. The value of the local absorptivity η was obtained from the assumed linear relationship between η and the relative inclination angle θ_L, which varies over various segments of the curved surface. As shown in Figure 6.10, the curved surface was divided into segments that are approximated as planes of characteristic length of the order of 0.25 mm. For each of these plane segments, the local relative inclination angle θ_i and the corresponding local absorptivity η_i were obtained. All heat exchange windows were assigned the same fictitious high temperature T_w = 130,000 °C, and Equation 2.11 was solved to determine the value of h_{eqv} for each window. Similar to the previous FE models, the heat transfer coefficient was set to a constant value of 20 W/m^2 K outside of the heat exchange windows to simulate free air convection [152, 234].

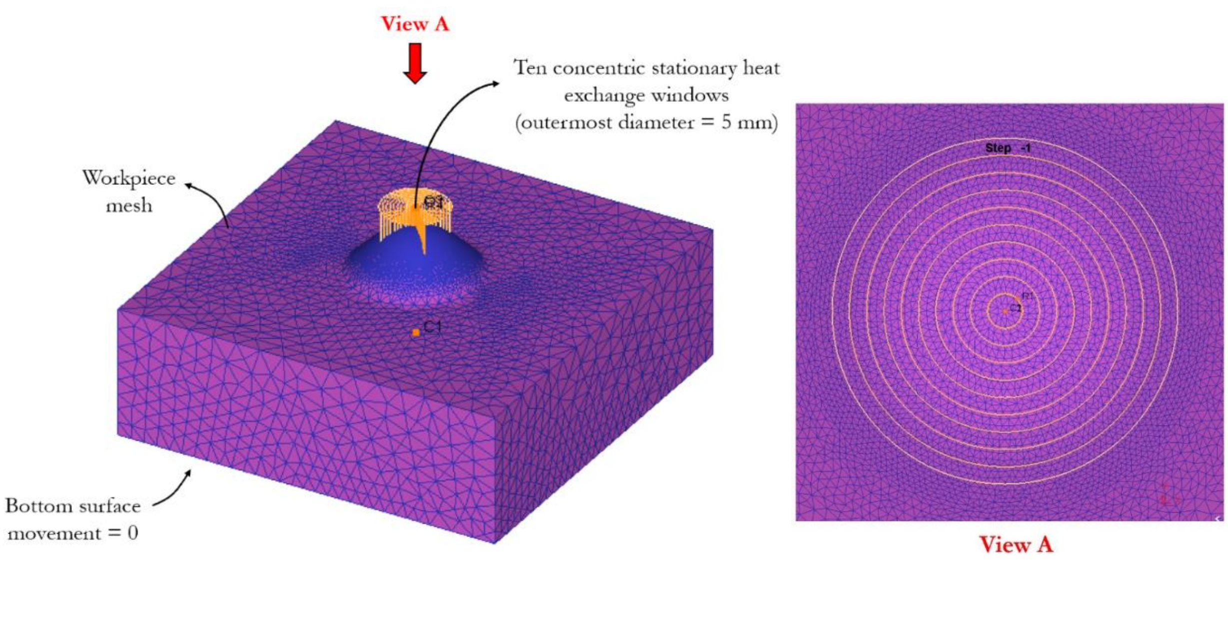

Figure 6.9. Laser heating FE model created for Case (d).

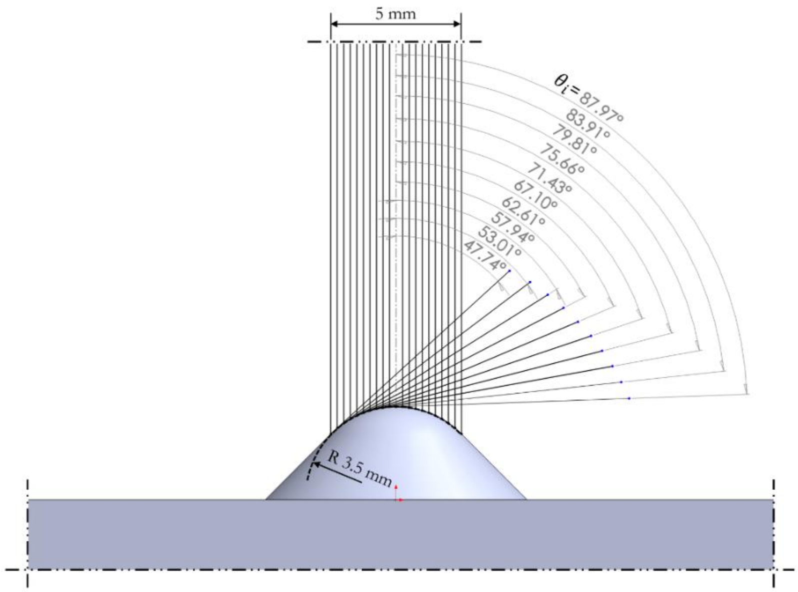

Figure 6.10. Determining ten local laser inclination angles for the curved surface of Case (d).

A comparison between the temperature fields of Case (a) and Case (d) at the end of the heating cycle is shown in Figure 6.11. As shown from both figures, as the surface curvature becomes steeper, the surface temperature decreases, since less laser power is absorbed by the surface. However, the largest difference in maximum surface temperature is predicted to be only 3.2%, which is negligible compared to the case with flat surface. This conclusion is consistent with the conclusion of the work done by Volpp et al. [233], who investigated the influence of complex geometries on the properties of laser hardened surfaces during laser surface heating.

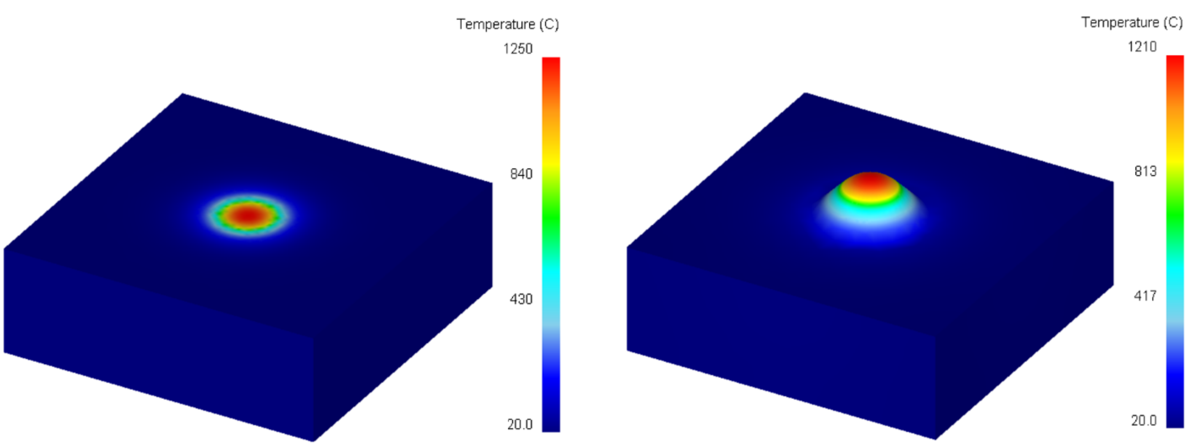

Figure 6.11. Comparison between temperature fields of Case (a) and Case (d) at the end of the heating cycle. The laser power was 1000 W and the heating time was 400 ms.

6.5 FE Modeling of LSH and LAML

6.5.1 FE Modeling of Heating Spots of Inclined Laser Beams

Figure 6.12 and Figure 6.13 illustrate the methodology used to model an elliptical laser heating spot, generated by an inclined laser beam on a flat surface to simulate LSH and LAML processes. The figures show an example for determining the power density curve when the inclination angle $\theta_L = 45^o$, using the Matlab script developed in previous section. For this case, the resulting heating spot is a 3.54 x 5 mm ellipse. For modelling the thermal interaction of the incident laser beam with the workpiece in Deform-3D, eleven elliptical heat exchange windows were used. The position of these elliptical windows and the values of their individual heat fluxes were taken from the power density curve, as shown in Figure 6.12. However, in Deform-3D, it is not possible to create elliptical heat exchange windows. Therefore, as shown in Figure 6.13, eleven inclined cylindrical heat exchange windows were used. The diameter $D_{cyl.i}$ of each of these cylinders (which is equal to the minor axis of each ellipse) was calculated from the length of the major axis of the corresponding ellipse $L_{m.axis.i}$ as follows:

$$D_{cyl.i} = L_{m.axis.i} \times \sin(\theta_L) \qquad (Equation\ 6.11)$$

The value of heat flux given to each window in Deform-3D is calculated while considering the overlap with the other cylinders. For example, at point 1 in Figure 6.13 view A, the only heat flux applied is from the most outer heat exchange window. However, for point 2, the heat flux applied by the two most outer windows should be considered.

This methodology was adopted in the next sections for the FE numerical modeling of LSH and LAML, and the modeling results were compared to the experimental tests performed in Chapter 4.

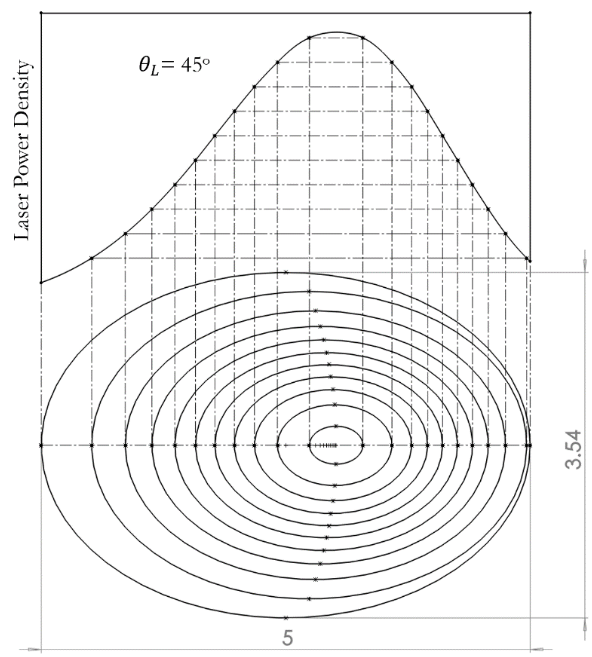

Figure 6.12. Elliptical laser heating spot generated by a laser beam inclined at a 45° angle. The schematic is drawn to-scale. Dimensions shown are in mm.

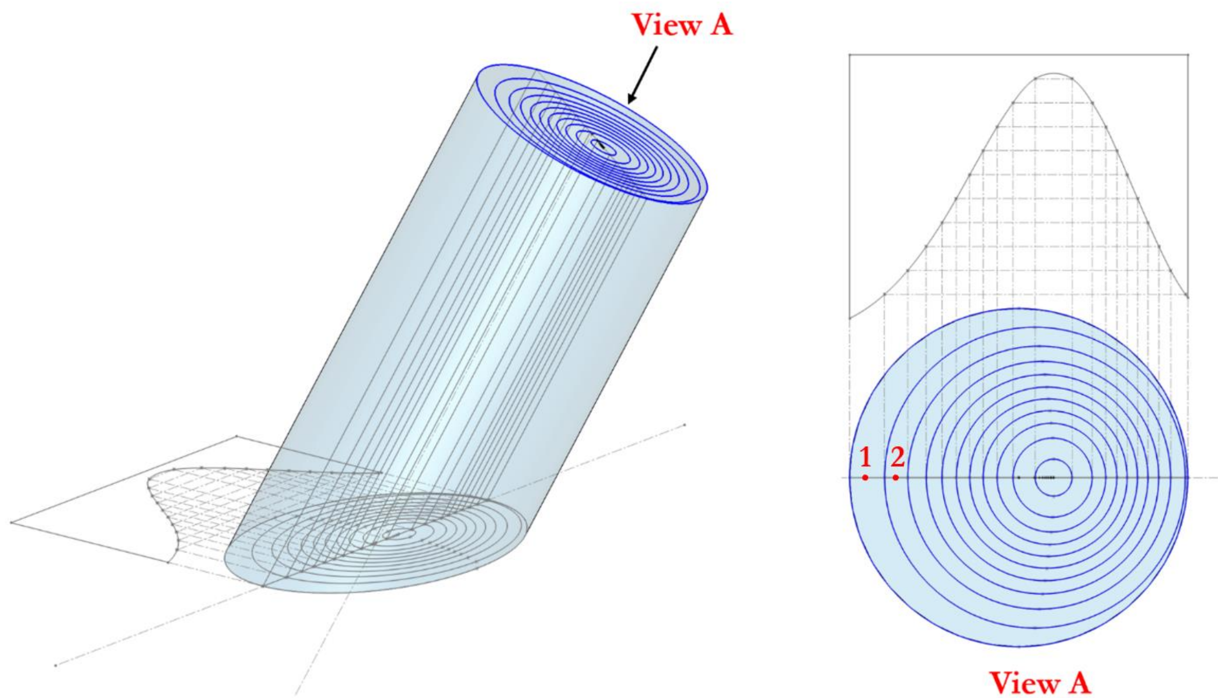

Figure 6.13. Inclined cylinders used to create elliptical heating spots on the workpiece surface for use in Deform-3D. The schematic is drawn to-scale.

6.5.2 FE Modeling of Laser Surface Heating

This section discusses the methodology used to develop a FE numerical model to predict the surface preheating temperatures and depths of the heat affected zones for the LSH process discussed previously in Chapter 4 in section 4.4. Moreover, the effect of laser beam inclination angle on the generated surface temperatures is investigated for both inclined and perpendicular laser beams. Furthermore, the effect of oscillating the laser beam in a zigzag manner on the surface temperature is investigated.

Figure 6.14 shows the three-dimensional FE model developed for LSH. As shown in the figure, the model consisted of a moving body (shown in green) that represented the laser source moving with a scanning speed f in a straight path or a zigzag path, eleven cylindrical heat exchange windows inclined at an angle θ_L that were moving with the same speed f, and a fixed workpiece.

Two values for the laser beam inclination angle θ_L were considered: 45° and 90°. The inclination angle value of 45° was the same value used for all experimental work presented previously in Chapter 4. For the 45° inclination angle, an absorptivity value of 0.55 was used as it resulted in the closest temperature predictions to the experimental results. For the 90° inclination angle, an absorptivity value of 0.86 was used since this value was validated in Chapter 5 in section 5.3. The length of the major axis of the heating spot in all cases was equal to 5 mm.

The straight path was considered in all cases except for two case where the zigzag path was considered to investigate its effect on surface temperature. In these two cases, the amplitude of the oscillation was 5 mm, and two frequencies were tested, 1.6 Hz and 3 Hz.

The workpiece dimensions used in this model were 10x30x80 mm. The workpiece had approximately 100,000 mesh elements ranging in size between 0.1 mm (for the finer mesh elements at the middle area of the part where the heating windows pass) to 3.5 mm for the coarse mesh used outside the middle area of the part. For the 45° inclination case, the eleven cylindrical heat exchange windows were used to simulate eleven elliptical windows on the workpiece surface as discussed in detail in the previous section. For the 90° inclination case, the heat windows were perpendicular to the workpiece surface to form circular symmetric heat exchange windows on the surface. The dimensions of each window were selected based on the detailed discussion presented in the previous section.

Similar to the previous FE models, each of the windows had a constant pseudo high temperature (130,000 ºC) temperature, and a uniform equivalent convective coefficient of heat transfer h_{eqv}. Each heat exchange window defined heat transfer in its local area as per Equation 5.1 discussed previously in Chapter 5. Equation 5.1 was solved for each of the eleven values selected from the power density curve generated by the Matlab script, as discussed previously in detail in section 6.3.

The heat transfer coefficient outside the heat exchange windows was set to 20 W/m^2 K, and H13 tool steel properties were used for the workpiece (Table 5.2).

Furthermore, this model uses the same experimentally validated microstructure kinetics models previously utilized and discussed in Chapter 5 in section 5.3.2. This model was used to predict the surface preheating temperatures and the depths of heat affected zones and its results are presented in section 6.5.5.

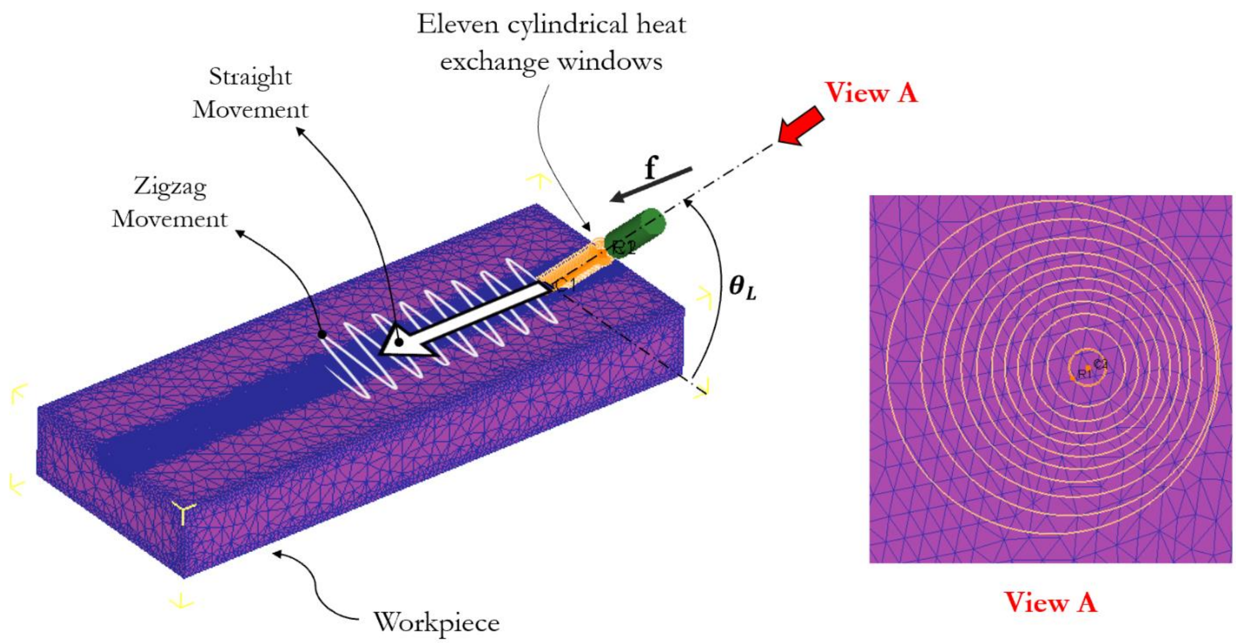

Figure 6.14. Three-dimensional finite-element-based model developed to simulate laser surface heating process using Deform-3D.

6.5.3 FE Modeling of 1D Laser-Assisted Milling

Figure 6.15 shows the three-dimensional FE model developed to simulate the 1D LAML process. As shown in the figure, the model consisted of a flat endmill, eleven inclined heat exchange windows, and a fixed workpiece. Only a 45° inclined laser beam was considered in this model, because as discussed previously in section 6.2, perpendicular laser beams are impossible to be used experimentally in LAML tests.

The cutting tool was created on the software Solidworks based on the dimensions of the carbide flat endmill used in the experimental LAML work in Chapters 4. The CAD model of the endmill was then imported into Deform-3D to be used as the cutting tool. The endmill had 4 flutes, with sharp corners, and a diameter of 6.35 mm. The endmill was modeled in Deform 3D as a rigid body, with approximately 8000 mesh tetrahedral elements, and was assigned the general material properties of carbide steel, which were provided by Deform-3D database. The key properties of carbide steel used in this model are listed in Table 6.1. Only 5 mm of the endmill height was considered in the model to decrease the total number of mesh elements. The endmill was assigned two movements: a feedrate, **f**, and a clock-wise rotational speed, **n**. The leading distance between the endmill and the heat exchange windows was 5 mm, and the axial depth of cut of the endmill into the workpiece was 0.5 mm, as was the case in the experimental work in Chapter 4 section 4.5.2.

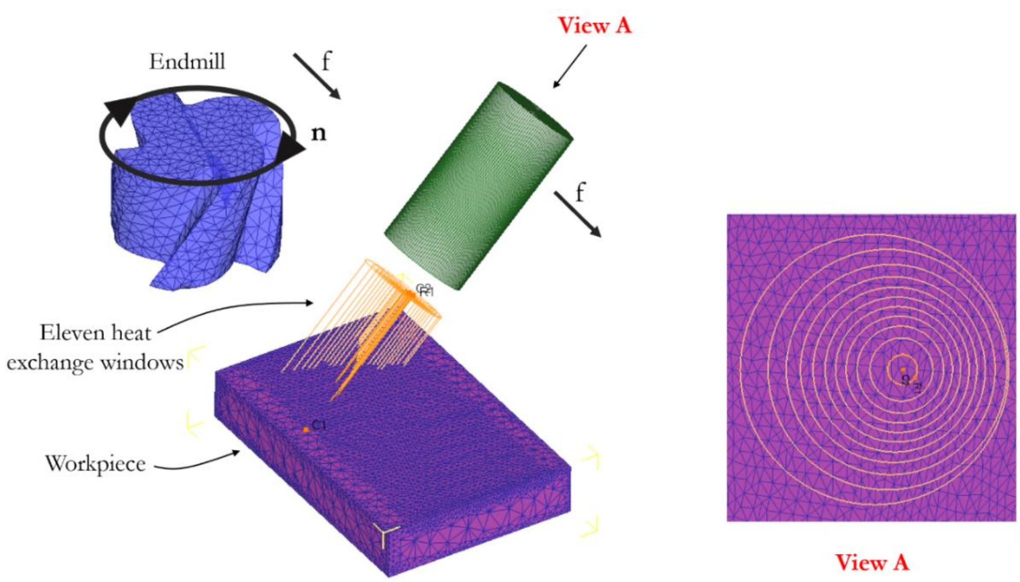

Figure 6.15. Three-dimensional finite-element-based model developed to simulate laser-assisted milling of a flat surface using Deform-3D.

Table 6.1. Key carbide endmill material propoerties used in Deform-3D [152].

Thermal conductivity [W/m K]	Specific Heat [J/kg K]	Density [g/cm^3]
82	290	15.7

The values of the heat convection coefficients and geometries of the eleven 45° inclined heat exchange windows, used to simulate the eleven elliptical windows on the workpiece surface, were defined similarly in the model discussed in the previous section, and the heat transfer coefficient outside the heat exchange windows was similarly set to 20 W/m^2 K for free air convection as well.

The workpiece was modeled with approximately 40,000 mesh tetrahedral elements and was assigned the properties of H13 tool steel (Table 5.1). The mesh element size ranged between 0.1 mm, inside the area of cutting and laser heating, and 1 mm for the outside mesh. The bottom surface of the workpiece was fixed, as well as its two side surfaces, to simulate vise clamping. The rectangular workpiece had dimensions of 2x8x12 mm.

The Johnson-Cook model, which was discussed previously in Chapter 2 and was proved accurate for modeling H13 tool steel machining [172-175], was used in this model to define the flow stress of the H13 tool steel material. The JC model (previously shown in Table 2.1) for H13 tool steel was provided by Deform-3D database as follows:

$$\bar{\sigma} = [564 + 241.88\,\bar{\varepsilon}^{\,0.24}]\,[1 + 0.03\ln[\dot{\bar{\varepsilon}}]]\left[1 - \left(\frac{T - 20}{1525 - 20}\right)^{0.97}\right], \qquad \text{(Equation 6.12)}$$

where $\bar{\sigma}$ is the flow stress, $\bar{\varepsilon}$ is the effective plastic strain, $\dot{\varepsilon}$ is the effective strain rate, and T is the instantaneous temperature.

In the model, the endmill-workpiece interactions were modeled using a constant heat transfer coefficient of 1000 kW/m^2 °C, and a hybrid sticking-sliding friction model (Equations 2.1 and 2.2 discussed previously in Chapter 2) with a friction coefficient of 0.55. These coefficients values for heat transfer and friction were selected since they resulted in predictions in close agreement with the experimental results. The initial range of these coefficients values were obtained by surveying the range of values reported in previous research work in literature [27, 149, 177, 178].

This model was used to predict the cutting forces during 1D LAML process for four different cases, and the results are presented in section 6.5.5.

6.5.4 FE Modeling of LAML of a 3D Surface

In order to validate the ability of the model presented in the previous section to be extended to predict cutting forces in LAML of workpieces with 3D surfaces, a segment of a 3D workpiece used in Chapter 4 section 4.5.3 (shown previously in Figure 4.21) was modeled on Deform-3D and used in this model, as shown in Figure 6.16. The movement of the endmill and the eleven inclined heat exchange windows were specified according to the paths obtained from Fusion360 in Chapter 4 section 4.5.3.

In this case, as illustrated in Figure 6.17, the laser beam is inclined at an inclination angle θ_L equals to 45° in the YZ plane. The value of θ_L is constant along the laser path since it is determined by the inclination of the laser focusing head itself, which is fixed. However, there is another laser inclination angle $\theta_{L_{sur}}$ relative to the workpiece surface. The value of $\theta_{L_{sur}}$ changes along the laser path (starting from 68° to 45° for this specific case) because the surface geometry changes. In this case, the laser beam effective inclination angle $\theta_{L_{eff}}$ in a plane perpendicular to the surface (plane B in Figure 6.17) changes from approximately 41° to 45° along the laser path.

For this FE model, $\theta_{L_{eff}}$ was considered to have a fixed value of 43°, and similar to the modeling methodology used in the previous section, the values of the heat fluxes for the 43° eleven inclined windows were selected from the power density curve calculated for a 43° inclined laser beam heating a flat workpiece surface with a constant absorptivity of 0.53.

The material constitutive equation as well as the heat transfer and friction models used in this model were the same as those used in the FE model described in the previous section. The model was used to predict the cutting forces during LAML of the 3D segment for two cases with different feedrates, and compared to the experimental results, as discussed in section 6.5.5.

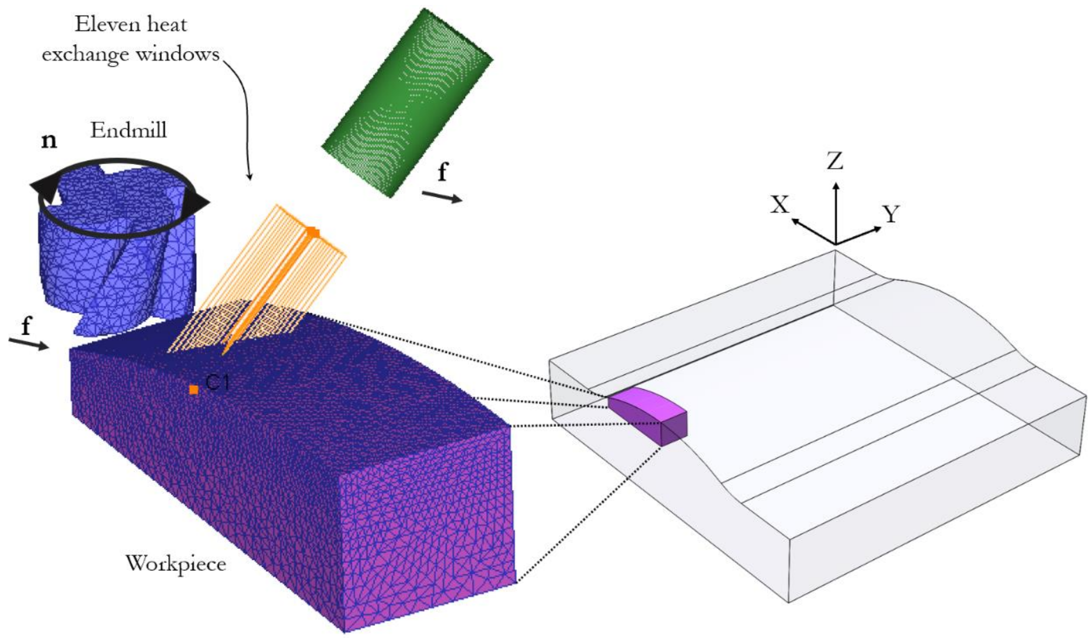

Figure 6.16. FE modeling of LAML of a 3D surface, which is a segment of the 3D workpiece used in previously in section 4.5.3 (shown in Figure 4.21).

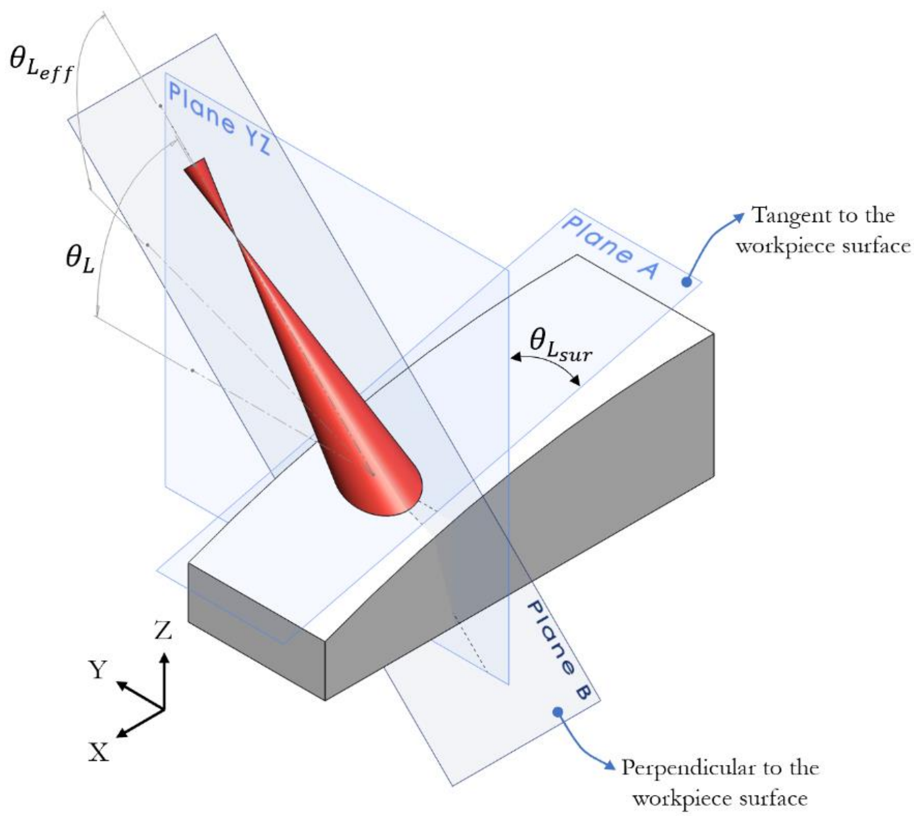

Figure 6.17. Determining the effective laser beam inclination relative to the workpiece surface.

6.5.5 FE Modeling Results and Discussion

Running the simulations for the three-dimensional FE numerical models developed in the previous sections was computationally very demanding and needed up to several days per case to run (the computer CPU used was a 2.10 GHz AMD Ryzen 5). For that reason, only few cases (ten cases for LSH, four cases for 1D LAML, and two cases for LAML of 3D surface) were considered and compared with the corresponding experimental results. Table 6.2 shows the cases considered in the models.

Section 6.5.5.1 presents the results for the first 4 cases, which correspond to actual experimental LSH tests performed in Chapter 4 section 4.4. In these 4 cases, only the laser power is varied to investigate its effect on surface temperatures.

Section 6.5.5.2 compares the results of the first 8 cases, to show the effect of changing the laser beam inclination angle from 45^{o} to 90^{o} on workpiece surface temperatures.

Section 6.5.5.3 presents the effect of oscillating the laser heating spot on workpiece surface temperatures.

Section 6.5.5.4 presents the predictions of the heat affected zone depths for the first 4 cases during LSH.

Finally, section 6.5.5.5 presents the predictions for the temperature field ahead of the cutting tool and the predictions for the cutting forces during LAML of flat and 3D surfaces (cases 5 to 10).

Table 6.2. The cases considered in the FE modeling.

<table>
<tr><th>FE Model</th><th>Case no.</th><th>Laser power [W]</th><th>Laser beam inclination angle (θ_L) [degrees]</th><th>Heating spot size (major axis length) [mm]</th><th>Cutting tool diameter [mm]</th><th>Cutting tool rotational speed [rpm]</th><th>Axial depth of Cut [mm]</th><th>Feedrate/ Laser scanning speed [mm/min]</th></tr>
<tr><td rowspan="9">LSH</td><td>1</td><td>500</td><td rowspan="4">45</td><td rowspan="15">5</td><td rowspan="9">N/A</td><td rowspan="9">N/A</td><td rowspan="9">N/A</td><td rowspan="13">1000 [mm/min]</td></tr>
<tr><td>2</td><td>700</td></tr>
<tr><td>3</td><td>900</td></tr>
<tr><td>4</td><td>1100</td></tr>
<tr><td>1_90</td><td>500</td><td rowspan="4">90</td></tr>
<tr><td>2_90</td><td>700</td></tr>
<tr><td>3_90</td><td>900</td></tr>
<tr><td>4_90</td><td>1100</td></tr>
<tr><td>4_zigzag</td><td>1100</td><td rowspan="7">45</td></tr>
<tr><td rowspan="4">1D LAML</td><td>5</td><td>500</td><td rowspan="6">6.35</td><td rowspan="6">4000</td><td rowspan="6">0.5</td></tr>
<tr><td>6</td><td>700</td></tr>
<tr><td>7</td><td>900</td></tr>
<tr><td>8</td><td>1100</td></tr>
<tr><td rowspan="2">LAML of a 3D Surface</td><td>9</td><td rowspan="2">1100</td><td>800</td></tr>
<tr><td>10</td><td>1000</td></tr>
</table>

6.5.5.1 Effect of Laser Power on Surface Temperatures

Figure 6.18 and Figure 6.19 show the results for the surface temperatures for the first four cases of Table 6.2 for LSH, which correspond to actual experimental LSH tests performed in Chapter 4 section 4.4. In these four cases, the laser beam inclination angle was 45°. Figure 6.18 shows an example of the asymmetric temperature distribution on the workpiece surface during LSH for case 3 at the beginning of heating spot movement (time=0.01 s). As shown in the figure, the temperature field has an elliptical shape with a distribution similar to the calculated power density distribution shown previously in Figure 6.4 and Figure 6.5. Figure 6.19 shows the comparison between the maximum predicted and maximum measured temperatures at the thermocouples position (the position is indicated in Figure

6.18). As expected, when the laser power increased, the surface temperature increased. The figure shows that the predicted temperatures are in good agreement with the experimental results (presented in section 3.3.2) with a maximum error of ± 10 %. This validates the methodology used to model the heating spot of an inclined laser beam, and confirms its reliability for predicting the surface preheating temperature for process development, design, and optimization. Since the error in temperature predictions is acceptable, this model was used to predict the heat affected zone depths (section 6.5.5.4) using the integrated microstructure evolution model that was experimentally validated in Chapter 5 section 5.3.3.

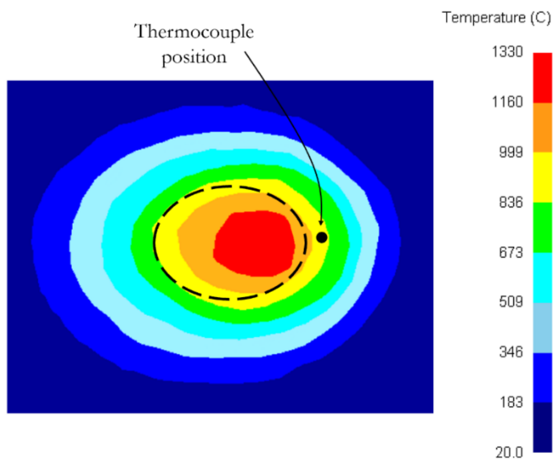

Figure 6.18. The predicted asymmetric temperature distribution on the workpiece surface during LSH (case 3 from Table 6.2) at the beginning of heating spot movement.

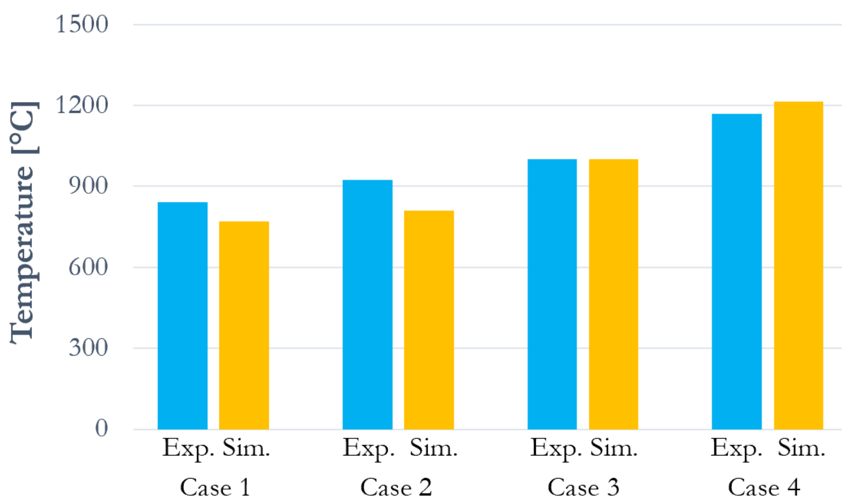

Figure 6.19. Comparison between the maximum surface temperatures predicted and measured at thermocouples position. The thermocouple position is shown in Figure 4.7. The experimental results were previously presented and discussed in section 4.4.

6.5.5.2 Effect of Laser Beam Inclination Angle on Surface Temperatures

Figure 6.20 and Figure 6.21 show the results for cases 1_90 to 4_90 from Table 6.2 where a perpendicular laser beam was used in modeling. Figure 6.20 shows an example of the generated temperature distribution on the workpiece surface during LSH for case 1_90 at the beginning of heating spot movement. As shown in the figure, the temperature field has a circular shape with a symmetric distribution, as opposed to the elliptical asymmetric temperature field shown previously in Figure 6.18. The circular shape of the temperature field is the result of the circular heating spot resulting from the intersection of the conical shape of the perpendicular beam with the workpiece surface. Figure 6.21 shows a comparison between the predictions for the maximum surface temperatures for the first eight cases of LSH from Table 6.2. Heating the workpiece surface using a perpendicular laser beam increased the maximum surface temperature by up to 14% compared to heating using a 45^o inclined laser beam. This increase in surface temperature was expected since the absorptivity increases when the laser beam inclination angle gets closer to 90^0.

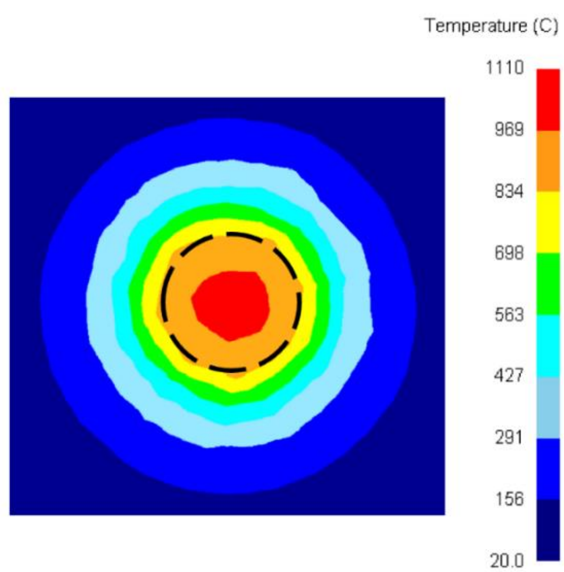

Figure 6.20. The predicted temperature distribution on the workpiece surface during LSH with a perpendicular laser beam at the beginning of heating spot movement (Case1_90 from Table 6.2).

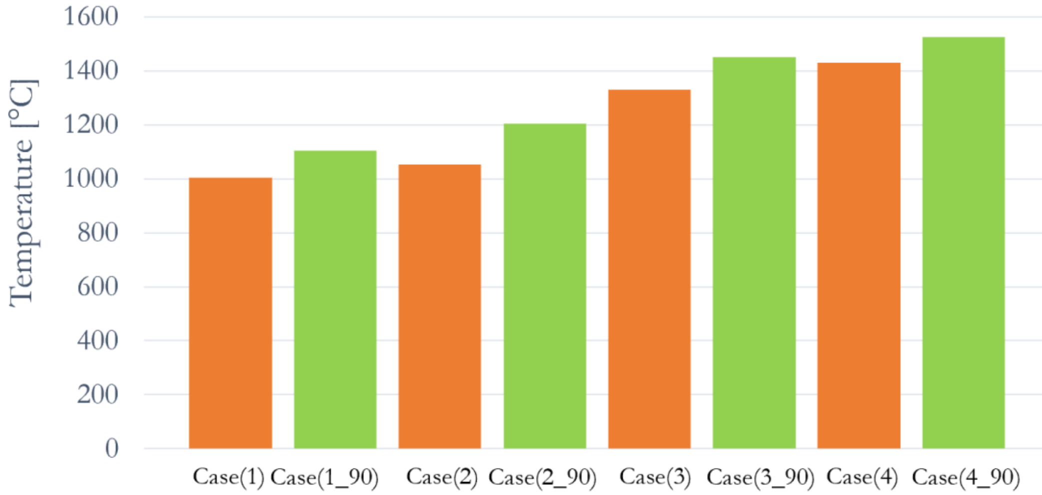

Figure 6.21. Maximum surface temperatures predicted by the FE model for the eight cases of LSH from Table 6.2. Heating the workpiece surface using a perpendicular laser beam increased the maximum surface temperature by up to 14% compared to heating using a 45° inclined laser beam.

6.5.5.3 Effect of Oscillating the Laser Heating Spot on Surface Temperatures

Figure 6.22 shows the predicted workpiece surface temperature for case 4_zigzag from Table 6.2 where a zigzag path was used for oscillating the laser heating spot with a frequency of 1.6 Hz. Case 4_zigzag has the same conditions as case 4, except for the path shape. Figure 6.23 and Figure 6.24 compare the predicted temperatures for case 4 and case 4_zigzag (at two different frequencies) along line A and across the workpiece depth starting at surface point B. As shown from the plots, changing the beam path from straight to zigzag has resulted in a wider coverage for laser heating. However, this led to a decrease in the maximum surface temperature by 27% and 35% for oscillation frequencies 1.6 and 3 Hz, respectively. This decrease in maximum temperature occurred since, in the case of oscillation, the laser beam is scanning a wider area with the same laser power. Moreover, increasing the oscillation frequency from 1.6 Hz to 3 Hz decreased the maximum temperature by 9% since the laser beam has less time to heat the surface. Therefore, in order to achieve similar surface preheating temperatures during laser beam oscillation, larger laser power level is needed.

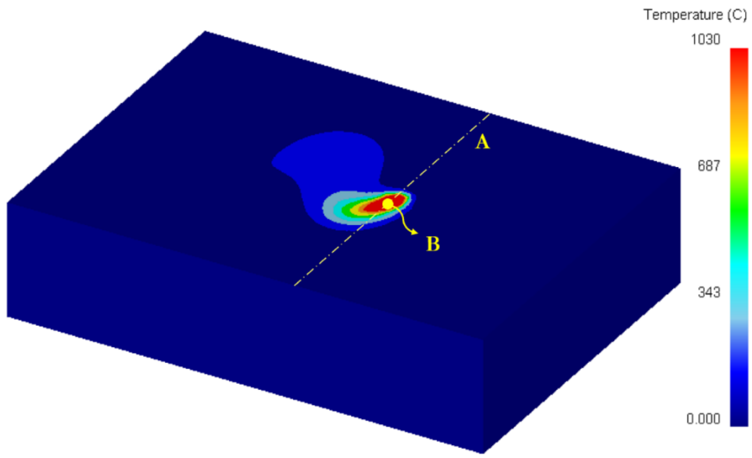

Figure 6.22. Predicted workpiece surface temperature for case 4_zigzag from Table 6.2. with a frequency equals to 1.6 Hz.

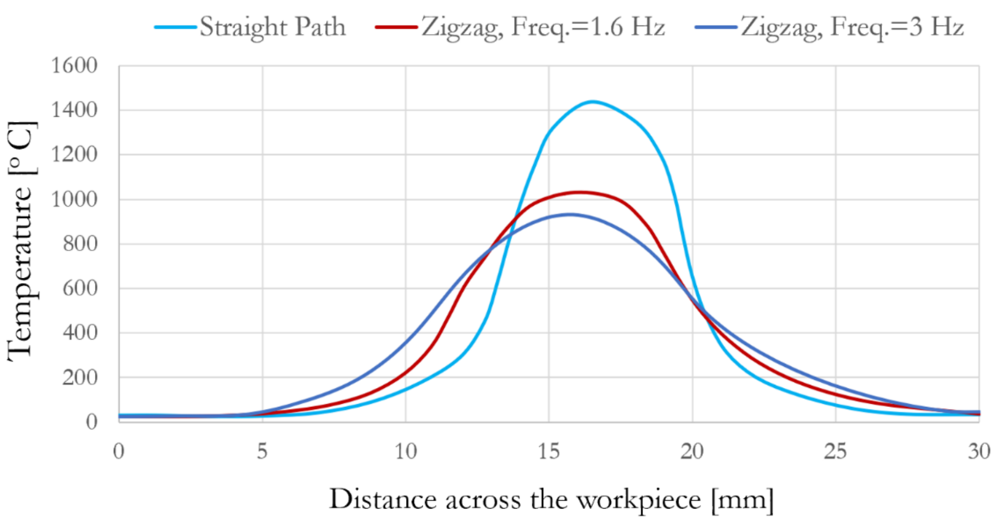

Figure 6.23. Comparison between the predicted surface temperatures for case 4 (straight path) and case 4_zigzag from Table 6.2 along line A of Figure 6.22.

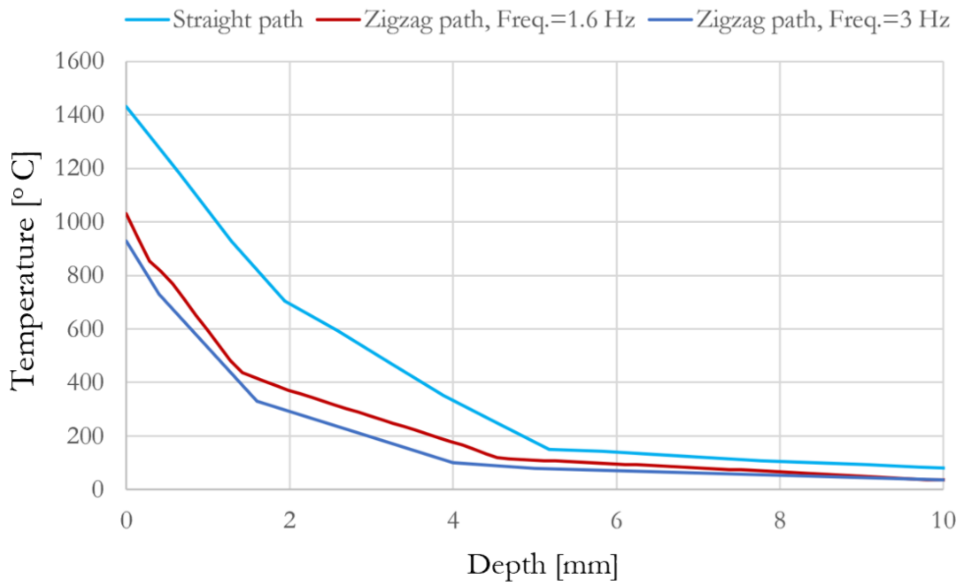

Figure 6.24. Comparison between the predicted surface temperatures for case 4 (straight path) and case 4_zigzag from Table 6.2 across the workpiece depth starting at surface point B of Figure 6.22.

6.5.5.4 Prediction of Heat Affected Zone Depths

The microstructure evolution model was used to predict the volume fraction of martensite formed during and after cooling for the first four cases in Table 6.2 for LSH. As shown in Figure 6.25, the predicted heat affected zone is asymmetric since the heat flux of the heating spot was asymmetric as a result of the 45° laser beam inclination. This asymmetric heat affected zone has also been observed experimentally and reported by Ayoola et al. [192] and shown in Figure 6.26. The figure shows the asymmetric HAZ created by laser surface heating of steel using a laser beam inclined at a 45° angle. The laser power *P* was 900 W and the scanning speed *f* was 690 mm/min. It is worth noting that when a perpendicular laser beam is used for LSHT, a symmetric circular heating spot and a symmetric HAZ are produced, as shown in Figure 5.15.

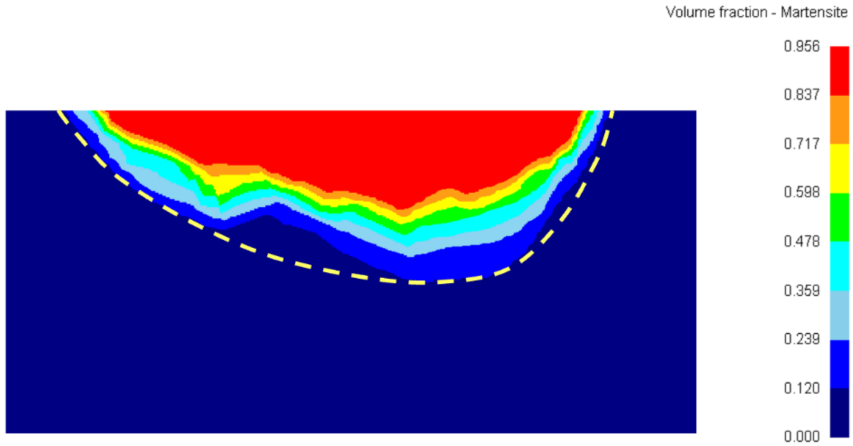

Figure 6.25. A cross section perpendicular to the direction of laser movement showing the predicted asymmetric heat affected zone formed as a result of the asymmetric laser heating spot. The figure shows the result for case 4 from Table 6.2.

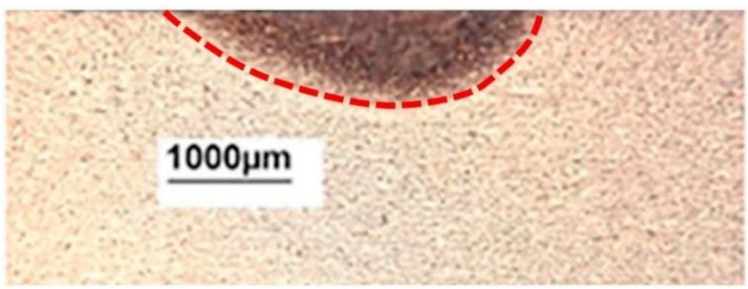

Figure 6.26. An example from the literature for an asymmetric heat affected zone formed by laser surface heating of steel using a laser beam inclined at an angle of 45°, as reported by Ayoola et al. [192]. The laser heating spot size was 2.35 mm, laser power was 900 W, and scanning speed was 690 mm/min.

Figure 6.27 shows the predictions for the depths of the heat affected zone (where any volume of martensite is formed beneath the surface - see the illustration of Figure 5.15) for the first four cases in Table 6.2. As shown from the predictions, the HAZ depth increases with increasing the laser power, which agrees with the experimental and numerical investigations reported in Chapter 5 section 5.3.3.2 in Figure 5.16.

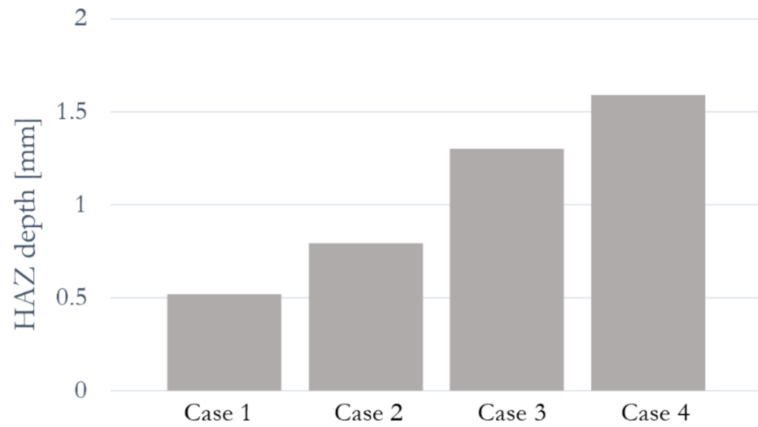

Figure 6.27. Predicted heat affected zones depths.

The prediction of the HAZ depth can be used for the LAML process design to determine the axial depths of cut (DOC) during milling, in order to remove the HAZ caused by laser heating. If the DOC is too large for a single path, then multiple cutting paths could be used. For example, LAML could be used for most of the roughing operations, and then by predicting the maximum HAZ depths caused by laser heating, finishing cutting operation(s) could be used at the end of the process without the assistance of laser heating.

Additionally, the prediction of martensite formation during laser heating can be used for the LAML process design to determine the range for the ideal leading distance between the laser beam and the edge of the cutting tool. As illustrated in Figure 6.28, the range of the leading distance should be between d_1 and d_2. In this range, austenite is being transformed into martensite, and martensite is still not fully formed yet. For leading distances below d_1, the martensite formation could be avoided altogether by removing the material. However, since the cutting tool is closer to the laser beam, excessive heating of the cutting tool could lower its life. For leading distances larger than d_2, the tool would be cutting hardened martensite, which is harder than the bulk workpiece material, which defeats the purpose of LAML. For these reasons it is recommended for the leading distance to be between d_1 and d_2. For the case shown in Figure 6.28, d_1 and d_2 were equal to approximately 4 mm and 6 mm, respectively. This range agrees with the experimental findings and recommendations reported in [144].

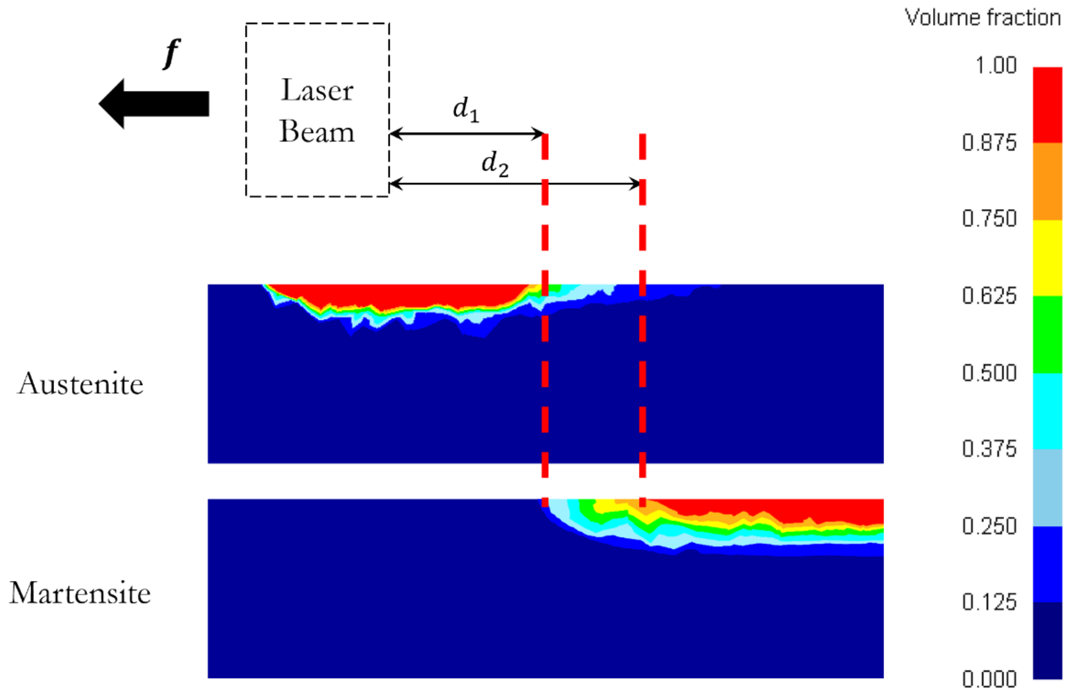

Figure 6.28. Cross-section along the direction of laser movement showing the microstructure transformation during LSH. The case shown is case 4 from Table 6.2.

It is also interesting to note that the prediction of HAZ depths is very useful for the design of the LSHT processes, where the formation of the hardened martensite is intentional and desirable for improving the material tribological properties. Using a moving laser source for surface heat treatment, as is the case in the FE model, is easily done for complex parts using the experimental setup developed in Chapters 3. Therefore, this way, surface heat treatment could be a part of a hybrid process in which LSHT is performed after LAML using the same laser source and setup, but with different parameters.

6.5.5.5 Prediction of Surface Temperature Field and Cutting Forces during LAML

Figure 6.29 (a) and (b) show two examples for the simulation of the FE models for LAML of flat and 3D surfaces. As shown previously in Figure 2.1, in order for the LAML of H13 tool steel to be effective, the temperature of the workpiece material right before its removal by the cutting tool needs to be approximately 450ºC or above. Using the LAML FE model, it is possible to predict the temperature field of the region ahead of the cutting tool that has a width equal to the diameter of the cutting tool (6.35 mm in this case) in order to make sure that the 450ºC condition is met right before the material removal by the cutting tool. If the coverage of the laser beam is not enough relative to the size of the cutting tool, then the laser beam could be oscillated in a zigzag movement ahead of the cutting tool to achieve the required coverage. All the LAML cases (cases 5 to 10) listed in Table 6.2 achieved the preheating temperature 450ºC, as shown in the examples of Figure 6.29. The experimental work performed in section 4.6.3 proved the significant reduction of cutting forces as a direct result of the effective workpiece material softening.

Figure 6.30 compares the mean value of the predicted cutting forces in the feed direction for cases 5 to 10 of Table 6.2, with the corresponding experimental results previously presented in Section 4.6.3. The comparison shows a good agreement between the predications and experimental results. The maximum error in the predications is within ± 12 %, which demonstrates the good capability of these models for the design and optimization of the LAML process.

As discussed previously in Chapters 2 and 4, LAML is really advantageous for roughing operations as it allows high material removal rates. However, increasing MRR increases the forces on the cutting tool and could lead to its breakage. As reported in Section 4.6.3, the carbide endmill used in the conventional milling experiments could only withstand cutting forces up to an average of 80 N. When the cutting forces in the feed direction exceeds this value, the tool broke. Therefore, a FE model, which is capable of accurately simulating the thermal interaction between the incident laser beam and the machined part, becomes an effective means for avoiding tool breakage. Finally, the good agreement of the predictions for cases 7 and 10 (for LAML of 3D surface) with the experimental results validates the ability of extending the methodology developed for modeling LAML of simple flat geometries to LAML for more complex parts.

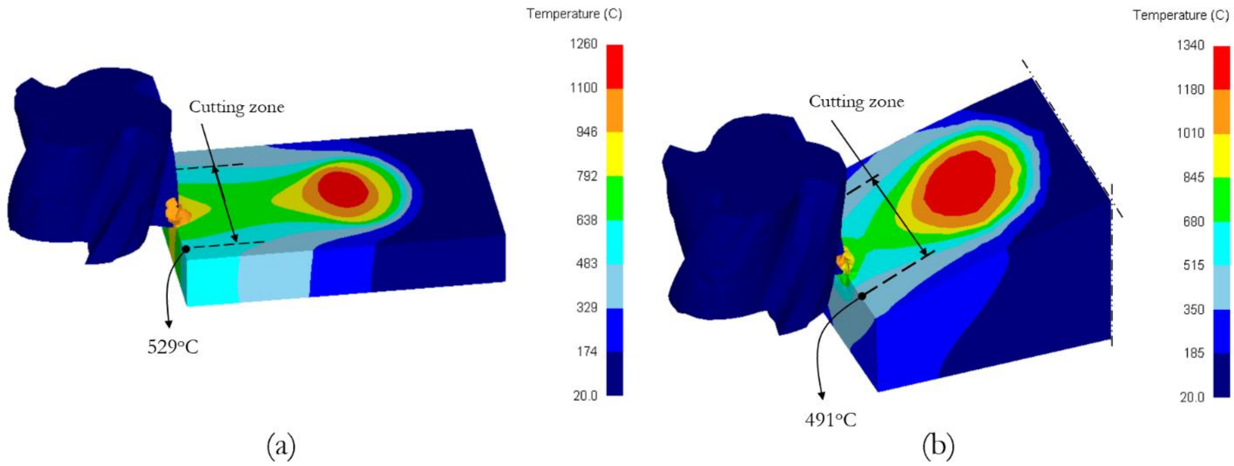

Figure 6.29. Simulation of LAML of flat and 3D surfaces. (a) case 7, and (b) case 10 from Table 6.2.

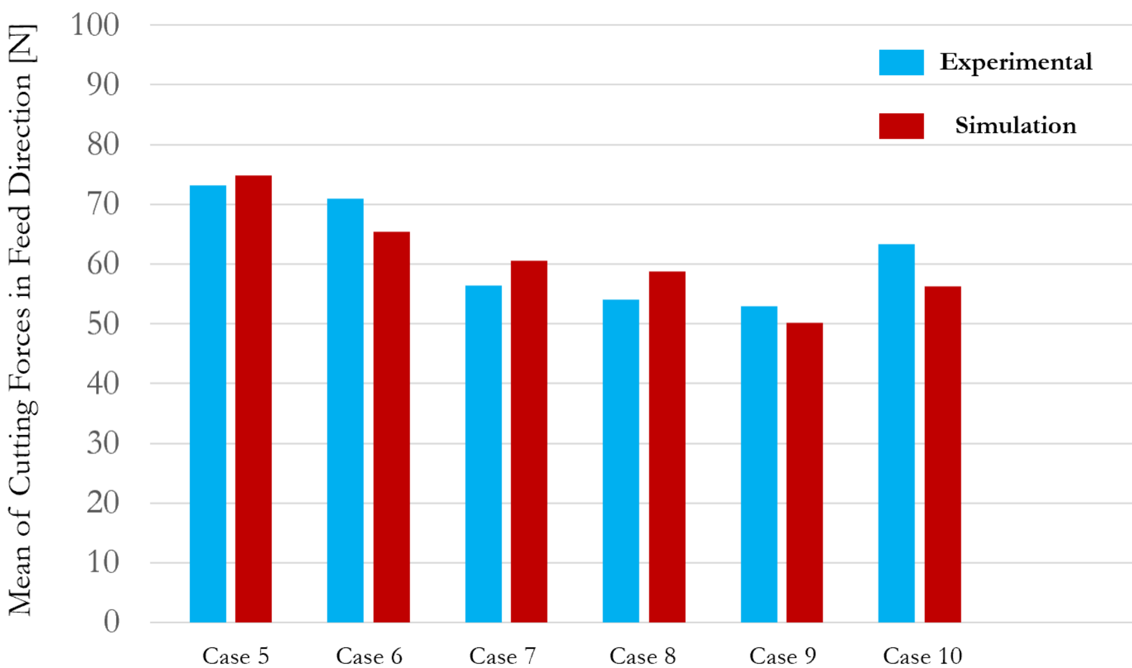

Figure 6.30. Comparison between the mean of cutting forces in feed direction obtained experimentally and numerically. The experimental results were previously presented and discussed in section 4.6.3.

6.6 Summary

This chapter presented the work done to develop finite-element-based numerical models for laser surface heating and laser-assisted milling of flat and 3D surfaces. A Matlab script was developed to generate the laser power density curves for laser beams inclined at any angle on a flat or curved workpiece surface. It has been demonstrated that the inclination angle had a significant effect on the shape of the heating spot and on the laser power density distribution.

The results of the Matlab script were adopted in the FE models to model a laser power density distribution using several elliptical heat exchange windows in Deform-3D. The FE models were used to predict surface temperatures, microstructure transformations, HAZ depths, and cutting forces. The model predictions were in good agreement with the experimental results, with a maximum error of $\pm$ 10 % for temperature predictions and $\pm$ 12 % for cutting forces predictions.

The effect of the workpiece surface curvature inside a small 5mm laser heating spot on the resulting surface temperatures during laser heating was investigated for different 3D surfaces. It was found that the reduction of the surface temperature due to the reduction of the local absorptivity is negligible compared to the surface temperatures obtained for a flat workpiece surface. However, changing the orientation of the laser beam from 45° to 90°, relative to the surface, had an effect of approx. 15% on the surface temperature.

For LAML, it is critical to predict the cutting forces, to avoid the tool breakage, and to determine the heat affected zone depth in order to ensure its removal either by adjusting the depth of cut or by designing multiple roughing and finishing passes. Furthermore, it is important for LAML to achieve the required preheating temperatures ahead of the tool before cutting. A zigzag path could be used to accommodate larger tools by covering a larger area of the workpiece, to achieve the required preheating temperatures.

For LSHT, the prediction of HAZ depths is important for the design of the process, where the intentional transformation of the material microstructure is desirable. Therefore, the developed FE models could be used to select the process parameters that result in the required depth of the desired microstructure. LSHT of complex parts could be conducted using the experimental setup developed in Chapters 3. Therefore, this process could be a part of a hybrid process to be performed after LAML using the same laser source and setup.

Chapter 7: Conclusions and Recommendations for Future Work

7.1 Conclusions

The work carried out in this thesis has met all the research objectives previously specified to address the important gaps related to laser-assisted milling of complex parts made of difficult-to-machine alloys. The laser-assisted milling techniques developed in this work have significantly improved the machinability of the material under investigation, AISI H13 tool steel, which can further broaden its use in many applications in industry. In addition, three-dimensional finite-element-based numerical models were developed for simulation of LSHT, LSH, and LAML, which proved to have strong predictive capabilities that are useful for process development, design, and optimization.

The following conclusions are drawn from the experimental work and finite-element-based numerical modeling that have been performed in this research.

7.1.1 Conclusions from the developed multi-axis laser-assisted milling system

1. The accuracy of the control system developed to automate and synchronize the movements of the multi-axis laser delivery system with the CNC machining center was validated by comparing the encoders measurements of the electric actuators to CNC spindle movements, and the maximum error in synchronization was found to be approximately 200 microns, which is negligible compared to the size of the tool and the laser heating spot.
2. Compared to conventional dry milling, the implementation of laser for workpiece preheating locally reduced the strength of H13 tool steel, leading to a significant reduction of cutting forces by up to 40% for 1-axis LAML, and up to 34% and 38% for 3- and 5-axis LAML, respectively. In addition, this increased the stability of the milling process by consistently reducing the fluctuation of cutting forces in all cases. Furthermore, the significant reduction in cutting forces allowed the increase of the maximum permissible feedrate by up to 1,300 mm/min, which is a 30% increase in material removal rate, which proved LAML advantage specially for roughing milling operations.
3. The implementation of laser-assisted milling (LAML) further reduced the surface roughness of H13 tool steel by up to 20% for 1-axis LAML, and up to 19% and 16% for 3- and 5-axis

LAML, respectively. This reduction of surface roughness was the result of the thermal softening of the material by laser heating, which facilitated material removal and thus surface tearing was reduced. In addition, laser heating resulted in the reduction of the feed marks sharpness on the machined surfaces.

4. Compared to conventional dry milling, the use of flood coolant reduced the cutting forces by a maximum of 18% and reduced the surface roughness by a maximum of 11%. However, this decrease in cutting forces was not enough to allow for an increase in MRR and led to the breakage of the endmill for feedrates above 1000 mm/min. This proved the significant advantage of LAML over conventional milling with flood coolant, as LAML had better results without the use of environmentally unfriendly coolants.
5. Undesirable tensile stresses were induced by LAML at the top surface of the H13 workpiece and deeper into the subsurface layer. These tensile stresses were induced as a result of the thermal loading produced by the laser heating and cutting. The mechanical loading of milling was able to induce counteracting compressive residual stresses beneath the surface but only to a shallow depth of 0.25 mm. Below this depth, undesirable tensile residual tensile stresses were found up to depths of 0.6 to 0.8 mm.
6. As clear from the conclusions above, LAML is significantly advantageous in reducing cutting forces, increasing MRR, and reducing surface roughness. However, LAML induces undesirable tensile stresses on the surface and deeper into the workpiece, which must be taken into consideration especially for applications with fatigue loadings. Therefore, for these applications, it is recommended to use LAML mainly for roughing milling operations, then a subsequent optimized finishing milling operation, without laser, could be performed to intentionally induce compressive stresses. Alternatively, a post-process, such as shot peening, burnishing, or laser-assisted burnishing (LAB) or laser-assisted peeing (LAP) could be used for that purpose as well. The advantage of LAB or LAP post-processing operations is to use the same laser head assembly and setup.

7.1.2 Conclusions from the investigation of microstructure transformations in LSHT

7. Experimental investigations of microstructure transformations in laser surface heat treatment of H13 tool steel were performed with various laser power levels from 800W to 1200W, and

laser heating times varying between 100 ms to 800 ms, to obtain hardened outer surface layers of depths between 0.5 mm to 1.6 mm. In this process, the heat introduced by laser was rapidly dissipated through the bulk material with rapid cooling rates (approximately 600º C/s) resulting in a localized hardened outer surface layer without changing the bulk material properties and microstructure.

8. Investigation of the resulting microstructure indicated the formation of only martensite near the top workpiece surface, then a transition zone was indicated where the volume fraction of martensite kept decreasing as the depth increased until the bulk material is reached, which was a mix of ferrite and pearlite. The depth of the heat affected zone (HAZ) increased by increasing laser power and/or increasing heating time.
9. A three-dimensional finite-element-based model was developed to simulate the laser surface heat treatment process of H13 tool steel using Deform-3D. The model used 10 concentric ring-shaped heat exchange windows, with local equivalent convective coefficients of heat transfer to approximate the Gaussian distribution of the laser power density. The model temperature predictions showed an excellent agreement with the experimental results with a maximum error of $\pm$ 7 %.
10. A microstructure evolution model was integrated into the three-dimensional finite element model, by which the phase volume fractions were calculated at each time step based on the temperature level. The simplified Avrami and Magee models were used for austenite and martensite volume fractions calculations, respectively. The model was able to predict the HAZ depths within $\pm$ 10 % of the experimental results. This acceptable error in prediction could be mainly attributed to the simplifications made to the kinetics models used.

7.1.3 Conclusions from the Finite-Element-Based Modeling of LSH and LAML

11. Three-dimensional thermo-mechanically coupled finite-element-based models were developed, using Deform-3D framework, to simulate laser surface heating and laser-assisted milling of flat and 3D surfaces of H13 tool steel. A Matlab code was developed to generate the laser power density curves for laser beams inclined to a flat workpiece surface. Results showed that the inclination angle had a significant effect on the shape of the heating spot and on the laser power density distribution. With the implementation of this code into the FE model, the model predictions were found to be in good agreement with the experimental

results, with maximum error of ± 10 % for temperature predictions and ± 12 % for cutting forces predictions. Furthermore, it was concluded that for rough machining of typical flat and curved ribs and die cast inserts made of H13 tool steel, the effect of surface curvature inside the laser heating spot has a negligible effect on the surface temperature.

12. As evident from the conclusions of sections 7.1.2 and 7.1.3, the finite-element-based modeling of LSHT and LAML proved to be a reliable and powerful predictive capability for the development, design and optimization of laser-assisted manufacturing processes.

7.2 Recommendations for Future Research Work

The following recommendations are suggested to be pursued for future research work:

1. Development of a CAD-CAM translator with direct data exchange to fully automate the conversion of workpiece geometry and cutting tool paths into laser tool paths. In addition, the software should be capable of validating the proper timing of laser turning on and off to avoid safety hazards associated with using such high-power lasers. Furthermore, the laser reflections occurring when milling materials with low absorptivity should be considered in the software, as well to avoid damaging other equipment of the machining center.
2. Development of in-process monitoring capabilities and adaptive control system to ensure the optimal operating conditions when machining complex parts. For example, an IR or embedded temperature sensors could be integrated with the multi-axis LAML system to measure the surface temperature in real-time. This could allow a real-time control over the laser source power to control the surface temperature.
3. A concept for fast multiscale modeling capabilities should be developed and implemented to predict subsurface damages and surface integrity, with the purpose of eliminating expensive and time consuming post-inspections. The real-time solution of the inverse heat conduction problem (IHCP) which was developed in [235] and based on generalized thermal transfer function approach [236] could be extended for a moving heat source on complex part geometry.
4. Experimental investigation of a hybrid milling process that combines laser-assisted milling (for preheating the workpiece) with the use of cryogenic cutting fluid to cool the tool. By making the

workpiece softer and the tool cooler, lower cutting forces, higher cutting speeds, and improved tool life could be achieved.

5. Further experimental work is recommended to investigate the effects of laser power, cutting tool materials, cutting tool coatings, and workpiece material on the cutting tool life for laser-assisted milling.
6. Optimizing the size of the multi-axis LAML system developed in this work in order to minimize the reduction of the workspace of the machining center retrofitted with this system. This could be achieved by: (a) utilizing a more compact laser focusing head, (b) making use of standard optics modules to incline the laser beam instead of inclining the focusing head itself, and hence reducing the lateral size of the system, and (c) using a more flexible laser optical fiber with a smaller bending radius.

References

[1] S. Lei and F. Pfefferkorn, "A review on thermally assisted machining," in *ASME 2007 International Manufacturing Science and Engineering Conference*, 2007: American Society of Mechanical Engineers, pp. 325-336.

[2] S. Sun, M. Brandt, and M. S. Dargusch, "Thermally enhanced machining of hard-to-machine materials—A review," *International Journal of Machine Tools and Manufacture,* vol. 50, no. 8, pp. 663-680, 2010, doi: 10.1016/j.ijmachtools.2010.04.008.

[3] K.-S. Kim, J.-H. Kim, J.-Y. Choi, and C.-M. Lee, "A review on research and development of laser assisted turning," *International Journal of Precision Engineering and Manufacturing,* vol. 12, no. 4, pp. 753-759, 2011.

[4] G. Venkatesh and D. Chakradhar, "Influence of thermally assisted machining parameters on the machinability of Inconel 718 superalloy," *Silicon,* vol. 9, no. 6, pp. 867-877, 2017.

[5] C. Brecher, C.-J. Rosen, and M. Emonts, "Laser-assisted milling of advanced materials," *Physics Procedia,* vol. 5, pp. 259-272, 2010, doi: 10.1016/j.phpro.2010.08.052.

[6] "German national Project innonet IN-3544, KeraForm – Ceramic inserts for Deep Drawing Tools," 09 2003 – 05 2006.

[7] D. Umbrello, S. Rizzuti, J. Outeiro, R. Shivpuri, and R. M'Saoubi, "Hardness-based flow stress for numerical simulation of hard machining AISI H13 tool steel," *Journal of Materials Processing Technology,* vol. 199, no. 1-3, pp. 64-73, 2008.

[8] P. Parishram, *Laser assisted repair welding of H13 tool steel for die casting*. University of Arkansas, 2007.

[9] C. Tekmen, M. Toparli, I. Ozdemir, I. Kusoglu, and K. Onel, "High temperature behaviour of H13 steel," *Zeitschrift fur Metallkunde,* vol. 96, no. 12, p. 1431, 2005.

[10] J. Outeiro, "Surface integrity predictions and optimisation of machining conditions in the turning of AISI H13 tool steel," *International Journal of Machining and Machinability of Materials 7,* vol. 15, no. 1-2, pp. 122-134, 2014.

[11] P. Dumitrescu, P. Koshy, J. Stenekes, and M. Elbestawi, "High-power diode laser assisted hard turning of AISI D2 tool steel," *International Journal of Machine Tools and Manufacture,* vol. 46, no. 15, pp. 2009-2016, 2006.

[12] B. Shi, "Hybrid LAM Cryogenic Machining," Internal Report AMTC-MR-1-2015, Aerospace Manufacturing Technologies Centre (AMTC) - National Research Council Canada (NRC), 2015.

[13] C. R. Dandekar, Y. C. Shin, and J. Barnes, "Machinability improvement of titanium alloy (Ti–6Al–4V) via LAM and hybrid machining," *International Journal of Machine Tools and Manufacture,* vol. 50, no. 2, pp. 174-182, 2010, doi: 10.1016/j.ijmachtools.2009.10.013.

[14] W. Konig and A. Zaboklicki, "Laser-assisted hot machining of ceramics and composite materials," *NIST Spec. Publ., 847 pp.,* vol. 455, 1993.

[15] S.-H. Moon and C.-M. Lee, "A study on the machining characteristics using plasma assisted machining of AISI 1045 steel and Inconel 718," *International Journal of Mechanical Sciences,* vol. 142, pp. 595-602, 2018.

[16] Y. Jeon, H. W. Park, and C. M. Lee, "Current research trends in external energy assisted machining," *International Journal of Precision Engineering and Manufacturing,* vol. 14, no. 2, pp. 337-342, 2013.

[17] L. L. De Lacalle, J. Sanchez, A. Lamikiz, and A. Celaya, "Plasma assisted milling of heat-resistant superalloys," *Journal of manufacturing science and engineering,* vol. 126, no. 2, pp. 274-285, 2004.

[18] Y. Jeon and C. M. Lee, "Current research trend on laser assisted machining," *International journal of precision engineering and manufacturing,* vol. 13, no. 2, pp. 311-317, 2012.

[19] O. Shams, A. Pramanik, and T. Chandratilleke, "Thermal-assisted machining of titanium alloys," in *Advanced manufacturing technologies*: Springer, 2017, pp. 49-76.

[20] J.-H. Kim, E.-J. Kim, and C.-M. Lee, "A study on the heat affected zone and machining characteristics of difficult-to-cut materials in laser and induction assisted machining," *Journal of Manufacturing Processes,* vol. 57, pp. 499-508, 2020.

[21] E. J. Kim and C. M. Lee, "A Study on the optimal machining parameters of the induction assisted milling with Inconel 718," *Materials,* vol. 12, no. 2, p. 233, 2019.

[22] E.-J. Kim and C.-M. Lee, "Experimental study on power consumption of laser and induction assisted machining with inconel 718," *Journal of Manufacturing Processes,* vol. 59, pp. 411-420, 2020.

[23] M. Baili, V. Wagner, G. Dessein, J. Sallaberry, and D. Lallement, "An experimental investigation of hot machining with induction to improve Ti-5553 machinability," in *Applied mechanics and Materials*, 2011, vol. 62: Trans Tech Publ, pp. 67-76.

[24] J.-H. Ha and C.-M. Lee, "A Study on the Thermal Effect by Multi Heat Sources and Machining Characteristics of Laser and Induction Assisted Milling," *Materials,* vol. 12, no. 7, p. 1032, 2019.

[25] M. S. Dargusch, T. Sivarupan, M. Bermingham, R. A. R. Rashid, S. Palanisamy, and S. Sun, "Challenges in laser-assisted milling of titanium alloys," *International Journal of Extreme Manufacturing,* vol. 3, no. 1, p. 015001, 2020.

[26] D. Xu, Z. Liao, D. Axinte, J. A. Sarasua, R. M'Saoubi, and A. Wretland, "Investigation of surface integrity in laser-assisted machining of nickel based superalloy," *Materials & Design,* vol. 194, p. 108851, 2020.

[27] E. Abboud, *Characterization of Machining-Induced Residual Stresses in Titanium-Based Alloys*. McGill University (Canada), 2015.

[28] M. Khajehzadeh and M. R. Razfar, "Process parameters influence on laser-assisted machining-induced residual stresses," *Materials and Manufacturing Processes,* vol. 35, no. 15, pp. 1680-1689, 2020.

[29] A. Vali, J. Longuemard, G. Marot, and J. Litwin, "Residual stress conditions in laser-assisted machining," *Welding international,* vol. 13, no. 4, pp. 296-299, 1999.

[30] G. Germain, J.-L. Lebrun, T. Braham-Bouchnak, D. Bellett, and S. Auger, "Laser-assisted machining of Inconel 718 with carbide and ceramic inserts," *International journal of material forming,* vol. 1, no. 1, pp. 523-526, 2008.

[31] S. M. Langan, D. Ravindra, and A. B. Mann, "Mitigation of damage during surface finishing of sapphire using laser-assisted machining," *Precision Engineering,* vol. 56, pp. 1-7, 2019.

[32] Y. Feng *et al.*, "Residual stress prediction in laser-assisted milling considering recrystallization effects," *The International Journal of Advanced Manufacturing Technology,* vol. 102, no. 1, pp. 393-402, 2019.

[33] M. Balbaa and M. N. Nasr, "Prediction of residual stresses after laser-assisted machining of Inconel 718 using SPH," *Procedia CIRP,* vol. 31, pp. 19-23, 2015.

[34] H. Ding and Y. C. Shin, "Laser-assisted machining of hardened steel parts with surface integrity analysis," *International Journal of Machine tools and manufacture,* vol. 50, no. 1, pp. 106-114, 2010.

[35] G. Germain, F. Morel, J. L. Lebrun, A. Morel, and B. Huneau, "Effect of laser assistance machining on residual stress and fatigue strength for a bearing steel (100Cr6) and a titanium alloy (Ti 6Al 4V)," in *Materials Science Forum*, 2006, vol. 524: Trans Tech Publ, pp. 569-574.

[36] G. Germain, F. Morel, J.-L. Lebrun, and A. Morel, "Machinability and Surface Integrity for a Bearing Steel and a Titanium Alloy in Laser Assisted Machining," *Lasers in Engineering (Old City Publishing),* vol. 17, 2007.

[37] G. Germain, P. Dal Santo, and J.-L. Lebrun, "Comprehension of chip formation in laser assisted machining," *International Journal of Machine tools and manufacture,* vol. 51, no. 3, pp. 230-238, 2011.

[38] B. Shi and H. Attia, "Integrated process of laser-assisted machining and laser surface heat treatment," *Journal of Manufacturing science and engineering,* vol. 135, no. 6, 2013.

[39] C. E. Leshock, J.-N. Kim, and Y. C. Shin, "Plasma enhanced machining of Inconel 718: modeling of workpiece temperature with plasma heating and experimental results," *International Journal of Machine Tools and Manufacture,* vol. 41, no. 6, pp. 877-897, 2001.

[40] H. Attia, S. Tavakoli, R. Vargas, and V. Thomson, "Laser-assisted high-speed finish turning of superalloy Inconel 718 under dry conditions," *CIRP Annals,* vol. 59, no. 1, pp. 83-88, 2010, doi: 10.1016/j.cirp.2010.03.093.

[41] Z. Pan *et al.*, "Heat affected zone in the laser-assisted milling of Inconel 718," *Journal of Manufacturing Processes,* vol. 30, pp. 141-147, 2017.

[42] J. Yang, S. Sun, M. Brandt, and W. Yan, "Experimental investigation and 3D finite element prediction of the heat affected zone during laser assisted machining of Ti6Al4V alloy," *Journal of Materials Processing Technology,* vol. 210, no. 15, pp. 2215-2222, 2010, doi: 10.1016/j.jmatprotec.2010.08.007.

[43] J. H. N. Yang, M. Brandt, and S. J. Sun, "Numerical and experimental investigation of the heat-affected zone in a laser-assisted machining of Ti-6Al-4V alloy process," in *Materials Science Forum*, 2009, vol. 618: Trans Tech Publ, pp. 143-146.

[44] K. Venkatesan, R. Ramanujam, and P. Kuppan, "Parametric modeling and optimization of laser scanning parameters during laser assisted machining of Inconel 718," *Optics & Laser Technology,* vol. 78, pp. 10-18, 2016.

[45] T. Chwalczuk, D. Przestacki, P. Szablewski, and A. Felusiak, "Microstructure characterisation of Inconel 718 after laser assisted turning," in *MATEC Web of Conferences*, 2018, vol. 188: EDP Sciences, p. 02004.

[46] J.-T. Baek, W.-S. Woo, and C.-M. Lee, "A study on the machining characteristics of induction and laser-induction assisted machining of AISI 1045 steel and Inconel 718," *Journal of Manufacturing Processes,* vol. 34, pp. 513-522, 2018.

[47] F. A. Khatir, M. H. Sadeghi, and S. Akar, "Investigation of surface integrity in the laser-assisted turning of AISI 4340 hardened steel," *Journal of Manufacturing Processes,* vol. 61, pp. 173-189, 2021.

[48] S. Akcan, W. S. Shah, S. Moylan, S. Chandrasekar, P. Chhabra, and H. Yang, "Formation of white layers in steels by machining and their characteristics," *Metallurgical and Materials Transactions A,* vol. 33, no. 4, pp. 1245-1254, 2002.

[49] C. Herbert, D. Axinte, M. Hardy, and P. Withers, "Influence of surface anomalies following hole making operations on the fatigue performance for a nickel-based superalloy," *Journal of Manufacturing Science and Engineering,* vol. 136, no. 5, 2014.

[50] M. Brown *et al.*, "Non-destructive detection of machining-induced white layers in ferromagnetic alloys," *Procedia CIRP,* vol. 87, pp. 420-425, 2020.

[51] Y. K. Chou and C. J. Evans, "White layers and thermal modeling of hard turned surfaces," *International Journal of Machine Tools and Manufacture,* vol. 39, no. 12, pp. 1863-1881, 1999.

[52] H. Soyama, C. R. Chighizola, and M. R. Hill, "Effect of compressive residual stress introduced by cavitation peening and shot peening on the improvement of fatigue strength of stainless steel," *Journal of Materials Processing Technology,* vol. 288, p. 116877, 2021.

[53] L. Tan, D. Zhang, C. Yao, D. Wu, and J. Zhang, "Evolution and empirical modeling of compressive residual stress profile after milling, polishing and shot peening for TC17 alloy," *Journal of Manufacturing Processes,* vol. 26, pp. 155-165, 2017.

[54] Q. Lin, H. Liu, C. Zhu, D. Chen, and S. Zhou, "Effects of different shot peening parameters on residual stress, surface roughness and cell size," *Surface and Coatings Technology,* vol. 398, p. 126054, 2020.

[55] M. Chen *et al.*, "Evaluation of the residual stress and microstructure character in SAF 2507 duplex stainless steel after multiple shot peening process," *Surface and Coatings Technology,* vol. 344, pp. 132-140, 2018.

[56] J. Champaigne, "Shot peening overview," *Metal Improvement Company,* 2001.

[57] S. Tekeli, "Enhancement of fatigue strength of SAE 9245 steel by shot peening," *Materials letters,* vol. 57, no. 3, pp. 604-608, 2002.

[58] R. Kubler, S. Berveiller, D. Bouscaud, R. Guiheux, E. Patoor, and Q. Puydt, "Shot peening of TRIP780 steel: Experimental analysis and numerical simulation," *Journal of Materials Processing Technology,* vol. 270, pp. 182-194, 2019.

[59] R. Bejjani, B. Shi, H. Attia, and M. Balazinski, "Laser assisted turning of Titanium Metal Matrix Composite," *CIRP Annals,* vol. 60, no. 1, pp. 61-64, 2011, doi: 10.1016/j.cirp.2011.03.086.

[60] G. Germain, P. Robert, J.-L. Lebrun, P. Dal Santo, and A. Poitou, "Experimental and numerical approaches of Laser assisted turning," 2005.

[61] E. Kaselouris *et al.*, "SIMULATIONS OF LASER ASSISTED MACHINING AND CONVENTIONAL CUTTING OF AISI H-13 STEEL."

[62] E. Kaselouris, A. Baroutsos, T. Papadoulis, N. A. Papadogiannis, M. Tatarakis, and V. Dimitriou, "A Study on the Influence of Laser Parameters on Laser-Assisted Machining of Aisi H-13 Steel," in *Key Engineering Materials*, 2020, vol. 827: Trans Tech Publ, pp. 92-97.

[63] P. Dumitrescu, "High-Power Diode Laser Assisted Hard Turning of AISI D2 Tool Steel," Master of Applied Science, McMaster University, 2004.

[64] K. P. Maity and P. K. Swain, "An experimental investigation of hot-machining to predict tool life," *Journal of Materials Processing Technology,* vol. 198, no. 1-3, pp. 344-349, 2008, doi: 10.1016/j.jmatprotec.2007.07.018.

[65] L. Özler, A. Inan, and C. Özel, "Theoretical and experimental determination of tool life in hot machining of austenitic manganese steel," *International Journal of Machine Tools and Manufacture,* vol. 41, no. 2, pp. 163-172, 2001.

[66] M. A. Lajis, A. Amin, A. Karim, C. Daud, M. Radzi, and T. L. Ginta, "Hot machining of hardened steels with coated carbide inserts," *American Journal of Engineering and Applied Sceices,* vol. 2, no. 2, pp. 421-427, 2009.

[67] J. Novak, Y. Shin, and F. Incropera, "Assessment of plasma enhanced machining for improved machinability of Inconel 718," *Journal of manufacturing science and engineering,* vol. 119, no. 1, pp. 125-129, 1997.

[68] A. Ibrahim, B. Shi, H. Attia, and V. Thomson, "Numerical and Experimental Investigation of Microstructure Transformations in Laser Surface Heat Treatment of AISI H13 Steel," presented at the Canadian Aeronautics and Space Institute - AERO 2019, 2019/5.

[69] K. Venkatesan, R. Ramanujam, and P. Kuppan, "Laser assisted machining of difficult to cut materials: research opportunities and future directions-a comprehensive review," *Procedia Engineering,* vol. 97, pp. 1626-1636, 2014.

[70] MONFORTS. "RNC 400 Laser Turn, http://www.monforts-wzm.de/produkte/rnc/rnc-maschinenbeschreibung.html " (accessed 25 March, 2018).

[71] K. Hanson. (2015, August 1) Booster Beam. *Cutting Tool Engineering*. Available: https://www.ctemag.com/news/articles/booster-beam#

[72] R. R. Rashid, S. Sun, G. Wang, and M. Dargusch, "An investigation of cutting forces and cutting temperatures during laser-assisted machining of the Ti–6Cr–5Mo–5V–4Al beta titanium alloy," *International Journal of Machine Tools and Manufacture,* vol. 63, pp. 58-69, 2012.

[73] R. R. Rashid, S. Sun, G. Wang, and M. Dargusch, "The effect of laser power on the machinability of the Ti-6Cr-5Mo-5V-4Al beta titanium alloy during laser assisted machining," *International Journal of machine tools and manufacture,* vol. 63, pp. 41-43, 2012.

[74] S. Sun, M. Brandt, and M. Dargusch, "The effect of a laser beam on chip formation during machining of Ti6Al4V alloy," *Metallurgical and Materials Transactions A,* vol. 41, no. 6, pp. 1573-1581, 2010.

[75] S. Sun, J. Harris, and M. Brandt, "Parametric investigation of laser-assisted machining of commercially pure titanium," *Advanced engineering materials,* vol. 10, no. 6, pp. 565-572, 2008.

[76] G. Hedberg, Y. Shin, and L. Xu, "Laser-assisted milling of Ti-6Al-4V with the consideration of surface integrity," *The International Journal of Advanced Manufacturing Technology,* vol. 79, no. 9, pp. 1645-1658, 2015.

[77] B. Shi, H. Attia, R. Vargas, and S. Tavakoli, "Numerical and experimental investigation of laser-assisted machining of Inconel 718," *Machining Science and Technology,* vol. 12, no. 4, pp. 498-513, 2008.

[78] S. Rajagopal, D. Plankenhorn, and V. Hill, "Machining aerospace alloys with the aid of a 15 kW laser," *Journal of Applied Metalworking,* vol. 2, no. 3, pp. 170-184, 1982.

[79] M. Anderson, R. Patwa, and Y. C. Shin, "Laser-assisted machining of Inconel 718 with an economic analysis," *International Journal of Machine Tools and Manufacture,* vol. 46, no. 14, pp. 1879-1891, 2006.

[80] H. Ding and Y. C. Shin, "Improvement of machinability of Waspaloy via laser-assisted machining," *The International Journal of Advanced Manufacturing Technology,* vol. 64, no. 1-4, pp. 475-486, 2013.

[81] S. Lei, Y. C. Shin, and F. P. Incropera, "Deformation mechanisms and constitutive modeling for silicon nitride undergoing laser-assisted machining," *International Journal of Machine tools and manufacture,* vol. 40, no. 15, pp. 2213-2233, 2000.

[82] J. C. Rozzi, F. E. Pfefferkorn, Y. C. Shin, and F. P. Incropera, "Experimental evaluation of the laser assisted machining of silicon nitride ceramics," *J. Manuf. Sci. Eng.,* vol. 122, no. 4, pp. 666-670, 2000.

[83] S. Lei, Y. C. Shin, and F. P. Incropera, "Experimental investigation of thermo-mechanical characteristics in laser-assisted machining of silicon nitride ceramics," *J. Manuf. Sci. Eng.,* vol. 123, no. 4, pp. 639-646, 2001.

[84] P. A. Rebro, Y. C. Shin, and F. P. Incropera, "Laser-assisted machining of reaction sintered mullite ceramics," *J. Manuf. Sci. Eng.,* vol. 124, no. 4, pp. 875-885, 2002.

[85] F. E. Pfefferkorn, Y. C. Shin, Y. Tian, and F. P. Incropera, "Laser-assisted machining of magnesia-partially-stabilized zirconia," *J. Manuf. Sci. Eng.,* vol. 126, no. 1, pp. 42-51, 2004.

[86] P. A. Rebro, Y. C. Shin, and F. P. Incropera, "Design of operating conditions for crackfree laser-assisted machining of mullite," *International Journal of Machine Tools and Manufacture,* vol. 44, no. 7-8, pp. 677-694, 2004.

[87] C.-W. Chang and C.-P. Kuo, "Evaluation of surface roughness in laser-assisted machining of aluminum oxide ceramics with Taguchi method," *International Journal of Machine Tools and Manufacture,* vol. 47, no. 1, pp. 141-147, 2007.

[88] J.-D. Kim, S.-J. Lee, and J. Suh, "Characteristics of laser assisted machining for silicon nitride ceramic according to machining parameters," *Journal of Mechanical Science and Technology,* vol. 25, no. 4, p. 995, 2011.

[89] P. A. Rebro, F. Pfefferkorn, Y. Shin, and F. Incropera, "Comparative assessment of laser-assisted machining for various ceramics," *Technical Papers - Society of Manufacturing Engieers,* 2002.

[90] Y. C. Shin, "Laser assisted machining: its potential and future," in *International Congress on Applications of Lasers & Electro-Optics*, 2010, vol. 2010, no. 1: Laser Institute of America, pp. 513-522.

[91] B. Yang, X. Shen, and S. Lei, "Mechanisms of edge chipping in laser-assisted milling of silicon nitride ceramics," *International Journal of Machine Tools and Manufacture,* vol. 49, no. 3-4, pp. 344-350, 2009.

[92] X. Dong and Y. C. Shin, "Multiscale finite element modeling of alumina ceramics undergoing laser-assisted machining," *Journal of Manufacturing Science and Engineering,* vol. 138, no. 1, 2016.

[93] J. C. Outeiro, "Residual Stresses in Machining, Chapter in Mechanics of Materials," in *Modern Manufacturing Methods and Processing Techniques*, V. V. Silberschmidt Ed.: Elsevier, 2020, pp. 297-360.

[94] S. Skvarenina and Y. Shin, "Laser-assisted machining of compacted graphite iron," *International Journal of Machine tools and manufacture,* vol. 46, no. 1, pp. 7-17, 2006.

[95] S. Masood, K. Armitage, and M. Brandt, "An experimental study of laser-assisted machining of hard-to-wear white cast iron," *International Journal of Machine tools and manufacture,* vol. 51, no. 6, pp. 450-456, 2011.

[96] W. B. Salem, G. Marot, A. Moisan, and J. Longuemard, "Laser assisted turning during finishing operation applied to hardened steels and Inconel 718," in *Laser Assisted Net Shape Engineering, Proceedings of the LANE*, 1994, vol. 94, pp. 455-464.

[97] M. Kumar, C.-J. Chang, S. N. Melkote, and V. Roshan Joseph, "Modeling and analysis of forces in laser assisted micro milling," *Journal of Manufacturing Science and Engineering,* vol. 135, no. 4, 2013.

[98] M. Anderson and Y. Shin, "Laser-assisted machining of P550 with an economic analysis," *Proc. Inst. Mech. Eng., Part B,* vol. 220, no. 12, pp. 2055-2067, 2006.

[99] Y. Wang, L. Yang, and N. Wang, "An investigation of laser-assisted machining of Al2O3 particle reinforced aluminum matrix composite," *Journal of materials processing technology,* vol. 129, no. 1-3, pp. 268-272, 2002.

[100] S. Barnes, R. Morgan, and A. Skeen, "Effect of laser pre-treatment on the machining performance of aluminum/SiC MMC," *J. Eng. Mater. Technol.,* vol. 125, no. 4, pp. 378-384, 2003.

[101] C. R. Dandekar and Y. C. Shin, "Experimental evaluation of laser-assisted machining of silicon carbide particle-reinforced aluminum matrix composites," *The International Journal of Advanced Manufacturing Technology,* vol. 66, no. 9-12, pp. 1603-1610, 2013.

[102] C. R. Dandekar and Y. C. Shin, "Multi-scale modeling to predict sub-surface damage applied to laser-assisted machining of a particulate reinforced metal matrix composite," *Journal of Materials Processing Technology,* vol. 213, no. 2, pp. 153-160, 2013.

[103] X. Kong, H. Zhang, L. Yang, G. Chi, and Y. Wang, "Carbide tool wear mechanisms in laser-assisted machining of metal matrix composites," *The International Journal of Advanced Manufacturing Technology,* vol. 85, no. 1, pp. 365-379, 2016.

[104] M.-S. Sim and C.-M. Lee, "A study on the laser preheating effect of inconel 718 specimen with rotated angle with respect to 2-axis," *International journal of precision engineering and manufacturing,* vol. 15, no. 1, pp. 189-192, 2014.

[105] R. R. Rashid, S. Sun, S. Palanisamy, G. Wang, and M. Dargusch, "A study on laser assisted machining of Ti10V2Fe3Al alloy with varying laser power," *The International Journal of Advanced Manufacturing Technology,* vol. 74, no. 1-4, pp. 219-224, 2014.

[106] B. Rao, C. R. Dandekar, and Y. C. Shin, "An experimental and numerical study on the face milling of Ti–6Al–4V alloy: tool performance and surface integrity," *Journal of Materials Processing Technology,* vol. 211, no. 2, pp. 294-304, 2011.

[107] S.-H. Ahn and C.-M. Lee, "A study on large-area laser processing analysis in consideration of the moving heat source," *International Journal of Precision Engineering and Manufacturing,* vol. 12, no. 2, pp. 285-292, 2011.

[108] R. Singh and S. N. Melkote, "Characterization of a hybrid laser-assisted mechanical micromachining (LAMM) process for a difficult-to-machine material," *International Journal of Machine Tools and Manufacture,* vol. 47, no. 7-8, pp. 1139-1150, 2007.

[109] C.-W. Chang and C.-P. Kuo, "An investigation of laser-assisted machining of Al2O3 ceramics planing," *International Journal of Machine Tools and Manufacture,* vol. 47, no. 3-4, pp. 452-461, 2007.

[110] Y. Tian and Y. C. Shin, "Laser-Assisted Machining of Damage-Free Silicon Nitride Parts with Complex Geometric Features via In-Process Control of Laser Power," *Journal of the American Ceramic Society,* vol. 89, no. 11, pp. 3397-3405, 2006.

[111] F. E. Pfefferkorn, F. P. Incropera, and Y. C. Shin, "Heat transfer model of semi-transparent ceramics undergoing laser-assisted machining," *International Journal of Heat and Mass Transfer,* vol. 48, no. 10, pp. 1999-2012, 2005.

[112] Y. C. Shin, B. Wu, S. Lei, G. J. Cheng, and Y. Lawrence Yao, "Overview of Laser Applications in Manufacturing and Materials Processing in Recent Years," *Journal of Manufacturing Science and Engineering,* vol. 142, no. 11, p. 110818, 2020.

[113] X. Wu, G. Feng, and X. Liu, "Design and implementation of a system for laser assisted milling of advanced materials," *Chinese journal of mechanical engineering,* vol. 29, no. 5, pp. 921-929, 2016.

[114] D.-H. Kim, W.-S. Woo, W.-S. Chu, S.-H. Ahn, and C.-M. Lee, "Development of Multi-Axis Laser-Assisted Milling Device," in *ASME 2017 12th International Manufacturing Science and Engineering Conference collocated with the JSME/ASME 2017 6th International Conference on Materials and Processing*, 2017: American Society of Mechanical Engineers, pp. V001T02A016-V001T02A016.

[115] R. Wiedenmann, S. Liebl, and M. F. Zaeh, "Influencing Factors and Workpiece's Microstructure in Laser-Assisted Milling of Titanium," *Physics Procedia,* vol. 39, pp. 265-276, 2012, doi: 10.1016/j.phpro.2012.10.038.

[116] Y. Feng *et al.*, "Inverse analysis of the cutting force in laser-assisted milling on Inconel 718," *The International Journal of Advanced Manufacturing Technology,* 2018, doi: 10.1007/s00170-018-1670-1.

[117] G. K. Hedberg and Y. C. Shin, "Laser assisted milling of Ti-6Al-4V ELI with the analysis of surface integrity and its economics," *Lasers in Manufacturing and Materials Processing,* vol. 2, no. 3, pp. 164-185, 2015.

[118] M. J. Bermingham, P. Schaffarzyk, S. Palanisamy, and M. S. Dargusch, "Laser-assisted milling strategies with different cutting tool paths," *The International Journal of Advanced Manufacturing Technology,* vol. 74, no. 9-12, pp. 1487-1494, 2014, doi: 10.1007/s00170-014-6093-z.

[119] R. Wiedenmann and M. F. Zaeh, "Laser-assisted milling—Process modeling and experimental validation," *CIRP Journal of Manufacturing Science and Technology,* vol. 8, pp. 70-77, 2015, doi: 10.1016/j.cirpj.2014.08.003.

[120] D.-H. Kim and C.-M. Lee, "A study of cutting force and preheating-temperature prediction for laser-assisted milling of Inconel 718 and AISI 1045 steel," *International Journal of Heat and Mass Transfer,* vol. 71, pp. 264-274, 2014.

[121] M. J. Bermingham, W. M. Sim, D. Kent, S. Gardiner, and M. S. Dargusch, "Tool life and wear mechanisms in laser assisted milling Ti–6Al–4V," *Wear,* vol. 322-323, pp. 151-163, 2015, doi: 10.1016/j.wear.2014.11.001.

[122] Y. Tian, B. Wu, M. Anderson, and Y. C. Shin, "Laser-assisted milling of silicon nitride ceramics and Inconel 718," *Journal of manufacturing science and engineering,* vol. 130, no. 3, 2008.

[123] Z. Pan *et al.*, "Force modeling of Inconel 718 laser-assisted end milling under recrystallization effects," *The International Journal of Advanced Manufacturing Technology,* vol. 92, no. 5, pp. 2965-2974, 2017.

[124] X. Shen and S. Lei, "Experimental study on operating temperature in laser-assisted milling of silicon nitride ceramics," *The International Journal of Advanced Manufacturing Technology,* vol. 52, no. 1-4, pp. 143-154, 2011.

[125] Y. Ito, T. Kizaki, R. Shinomoto, M. Ueki, N. Sugita, and M. Mitsuishi, "High-efficiency and precision cutting of glass by selective laser-assisted milling," *Precision Engineering,* vol. 47, pp. 498-507, 2017.

[126] Y. Jeon and F. Pfefferkorn, "Effect of laser preheating the workpiece on micro end milling of metals," *Journal of manufacturing science and engineering,* vol. 130, no. 1, 2008.

[127] J. A. Shelton and Y. C. Shin, "Experimental evaluation of laser-assisted micromilling in a slotting configuration," *Journal of manufacturing science and engineering,* vol. 132, no. 2, 2010.

[128] J. A. Shelton and Y. C. Shin, "Comparative evaluation of laser-assisted micro-milling for AISI 316, AISI 422, TI-6AL-4V and Inconel 718 in a side-cutting configuration," *Journal of Micromechanics and Microengineering,* vol. 20, no. 7, p. 075012, 2010.

[129] J. Shelton and Y. Shin, "Laser-assisted micro-milling of difficult-to-machine materials in a side cutting configuration," *J Micromech Microeng,* vol. 20, no. 7, p. 075012, 2010.

[130] S. Melkote, M. Kumar, F. Hashimoto, and G. Lahoti, "Laser assisted micro-milling of hard-to-machine materials," *CIRP annals,* vol. 58, no. 1, pp. 45-48, 2009.

[131] H. Ding, N. Shen, and Y. C. Shin, "Thermal and mechanical modeling analysis of laser-assisted micro-milling of difficult-to-machine alloys," *Journal of Materials Processing Technology,* vol. 212, no. 3, pp. 601-613, 2012.

[132] M. Kumar and S. N. Melkote, "Process capability study of laser assisted micro milling of a hard-to-machine material," *Journal of Manufacturing Processes,* vol. 14, no. 1, pp. 41-51, 2012.

[133] Y. Tian and Y. C. Shin, "Thermal modelling and experimental evaluation of laser-assisted dressing of superabrasive grinding wheels," *Proceedings of the Institution of Mechanical Engineers, Part B: Journal of Engineering Manufacture,* vol. 221, no. 4, pp. 605-616, 2007.

[134] Z. Li *et al.*, "Material removal mechanism of laser-assisted grinding of RB-SiC ceramics and process optimization," *Journal of the European Ceramic Society,* vol. 39, no. 4, pp. 705-717, 2019.

[135] J.-F. Wu and Y.-B. Guu, "Laser assisted machining method and device," ed: Google Patents, 2006.

[136] Y. C. Shin, "Laser assisted machining process with distributed lasers," ed: Google Patents, 2011.

[137] M. Anderson and Y. Shin, "Laser-assisted machining of an austenitic stainless steel: P550," *Proceedings of the Institution of Mechanical Engineers, Part B: Journal of Engineering Manufacture,* vol. 220, no. 12, pp. 2055-2067, 2006.

[138] Y. Wei, "Hybrid Machining using Direct Laser Assistance and Micro Texturing," Doctoral Thesis in Mechanical Engineering, University of Calgary, 2018. [Online]. Available: http://hdl.handle.net/1880/108048

[139] Y. Wei, C. Park, and S. S. Park, "Experimental evaluation of direct laser assisted turning through a sapphire tool," *Procedia Manufacturing,* vol. 10, pp. 546-556, 2017.

[140] S. Park, Y. Wei, and X. Jin, "Direct laser assisted machining with a sapphire tool for bulk metallic glass," *CIRP Annals,* vol. 67, no. 1, pp. 193-196, 2018.

[141] C. Park, Y. Wei, M. Hassani, X. Jin, J. Lee, and S. Park, "Low power direct laser-assisted machining of carbon fibre-reinforced polymer," *Manufacturing Letters,* vol. 22, pp. 19-24, 2019.

[142] C. Brecher, M. Emonts, C.-J. Rosen, and J.-P. Hermani, "Laser-assisted Milling of Advanced Materials," *Physics Procedia,* vol. 12, pp. 599-606, 2011, doi: 10.1016/j.phpro.2011.03.076.

[143] H. S. Carslaw and J. C. Jaeger, "Conduction of heat in solids," Clarendon Press, 1959.

[144] S.-J. Hwang, W.-J. Oh, and C.-M. Lee, "A study of preheating characteristics according to various preheating methods for laser-assisted machining," *The International Journal of Advanced Manufacturing Technology,* vol. 86, no. 9, pp. 3015-3024, 2016.

[145] Z. Shang, Z. Liao, J. A. Sarasua, J. Billingham, and D. Axinte, "On modelling of laser assisted machining: Forward and inverse problems for heat placement control," *International Journal of Machine Tools and Manufacture,* vol. 138, pp. 36-50, 2019.

[146] "2D Scanning Products." www.ipgphotonics.com (accessed August 2021.

[147] D. Kang and C. Lee, "A study on the development of the laser-assisted milling process and a related constitutive equation for silicon nitride," *CIRP Annals,* vol. 63, no. 1, pp. 109-112, 2014.

[148] D.-H. Kim and C.-M. Lee, "A study on the laser-assisted ball-end milling of difficult-to-cut materials using a new back-and-forth preheating method," *The International Journal of Advanced Manufacturing Technology,* vol. 85, no. 5, pp. 1825-1834, 2016.

[149] WitGrzesik, *Modelling and Simulation of Machining Processes and Operations, in Advanced Machining Processes of Metallic Materials*. Elsevier, 2008, pp. 49-67.

[150] A. J. Jutta Rohde, "Literature review of heat treatment simulations with respect to phase transformation, residual stresses and distortion," *SCANDINAVIAN JOURNAL OF METALLURGY,* vol. 29, pp. 47 - 62, 2000.

[151] E. Abboud, Shi, B., and Attia, H., "Modelling and Simulation of Microstructure Transformations in Laser-Assisted Machining," presented at the 1st International Conference on Virtual Machining Process Technology (CIRP sponsored), Montreal, Canada., 2012.

[152] *DEFORM Integrated 2D-3D Version 10 User's Manual*. Scientific Forming Technologies Corporation (SFTC), Columbus, Ohio, 2011.

[153] G. R. Johnson, "A constitutive model and data for materials subjected to large strains, high strain rates, and high temperatures," *Proc. 7th Inf. Sympo. Ballistics,* pp. 541-547, 1983.

[154] G. R. Johnson and W. H. Cook, "Fracture characteristics of three metals subjected to various strains, strain rates, temperatures and pressures," *Engineering fracture mechanics,* vol. 21, no. 1, pp. 31-48, 1985.

[155] F. J. Zerilli and R. W. Armstrong, "Dislocation-mechanics-based constitutive relations for material dynamics calculations," *Journal of applied physics,* vol. 61, no. 5, pp. 1816-1825, 1987.

[156] F. J. Zerilli, "Dislocation mechanics-based constitutive equations," *Metallurgical and Materials Transactions A,* vol. 35, no. 9, pp. 2547-2555, 2004.

[157] F. J. Zerilli and R. W. Armstrong, "Constitutive relations for the plastic deformation of metals," in *AIP conference proceedings*, 1994, vol. 309, no. 1: American Institute of Physics, pp. 989-992.

[158] P. L. B. Oxley and M. C. Shaw, "Mechanics of machining: an analytical approach to assessing machinability," 1990.

[159] A. Adibi-Sedeh, M. Vaziri, V. Pednekar, V. Madhavan, and R. Ivester, "Investigation of the effect of using different material models on finite element simulations of machining," in *Proceedings of the 8th CIRP International Workshop on Modeling of Machining Operations, Chemnitz*, 2005, pp. 215-224.

[160] J. Shi and C. R. Liu, "The influence of material models on finite element simulation of machining," *J. Manuf. Sci. Eng.,* vol. 126, no. 4, pp. 849-857, 2004.

[161] A. Moufki, A. Molinari, and D. Dudzinski, "Modelling of orthogonal cutting with a temperature dependent friction law," *Journal of the Mechanics and Physics of Solids,* vol. 46, no. 10, pp. 2103-2138, 1998.

[162] J. Xie, A. Bayoumi, and H. Zbib, "A study on shear banding in chip formation of orthogonal machining," *International Journal of Machine Tools and Manufacture,* vol. 36, no. 7, pp. 835-847, 1996.

[163] T. Vinh, M. Afzali, and A. Roche, "Fast fracture of some usual metals at combined high strain and high strain rate," in *Mechanical behaviour of materials*: Elsevier, 1980, pp. 633-642.

[164] K. Maekawa, T. Shirakashi, and E. Usui, "Flow stress of low carbon steel at high temperature and strain rate. ii: flow stress under variable temperature and variable strain rate," *Bulletin of the Japan Society of Precision Engineering,* vol. 17, no. 3, pp. 167-172, 1983.

[165] B. Shi and M. Attia, "Evaluation criteria of the constitutive law formulation for the metal-cutting process," *Proceedings of the Institution of Mechanical Engineers, Part B: Journal of Engineering Manufacture,* vol. 224, no. 9, pp. 1313-1328, 2010.

[166] Abaqus, *Analysis Manual* Vélizy-Villacoublay, France: Dassault Systèmes.

[167] S. Akram, S. H. I. Jaffery, M. Khan, M. Fahad, A. Mubashar, and L. Ali, "Numerical and experimental investigation of Johnson–Cook material models for aluminum (Al 6061-T6) alloy using orthogonal machining approach," *Advances in Mechanical Engineering,* vol. 10, no. 9, p. 1687814018797794, 2018.

[168] Y. Zhang, J. Outeiro, and T. Mabrouki, "On the selection of Johnson-Cook constitutive model parameters for Ti-6Al-4 V using three types of numerical models of orthogonal cutting," *Procedia Cirp,* vol. 31, pp. 112-117, 2015.

[169] D. Umbrello, R. M'saoubi, and J. Outeiro, "The influence of Johnson–Cook material constants on finite element simulation of machining of AISI 316L steel," *International Journal of Machine Tools and Manufacture,* vol. 47, no. 3-4, pp. 462-470, 2007.

[170] A. Shrot and M. Bäker, "Determination of Johnson–Cook parameters from machining simulations," *Computational Materials Science,* vol. 52, no. 1, pp. 298-304, 2012.

[171] Y. Guo, "An integral method to determine the mechanical behavior of materials in metal cutting," *Journal of materials processing technology,* vol. 142, no. 1, pp. 72-81, 2003.

[172] P. Sartkulvanich, F. Koppka, and T. Altan, "Determination of flow stress for metal cutting simulation—a progress report," *Journal of Materials Processing Technology,* vol. 146, no. 1, pp. 61-71, 2004.

[173] E.-G. Ng and D. K. Aspinwall, "Modelling of hard part machining," *Journal of materials processing technology,* vol. 127, no. 2, pp. 222-229, 2002.

[174] M. Shatla, C. Kerk, and T. Altan, "Process modeling in machining. Part I: determination of flow stress data," *International Journal of Machine Tools and Manufacture,* vol. 41, no. 10, pp. 1511-1534, 2001.

[175] M. Shatla, C. Kerk, and T. Altan, "Process modeling in machining. Part II: validation and applications of the determined flow stress data," *International Journal of Machine Tools and Manufacture,* vol. 41, no. 11, pp. 1659-1680, 2001.

[176] B. Shi, H. Attia, and T. Wang, "Simulation of the machining process, considering the thermal constriction resistance of multi-layer coated tools," in *8th CIRP International Workshop on Modeling of Machining Operations, Chemnitz, Germany*, 2005.

[177] J. Outeiro, D. Umbrello, and R. M'saoubi, "Experimental and numerical modelling of the residual stresses induced in orthogonal cutting of AISI 316L steel," *International Journal of Machine Tools and Manufacture,* vol. 46, no. 14, pp. 1786-1794, 2006.

[178] M. N. Nasr, E.-G. Ng, and M. Elbestawi, "Effects of strain hardening and initial yield strength on machining-induced residual stresses," 2007.

[179] M. Attia and L. Kops, "A new approach to cutting temperature prediction considering the thermal constriction phenomenon in multi-layer coated tools," *CIRP Annals,* vol. 53, no. 1, pp. 47-52, 2004.

[180] J. T. Carroll III and J. S. Strenkowski, "Finite element models of orthogonal cutting with application to single point diamond turning," *International Journal of Mechanical Sciences,* vol. 30, no. 12, pp. 899-920, 1988.

[181] P. Sartkulvanich, T. Altan, and A. Göcmen, "Effects of flow stress and friction models in finite element simulation of orthogonal cutting—a sensitivity analysis," *Machine Science and Technology,* vol. 9, no. 1, pp. 1-26, 2005.

[182] N. Zorev, "Inter-relationship between shear processes occurring along tool face and shear plane in metal cutting," *International research in production engineering,* vol. 49, pp. 143-152, 1963.

[183] S. N. Melkote *et al.*, "Advances in material and friction data for modelling of metal machining," *Cirp Annals,* vol. 66, no. 2, pp. 731-754, 2017.

[184] E. Hawbolt, B. Chau, and J. Brimacombe, "Kinetics of austenite-ferrite and austenite-pearlite transformations in a 1025 carbon steel," *Metallurgical Transactions A,* vol. 16, no. 4, pp. 565-578, 1985.

[185] M. Pernach, K. Bzowski, R. Kuziak, and M. Pietrzyk, "Experimental validation of the carbon diffusion model for transformation of ferritic-pearlitic microstructure into austenite during continuous annealing of dual phase steels," in *Materials Science Forum*, 2013, vol. 762: Trans Tech Publ, pp. 699-704.

[186] M. V. Allmen and A. Blatter, *Laser-beam interactions with materials: physical principles and applications*. Springer Science & Business Media, 2013.

[187] A. Bejan and A. D. Kraus, *Heat transfer handbook*. John Wiley & Sons, 2003.

[188] F. P. Incropera, D. P. DeWitt, T. L. Bergman, and A. S. Lavine, *Fundamentals of heat and mass transfer*. Wiley New York, 1996.

[189] R. Singh, M. J. Alberts, and S. N. Melkote, "Characterization and prediction of the heat-affected zone in a laser-assisted mechanical micromachining process," *International Journal of Machine Tools and Manufacture,* vol. 48, no. 9, pp. 994-1004, 2008.

[190] M. Kubiak, W. Piekarska, and S. Stano, "Modelling of laser beam heat source based on experimental research of Yb: YAG laser power distribution," *International Journal of Heat and Mass Transfer,* vol. 83, pp. 679-689, 2015.

[191] R. Li, Y. Jin, Z. Li, and K. Qi, "A comparative study of high-power diode laser and CO 2 laser surface hardening of AISI 1045 steel," *Journal of Materials Engineering and Performance,* vol. 23, no. 9, pp. 3085-3091, 2014.

[192] W. Ayoola, W. Suder, and S. Williams, "Effect of beam shape and spatial energy distribution on weld bead geometry in conduction welding," *Optics & Laser Technology,* vol. 117, pp. 280-287, 2019.

[193] "SIMOTICS T-1FW6 built-in torque motors - Configuration Manual." Siemens. https://cache.industry.siemens.com/dl/files/518/109764518/att_1020328/v1/1FW6_High_Speed_config_man_0120_en-US.pdf (accessed April, 2021).

[194] "Slewingrings."Schaeffler. https://www.schaeffler.com/remotemedien/media/_shared_media/08_media_library/01_publications/schaeffler_2/catalogue_1/downloads_6/404_de_en_1.pdf (accessed April, 2021).

[195] "RESOLUTE™ encoder series." Renishaw. https://www.renishaw.com/en/resolute-encoder-series--37823 (accessed April, 2021).

[196] Makino. "Makino's A88e Maintenance Manual." www.makino.com (accessed April, 2021).

[197] *ASTM E837-20 - Standard test method for determining residual stresses by the hole-drilling strain-gage method*, A. S. f. T. a. Materials, West Conshohocken, PA, USA, 2020. [Online]. Available: http://www.astm.org/cgi-bin/resolver.cgi?E837

[198] H. Chandrasekaran *et al.*, "Development of machinability enhanced tool steels for improved product economy in hard milling," *EUR,* no. 21726, pp. A-233, 2005.

[199] Y. Guo, W. Li, and I. Jawahir, "Surface integrity characterization and prediction in machining of hardened and difficult-to-machine alloys: a state-of-art research review and analysis," *Machining Science and Technology,* vol. 13, no. 4, pp. 437-470, 2009.

[200] S. Zhang, T. Ding, and J. Li, "Determination of surface and in-depth residual stress distributions induced by hard milling of H13 steel," *Production Engineering,* vol. 6, no. 4-5, pp. 375-383, 2012.

[201] "PowerMonitorPM." https://www.primes.de/en/products/laser-power/continuous-radiation/powermonitor-pm.html (accessed June 20 2021).

[202] "FocusMonitorFM+." https://www.primes.de/en/products/beam-distribution/focus-measurement/focusmonitor-fmplus.html (accessed June 2021.

[203] R. Wiedenmann, *Prozessmodell und Systemtechnik für das laserunterstützte Fräsen*. Herbert Utz Verlag, 2014.

[204] F. Klocke, M. Zeis, A. Klink, and D. Veselovac, "Technological and economical comparison of roughing strategies via milling, EDM and ECM for titanium-and nickel-based blisks," *Procedia Cirp,* vol. 2, pp. 98-101, 2012.

[205] S. Tavakoli, H. Attia, R. Vargas, and V. Thomson, "Laser assisted finish turning of Inconel 718: process optimization," in *International Manufacturing Science and Engineering Conference*, 2009, vol. 43611, pp. 833-840.

[206] M. Todinov, "Mechanism for formation of the residual stresses from quenching," *Modelling and Simulation in Materials Science and Engineering,* vol. 6, no. 3, p. 273, 1998.

[207] M. Todinov, "A probabilistic method for predicting fatigue life controlled by defects," *Materials Science and Engineering: A,* vol. 255, no. 1-2, pp. 117-123, 1998.

[208] A. Nedoseka, *Fundamentals of evaluation and diagnostics of welded structures*. Elsevier, 2012.

[209] B. Shi, "Laser Surface Burnishing," Aerospace Manufacturing Technologies Centre - National Research Council of Canada, Montreal, Quebec, Canada, 2017.

[210] Y. Tian and Y. C. Shin, "Laser-assisted burnishing of metals," *International Journal of Machine Tools and Manufacture,* vol. 47, no. 1, pp. 14-22, 2007.

[211] K. Zhan, C. Jiang, and V. Ji, "Uniformity of residual stress distribution on the surface of S30432 austenitic stainless steel by different shot peening processes," *Materials Letters,* vol. 99, pp. 61-64, 2013.

[212] K. J. Marsh, "Shot peening: techniques and applications," *Engineering Materials Advisory Service Ltd.(United Kingdom), 1993,* p. 320, 1993.

[213] J. D. Almer, J. Cohen, and R. Winholtz, "The effects of residual macrostresses and microstresses on fatigue crack propagation," *Metallurgical and Materials Transactions A,* vol. 29, no. 8, pp. 2127-2136, 1998.

[214] G. Farrahi, J. Lebrijn, and D. Couratin, "Effect of shot peening on residual stress and fatigue life of a spring steel," *Fatigue & Fracture of Engineering Materials & Structures,* vol. 18, no. 2, pp. 211-220, 1995.

[215] G. Webster and A. Ezeilo, "Residual stress distributions and their influence on fatigue lifetimes," *International Journal of Fatigue,* vol. 23, pp. 375-383, 2001.

[216] P. Zhang and J. Lindemann, "Influence of shot peening on high cycle fatigue properties of the high-strength wrought magnesium alloy AZ80," *Scripta materialia,* vol. 52, no. 6, pp. 485-490, 2005.

[217] Y. Harada and K. Mori, "Effect of processing temperature on warm shot peening of spring steel," *Journal of materials processing technology,* vol. 162, pp. 498-503, 2005.

[218] R. Murthy and B. Kotiveerachari, "Burnishing of metallic surfaces—a review," *Precision engineering,* vol. 3, no. 3, pp. 172-179, 1981.

[219] W. Bouzid, O. Tsoumarev, and K. Sai, "An investigation of surface roughness of burnished AISI 1042 steel," *The International Journal of Advanced Manufacturing Technology,* vol. 24, no. 1, pp. 120-125, 2004.

[220] A. M. Hassan and A. S. Al-Bsharat, "Influence of burnishing process on surface roughness, hardness, and microstructure of some non-ferrous metals," *Wear,* vol. 199, no. 1, pp. 1-8, 1996.

[221] M. El-Axir, "An investigation into roller burnishing," *International Journal of Machine Tools and Manufacture,* vol. 40, no. 11, pp. 1603-1617, 2000.

[222] W. B. Saï and J. Lebrun, "Influence of finishing by burnishing on surface characteristics," *Journal of Materials Engineering and Performance,* vol. 12, no. 1, pp. 37-40, 2003.

[223] T. Segawa, H. Sasahara, and M. Tsutsumi, "Development of a new tool to generate compressive residual stress within a machined surface," *International Journal of Machine Tools and Manufacture,* vol. 44, no. 11, pp. 1215-1221, 2004.

[224] J. Kodácsy, J. Danyi, A. Szabó, and G. Fülöp, "Magnetic aided roller burnishing metal parts," in *7th International Conference on Deburring and Surface Finishing, UC Berkeley (USA)*, 2004, pp. 375-378.

[225] P. S. Prevéy and J. T. Cammett, "The influence of surface enhancement by low plasticity burnishing on the corrosion fatigue performance of AA7075-T6," *International Journal of Fatigue,* vol. 26, no. 9, pp. 975-982, 2004.

[226] A. M. Hassan and S. Z. Al-Dhifi, "Improvement in the wear resistance of brass components by the ball burnishing process," *Journal of materials processing technology,* vol. 96, no. 1-3, pp. 73-80, 1999.

[227] P. Peyre *et al.*, "Surface modifications induced in 316L steel by laser peening and shot-peening. Influence on pitting corrosion resistance," *Materials Science and Engineering: A,* vol. 280, no. 2, pp. 294-302, 2000.

[228] G. F. Vander Voort, *Atlas of time-temperature diagrams for irons and steels*. ASM international, 1991.

[229] C. Magee, "Phase transformations," *ASM, Metals Park, OH,* vol. 11556, 1970.

[230] *JMatPro*. (2007). Sente Software Ltd., Surrey, UK.

[231] R. Indhu, V. Vivek, L. Sarathkumar, A. Bharatish, and S. Soundarapandian, "Overview of laser absorptivity measurement techniques for material processing," *Lasers in Manufacturing and Materials Processing,* vol. 5, no. 4, pp. 458-481, 2018.

[232] F. Dausinger and J. Shen, "Energy coupling efficiency in laser surface treatment," *ISIJ international,* vol. 33, no. 9, pp. 925-933, 1993.

[233] J. Volpp, H. S. Dewi, A. Fischer, and T. Niendorf, "Influence of complex geometries on the properties of laser-hardened surfaces," *The International Journal of Advanced Manufacturing Technology,* vol. 107, no. 9, pp. 4255-4260, 2020.

[234] B. Shi, A. Elsayed, A. Damir, H. Attia, and R. M'Saoubi, "A hybrid modeling approach for characterization and simulation of cryogenic machining of Ti–6Al–4V alloy," *Journal of Manufacturing Science and Engineering,* vol. 141, no. 2, 2019.

[235] S. Fraser, M. Attia, and M. Osman, "Modelling, identification and control of thermal deformation of machine tool structures, part 3: Real-time estimation of heat sources," 1999.

[236] S. Fraser, M. Attia, and M. Osman, "Modelling, identification and control of thermal deformation of machine tool structures, part 2: Generalized transfer functions," 1998.